

Carnegie Mellon University
MELLON COLLEGE OF SCIENCE

THESIS

SUBMITTED IN PARTIAL FULFILLMENT OF THE REQUIREMENTS
FOR THE DEGREE OF

DOCTOR OF PHILOSOPHY IN THE FIELD OF PHYSICS

TITLE: "Measurement of spin density matrix elements in the reaction $\gamma p \rightarrow K^+ \Lambda(1520)$ using CLAS at Jefferson Lab"

PRESENTED BY: William Levine

ACCEPTED BY THE DEPARTMENT OF PHYSICS

CURTIS MEYER	02/22/16
<hr/>	
CURTIS MEYER, CHAIR PROFESSOR	DATE

STEPHEN GAROFF	02/22/16
<hr/>	
STEPHEN GAROFF, DEPT HEAD	DATE

APPROVED BY THE COLLEGE COUNCIL

FRED GILMAN	02/22/16
<hr/>	
FRED GILMAN, DEAN	DATE

**Measurement of spin density matrix elements in
the reaction $\gamma p \rightarrow K^+ \Lambda(1520)$ using CLAS at
Jefferson Lab**

by

William I. Levine

Submitted in partial fulfillment of the
requirements for the degree of
Doctor of Philosophy

at

Carnegie Mellon University
Department of Physics
Pittsburgh, Pennsylvania

Advised by Professor Curtis Meyer

February 22, 2016

Abstract

This work presents a measurement of the spin density matrix elements of the $\Lambda(1520)$ in the reaction $\gamma p \rightarrow K^+ \Lambda(1520)$. The elements measured are ρ_{11} , $\text{Re}(\rho_{31})$, and $\text{Re}(\rho_{3-1})$. The spin density matrix elements, together with differential cross sections, can provide information about the production mechanism of the $\Lambda(1520)$. The data used is from the g11a run period, collected at the CLAS detector at Jefferson Lab. The $\Lambda(1520)$ was detected via the pK^- decay mode, and three topologies, $p(K^+)K^-$, $pK^+(K^-)$, and pK^+K^- , were studied to maximize kinematic coverage. The measurements cover the center-of-mass energy range from 2.04 GeV to 2.82 GeV and almost the full range of the production angle. These are the first measurements of these quantities over much of this kinematic region, and the large dataset allows us to use much finer binning than all previous measurements. These measurements do not match predictions from existing models and can provide the basis for a better theoretical understanding of $\Lambda(1520)$ photoproduction.

Acknowledgments

First of all, I would like to thank my advisor, Curtis Meyer, who has given me guidance and support for over six years, since my first semester at CMU. Obviously, this work would not exist with him. Thanks to Reinhard Schumacher for lending an ear whenever I had a tricky problem, and for help navigating the CLAS collaboration. Thanks also go to the rest of my thesis committee, Brian Quinn, Gregg Franklin, and Justin Stevens, whose tough questions and helpful comments were much appreciated and helped make this thesis better.

Thanks to the rest of the CMU medium energy group as well. Yves Van Haarlem helped me with my first project here and Brian Vernarsky taught me about all the software I used for this analysis. Kei Moriya gave me the idea to work on the $\Lambda(1520)$ in the first place and has been a friend and mentor. Thanks to the post-docs Paul Mattione, Haiyun Lu, and Vahe Mamyan for everything, but especially for ping-pong breaks. I have been lucky enough to share my office with extraordinary people: my wonderful current officemates Naomi Jarvis and Will McGinley and my completely excellent former officemate Megan Friend. I met Dao Ho even before I moved to Pittsburgh, and we've been friends since. Mike Staib has been great to talk to about both physics and non-physics matters.

Huge thanks to all the members of the CLAS and GlueX collaborations. Literally none of my work would have been possible without you. Special thanks to the grad student contingent of both collaborations who always ensured that my trips to JLab were not just productive, but fun.

Thanks so much to all of my fellow CMU grad students, you made grad school bearable. Special thanks to Ying Zhang, who was a great roommate, always up for watching a movie, or for a discussion on world politics. Udom Sae-Ueng, You-Cyuan Jhang, Yu Feng, Yutaro Iiyama, Patrick Mende, and Robert Haussman also deserve thanks; I can't even describe how much your friendship has meant to me. Zach McDargh has been a good friend and a steadfast source of rides to cool music shows.

Of course, there are people outside of physics who deserve thanks as well. Thanks to my Pittsburgh friends Mike McCann and Matt Cleinman for lunch, puzzles, shows, and everything else; I couldn't imagine any better people to spend my time outside Wean Hall with. Thanks to my non-Pittsburgh friends, especially Tony Pham, who I chatted with so often it almost felt like he was in Pittsburgh. And finally, thanks to my family, who have always been there for me.

Contents

1	Introduction	1
1.1	The strong force	1
1.1.1	The quark model	1
1.1.2	QCD	2
1.2	The $\Lambda(1520)$	3
1.3	$\Lambda(1520)$ photoproduction	4
1.3.1	Possible production methods	4
1.3.2	Differential cross sections, polarization observables, and the spin density matrix	6
1.3.3	Previous results	6
1.3.4	Theoretical models and predictions	10
1.4	Summary	12
2	The spin density matrix in spin-$\frac{3}{2}$ photoproduction	13
2.1	The spin density matrix	14
2.1.1	The photon spin density matrix	14
2.1.2	Spin- $\frac{3}{2}$ spin density matrix	15
2.1.3	The spin density matrix in scattering reactions	16
2.2	The $\gamma p \rightarrow K^+ \Lambda(1520)$ reaction	17
2.2.1	Decomposition of ρ^Λ	18
2.2.2	Parity relations	19
2.2.3	Decay amplitudes	20
2.2.4	Decay distributions	21
2.2.5	Reference frames	23
2.2.6	Spin density matrix elements from fit amplitudes	24
3	Experimental apparatus	25
3.1	CEBAF	25
3.2	Photon beam and tagger	27
3.3	The CLAS detector	28
3.3.1	Target	29
3.3.2	Start Counter	29
3.3.3	Toroidal Magnet and Drift Chambers	31
3.3.4	Time-of-Flight Scintillators	31
3.3.5	CLAS Coordinate Systems	34
3.4	Trigger and Data Acquisition	34

4	Event Selection	35
4.1	Excluded runs	35
4.2	Kinematic fitting	36
4.3	Energy and momentum corrections	37
4.3.1	Energy loss corrections	37
4.3.2	Momentum corrections and tagger energy corrections	38
4.4	Particle ID from timing measurements	38
4.5	Detector performance cuts	39
4.5.1	Fiducial cuts	39
4.5.2	TOF paddles	39
4.6	pK^+K^- topology	40
4.6.1	Skimming	40
4.6.2	Timing Cuts	40
4.6.3	Kinematic fitting	42
4.7	$pK^+(K^-)$ topology	43
4.7.1	Skimming	43
4.7.2	Timing cuts	43
4.7.3	Kinematic fitting	43
4.8	$pK^-(K^+)$ topology	45
4.8.1	Skimming	45
4.8.2	Timing cuts	45
4.8.3	Kinematic fitting	45
4.9	ϕ cut	45
5	Acceptance and Monte Carlo	49
5.1	Simulation	49
5.1.1	Event generation	49
5.1.2	GSIM and GPP	50
5.1.3	Momentum smearing	50
5.1.4	Trigger simulation	50
5.1.5	Summary	53
6	Background	54
6.1	The Q-value method	54
6.2	3-track topology	56
6.2.1	Baseline fit	57
6.2.2	Variations on the baseline	60
6.3	Missing K^+ topology	61
6.4	Missing K^- topology	61
6.4.1	Stage 1	63
6.4.2	Stage 2	69
6.5	Differential cross sections	69
6.6	Summary	69
7	Results and discussion	74
7.1	SDME extraction	74
7.1.1	Statistical errors and the bootstrap method	74
7.1.2	Fit quality	78
7.1.3	Acceptance-corrected angular distributions	83
7.2	Combining topologies	83
7.3	Other systematics	87

7.3.1	Background	87
7.3.2	$\Lambda(1520)$ peak selection	89
7.3.3	ϕ cut	93
7.3.4	Non- pK^- decays of the $\Lambda(1520)$	93
7.3.5	Combining errors	93
7.4	Discussion	99
7.4.1	Comparison with models	99
7.4.2	Comparison with earlier results	99
7.4.3	Summary and conclusion	102
A	Maximum likelihood fitting	109
A.1	Using Monte Carlo method to account for acceptance in maximum likelihood fits . . .	110
B	Lineshapes	112
C	Resonant amplitudes, the mother fit, and differential cross section extraction	117
C.1	Spin- $\frac{1}{2}$ representation	117
C.2	Spin-1 representation	119
C.2.1	Massless vector particles	120
C.3	Integer spin $J > 1$ polarization tensors	120
C.4	$J > \frac{1}{2}$ fermions	121
C.5	Orbital angular momentum tensors	122
C.6	Parity	122
C.7	$J^P \rightarrow NV$	123
C.7.1	Angular Momentum Coupling	123
C.7.2	$P = (-)^{J+\frac{1}{2}}$ amplitudes $(\frac{1}{2}^-, \frac{3}{2}^+, \frac{5}{2}^-, \dots)$	124
C.7.3	$P = (-)^{J-\frac{1}{2}}$ amplitudes $(\frac{1}{2}^+, \frac{3}{2}^-, \frac{5}{2}^+, \dots)$	124
C.8	$\gamma p \rightarrow J^P$	125
C.8.1	$P = (-)^{J+\frac{1}{2}}$ amplitudes $(\frac{1}{2}^-, \frac{3}{2}^+, \frac{5}{2}^-, \dots)$	127
C.8.2	$P = (-)^{J-\frac{1}{2}}$ amplitudes $(\frac{1}{2}^+, \frac{3}{2}^-, \frac{5}{2}^+, \dots)$	127
C.9	$\frac{3}{2}^- \rightarrow \frac{1}{2}^+ 0^-$	127
C.10	$J^P \rightarrow \frac{3}{2}^- 0^-$	127
C.10.1	$P = (-)^{J+\frac{1}{2}}$ amplitudes $(\frac{1}{2}^-, \frac{3}{2}^+, \frac{5}{2}^-, \dots)$	128
C.10.2	$P = (-)^{J-\frac{1}{2}}$ amplitudes $(\frac{1}{2}^+, \frac{3}{2}^-, \frac{5}{2}^+, \dots)$	128
C.11	Full amplitude	128
C.12	How the amplitudes are really calculated	129
C.13	Mother fit and differential cross section extraction	129
C.13.1	Photon flux and normalization	131
D	Table of results and additional plots	132
D.1	Table of spin density matrix elements	132
D.2	Additional plots	136

Chapter 1

Introduction

1.1 The strong force

The existence of a force other than electromagnetism and gravity is demanded by the existence of nuclei, in which positively charged protons and electrically neutral neutrons are tightly bound together. This force, which is simply called the strong force, is characterized by its strength relative to the electromagnetic force (which allows nuclei to form despite Coulomb repulsion) and by the short distance range of the force (which means that it can be ignored for any system in which particles are separated by more than a few femtometers). A fourth force, the weak force, is also a short-range force and is distinguished because it can transmute particles between different species. The observed particles that interact via the strong force are called hadrons. Hadrons consist of baryons, which are fermions, and mesons, which are bosons. After the proton and neutron (both baryons), the next hadron to be discovered was a meson, the pion. Then, the particles now known as the kaon or K (a meson) and Λ (a baryon) were discovered; these particles were called “strange” particles. They are produced in strong reactions but decay slowly (a characteristic of weak interactions). Strange particles were also observed to be produced in pairs. Because of this, Gell-Mann and Nishijima proposed that there exists a quantity called strangeness, which is conserved in strong reactions, but not in weak reactions. The Λ has strangeness -1 while different varieties of the kaon have either strangeness $+1$ or -1 .

1.1.1 The quark model

The first hadrons to be discovered—the π , K , and Λ , as well as the strange baryon Σ and the strangeness -2 Ξ baryon—were all discovered in reactions originating from cosmic rays. With the advent of particle accelerators in the 1950s, the number of known hadrons increased greatly.

Gell-Mann and Ne’eman organized the multitude of hadrons according to the Eightfold way, shown in Figure 1.1, which is based on $SU(3)$ flavor symmetry. This leads to the quark model. In the quark model, baryons are composed of three quarks, and mesons of one quark and one antiquark. Originally only three types (or flavors) of quarks were known: up ($q = \frac{2}{3}$), down ($q = -\frac{1}{3}$), and strange ($q = -\frac{1}{3}$ with strangeness $S = -1$). $SU(3)$ flavor symmetry originates from the symmetry between the three types of quarks. In fact, $SU(3)$ symmetry is broken since the strange quark is significantly more massive than the other two, which are approximately the same mass, and $SU(2)$ “isospin” symmetry, which involves only up and down quarks, is a much better symmetry. However, the representations of $SU(3)$ still explain the observed pattern of hadrons lying in singlets, octets, and decuplets.

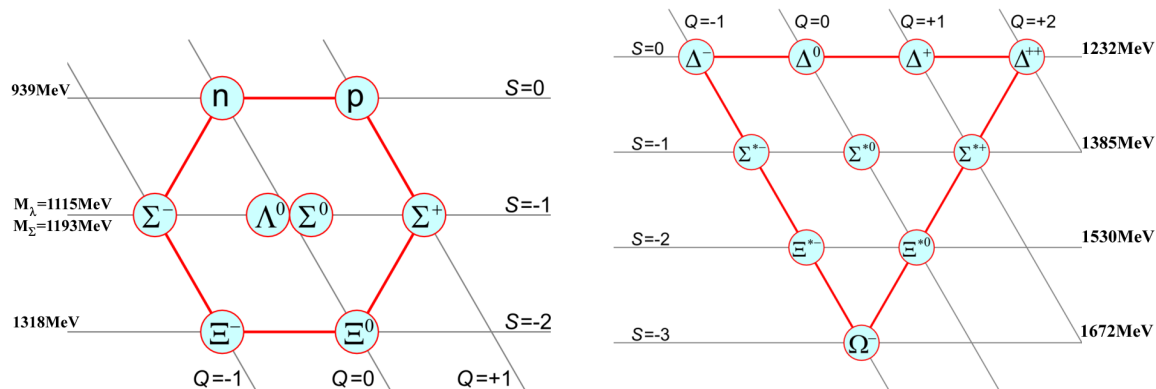


Figure 1.1: Ground state octet and decuplet baryons. The arrangement and properties of these particles are dictated by SU(3) flavor symmetry. Mesons can be similarly presented.

1.1.2 QCD

The quark model did not provide a complete theory of the strong interaction. It did not explain why only qqq or $q\bar{q}$ states are ever observed, while single quarks and qq states are never observed. In addition, in the first version of the quark model, states like the Δ^{++} , with quark content uuu , seemed to be forbidden by the Pauli exclusion principle. To resolve this, it was proposed that each quark carries an additional property called “color”, which can take on one of three values, called red, green, and blue. There is a symmetry between these three colors called SU(3) color, to distinguish from SU(3) flavor. It was also declared that only color singlets (which can be formed by either combining a color with its anti-color or by an anti-symmetric combination of all three colors) can be observed in nature. If this is assumed, the observation of single quarks is forbidden.

It turned out that rather than being an ad-hoc correction, SU(3) color is of fundamental importance. Quantum chromodynamics (QCD) is the quantum field theory constructed by introducing SU(3) color as a gauge symmetry. This gauge symmetry mandates the existence of colored gauge bosons, called gluons, which carry the strong force. Since gluons are colored, they, like quarks, cannot be observed in isolation. It was eventually accepted that QCD is the underlying theory of the strong interaction. QCD has several important lessons.

The underlying degrees of freedom in QCD are quarks and gluons. However, QCD quarks (“current” quarks) are not really the same as quark-model quarks (“constituent” quarks). Both types of quarks come in the same flavors, but the current-quark masses are much smaller than the corresponding constituent-quark masses. Roughly, a hadron can be thought of as consisting of valence quarks (the qqq or $q\bar{q}$ from the quark model) which determine the flavor of the hadron, as well as sea quarks (always in matching $q\bar{q}$ pairs) and gluons. A hadron’s mass (or a constituent quark mass) comes from the energy of the sea quarks and gluons as well as the valence quarks.

Gluons only couple to colored objects: quarks and other gluons. The strong force was originally observed in interactions between hadrons, but it is also responsible for interactions within hadrons. The interactions with hadrons are mediated directly by gluons, while the interactions between hadrons are mediated by other hadrons.

As shown in Figure 1.2, the coupling, or strength, of the QCD interaction varies strongly with energy scale, as measured by the four-momentum transfer Q . At high energies (or equivalently short distances), the coupling is small so quarks only interact weakly. This is known as asymptotic freedom. In this range, perturbative methods can be used to solve QCD. Good agreement between theory and experiment is found. At larger distance scales, the coupling is strong and perturbative methods cannot be used. This means it is difficult to apply QCD to understand hadrons and nuclei. Lattice QCD, which consists of numerical simulation of quark and gluon fields in a discretized version

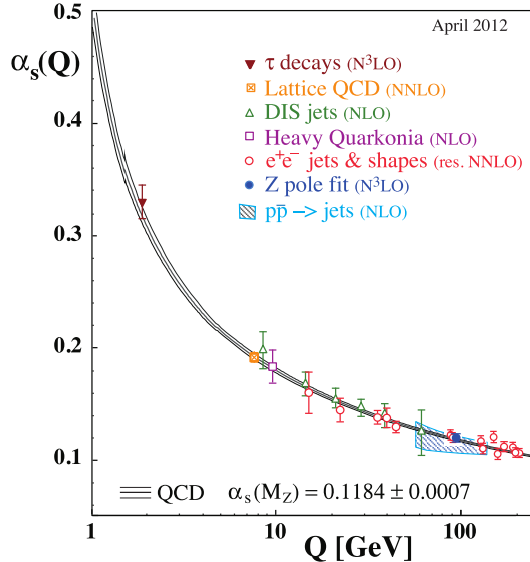


Figure 1.2: Plot of the strong coupling, α_s , as a function of four-momentum transfer Q . From [1].

of spacetime, is one non-perturbative method for studying hadrons, but is limited by the massive computational power required. To understand hadrons, various non-QCD models (including the quark model), which provide approximate calculations at best, are still used.

Confinement, the restriction that colored particles (quarks and gluons) are always tightly confined in color singlet particles (hadrons), is not fully understood as a mathematical consequence of QCD, but can be shown to exist in lattice gauge theories [2].

1.2 The $\Lambda(1520)$

The $\Lambda(1520)$ is a baryon with spin and parity $J^P = \frac{3}{2}^-$, first observed in 1962 in the hadronic reaction $K^-p \rightarrow \Lambda(1520)$ [3]. Like all Λ baryons it is an isoscalar with quark content uds . The largest decay modes are NK (45%), $\Sigma\pi$ (42%), and $\Lambda\pi\pi$ (including $\Sigma(1385)\pi$) (10%). It has mass $M = 1519.5 \pm 1.0$ MeV and width $\Gamma = 15.6 \pm 1.0$ MeV [1]; this is a much smaller width than typical for strongly decaying baryons containing only up, down, and strange quarks (only the doubly-strange $\Xi(1530)$ is narrower).

Λ baryons always belong to SU(2) isospin singlets, but can belong either to SU(3) octets or singlets. The $\Lambda(1520)$ is sometimes classified within the quark model as a SU(3) flavor singlet state [1]. However, because SU(3) symmetry is broken, octet-singlet mixing is possible. One indication that the $\Lambda(1520)$ cannot be a pure SU(3) singlet is that the $\Sigma(1385)\pi$ decay mode is observed, while SU(3) symmetry forbids a pure singlet decay into a decuplet baryon and an octet meson. The $\Sigma(1385)\pi$ branching ratio can be used to calculate a singlet-octet mixing angle [4]. Other theoretical [5] and experimental [6] approaches also confirm that, within a quark model interpretation, the $\Lambda(1520)$ is predominantly singlet, but with some octet mixing. One problem with the quark model interpretation is that quark-model calculations tend to predict that the lightest $\Lambda\frac{3}{2}^-$ and the lightest $\Lambda\frac{1}{2}^-$ (both predominantly singlet) should be nearly degenerate [7]. In reality, the lowest $\Lambda\frac{1}{2}^-$ is the $\Lambda(1405)$, and there is no $\Lambda\frac{1}{2}^-$ state near the $\Lambda(1520)$. For this reason, non-three-quark explanations of both the $\Lambda(1405)$ and $\Lambda(1520)$ have been pursued. It has been proposed that the $\Lambda(1520)$ is a quasibound state of $\Sigma(1385)\pi$ [8], suggested because the $\Lambda(1520)$ mass is nearly equal to the sum

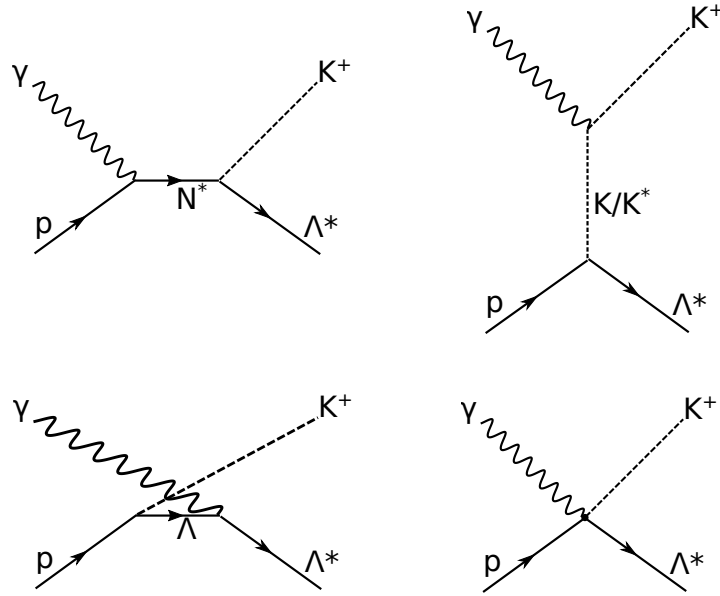


Figure 1.3: Possible production mechanisms: s -channel, t -channel, u -channel, and contact term. The first three diagrams also apply to photoproduction off the neutron with the K^+ replaced by K^- . The contact term is absent for photoproduction off the neutron.

of the $\Sigma(1385)$ and the π masses, and also because the decay $\Lambda(1520) \rightarrow \Sigma(1385)\pi$ is strong despite being kinematically unfavored.

1.3 $\Lambda(1520)$ photoproduction

With the operation of modern facilities like Jefferson Lab, electromagnetic production of hadrons (both photoproduction and electroproduction) has given us much insight into hadronic physics. The $\Lambda(1520)$ is created by different mechanisms in photoproduction than in hadronic beam experiments.

1.3.1 Possible production methods

At low energies, the photoproduction of the $\Lambda(1520)$, $\gamma N \rightarrow K\Lambda(1520)$, can be modeled using hadronic interactions, including the tree-level diagrams shown in Figure 1.3 and discussed below.

s -channel production of $K\Lambda(1520)$ is of theoretical interest. Because the $\Lambda(1520)$ is an isoscalar, the s -channel exchange particle must be an N^* . The narrow width of the $\Lambda(1520)$ means the $N^* \rightarrow K\Lambda(1520)$ decay can be treated like a two-body decay, and the high mass of the $K\Lambda(1520)$ system (relative to other two-body N^* decays) could make it a preferred decay channel for high-mass baryons. The problem of “missing” baryons, which are predicted by the quark model but not observed, is particularly acute at high masses. Capstick and Roberts, using the 3P_0 pair creation model together with a relativistic quark model, have predicted N^* couplings to both $K\Lambda(1520)$ and γN [9]. They predict that in the $\gamma N \rightarrow K\Lambda(1520)$ reaction, three quark-model N^* states should contribute significantly: $\frac{1}{2}^-(1945)$, $\frac{5}{2}^-(2080)$, $\frac{3}{2}^-(1960)$. These three quark-model states may correspond to tentatively established observed states listed in the PDG (the Capstick and

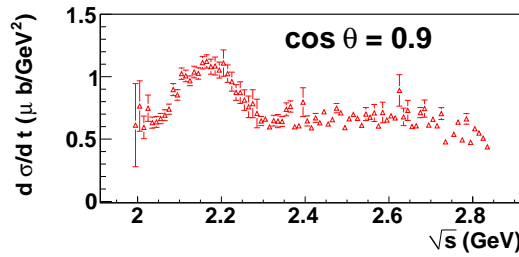


Figure 1.4: $\gamma p \rightarrow \phi p$ differential cross section at forward angle vs center-of-mass energy [12].

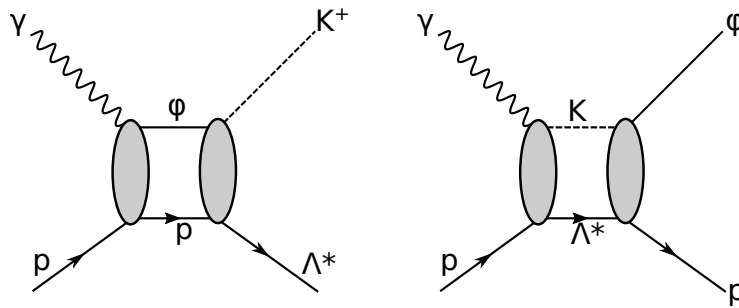


Figure 1.5: Box diagrams illustrating $K^+\Lambda(1520)$ - ϕp coupled-channel effects, which could be significant in both channels.

Roberts paper claimed that the $\frac{5}{2}^-$ state was missing, while the other two corresponded to known states, however the experimental situation has changed since then and this is no longer clearly the case).

t -channel production can proceed by the exchange of a pseudoscalar K or a vector K^* . It is usually characterized by a step rise in differential cross section at forward angles.

u -channel production involves the exchange of a ground-state or excited Λ . It will produce a rise in differential cross section at backwards angle.

The contact term is introduced to preserve gauge invariance. It is absent for photoproduction off neutron: $\gamma n \rightarrow K^0\Lambda(1520)$. Thus, the contribution of the contact term will be apparent when comparing cross sections off the proton vs neutron.

It has also been proposed that the interaction of the $K^+\Lambda(1520)$ system with the ϕp system could be significant [10, 11]. This could lead to the production of a $K^+\Lambda(1520)$ system via a ϕp intermediate state, as shown in Figure 1.5. This idea is motivated by a bump in the $\gamma p \rightarrow \phi p$ differential cross section (only at forward angles) near the $K\Lambda(1520)$ threshold (see Figure 1.4), which does not seem to come from an s -channel resonance. The $\gamma p \rightarrow K^+\Lambda(1520)$ cross section data also shows a similar bump (see Figure 1.8). Thus studying $\Lambda(1520)$ photoproduction may elucidate ϕ photoproduction and vice versa.

At higher energies, where contributions from resonances are smaller, Regge theory, a pre-QCD theory of the strong interaction, is known to give a good model of reactions.

1.3.2 Differential cross sections, polarization observables, and the spin density matrix

Experimental observables are the things we can measure in $\Lambda(1520)$ photoproduction, which help us understand which of the above production mechanisms contribute.

The simplest observable is the differential cross section, which, along with the luminosity, determines the rate at which the process occurs as a function of the angle of the produced particles. Details on calculating the differential cross section from experimental data are given in Eq. (C.87).

The other observables are polarization observables, which include both information about the spin state of the outgoing $\Lambda(1520)$ and also information on how the polarization of the initial state photon and proton affects the reaction. Polarization observables are discussed most generally in a density matrix formalism. The spin density matrix of the $\Lambda(1520)$ is determined by observing the angular distribution of its decay products; the full details are given in Chapter 2 (although we do not discuss the case where the initial state proton is polarized).

To interpret these observables, a model is generally needed (see Section 1.3.4). However, some simple interpretations are possible by just looking at the data. As discussed above, t - and u -channel exchanges tend to produce rising cross section at forward and backward angles, respectively. Also, a simple interpretation of spin density matrix elements (SDMEs) in terms of t -channel exchanges is given in Section 2.2.5. However, in general, several processes will contribute rather than a single one and identifying these can be quite tricky.

1.3.3 Previous results

Several studies of the photoproduction of the $\Lambda(1520)$ have been published; some report only cross sections, a few also report decay distributions or spin density matrix elements. Early measurements by Crouch et al. [13] and Blanpied et al. [14] at the Cambridge Electron Accelerator, Mistry et al. [15] at Cornell, and Boyarski et al. [16] at SLAC provided the first measurements of the $\gamma p \rightarrow K^+ \Lambda(1520)$ differential and total cross sections.

The LAMP2 collaboration at Daresbury (Barber et al.) [17] measured the total cross section at several energies in the range $2.8 < E_\gamma < 4.8 \text{ GeV}$ ($2.5 < \sqrt{s} < 3.1 \text{ GeV}$) and the differential cross section, averaged over this energy range, at several values of t . As shown in Figure 1.6, they also measured the decay angular distribution in the Gottfried-Jackson frame (the Gottfried-Jackson frame is defined in Section 2.2.5). From these distributions, they extracted the spin density matrix elements ρ_{33} , ρ_{11} , $\text{Re } \rho_{31}$, and $\text{Re } \rho_{3-1}$. However, the distribution is averaged over all energies and angles.

The LEPS Collaboration has published two papers on $\Lambda(1520)$ photoproduction, both with photon energies near threshold. In the first, Muramatsu et al. [18] provide results for $\Lambda(1520)$ photoproduction from both protons and deuterons. These are the only published results on $\Lambda(1520)$ photoproduction from deuterons. These results indicate that, at backwards K^+/K^0 angles, where the measurements off the deuteron were made, the differential cross section for the process $\gamma n \rightarrow K^0 \Lambda(1520)$ is at least an order of magnitude smaller than for $\gamma p \rightarrow K^+ \Lambda(1520)$. Interestingly, not-yet-published results from the thesis of Zhiwen Zhao [19], using CLAS photoproduction data with a deuteron target, indicate that the $\gamma n \rightarrow K^0 \Lambda(1520)$ and $\gamma p \rightarrow K^+ \Lambda(1520)$ cross sections are roughly equal, at least at forward angles. In addition to their cross section measurements, Muramatsu et al. also report a measurement of the photon beam asymmetry Σ (from protons) (see Section 2.2.4) at forward angles, which is consistent with zero, and measurements of the decay distributions (also from protons). As shown in Figure 1.7, they report the angular distributions separately for forward and backwards production angles, but average over the full energy range of the experiment. They fit these distributions to a function of the form

$$\alpha \left(\frac{1}{3} + \cos^2 \theta \right) + \beta \sin^2 \theta + \gamma \cos \theta, \quad (1.1)$$

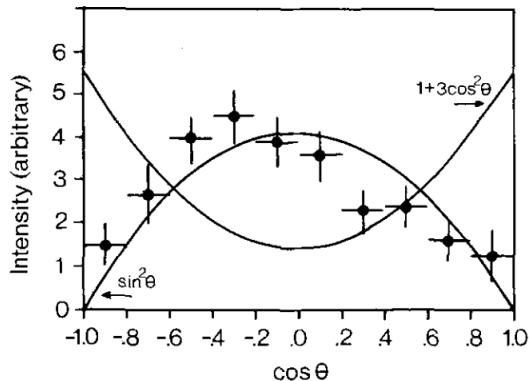


Figure 1.6: Decay angular distribution in Gottfried-Jackson frame measured by Barber et al. [17]. Includes events with energies in the range $2.5 < \sqrt{s} < 3.1$ GeV and at all production angles. The curves show the distributions that would be measured if the $\Lambda(1520)$ were produced entirely in the $\pm\frac{3}{2}(\sin^2\theta)$ or $\pm\frac{1}{2}(1+3\cos^2\theta)$ spin substates.

as suggested by Barrow et al. [20]. The first term is from the contribution of $\Lambda(1520)$ in the $m_z = \pm\frac{1}{2}$ substate, the second for $\Lambda(1520)$ $m_z = \pm\frac{3}{2}$, and the third term could come from interference terms between spin- $\frac{1}{2}$ hyperons and the spin- $\frac{3}{2}$ $\Lambda(1520)$. A pure spin- $\frac{1}{2}$ contribution would give a flat decay distribution which would contribute equally to the first two terms. No measurement of ϕ_{GJ} (azimuthal decay angle) distributions are reported. Neither beam asymmetry nor decay distribution measurements are reported for photoproduction on deuterons. The second LEPS paper, by Kohri et al. [21], only deals with the $\gamma p \rightarrow K^+\Lambda(1520)$ reaction and reports differential cross sections and beam asymmetries, but not decay distributions. These results are notable as they reveal a “bump” structure in the cross section at around $\sqrt{s} = 2110$ MeV, as shown in Figure 1.8.

Results from Wieland et al. from SAPHIR [23] and Moriya et al. from CLAS [24] confirm a peak in the cross section at around $\sqrt{s} = 2100$ MeV. The CLAS paper reports differential cross sections across a wide range of production angles, shown in Figure 1.9, which show a slight rise at backward angles, possibly indicating u -channel production. SAPHIR also measured decay distributions, shown in Figure 1.10. However, the SAPHIR paper may have used an incorrect definition of the Gottfried-Jackson frame (t -channel helicity frame). In the text, they write “the t -channel helicity frame z -axis is defined as anti-parallel to the incident photon in the $\Lambda(1520)$ rest frame”, which is incorrect. For meson decays, the Gottfried-Jackson frame is defined in this way, but for baryon decays the z -axis is defined as anti-parallel to the target nucleon direction in the $\Lambda(1520)$ rest frame (see Section 2.2.5). In the $\Lambda(1520)$ rest frame, the target nucleon and the incident photon are not back-to-back, so the difference between these two definitions is non-trivial. However, despite the mistake in the text, in Figure 15 of the paper, illustrating the Gottfried-Jackson frame, they show the correct definition of the decay angle θ_{GJ} .

The electroproduction reaction $ep \rightarrow eK^+\Lambda(1520)$ is closely related to the photoproduction reaction, proceeding by the same electromagnetic process, but with photon virtuality $Q^2 \neq 0$. In addition to an early cross section measurement [27], the process was studied by the CLAS collaboration, with Barrow et al. [20] publishing decay distributions (ϕ_{GJ} distributions as well as $\cos\theta_{GJ}$ distributions, see Figure 1.11) as well as cross sections. Qiang et al. studied the electroproduction process to measure the mass and width of the $\Lambda(1520)$ [28].

Preliminary results available in the Zhao’s thesis report differential cross sections and decay angular distributions off protons and neutrons as measured in the reactions $\gamma d \rightarrow K^+\Lambda(1520)(n)$ and $\gamma d \rightarrow K^0\Lambda(1520)(p)$ [19].

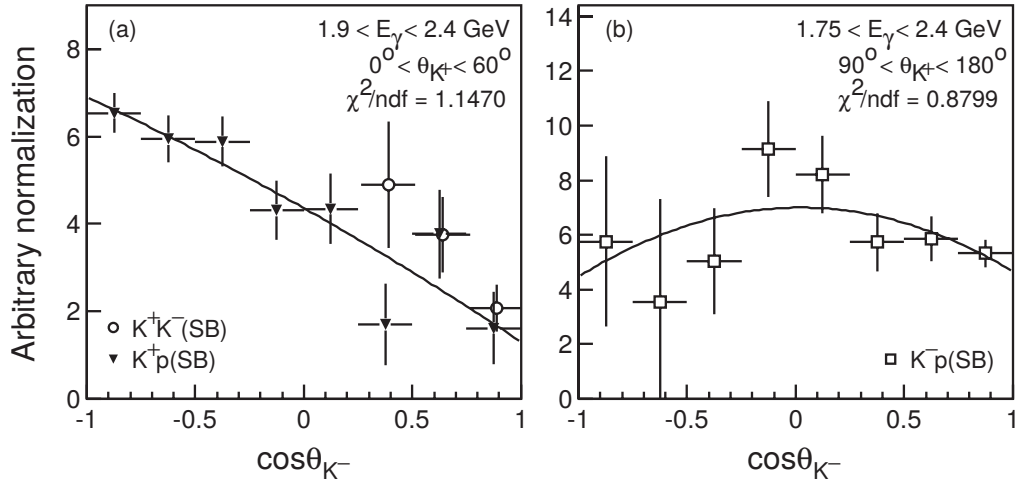


Figure 1.7: Decay angular distribution in Gottfried-Jackson frame measured by Muramatsu et al. [18]. On the left is the distribution at forward production angles ($0^\circ < \theta_{K^+} < 60^\circ$) and on the right at backwards production angles ($90^\circ < \theta_{K^+} < 180^\circ$). Since LEPS can only detect particles at forward angles, backwards production angles are only accessible if the K^+ is not detected ($K^-p(K^+)$ topology, open squares). The results at forward angle come from the $K^+K^-(p)$ topology (open circles) and the $K^+p(K^-)$ topology (closed triangles). Both plots cover the full range of energies measured. The curves are best fits to the function (1.1).

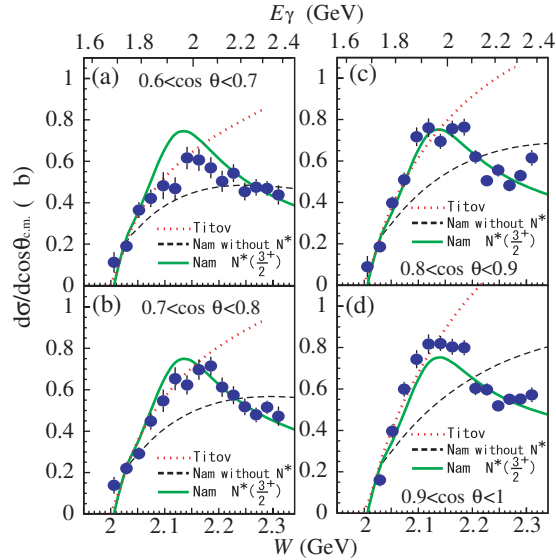


Figure 1.8: Differential cross sections as a function of energy, in four different angular bins, as measured by Kohri et al. [21]. The red dotted curve shows the prediction of Titov et al. [22] (discussed in further detail in Section 1.3.4). The green solid (black dashed) curve shows the model of Nam et al., fitted to the plotted data, with (without) a contribution from a hypothesized $\frac{3}{2}^+ N^*$ state.

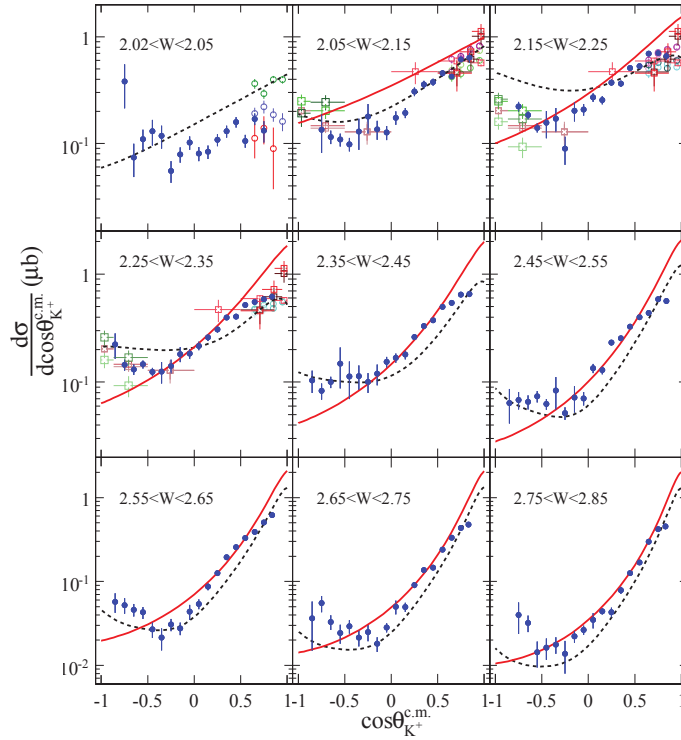


Figure 1.9: Differential cross sections as measured by the CLAS collaboration, shown in solid blue circles [24]. Also shown are results from both LEPS papers: Muramatsu et al. [18] (hollow squares) and Kohri et al. [21] (hollow circles). The red curve shows the model curve of Nam and Kao [25] and the dashed black curve shows the model of He and Chen [26].

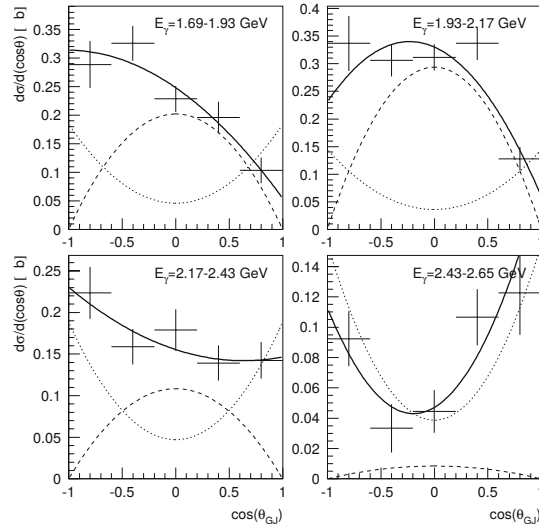


Figure 1.10: Decay distributions in four bins of energies, summed over all production angles, measured by Wieland et al. [23]. Solid curves are fits to the function (1.1), dashed curve are the components of the fits corresponding to the first two terms.

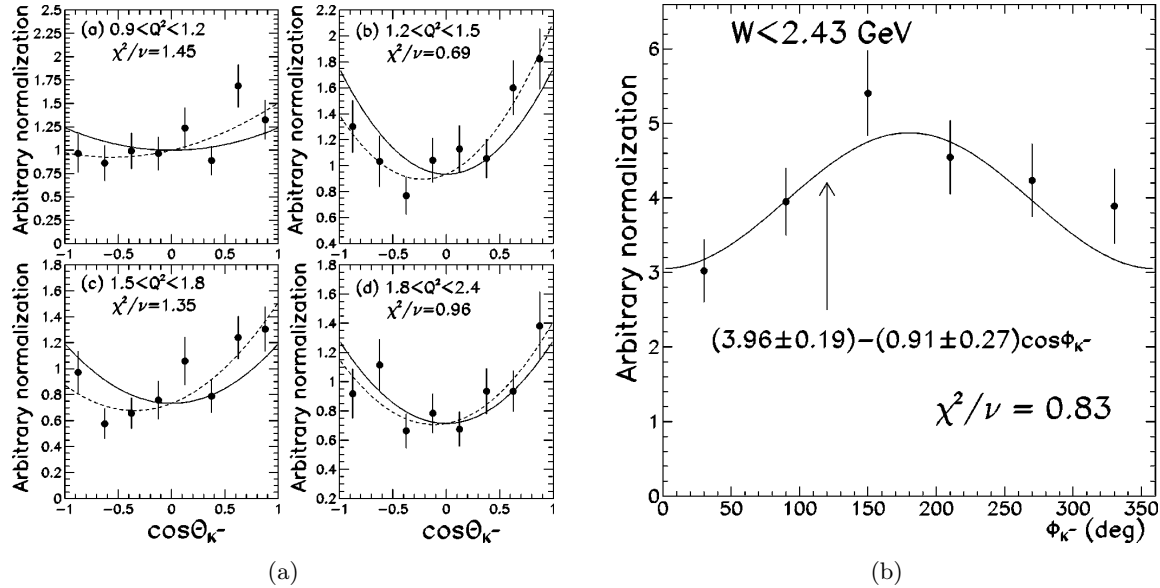


Figure 1.11: $\Lambda(1520)$ decay distribution in electroproduction [20]. ϕ_{GJ} distribution (b) is averaged over all kinematic variables, while the $\cos\theta_{GJ}$ distributions (a) are binned in Q^2 and averaged over all other variables. W , the invariant mass of the $K^+\Lambda(1520)$, ranges from threshold to 2.43 GeV. In (a), the dashed curve is a fit to the function (1.1), the solid curve shows the sum of the first two terms of the function only. In (b), the curve is a best fit to $A + B \cos\phi$.

1.3.4 Theoretical models and predictions

Nam et al. have published a series of papers predicting $\Lambda(1520)$ photoproduction observables using an effective-Lagrangian model with K and K^* t -channel exchange, s -channel exchange, u -channel exchange, and a contact term [29, 30, 25]. The parameters for their models are chosen using guidance from the quark model as well as the experimental data from LAMP2 and SLAC. They claim that the process is dominated by the contact term, and that the SDME measurements from LAMP2, which were thought to be evidence for K^* exchange, are actually due to the contact term. Due to the contact term, they predict that the neutron cross section should be much smaller, a prediction which was confirmed at backwards angles by Muramatsu et al. at LEPS, but appears to be contradicted by preliminary results from Zhao. The most interesting paper is the most recent one, which also incorporates both results from LEPS. This also includes an s -channel contribution from the $D_{13}(2080) N^*$ state (now called $N^*(2120)\frac{3}{2}^-$ by the PDG), as suggested by Capstick and Roberts. Additionally, this paper uses a Regge model for the t -channel exchanges. This predicts decay angular distributions as shown in Figure 1.12. Predictions are also made for differential cross sections, beam asymmetry, and polarization-transfer coefficients (observables measured with circularly-polarized beam).

Titov et al. also use an effective-Lagrangian plus Regge approach [22, 31], but only predict differential cross sections, which are shown compared to experimental data in Figure 1.8. Toki et al. consider three models for $\gamma p \rightarrow K^+\Lambda(1520)$: an effective-Lagrangian model near threshold, a Regge model at higher energies, and a hybrid model for intermediate energies [32]. In this model, they conclude that the t -channel is dominated by the pseudoscalar K exchange and the contribution from the K^* is negligible, which is the opposite claim as that made by Titov. Only differential cross sections are predicted. Xie et al., using an effective-Lagrangian model, also claim that K^* exchange is negligible, and claim to be able to match both LEPS and CLAS differential cross sections [33].

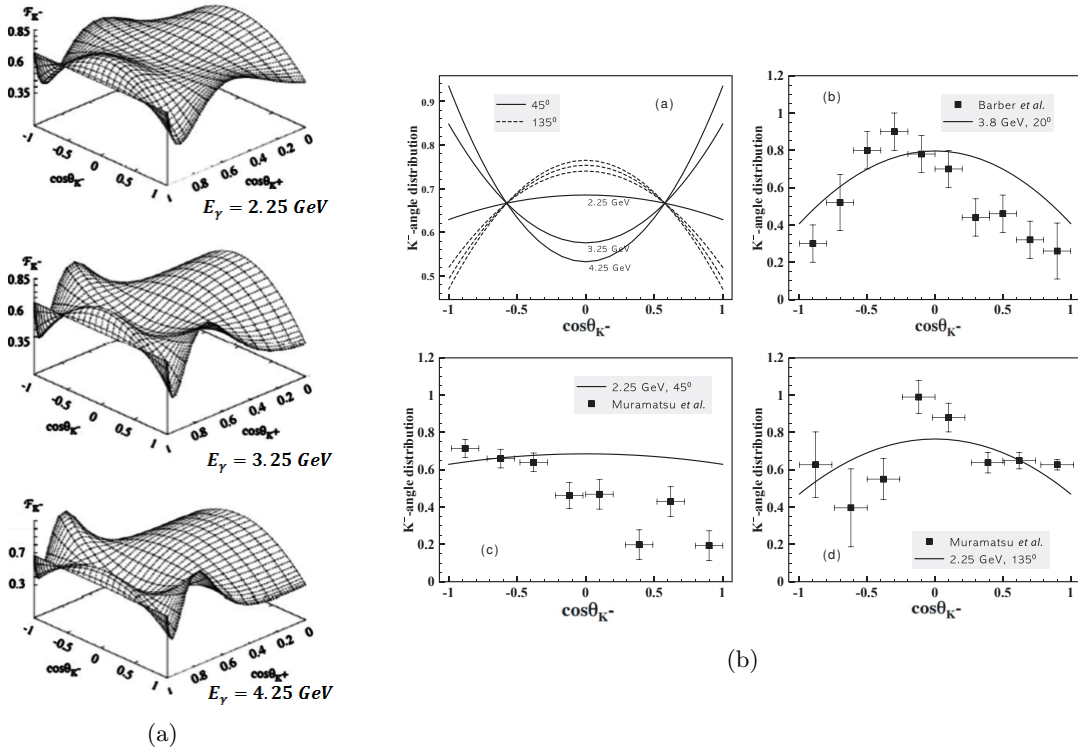


Figure 1.12: Angular distributions predicted by Nam and Kao [25]. (a) shows $\cos \theta_{K^-}$ distributions ($\cos \theta_{K^-}$ denotes the decay angle in the Gottfried-Jackson frame) as a function of $\cos \theta_{K^+}$ (the production angle in the center-of-mass frame) for three different energies. The upper-left plot in (b) shows decay distributions at $\theta_{K^+} = 45^\circ$ and $\theta_{K^+} = 135^\circ$ at the same three energies. The next three plots in (b) compare experimental results with the model at the appropriate energy and angle.

This model includes an s -channel contribution from $N^*(2120)$ and a u -channel Λ contribution; the authors claim that these contributions are both significant. Only differential cross sections are predicted. A later paper by the same authors, which uses an effective-Lagrangian plus Regge approach, confirms their earlier results in terms of the contribution from s -channel $N^*(2120)$ and u -channel Λ and the lack of a K^* exchange; they also report that at higher energies, the introduction of a K -Regge-trajectory exchange is important for matching experimental results [34]. He and Chen study the contribution of nucleon resonances using the LEPS results and the earlier LAMP2 and SLAC results [26]. They use an effective Lagrangian with the standard diagrams. They find the $D_{13}(2080)$ (aka $N^*(2120)$) to contribute strongly, and also find experimental evidence for a $\frac{5}{2}^-$ state at around 2080 MeV, as predicted by Capstick and Roberts (the 2014 PDG has a $N^*(2060)\frac{5}{2}^-$ state, which before 2012 was listed as $N^*(2200)$). Predictions for differential cross sections and beam asymmetry are given. A later paper by He, which also incorporates the CLAS differential cross section results, also finds that a contribution from the $N^*(2120)$ is needed to match experimental results [35].

Sibirtsev et al. take a different approach, studying the general $\gamma N \rightarrow K \bar{K} N$ reaction rather than $\gamma N \rightarrow K \Lambda(1520)$ [36]. They attempt to use only the Drell mechanism, which involves only pseudoscalar K exchange, but they find that they must add an additional contribution from K^* exchange to match the $\Lambda(1520)$ cross section results from LAMP2.

Papers by Ozaki et al. [10] and Ryu et al. [11] discuss coupled-channel effects between the $\gamma p \rightarrow K^+ \Lambda(1520)$ and $\gamma p \rightarrow \phi p$ channels. Both papers briefly discuss the $K^+ \Lambda(1520)$ differential cross section, but are mostly focused on the ϕ .

1.4 Summary

In this thesis, we study the process $\gamma p \rightarrow K^+ \Lambda(1520)$, which is governed by the strong force. QCD is the theory of the strong force, but is useless at making predictions about this process and many other similar processes in hadronic physics. We are left with mere models, which are all in disagreement. Particular points of disagreement include the role of K vs K^* exchange, the contribution from s -channel N^* resonances, and a possible interaction with the ϕp system. The additional data presented here should help constrain these models and advance our understanding.

Chapter 2

The spin density matrix in spin- $\frac{3}{2}$ photoproduction

The density operator formalism provides the most general way of describing a quantum mechanical system, capable of describing both pure and mixed states. A pure state is a state that corresponds to a single state vector. For example, if a beam of light has passed through a polarizer, then the spin state of any photon in the beam is known exactly, can be expressed with a single state vector, and is a pure state. Systems can also exist in mixed states, which are probabilistic mixtures of pure states. There are two common situations in which mixed states arise. The first is when a system is part of a statistical mixture, for which ensemble averages are known, but not the exact properties of the individual systems. For example, in an unpolarized beam of light, the total polarization is known, but the exact state of an individual photon is unknown. The state of an individual photon cannot be expressed as a state vector, however, it can be expressed as a probabilistic mixture of pure states. Mixed states also occur if the system of interest is entangled within a larger system (the larger system itself may be in a pure state). It is only possible to specify a state vector for the larger system, and it is not possible to describe the subsystem with a single state vector. As in the case above, the subsystem can also be expressed as a probabilistic mixture of pure states. The density operator is particularly useful for dealing with mixed states, but also can describe pure states. For finite-dimensional systems, the density operator can be expressed in terms of a density matrix, after choosing a basis of states. A good reference on the density operator is provided by Nielsen and Chuang [37]. We will review some relevant facts. A density operator ρ must satisfy two conditions: the trace condition, $\text{Tr } \rho = 1$, and the positivity condition, which requires that all eigenvalues of ρ are non-negative. Given these two properties, it is always possible to find a (not necessarily unique) decomposition of ρ :

$$\rho = \sum_i p_i |\psi_i\rangle \langle \psi_i|, \quad (2.1)$$

such that the vectors $|\psi_i\rangle$ are orthogonal, p_i are the (non-negative) eigenvalues of ρ , and $\sum_i p_i = 1$. This decomposition makes it apparent how ρ can describe a system that is a probabilistic mixture of pure states: the system has a probability p_i of being in the pure state described by $|\psi_i\rangle$.

Having defined ρ , we can now derive its properties. Time evolution of an ordinary quantum state is described by a unitary transformation U , such that $|\psi\rangle \rightarrow U|\psi\rangle$. From (2.1), it can be seen that the time evolution of a density operator describing a closed system is given by the transformation

$$\rho \rightarrow U\rho U^\dagger. \quad (2.2)$$

Quantum measurements are often described in terms of an observable, which corresponds to a single Hermitian operator on the space of states. However, we present here a different way of

describing a measurement, which can be shown to be equivalent. A measurement on a quantum system is described by a set of measurement operators $\{M_m\}$, where m labels possible measurement outcomes, with $\sum_m M_m^\dagger M_m = I$. If a system is initially in state $|\psi\rangle$ and is then measured, with the outcome of the measurement being m' , the system is then in state $\frac{M_{m'}|\psi\rangle}{\sqrt{\langle\psi|M_{m'}^\dagger M_{m'}|\psi\rangle}}$. Thus for a system initially described by ρ , then measured as m' , the system is described by the new density operator

$$\rho' = \frac{M_{m'}\rho M_{m'}^\dagger}{\text{Tr}(M_{m'}^\dagger M_{m'}\rho)}. \quad (2.3)$$

The probability of measuring outcome m' is

$$P(m') = \text{Tr}(M_{m'}^\dagger M_{m'}\rho). \quad (2.4)$$

The density operator ρ of a composite quantum system of n unentangled subsystems is given by the tensor product of the density operators ρ_i of the component systems:

$$\rho = \rho_1 \otimes \rho_2 \otimes \cdots \otimes \rho_n. \quad (2.5)$$

To reverse this procedure, and obtain the density operator of a subsystem of a composite system, we must introduce the concept of the partial trace. For a composite system of subsystems A and B , described by density operator ρ^{AB} , the density operator of subsystem A is

$$\rho^A = \text{Tr}_B(\rho^{AB}), \quad (2.6)$$

where the partial trace over B , Tr_B , is defined as a linear operator such that

$$\text{Tr}_B(|a_1\rangle\langle a_2| \otimes |b_1\rangle\langle b_2|) = |a_1\rangle\langle a_2| \text{Tr}(|b_1\rangle\langle b_2|), \quad (2.7)$$

for any vectors $|a_1\rangle, |a_2\rangle$ in A and $|b_1\rangle, |b_2\rangle$ in B . It can easily be seen that this gives the correct result when the composite system is built using (2.5), but the partial trace prescription also works in cases where the subsystems are entangled with each other and (2.5) does not apply.

2.1 The spin density matrix

For finite-dimensional quantum systems (like the spin of a particle), the density operator can be expressed as a matrix called the density matrix.

2.1.1 The photon spin density matrix

The simplest non-trivial density matrix is that of a two-state quantum system which is just a 2×2 matrix. This will describe the spin state of a spin- $\frac{1}{2}$ particle or a massless gauge boson like the photon. Since the photon is relevant to us, we will study this case further. We will use the helicity basis $\{|\lambda_\gamma = +1\rangle, |\lambda_\gamma = -1\rangle\}$, where the photon helicity λ_γ is the projection of the spin onto the direction of momentum. $\lambda_\gamma = +1$ corresponds to right-circularly polarized light and $\lambda_\gamma = -1$ to left-circularly polarized light (unlike other spin-1 particles, the photon can never have $\lambda_\gamma = 0$). For linearly polarized photons, we follow the convention of Schilling [38]. Consider a linearly polarized photon with momentum parallel to the z -axis. The polarization vector of this photon has no components parallel to the momentum and can be written

$$\vec{\epsilon} = (\cos \Phi, \sin \Phi, 0). \quad (2.8)$$

We then write the state vector of this photon:

$$|\gamma\Phi\rangle = -\frac{1}{\sqrt{2}}(e^{-i\Phi} |\lambda_\gamma = +1\rangle - e^{i\Phi} |\lambda_\gamma = -1\rangle). \quad (2.9)$$

Using the hermiticity (implied by positivity) and trace conditions we can write the general form of the density matrix:

$$\rho^\gamma = \begin{pmatrix} a & c \\ c^* & 1-a \end{pmatrix}, \quad (2.10)$$

where a is a real number and c is complex. The full positivity condition requires $0 \leq a(1-a) - |c|^2 \leq \frac{1}{4}$. This can be rewritten in the form

$$\rho^\gamma = \frac{1}{2}(I + \vec{P}_\gamma \cdot \vec{\sigma}), \quad (2.11)$$

where I is the identity matrix, \vec{P}_γ is any 3-vector with $0 \leq |\vec{P}_\gamma| \leq 1$, and $\vec{\sigma}$ are the standard Pauli matrices. The polarization of a photon beam is specified by the vector \vec{P}_γ . Using (2.1) and the definition of the polarization states above we can interpret the meaning of \vec{P}_γ . We find that for an unpolarized beam $\vec{P}_\gamma = \vec{0}$, for a circularly polarized beam $\vec{P}_\gamma = P_\gamma(0, 0, \pm 1)$, where P_γ is the degree of polarization, and for a linearly polarized beam $\vec{P}_\gamma = P_\gamma(-\cos 2\Phi, -\sin 2\Phi, 0)$, where Φ is used as defined in (2.8) to specify the polarization vector. Elliptical polarization can also be described by adding the linear and circularly polarized cases.

2.1.2 Spin- $\frac{3}{2}$ spin density matrix

For a spin- $\frac{3}{2}$ particle like the $\Lambda(1520)$, the spin density matrix can be expressed as a 4×4 Hermitian matrix. For notational simplicity, we denote the elements as $\rho_{2\lambda_\Lambda 2\lambda'_\Lambda}$. Thus, the $+\frac{3}{2}, +\frac{3}{2}$ element will be denoted as ρ_{33} . Because the matrix is Hermitian, the 4 diagonal elements are real, and the off-diagonal elements satisfy the relationship $\rho_{\lambda\lambda'} = \rho_{\lambda'\lambda}^*$:

$$\rho^\Lambda = \begin{pmatrix} \rho_{33} & \rho_{31} & \rho_{3-1} & \rho_{3-3} \\ \rho_{31}^* & \rho_{11} & \rho_{1-1} & \rho_{1-3} \\ \rho_{3-1}^* & \rho_{1-1}^* & \rho_{-1-1} & \rho_{-1-3} \\ \rho_{3-3}^* & \rho_{1-3}^* & \rho_{-1-3}^* & \rho_{-3-3} \end{pmatrix}. \quad (2.12)$$

The diagonal elements must satisfy the trace condition

$$\rho_{33} + \rho_{11} + \rho_{-1-1} + \rho_{-3-3} = 1. \quad (2.13)$$

The positivity condition will enforce additional restrictions (inequalities) on the ρ elements, which we will not derive here. We note that ρ^Λ is specified by 15 real parameters: 3 come from the 4 real diagonal ρ elements with one constraint, plus 12 from the 6 unique complex off-diagonal ρ elements.

The density matrix can also be expressed in terms of the parameters t_{LM} , which are called multipole parameters or statistical tensors. Using the following equations from Jackson [39], we can derive the relationships between the t_{LM} and the elements of ρ :

$$\rho_{mm'} = \frac{1}{2j+1} \sum_{LM} (2L+1) \langle jm | jLm' M \rangle t_{LM}^* \quad (2.14)$$

$$t_{L,-M} = (-1)^M t_{LM}^* \quad (2.15)$$

$$t_{00} = 1. \quad (2.16)$$

In our case $j = \frac{3}{2}$. Calculating explicitly:

$$\rho_{33} = \frac{1}{4} \left(1 + 3\sqrt{\frac{3}{5}}t_{10} + 5\sqrt{\frac{1}{5}}t_{20} + 7\sqrt{\frac{1}{35}}t_{30} \right) \quad (2.17a)$$

$$\rho_{-3-3} = \frac{1}{4} \left(1 - 3\sqrt{\frac{3}{5}}t_{10} + 5\sqrt{\frac{1}{5}}t_{20} - 7\sqrt{\frac{1}{35}}t_{30} \right) \quad (2.17b)$$

$$\rho_{11} = \frac{1}{4} \left(1 + 3\sqrt{\frac{1}{15}}t_{10} - 5\sqrt{\frac{1}{5}}t_{20} - 7\sqrt{\frac{9}{35}}t_{30} \right) \quad (2.17c)$$

$$\rho_{-1-1} = \frac{1}{4} \left(1 - 3\sqrt{\frac{1}{15}}t_{10} - 5\sqrt{\frac{1}{5}}t_{20} + 7\sqrt{\frac{9}{35}}t_{30} \right) \quad (2.17d)$$

$$\rho_{31} = \frac{1}{4} \left(-3\sqrt{\frac{2}{5}}t_{11}^* - 5\sqrt{\frac{2}{5}}t_{21}^* - 7\sqrt{\frac{4}{35}}t_{31}^* \right) \quad (2.17e)$$

$$\rho_{-1-3} = \frac{1}{4} \left(-3\sqrt{\frac{2}{5}}t_{11}^* + 5\sqrt{\frac{2}{5}}t_{21}^* - 7\sqrt{\frac{4}{35}}t_{31}^* \right) \quad (2.17f)$$

$$\rho_{3-1} = \frac{1}{4} \left(5\sqrt{\frac{2}{5}}t_{22}^* + 7\sqrt{\frac{2}{7}}t_{32}^* \right) \quad (2.17g)$$

$$\rho_{1-3} = \frac{1}{4} \left(5\sqrt{\frac{2}{5}}t_{22}^* - 7\sqrt{\frac{2}{7}}t_{32}^* \right) \quad (2.17h)$$

$$\rho_{3-3} = \frac{1}{4} \left(-7\sqrt{\frac{4}{7}}t_{33}^* \right) \quad (2.17i)$$

$$\rho_{1-1} = \frac{1}{4} \left(-3\sqrt{\frac{8}{15}}t_{11}^* + 7\sqrt{\frac{12}{35}}t_{31}^* \right). \quad (2.17j)$$

Again ρ is specified by 15 real numbers: 3 real parameters t_{L0} and 6 unique complex parameters $t_{L,M>0}$. One feature of this expansion is that the t_{LM} are defined in such a way that they transform like the spherical harmonics Y_{LM} under rotation. t_{1M} transforms like a vector (in the spherical basis), t_{2M} like a rank-2 tensor, etc. Transforming from the spherical basis to Cartesian coordinates and applying the appropriate normalization [39], we can calculate $\langle \vec{S} \rangle$, the expectation value of the spin, in terms of t_{LM} :

$$\langle \vec{S} \rangle = \sqrt{\frac{15}{4}}(-\sqrt{2} \operatorname{Re} t_{11}, -\sqrt{2} \operatorname{Im} t_{11}, t_{10}). \quad (2.18)$$

2.1.3 The spin density matrix in scattering reactions

The discussion in section 2.1.2 applies to any spin- $\frac{3}{2}$ particle, no matter now it was created. Now we discuss the spin density matrix of a particle produced in a scattering reaction. We begin with the general case.

Consider a scattering reaction where the initial state is specified by one discrete spin label λ_i and the final state of interest is specified by one continuous variable Ω and one discrete variable λ_f (for now we ignore the fact that there might be other variables like the total energy that are not fixed). The initial state is given by the density operator ρ^i :

$$\rho^i = \sum_{\lambda_i \lambda'_i} \rho_{\lambda_i \lambda'_i}^i |\lambda_i\rangle \langle \lambda'_i|. \quad (2.19)$$

The details of scattering process are given in the transition operator:

$$T_{\lambda_f \lambda_i}(\Omega) = \sum_{\lambda_i} \sum_{\lambda_f} \int d\Omega T_{\lambda_f \lambda_i}(\Omega) |\Omega \lambda_f\rangle \langle \lambda_i|. \quad (2.20)$$

The final-state density operator is

$$\rho^f = CT\rho^i T^\dagger = C \sum_{\lambda_f \lambda'_f} \sum_{\lambda_i \lambda'_i} \int d\Omega d\Omega' \rho_{\lambda_i \lambda'_i}^i T_{\lambda_f \lambda_i}(\Omega) T_{\lambda'_f \lambda'_i}^*(\Omega') |\Omega \lambda_f\rangle \langle \Omega' \lambda'_f|, \quad (2.21)$$

where the constant C is chosen so that ρ^f will be a legitimate density operator with trace 1. It is necessary to include this constant since T is not normalized so that $\text{Tr}(T^\dagger T) = 1$, instead T is normalized so that it is related to the cross section by something like equation (2.27).

ρ^f is not a spin density matrix, since it includes information about the continuous variable Ω as well as the spin information. To measure the spin density matrix, we need to take into account that we have already measured Ω . Let's say we measured the value of Ω as Ω_m . The operator associated with this measurement value is $M(\Omega_m) = |\Omega_m\rangle \langle \Omega_m| \otimes I$, where I is the identity operator in spin- $\frac{3}{2}$ space. Thus $M(\Omega_m)$ projects out the part of the state with Ω_m , while leaving the spin part unchanged. According to (2.3), the density operator after this measurement is given by

$$\rho^{f'}(\Omega_m) = \frac{M(\Omega_m)\rho^f M^\dagger(\Omega_m)}{\text{Tr}(M^\dagger(\Omega_m)M(\Omega_m)\rho^f)} = \frac{1}{N(\Omega_m)} \sum_{\lambda_f \lambda'_f} \sum_{\lambda_i \lambda'_i} \rho_{\lambda_i \lambda'_i}^i T_{\lambda_f \lambda_i}(\Omega_m) T_{\lambda'_f \lambda'_i}^*(\Omega_m) |\Omega_m \lambda_f\rangle \langle \Omega_m \lambda'_f|, \quad (2.22)$$

with

$$N(\Omega_m) = \sum_{\lambda_f} \sum_{\lambda_i \lambda'_i} \rho_{\lambda_i \lambda'_i}^i T_{\lambda_f \lambda_i}(\Omega_m) T_{\lambda_f \lambda'_i}^*(\Omega_m). \quad (2.23)$$

At this point, since Ω_m is fixed, we can drop the label Ω_m in the vector $|\Omega_m \lambda_f\rangle$ and interpret $\rho^{f'}(\Omega_m)$ as a true spin density matrix.

2.2 The $\gamma p \rightarrow K^+ \Lambda(1520)$ reaction

In studying the reaction $\gamma p \rightarrow K^+ \Lambda(1520)$, we will consider the case of a polarized photon beam, specified by a spin density matrix ρ^γ , but not the case in which the target nucleons are polarized. To be complete, we would use (2.5) to include both photon and nucleon spin in the initial-state spin density matrix. However, since we are considering an unpolarized target, this would just tell us to average over initial nucleon spins, which we can do just as easily without dealing with the extra notation that the nucleon spin density matrix would introduce.

We also make the simplifying assumption that the transition operator does not depend on the invariant mass of the $\Lambda(1520)$. This approximation would hold exactly if the width of the $\Lambda(1520)$ was 0.

We define our coordinate system in the overall center-of-mass (CM) frame with the z -axis parallel to the photon momentum and the y -axis normal to the production plane. Formally, we define \vec{k} as the photon momentum, \vec{q} as the K^+ momentum and the three axes as

$$\hat{z} = \frac{\vec{k}}{|\vec{k}|}; \quad \hat{y} = \frac{\vec{k} \times \vec{q}}{|\vec{k} \times \vec{q}|}; \quad \hat{x} = \hat{y} \times \hat{z}. \quad (2.24)$$

Since \vec{q} has no y -component, when specifying the production angle of the K^+ we only need to use one angle θ_{K^+} , rather than two angles θ_{K^+} and ϕ_{K^+} . However, if we have a linearly polarized photon beam, the photon polarization angle Φ , which is fixed in the lab frame, is not fixed in the

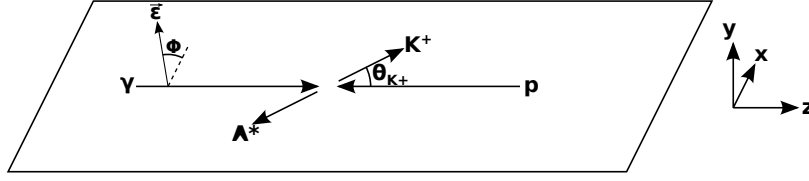


Figure 2.1: Illustration of the coordinate frame used for studying the production process. The $\vec{\epsilon}$ and Φ are only relevant in the case of a linearly polarized photon beam

frame we have just defined and needs to be specified on an event-by-event basis. This is illustrated in Figure 2.1.

Following Schilling [38], we define ρ^Λ in the helicity basis:

$$\rho_{\lambda_\Lambda \lambda'_\Lambda}^\Lambda(\theta_{K^+}) = \frac{1}{N(\theta_{K^+})} \sum_{\lambda_N \lambda_\gamma \lambda'_\gamma} T_{\lambda_\Lambda \lambda_\gamma \lambda_N}(\theta_{K^+}) \rho_{\lambda_\gamma \lambda'_\gamma}^\gamma T_{\lambda'_\Lambda \lambda'_\gamma \lambda_N}^*(\theta_{K^+}), \quad (2.25)$$

where λ_N is the helicity of the target nucleon ($\lambda_N = \pm\frac{1}{2}$), λ_Λ is the $\Lambda(1520)$ helicity, T is the transition matrix for the production process (also expressed in the helicity basis), and N is the normalization factor:

$$N(\theta_{K^+}) = \frac{1}{2} \sum_{\lambda_N \lambda_\gamma \lambda_\Lambda} |T_{\lambda_\Lambda \lambda_\gamma \lambda_N}(\theta_{K^+})|^2. \quad (2.26)$$

This definition of ρ^Λ is similar to the form of ρ which we derived above (equations (2.22) and (2.23)), but crucially it differs in the normalization. The normalization (2.23) is guaranteed to give us a bona fide trace-1 density matrix, while the normalization (2.26) (following Schilling) may or may not, depending on the polarization of the initial state. As we will see below, it is sometimes more convenient to work with the unnormalized form, which is why we have introduced it here. The good news is that this is just a normalization difference, so ρ^Λ can be made into a proper density matrix just by scaling it so that its trace is 1. To distinguish, we will always use a bold ρ for a density matrix that may not be properly normalized.

The normalization of T is the standard normalization in which the unpolarized cross section is given as

$$\frac{d\sigma}{d\Omega} = \left(\frac{2\pi}{k}\right)^2 \frac{1}{4} \sum_{\lambda_N \lambda_\gamma \lambda_\Lambda} |T_{\lambda_\Lambda \lambda_\gamma \lambda_N}(\theta_{K^+})|^2. \quad (2.27)$$

2.2.1 Decomposition of ρ^Λ

Recall that the photon spin density matrix can be decomposed and expressed in terms of the vector \vec{P}_γ (equation (2.11)). We can decompose ρ^Λ in a similar way to show its explicit dependence on photon polarization. We define four component matrices ρ^α :

$$(\rho^0, \rho^i) = N^{-1} T \left(\frac{1}{2} I, \frac{1}{2} \sigma^i \right) T^\dagger. \quad (2.28)$$

We suppress writing the dependence on θ_{K^+} in this section. We can then write

$$\rho^\Lambda = \rho^0 + \sum_{i=1}^3 P_\gamma^i \rho^i, \quad (2.29)$$

where \vec{P}_γ parametrizes the initial-state density matrix ρ^γ . Explicitly writing these out, we find

$$\rho_{\lambda_\Lambda \lambda'_\Lambda}^0 = \frac{1}{2N} \sum_{\lambda_\gamma \lambda_N} T_{\lambda_\Lambda \lambda_\gamma \lambda_N} T_{\lambda'_\Lambda \lambda_\gamma \lambda_N}^* \quad (2.30a)$$

$$\rho_{\lambda_\Lambda \lambda'_\Lambda}^1 = \frac{1}{2N} \sum_{\lambda_\gamma \lambda_N} T_{\lambda_\Lambda - \lambda_\gamma \lambda_N} T_{\lambda'_\Lambda \lambda_\gamma \lambda_N}^* \quad (2.30b)$$

$$\rho_{\lambda_\Lambda \lambda'_\Lambda}^2 = \frac{i}{2N} \sum_{\lambda_\gamma \lambda_N} \lambda_\gamma T_{\lambda_\Lambda - \lambda_\gamma \lambda_N} T_{\lambda'_\Lambda \lambda_\gamma \lambda_N}^* \quad (2.30c)$$

$$\rho_{\lambda_\Lambda \lambda'_\Lambda}^3 = \frac{1}{2N} \sum_{\lambda_\gamma \lambda_N} \lambda_\gamma T_{\lambda_\Lambda \lambda_\gamma \lambda_N} T_{\lambda'_\Lambda \lambda_\gamma \lambda_N}^* \quad (2.30d)$$

We note that $\text{Tr} \rho^0 = 1$ due to the definition (2.26) of N .

2.2.2 Parity relations

Using symmetry under the operator Π_y , which reflects the system across the x - z plane, we can derive the following relation [40]:

$$\begin{aligned} T_{\lambda_\Lambda \lambda_\gamma \lambda_N}(\theta_{K^+}) &= \eta_\Lambda \eta_\gamma \eta_N \eta_K (-1)^{s_\gamma + s_N - s_\Lambda} (-1)^{-(\lambda_\gamma - \lambda_N) - \lambda_\Lambda} T_{-\lambda_\Lambda - \lambda_\gamma - \lambda_N}(\theta_{K^+}) \\ &= -(-1)^{-\lambda_\gamma + \lambda_N - \lambda_\Lambda} T_{-\lambda_\Lambda - \lambda_\gamma - \lambda_N}(\theta_{K^+}), \end{aligned} \quad (2.31)$$

where the η 's are the intrinsic parities of the particles involved and s are the spins. Note that our choice of coordinate system is important for deriving this relationship: as all the momentum vectors lie in the x - z plane, Π_y does not change the momenta of the particles, only the helicity.

Using equations (2.30) and (2.31) we find

$$\rho_{\lambda \lambda'}^0 = (-1)^{\lambda - \lambda'} \rho_{-\lambda - \lambda'}^0 \quad (2.32a)$$

$$\rho_{\lambda \lambda'}^1 = (-1)^{\lambda - \lambda'} \rho_{-\lambda - \lambda'}^1 \quad (2.32b)$$

$$\rho_{\lambda \lambda'}^2 = -(-1)^{\lambda - \lambda'} \rho_{-\lambda - \lambda'}^2 \quad (2.32c)$$

$$\rho_{\lambda \lambda'}^3 = -(-1)^{\lambda - \lambda'} \rho_{-\lambda - \lambda'}^3 \quad (2.32d)$$

We found earlier that $\text{Tr} \rho^0 = 1$, while (2.32c) and (2.32d) imply that $\text{Tr} \rho^2 = \text{Tr} \rho^3 = 0$. However, there is no restriction on $\text{Tr} \rho^1$, so using equation (2.29), we see, as emphasized before, that $\text{Tr} \rho^\Lambda$ is not guaranteed to be 1. Using equation (2.32a) and the trace condition, we can express all the elements of ρ^0 in terms of seven real numbers:

$$\rho^0 = \begin{pmatrix} \frac{1}{2} - \rho_{11}^0 & \text{Re}(\rho_{31}^0) + i \text{Im}(\rho_{31}^0) & \text{Re}(\rho_{3-1}^0) + i \text{Im}(\rho_{3-1}^0) & i \text{Im}(\rho_{3-3}^0) \\ & \rho_{11}^0 & i \text{Im}(\rho_{1-1}^0) & \text{Re}(\rho_{3-1}^0) - i \text{Im}(\rho_{3-1}^0) \\ & & \rho_{11}^0 & -\text{Re}(\rho_{31}^0) + i \text{Im}(\rho_{31}^0) \\ & & & \frac{1}{2} - \rho_{11}^0 \end{pmatrix}, \quad (2.33)$$

where the missing elements in the lower half can be found by Hermitian conjugation. ρ^1 has the same structure as ρ^0 , except that the trace condition does not hold, so we have eight real parameters:

$$\rho^1 = \begin{pmatrix} \rho_{33}^1 & \text{Re}(\rho_{31}^1) + i \text{Im}(\rho_{31}^1) & \text{Re}(\rho_{3-1}^1) + i \text{Im}(\rho_{3-1}^1) & i \text{Im}(\rho_{3-3}^1) \\ & \rho_{11}^1 & i \text{Im}(\rho_{1-1}^1) & \text{Re}(\rho_{3-1}^1) - i \text{Im}(\rho_{3-1}^1) \\ & & \rho_{11}^1 & -\text{Re}(\rho_{31}^1) + i \text{Im}(\rho_{31}^1) \\ & & & \rho_{33}^1 \end{pmatrix}. \quad (2.34)$$

ρ^2 and ρ^3 share the same symmetry relations and the same form:

$$\rho^2 = \begin{pmatrix} \rho_{33}^2 & \text{Re}(\rho_{31}^2) + i \text{Im}(\rho_{31}^2) & \text{Re}(\rho_{3-1}^2) + i \text{Im}(\rho_{3-1}^2) & \text{Re}(\rho_{3-3}^2) \\ & \rho_{11}^2 & \text{Re}(\rho_{1-1}^2) & -\text{Re}(\rho_{3-1}^2) + i \text{Im}(\rho_{3-1}^2) \\ & & -\rho_{11}^2 & \text{Re}(\rho_{31}^2) - i \text{Im}(\rho_{31}^2) \\ & & & -\rho_{33}^2 \end{pmatrix} \quad (2.35)$$

$$\rho^3 = \begin{pmatrix} \rho_{33}^3 & \text{Re}(\rho_{31}^3) + i \text{Im}(\rho_{31}^3) & \text{Re}(\rho_{3-1}^3) + i \text{Im}(\rho_{3-1}^3) & \text{Re}(\rho_{3-3}^3) \\ & \rho_{11}^3 & \text{Re}(\rho_{1-1}^3) & -\text{Re}(\rho_{3-1}^3) + i \text{Im}(\rho_{3-1}^3) \\ & & -\rho_{11}^3 & \text{Re}(\rho_{31}^3) - i \text{Im}(\rho_{31}^3) \\ & & & -\rho_{33}^3 \end{pmatrix}. \quad (2.36)$$

2.2.3 Decay amplitudes

Up to this point we have calculated the spin density matrix in terms of the transition matrix T . But in reality, T is unknown and we want to measure ρ to help determine T rather than vice versa. To do this, we need to measure the polarization of the $\Lambda(1520)$, which we access through its decay products. To understand how the polarization of the $\Lambda(1520)$ transfers to its decay products, we need to understand the structure of the decay amplitude. The basic form of this amplitude depends only on the spins and parities of the particles involved.

We are interested in the decay $\Lambda(1520) \rightarrow pK^-$, although the formalism developed here applies equally well to $\Lambda(1520) \rightarrow \Sigma\pi$, or any other decay of the form $\frac{3}{2}^- \rightarrow \frac{1}{2}^+ 0^-$. The parities of the particles involved require that the decay must proceed with angular momentum that is even, while, in order to couple spin $\frac{3}{2}$ to spin $\frac{1}{2}$, we must have $L = 1$ or $L = 2$. Thus we know that this is an $L = 2$ decay.

We considered the production process in the overall CM frame with the z -direction pointing along the direction of photon momentum (Figure 2.1), but it is more convenient to use a different frame for analyzing the decay. We consider the decay in the rest frame of the $\Lambda(1520)$. We define the z -axis parallel to the direction of $\Lambda(1520)$ flight in the CM frame (or equivalently, opposite to the direction of K^+ flight in the $\Lambda(1520)$ rest frame). As before, we choose the y -axis so that it is normal to the production plane. We choose to define the z -axis in this way to ensure that M , the z -component of spin of the $\Lambda(1520)$, is the same as its helicity λ_Λ . This allows us to continue to use ρ^Λ in the helicity basis exactly as we have defined it in Equation (2.25), together with the parity relations (2.32), also derived in the helicity basis. It is this careful choice of coordinate system that allows us to switch frames in the middle of our calculation. This new frame is called the helicity frame. Eventually we will want to study the decay in a different coordinate system with a different quantization axis, this is discussed below in Section 2.2.5.

We can write the decay amplitude in the helicity formalism. The initial state $|J = \frac{3}{2}; M\rangle$ is fully specified by M , the z -component of spin of the $\Lambda(1520)$. The final state $|\theta, \phi; \lambda_N\rangle$ is specified by the direction (θ, ϕ) of the K^- and the helicity (λ_N) of the decay proton. We will call the amplitude A . Following the convention of Chung [40], we write the decay amplitude:

$$\begin{aligned} A_{\lambda_N, M}(\theta, \phi) &= \left\langle \theta, \phi; \lambda_N \left| A \right| J = \frac{3}{2}; M \right\rangle \\ &= N F_{\lambda_N} D_{M\lambda_N}^{J=\frac{3}{2}*}(\phi, \theta, 0), \end{aligned} \quad (2.37)$$

where $D^{J=\frac{3}{2}}$ is the Wigner D-matrix and $N = \frac{1}{\pi}$ is a normalization factor. The factor F_{λ_N} is unknown but using a parity relationship from Chung:

$$F_{\lambda_N} = \eta_\Lambda \eta_N \eta_K (-1)^{s_\Lambda - s_N} F_{-\lambda_N}, \quad (2.38)$$

we find simply

$$F_{\frac{1}{2}} = -F_{-\frac{1}{2}}. \quad (2.39)$$

We can rewrite the decay amplitude in terms of a constant $C = NF_{\frac{1}{2}}$:

$$A_{\lambda_N = \pm \frac{1}{2}, M}(\theta, \phi) = \pm CD_{M\lambda_N}^{\frac{3}{2}*}(\phi, \theta, 0). \quad (2.40)$$

2.2.4 Decay distributions

We are now at the point where we can connect the angular distribution of the decay products with the $\Lambda(1520)$ spin density matrix elements.

Since the $\Lambda(1520)$ density matrix can vary with production angle θ_{K^+} , this analysis should be done separately for different production angles. In practice, we bin the data into ranges of θ_{K^+} to determine the production-angle dependence of ρ . Likewise with the CM energy \sqrt{s} . We suppress writing the dependence of ρ on θ_{K^+} and \sqrt{s} in this section.

After the decay, the density operator is

$$\rho^f \propto A \rho^\Lambda A^\dagger = \sum_{\lambda_\Lambda \lambda'_\Lambda} \sum_{\lambda_N \lambda'_N} \int d\Omega d\Omega' A_{\lambda_N \lambda_\Lambda}(\Omega) \rho_{\lambda_\Lambda \lambda'_\Lambda}^\Lambda A_{\lambda'_N \lambda'_\Lambda}^*(\Omega') |\Omega \lambda_N\rangle \langle \Omega' \lambda'_N|, \quad (2.41)$$

where we have switched from using (θ, ϕ) to Ω to denote the decay angles. Repeating the process we used in section 2.1.3, we can find the nucleon spin density matrix as a function of decay angle:

$$\rho_{\lambda_N \lambda'_N}^N(\Omega) = \frac{1}{N(\Omega)} \sum_{\lambda_\Lambda \lambda'_\Lambda} A_{\lambda_N \lambda_\Lambda}(\Omega) \rho_{\lambda_\Lambda \lambda'_\Lambda}^\Lambda A_{\lambda'_N \lambda'_\Lambda}^*(\Omega), \quad (2.42)$$

where $N(\Omega)$ is a normalization factor. But since we don't measure the nucleon polarization, this is not so interesting. What we do measure is the angular distribution $W(\Omega)$, which we can calculate as the probability density of measuring angle Ω . Defining the operator associated with measuring Ω as $M(\Omega) = |\Omega\rangle \langle \Omega| \otimes I$, where I is the spin-space identity, and using equation (2.4), we get

$$W(\Omega) = P(\Omega) = \text{Tr}(M^\dagger(\Omega) M(\Omega) \rho^f) \propto \sum_{\lambda_N} \sum_{\lambda_\Lambda \lambda'_\Lambda} A_{\lambda_N \lambda_\Lambda}(\Omega) \rho_{\lambda_\Lambda \lambda'_\Lambda}^\Lambda A_{\lambda'_N \lambda'_\Lambda}^*(\Omega). \quad (2.43)$$

We evaluate W for the general spin density matrix (2.12):

$W(\cos \theta, \phi) \propto$

$$\begin{aligned} & \rho_{33}(|A_{13}|^2 + |A_{-13}|^2) + \rho_{-3-3}(|A_{1-3}|^2 + |A_{-1-3}|^2) \\ & + \rho_{11}(|A_{11}|^2 + |A_{-11}|^2) + \rho_{-1-1}(|A_{1-1}|^2 + |A_{-1-1}|^2) \\ & + \text{Re}[\rho_{1-1}]2 \text{Re}[A_{11}A_{1-1}^* + A_{-11}A_{-1-1}^*] - \text{Im}[\rho_{1-1}]2 \text{Im}[A_{11}A_{1-1}^* + A_{-11}A_{-1-1}^*] \\ & + \text{Re}[\rho_{3-3}]2 \text{Re}[A_{13}A_{1-3}^* + A_{-13}A_{-1-3}^*] - \text{Im}[\rho_{3-3}]2 \text{Im}[A_{13}A_{1-3}^* + A_{-13}A_{-1-3}^*] \\ & + \text{Re}[\rho_{31}]2 \text{Re}[A_{13}A_{11}^* + A_{-13}A_{-11}^*] - \text{Im}[\rho_{31}]2 \text{Im}[A_{13}A_{11}^* + A_{-13}A_{-11}^*] \\ & + \text{Re}[\rho_{-1-3}]2 \text{Re}[A_{1-1}A_{1-3}^* + A_{-1-1}A_{-1-3}^*] - \text{Im}[\rho_{-1-3}]2 \text{Im}[A_{1-1}A_{1-3}^* + A_{-1-1}A_{-1-3}^*] \\ & + \text{Re}[\rho_{3-1}]2 \text{Re}[A_{13}A_{1-1}^* + A_{-13}A_{-1-1}^*] - \text{Im}[\rho_{3-1}]2 \text{Im}[A_{13}A_{1-1}^* + A_{-13}A_{-1-1}^*] \\ & + \text{Re}[\rho_{1-3}]2 \text{Re}[A_{11}A_{1-3}^* + A_{-11}A_{-1-3}^*] - \text{Im}[\rho_{1-3}]2 \text{Im}[A_{11}A_{1-3}^* + A_{-11}A_{-1-3}^*], \end{aligned} \quad (2.44)$$

where, for notational convenience, we have written the amplitude $A_{\lambda_N \lambda_\Lambda}(\theta, \phi)$ as $A_{2\lambda_N 2\lambda_\Lambda}$. Com-

binning equations (2.40) and (2.44) and using the explicit forms of the D matrix, we find:

$$\begin{aligned}
W(\cos \theta, \phi) \propto & \\
& (\rho_{33} + \rho_{-3-3}) \frac{3}{4} \sin^2 \theta \\
& + (\rho_{11} + \rho_{-1-1}) \frac{1}{4} (1 + 3 \cos^2 \theta) \\
& - \operatorname{Re}[\rho_{31}] \frac{\sqrt{3}}{2} \cos \phi \sin 2\theta + \operatorname{Im}[\rho_{31}] \frac{\sqrt{3}}{2} \sin \phi \sin 2\theta \\
& + \operatorname{Re}[\rho_{-1-3}] \frac{\sqrt{3}}{2} \cos \phi \sin 2\theta - \operatorname{Im}[\rho_{-1-3}] \frac{\sqrt{3}}{2} \sin \phi \sin 2\theta \\
& - \operatorname{Re}[\rho_{3-1}] \frac{\sqrt{3}}{2} \cos 2\phi \sin^2 \theta + \operatorname{Im}[\rho_{3-1}] \frac{\sqrt{3}}{2} \sin 2\phi \sin^2 \theta \\
& - \operatorname{Re}[\rho_{1-3}] \frac{\sqrt{3}}{2} \cos 2\phi \sin^2 \theta + \operatorname{Im}[\rho_{1-3}] \frac{\sqrt{3}}{2} \sin 2\phi \sin^2 \theta.
\end{aligned} \tag{2.45}$$

The ρ_{1-1} and ρ_{3-3} terms drop out entirely and are unobservable in the decay distribution, as are the combinations $(\rho_{33} - \rho_{-3-3})$ and $(\rho_{11} - \rho_{-1-1})$. These can only be measured if the polarization of the decay baryon is measured.

Specializing to the case of a photoproduced $\Lambda(1520)$, we use the decomposition (2.29) to break up the angular distribution:

$$W(\cos \theta, \phi) = C \left[W^0(\cos \theta, \phi) + \sum_{i=1}^3 P_\gamma^i W^i(\cos \theta, \phi) \right], \tag{2.46}$$

where C is a normalization constant so that $\int d\Omega W = 1$.

The W^α 's have the following forms:

$$\begin{aligned}
W^0(\cos \theta, \phi) = \frac{1}{4\pi} \left[3 \left(\frac{1}{2} - \rho_{11}^0 \right) \sin^2 \theta + \rho_{11}^0 (1 + 3 \cos^2 \theta) \right. \\
\left. - 2\sqrt{3} \operatorname{Re}[\rho_{31}^0] \cos \phi \sin 2\theta - 2\sqrt{3} \operatorname{Re}[\rho_{3-1}^0] \cos 2\phi \sin^2 \theta \right]
\end{aligned} \tag{2.47a}$$

$$\begin{aligned}
W^1(\cos \theta, \phi) = \frac{1}{4\pi} \left[3\rho_{33}^1 \sin^2 \theta + \rho_{11}^1 (1 + 3 \cos^2 \theta) \right. \\
\left. - 2\sqrt{3} \operatorname{Re}[\rho_{31}^1] \cos \phi \sin 2\theta - 2\sqrt{3} \operatorname{Re}[\rho_{3-1}^1] \cos 2\phi \sin^2 \theta \right]
\end{aligned} \tag{2.47b}$$

$$W^2(\cos \theta, \phi) = \frac{1}{4\pi} \left[2\sqrt{3} \operatorname{Im}[\rho_{31}^2] \cos \phi \sin 2\theta + 2\sqrt{3} \operatorname{Im}[\rho_{3-1}^2] \cos 2\phi \sin^2 \theta \right] \tag{2.47c}$$

$$W^3(\cos \theta, \phi) = \frac{1}{4\pi} \left[2\sqrt{3} \operatorname{Im}[\rho_{31}^3] \cos \phi \sin 2\theta + 2\sqrt{3} \operatorname{Im}[\rho_{3-1}^3] \cos 2\phi \sin^2 \theta \right] \tag{2.47d}$$

The normalization is chosen so that $\int d\Omega W^0 = 1$. We also find that $\int d\Omega W^{2,3} = 0$. But $\int d\Omega W^1 = 2(\rho_{33}^1 + \rho_{11}^1)$, which is the reason we need the normalization constant in equation (2.46). With an unpolarized beam, we can only measure W^0 , which allows us to measure three independent observables. A linearly polarized beam gives us access to W^1 and W^2 , allowing us to measure six more observables. With a circularly polarized beam we can access W^3 and two more observables.

After this chapter, we will only discuss the case of an unpolarized photon beam, where $\rho = \rho^0$, so we will drop the superscript on ρ^0 .

We can study the unpolarized case in terms of the statistical tensors discussed in Section 2.1.2. We use the parity relation (2.32a) in combination with our tensor/SDME conversion (2.17) and the decay distribution (2.47a). We find that $t_{10} = 0$ and that t_{11} is purely imaginary and cannot be

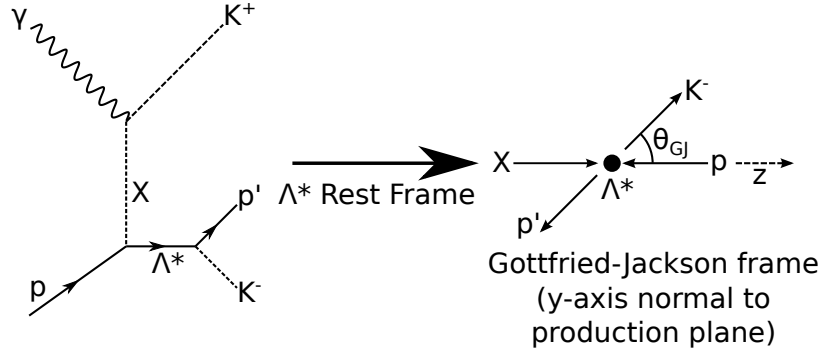


Figure 2.2: Relationship between the Gottfried-Jackson frame and t -channel exchange processes. The diagram on the left is a Feynman-like diagram, which is not intended to show momentum, while the one on the right shows actual momentum vectors viewed in the $\Lambda(1520)$ rest frame.

measured from the decay distribution. Using (2.18) this means the average spin points along the y -axis (normal to the production plane), as we would expect from symmetry considerations. In addition we find that $t_{30} = 0$, while t_{31} , t_{32} , and t_{33} are pure imaginary and not measurable. Using (2.47a), we can only measure the rank-2 tensor polarization t_{20} , t_{21} , and t_{22} , which are all pure real. Similar analysis can be done for the polarized case.

For convenience, we also define the beam asymmetry observable, Σ , measured using a linearly polarized photon beam. This is measured by the LEPS collaboration [18, 21]. Nam and Kao define the beam asymmetry as

$$\Sigma = \frac{\frac{d\sigma}{d\Omega}_{\perp} - \frac{d\sigma}{d\Omega}_{\parallel}}{\frac{d\sigma}{d\Omega}_{\perp} + \frac{d\sigma}{d\Omega}_{\parallel}}, \quad (2.48)$$

where \perp and \parallel denote photon polarizations perpendicular and parallel to the production plane. This can be computed in terms of spin density matrix elements:

$$\Sigma = \int d\Omega W^1 = 2(\rho_{33}^1 + \rho_{11}^1). \quad (2.49)$$

2.2.5 Reference frames

The coordinate system defined in Section 2.2.3 is called the helicity frame. But it is conventional to use a different frame, the Gottfried-Jackson frame, for analyzing the $\Lambda(1520)$ decay. The Gottfried-Jackson frame, also called the t -channel helicity frame, is defined so that the z -axis is opposite to the direction of target nucleon in the $\Lambda(1520)$ rest frame. As before, the y -axis is defined to be normal to the production plane. The usefulness of this frame choice becomes apparent if we assume that the $\Lambda(1520)$ has been produced in a t -channel exchange process. As shown in Figure 2.2, the z -axis is parallel to the momentum of X , the exchanged particle. Since the proton and X momenta lie along the z -axis, any orbital angular momentum between the two particles must have a z -component of zero and we find that the z -component of $\Lambda(1520)$ spin must be $m_{\Lambda} = \lambda_p + \lambda_X$. In particular, if the process is mediated entirely by pseudoscalar K exchange: $m_{\Lambda} = \lambda_p$, the $\Lambda(1520)$ is produced only in $m = \pm \frac{1}{2}$ substates, and (if the target is unpolarized) $\rho_{11}^{\Lambda} = \rho_{-11}^{\Lambda} = \frac{1}{2}$ with all other ρ elements zero.

There are two ways we could get the $\rho_{mm'}^{\Lambda}$ elements in the GJ frame. First, we could start with the $\rho_{\lambda\lambda'}^{\Lambda}$ which we have been working with above, and apply a transformation that takes us from the helicity frame to our chosen frame, so that we get $\rho_{mm'}^{\Lambda}$ in our newly chosen frame. Like applying a rotation to a spin state, applying a rotation to a spin density matrix is done using Wigner D

matrices. Since the helicity frame and the GJ frame have their y axes in the same direction, all we are doing is a rotation around the y -axis, so we only need the small d matrix. The d matrix for spin- $\frac{3}{2}$ is

$$d^{\frac{3}{2}}(\beta) = \begin{pmatrix} \frac{1}{2}(1 + \cos \beta) \cos \frac{\beta}{2} & -\frac{\sqrt{3}}{2}(1 + \cos \beta) \sin \frac{\beta}{2} & \frac{\sqrt{3}}{2}(1 - \cos \beta) \cos \frac{\beta}{2} & -\frac{1}{2}(1 - \cos \beta) \sin \frac{\beta}{2} \\ \frac{\sqrt{3}}{2}(1 + \cos \beta) \sin \frac{\beta}{2} & \frac{1}{2}(3 \cos \beta - 1) \cos \frac{\beta}{2} & -\frac{1}{2}(3 \cos \beta + 1) \sin \frac{\beta}{2} & \frac{\sqrt{3}}{2}(1 - \cos \beta) \cos \frac{\beta}{2} \\ \frac{\sqrt{3}}{2}(1 - \cos \beta) \cos \frac{\beta}{2} & \frac{1}{2}(3 \cos \beta + 1) \sin \frac{\beta}{2} & \frac{1}{2}(3 \cos \beta - 1) \cos \frac{\beta}{2} & -\frac{\sqrt{3}}{2}(1 + \cos \beta) \sin \frac{\beta}{2} \\ \frac{1}{2}(1 - \cos \beta) \sin \frac{\beta}{2} & \frac{\sqrt{3}}{2}(1 - \cos \beta) \cos \frac{\beta}{2} & \frac{\sqrt{3}}{2}(1 + \cos \beta) \sin \frac{\beta}{2} & \frac{1}{2}(1 + \cos \beta) \cos \frac{\beta}{2} \end{pmatrix}. \quad (2.50)$$

A rotation of the coordinate system (passive rotation) of angle β about the y -axis is implemented by the operator $d^{\frac{3}{2}}(-\beta)$ acting on a spin- $\frac{3}{2}$ angular momentum state. So the transformation on the spin density matrix is given by

$$\rho^\Lambda \rightarrow \rho'^\Lambda = d^{\frac{3}{2}}(-\beta)\rho^\Lambda d^{\frac{3}{2}}(\beta), \quad (2.51)$$

where we have used the relationship $d^{\frac{3}{2}\dagger}(-\beta) = d^{\frac{3}{2}}(\beta)$. To rotate from the helicity frame to the Gottfried-Jackson frame we use the angle:

$$\beta_{\text{Hel} \rightarrow \text{GJ}} = \cos^{-1} \left(\frac{\beta_\Lambda - \cos(\theta_{K^+})}{1 - \beta_\Lambda \cos(\theta_{K^+})} \right), \quad (2.52)$$

where θ_{K^+} is the K^+ production angle in the CM frame and β_Λ is the $\Lambda(1520)$ velocity in the CM frame.

The other method is to use the decay distributions measured in this new frame and derive the $\rho_{mm'}^\Lambda$ directly from them. As discussed in Schilling [38], the parity relations (2.32), which we derived only in the helicity basis, actually hold for $\rho_{mm'}^\Lambda$ in any basis as long as the z -axis lies in the production plane. This means that our whole discussion above, including the decay distributions (2.47), still applies in the Gottfried-Jackson frame. So we can extract the $\rho_{mm'}^{GJ}$ elements directly from the decay distributions in the GJ frame.

2.2.6 Spin density matrix elements from fit amplitudes

Another way to extract spin density matrix elements is used by Williams [41]. If the experimental results can be described well by a set of amplitudes fitted to the data, the spin density matrix elements can be projected out directly from the fit amplitudes using equation (2.30) or the equivalent. If, as in equation (2.30), the amplitude is written in the helicity formalism, the ρ elements extracted will be in the helicity frame. If the amplitudes are constructed in terms of normal spin components with a fixed quantization axis, then the ρ elements projected out from the amplitudes will be in whatever frame the amplitudes were constructed in.

Chapter 3

Experimental apparatus

The data used for this analysis was from the g11a dataset, taken in 2004 at Thomas Jefferson National Accelerator Facility (known as Jefferson Lab or JLab, and shown in Figure 3.1) in Newport News, Virginia. The largest facility at JLab is an electron accelerator known as the Continuous Electron Beam Accelerator Facility (CEBAF), which is now capable of accelerating electrons up to 12 GeV, though in 2004 the maximum energy was 6 GeV. The electron beam is delivered to four different experimental halls, Halls A, B, C, and D, which contain targets for the beam and various particle detectors (Hall D was not operational in the 6 GeV era). The g11a data comes from Hall B. In the 6 GeV era, Hall B contained the CEBAF Large Acceptance Spectrometer (CLAS), as well as a photon tagger that could use the electron beam to produce an energy-tagged photon beam. In this chapter we will discuss the components of these systems that are important for this analysis.

3.1 CEBAF

As mentioned above, the Continuous Electron Beam Accelerator Facility [43] is an electron accelerator, which in 2004 had a maximum energy of 6 GeV. We will only discuss the configuration of the accelerator in this era, before the 12 GeV upgrade. The accelerator uses superconducting RF cavities (made from niobium), which is important because it eliminates resistive heating which would otherwise limit the time the cavities are operable. Because of the superconducting cavities, CEBAF can deliver a “continuous” electron beam. What this actually means that it can regularly accelerate electrons in bunches separated in time by 2 ns (or thirds of 2 ns, when beam is being delivered to multiple halls), without breaks. Niobium has a critical temperature of 9.2 K, below which it is superconducting. Thus the cavities are operated in cryomodules, cooled by liquid helium to 2.08 K. Two RF cavities are shown in Figure 3.2. The cavities are driven by a 1497 MHz RF signal that is synchronized with the electron beam bunches.

Beam electrons originate from a single GaAs photocathode illuminated by pulsed lasers. Each experimental hall has a separate laser which provides electrons destined for that hall, so that different halls can have different beam characteristics. Each laser is pulsed at 499 MHz, hence the (approximately) 2 ns bunch spacing mentioned above. The three lasers for the three different halls are out of phase by 120° so that the bunches for each hall are equally separated in time, forming a 1497 MHz beam. The injector provides the initial acceleration to the electrons up to about 45 MeV. The beam then enters the racetrack-shaped main accelerator (1.4 km in total length), which consists of two straight segments and two semi-circular segments. Each straight segment contains a linac, and the semi-circular segments contain in total nine recirculating arcs, which bend the beam between the two linacs (the beam must travel in a different recirculating arc each pass around the accelerator). In the 6 GeV era, each linac contained 20 cryomodules (160 cavities) and accelerated the beam about 600 MeV, so that a full circuit, or pass, around the accelerator provided 1200 MeV.



Figure 3.1: An aerial view of the Jefferson Lab site. The outline of the racetrack shaped accelerator can be seen on the surface. The three mounds of earth in the lower right cover Halls A, B, and C, from left to right. Hall D is seen in the upper left. From [42].



Figure 3.2: Two superconducting niobium RF cavities. In the accelerator, the cavities are located in cryomodules which use liquid helium to cool the cavities to become superconducting. From [43].

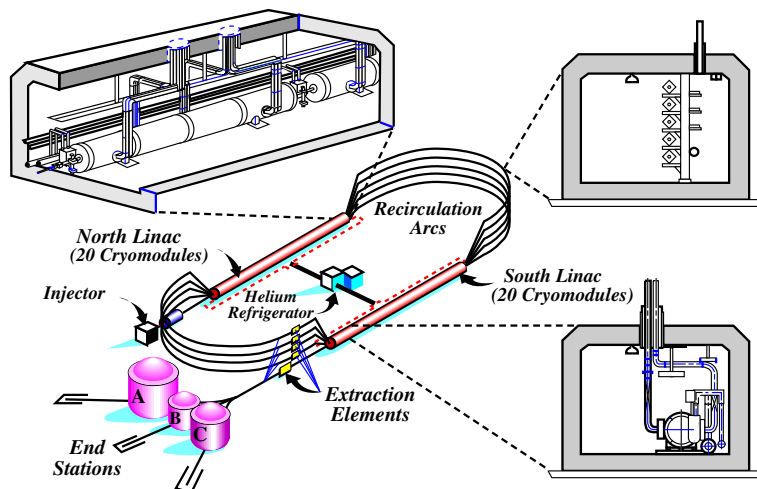


Figure 3.3: Schematic diagram of CEBAF as it operated in the 6 GeV era.

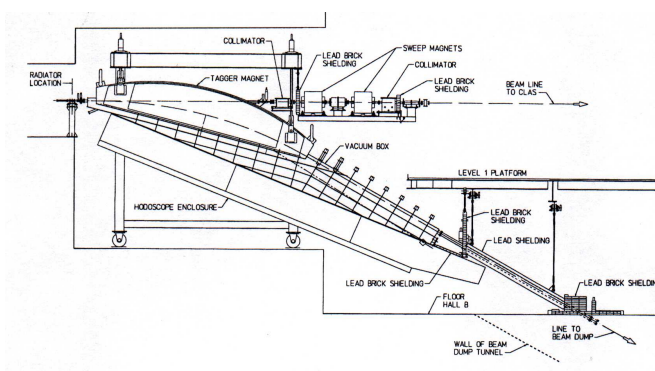


Figure 3.4: Diagram of Hall B photon beamline and tagger. From [44].

Beam delivered to the halls can have undergone five or fewer passes, hence the 6 GeV maximum. After acceleration to the desired energy, a beam bunch is extracted from the accelerator and delivered to the intended hall using RF separator cavities, which operate at 499 MHz, thus deflecting bunches differently depending on their intended hall. Figure 3.3 provides a diagram of the important accelerator components. CEBAF is capable of providing beam currents up to $200 \mu\text{A}$ (for all halls combined), but currents delivered to Hall B are typically much smaller (for g11a, the beam current was around 65 nA). CEBAF is also capable of making a polarized electron beam, but an unpolarized beam was used for g11a.

3.2 Photon beam and tagger

Hall B can operate with either an electron beam or a photon beam incident on the target. Since g11a used a photon beam, we discuss the photon beam here.

To make a photon beam from an electron beam, we begin by placing a thin radiator in the path of the electron beam. Some electrons in the beam interact with the nuclei in the radiator and radiate photons via bremsstrahlung. For g11a production runs, a gold radiator with a thickness of 10^{-4} radiation lengths was used.

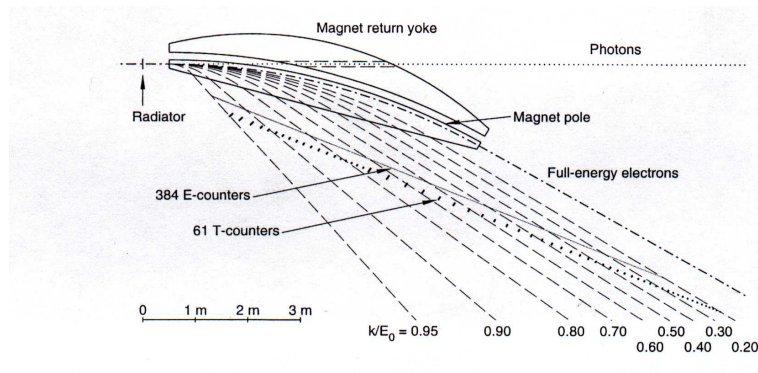


Figure 3.5: Shows trajectory of particles in the tagger and location of hodoscope planes. Electron trajectories are labeled by the fraction of incident energy transferred to the photon. From [44].

After passing through the radiator, the beam consists of electrons and photons. To remove the electrons from the beam and measure their momentum, the beam passes through a dipole magnetic field. Electrons with full energy are bent towards the beam dump, while electrons that produced photons are bent towards a tagging hodoscope. The photons continue undisturbed to the target. These particle trajectories along with the geometry of the tagger are shown in Figure 3.5.

The tagger is made up of two hodoscope planes that measure the position and time of electrons when they cross the plane. The first plane is more finely segmented in space, being designed to measure the momentum (and thus the energy) of the scattered electron. This, in turn tells us the energy of the beam photon created by this electron (by conservation of energy, since the energy of the original beam electron is also known). This plane is called the E-plane. It consists of 384 narrow scintillators. Each scintillator has a one-third overlap with its two neighbors, so that the 767 different photon energies can be measured. The photon energy resolution from this setup is 0.1% of the electron beam energy. The second plane, called the T-plane, is designed for precise timing measurements. The thicker scintillators of the T-plane (2 cm vs 4 mm thick in E-plane) result in more light and thus have better timing resolution. The T-plane has 61 paddles. The timing resolution of the T-plane is 110 ps, which is sufficient to identify which beam bunch the electron came from. The tagger detects electrons which produce photons with energy between 20–95% of the incident electron beam energy.

Since the T-plane provides the most precise timing measurements (excluding the accelerator RF), it is used to identify which beam bucket the interacting electron comes from, which determines the event start time (the time at which an electron from the given beam bunch would have reached the reconstructed event vertex). This is very important for our particle identification as discussed in Section 4.4.

Because there can be multiple photons in one readout window, timing is also measured from the E-plane. A coincidence between the E-plane and T-plane is needed to determine both the photon energy and time of an event.

Other components of the photon beamline are two collimators, which reduce the profile of the beam, and sweep magnets, which remove charged particles produced in the first collimator.

Details of the Hall B photon beam and tagger can be found in Sober et al. [44].

3.3 The CLAS detector

The CEBAF Large Acceptance Spectrometer (CLAS) was designed to detect particles produced when the beam (either electron or photon beam) interacts with a target at the center of the device.



Figure 3.6: Photo of CLAS detector during maintenance, when the outer detectors (TOF scintillators, Cherenkov counters, electromagnetic calorimeters) were separated from the inner detectors. From [42].

CLAS (shown in Figure 3.6) has a relatively large acceptance, allowing for detection of multi-particle final states with reasonable efficiency. An overview of CLAS is available in [45]. CLAS was disassembled in 2012 after the end of 6 GeV running at JLab. A new detector, CLAS12, is currently being built in Hall B as part of the JLab 12 GeV upgrade.

CLAS is divided into six sectors with six-fold azimuthal symmetry. The detector is composed in layers and has an onion-like appearance as shown in Figures 3.7 and 3.12. The layers of this onion are the various subdetectors which make up the full CLAS detector. Of these, the start counter, drift chambers, and time-of-flight scintillators are discussed below, while the Cherenkov counters, electromagnetic calorimeters, and large angle calorimeters were not used in this analysis and are not discussed further.

3.3.1 Target

For g11a, the target was liquid hydrogen, which provided a proton target. The liquid hydrogen was contained in a target cell, made of Kapton, which was 40 cm long and 2 cm in radius. The target cell is shown in Figure 3.8. Full target specifications are available in [46].

3.3.2 Start Counter

The start counter (shown in Figure 3.9) surrounds the target and is designed to measure the timing of particles exiting the target. It is used in the trigger (see Section 3.4), but otherwise is not used in this analysis. The start counter comprises 24 scintillator paddles, four for each sector. The timing resolution is around 400 ps. More information is available in [48].

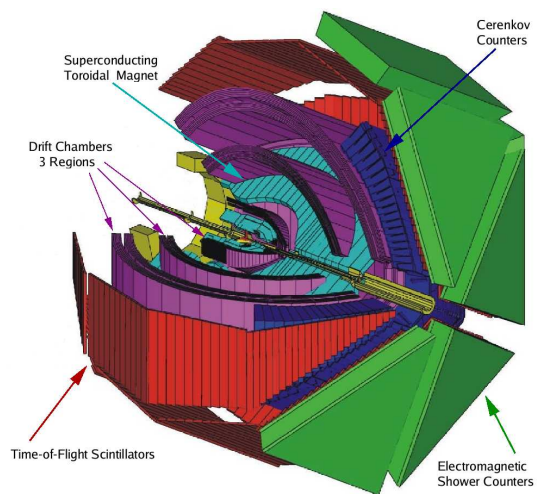


Figure 3.7: Diagram of CLAS detector elements. From [42].



Figure 3.8: g11a target cell. From [47].

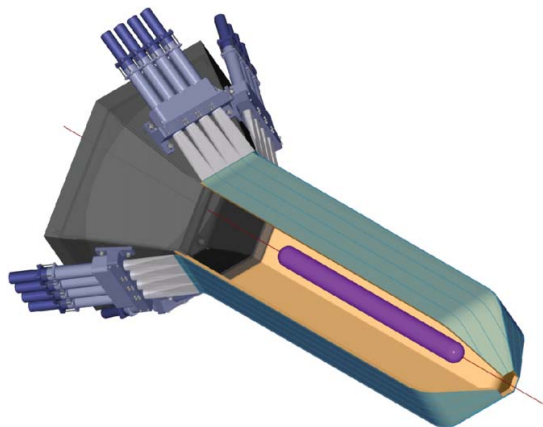


Figure 3.9: CLAS start counter, newly installed for g11a. From [48].



Figure 3.10: Coil cryostats of the toroidal magnet before installation of detectors. From [49].

3.3.3 Toroidal Magnet and Drift Chambers

Determination of the momenta of charged particles is done by tracking the trajectory of these particles as they are bent by a known magnetic field. In the case of CLAS, the magnetic field is provided by a superconducting toroidal magnet. The toroid consists of six kidney-shaped superconducting coils cooled by liquid helium in cryostats, as shown in Figure 3.10. The cryostats define the boundaries between the six sectors of the detector. The magnetic field generally points in the azimuthal direction (see Figure 3.11), so that a particle initially traveling roughly parallel to the z -axis will initially feel a force in the radial direction (radial in the cylindrical sense: towards or away from the beamline). g11a ran using the so-called normal field configuration of the magnet, which causes forward-going negatively-charged particles to bend towards the beamline (where they are less likely to be detected) and positively-charged particles to bend away. Because the coil cryostats converge as they near the beamline in the forward direction and no detector elements can overlap with them, the azimuthal acceptance of CLAS decreases in the forward direction (see Figure 4.1).

Charged particles are tracked by a drift chamber system that is divided into three regions. Because of the sector geometry of CLAS, this means that CLAS contains 18 drift chambers. Region 1 is located closest to the beamline in a low-magnetic-field region. Region 2 is located between the magnet coils and thus in a high-field region. Region 3 is outside the torus coils, farthest from the beamline in another low-field region. The location of each region with respect to the coils is shown in Figure 3.12. Each drift chamber region consists of two superlayers, each consisting of several wire layers; one superlayer has wires parallel to the azimuthal direction (roughly parallel to the magnetic field) and the other has wires oriented at a 6° stereo angle (for determination of the azimuthal position of a particle track). More details on the CLAS drift chambers can be found in [50].

3.3.4 Time-of-Flight Scintillators

Outside of the drift chambers are located the time-of-flight (TOF) walls. These measure the time when a particle reaches the scintillator. Since we can use the drift chamber to calculate the distance a particle travels through the detector, this allows us to compute the speed of the particle, which can be used for particle identification (distinguishing a pion from a proton or kaon). The particle identification method will be discussed in detail in Chapter 4.

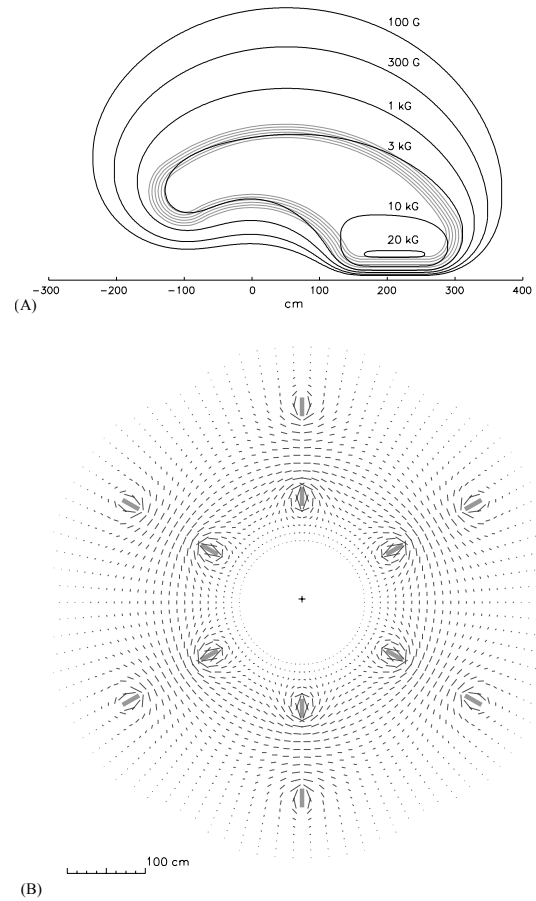


Figure 3.11: Magnetic field of the toroidal magnet. (A) shows contours of constant field strength at the azimuthal center of a sector, with z -position shown in the horizontal direction and radial distance from the beamline in the vertical direction. The gray curves show the location of the coils. (B) shows the magnitude and direction of field vectors in a plane transverse to the beamline, centered on the target. From [45].

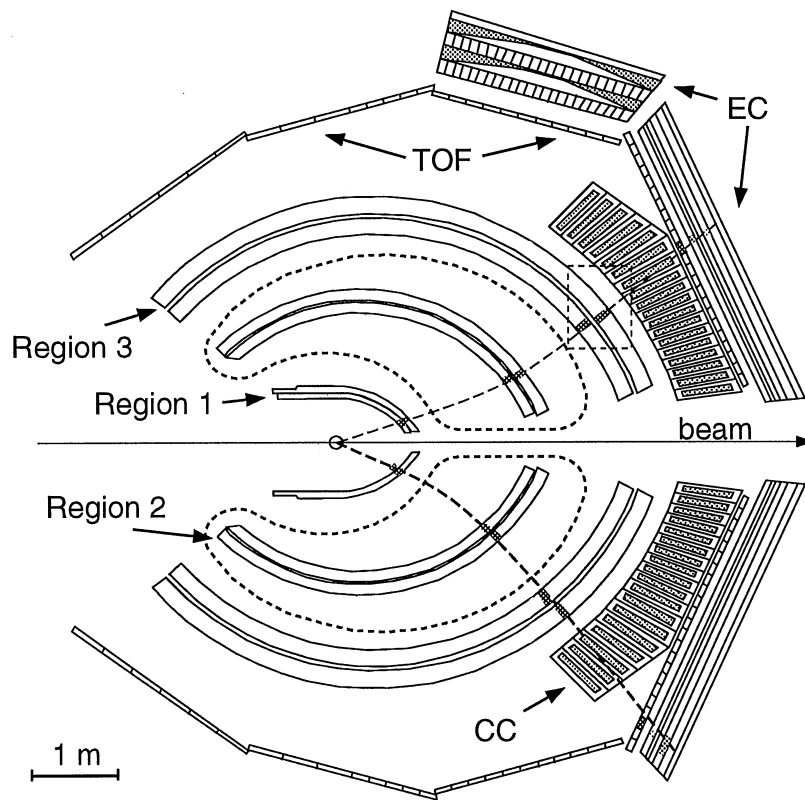


Figure 3.12: Diagram of the spectrometer showing the position of the drift chamber regions relative to the coil location. The short dashed lines show the location of the magnet coils. The long dashed line show the trajectories of two charged particles. From [50].

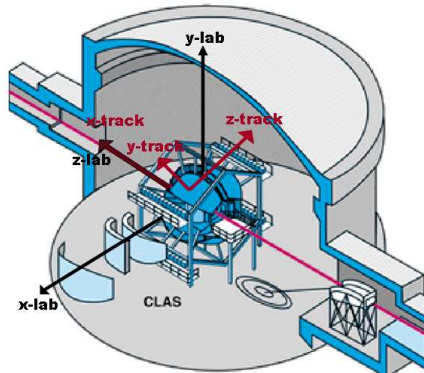


Figure 3.13: Lab coordinate system and tracking coordinate system for sector 2.

In each sector the time-of-flight wall is made of 57 scintillator bars varying in length and width. The timing resolution varies between 80–160 ps, depending on the length of the bar. Full details on the TOF system are available in [51].

3.3.5 CLAS Coordinate Systems

Three standard coordinate systems are used in CLAS: the lab system, the sector system, and the tracking system. The lab system (illustrated in Figure 3.13) is defined with the z -axis parallel to the beamline (positive z pointing downstream), the x -axis being horizontal and pointing in the direction from the beamline to the center of sector 1, and the y -axis pointing up (towards the coils between sectors 2 and 3). The origin is located on the beamline, with its location in the z -direction relative to the coils shown in Figure 3.11. The polar and azimuthal angles θ and ϕ are defined in the standard way. The other coordinate systems will not be discussed in this analysis.

3.4 Trigger and Data Acquisition

The trigger is designed to identify events of interest, so that the signals from these events are read out by the data acquisition (DAQ) system and written to tape, while detector signals not associated with an event of interest (for example signals from a cosmic ray entering the detector) are not read out. The g11a trigger required a coincidence (within 15 ns) between the tagger Master OR and the CLAS Level 1 trigger. The Master OR requires a signal in one or more of the 40 highest-energy counters in the tagger T-plane. This biases the distribution of events towards events with photon energy above 1.57 GeV, which was the energy region of interest for g11a. Though only the higher-energy counters are part of the trigger, all tagger paddles are read out, so that events from lower-energy photons will only be recorded if they occur in coincidence with a higher-energy tagger hit. The CLAS Level 1 trigger is sector-based. For g11a, it required two sectors to have a start counter hit and a TOF hit in coincidence (within a timing window of 150 ns). Together the Master OR and Level 1 trigger require the production of a high-energy beam photon in coincidence with an interaction producing multiple charged particles in the target region. Once the trigger is passed, detector signals are collected by the DAQ and written out for further analysis.

Chapter 4

Event Selection

This analysis uses the CLAS g11a dataset, which was collected in 2004. The electron-beam energy was fixed at 4.019 GeV for most of this dataset. The data consists of about 20 billion triggers, or events written to disk. The process of taking the raw data recorded from the detector and turning it into data useful for physics analysis is called cooking, and involves applying calibrations and fitting tracks. Details on this can be found in Reference [52].

The event-selection procedures described in this chapter are designed to identify events in which the $\gamma p \rightarrow K^+ K^- p$ reaction occurred and to reject events involving all other reactions (e.g. $\gamma p \rightarrow \pi^+ \pi^- p$). In addition, we are mostly interested in $\gamma p \rightarrow K^+ K^- p$ reactions in which the $K^- p$ pair could plausibly be from the decay of a $\Lambda(1520)$. The procedures in this chapter are only the first steps in identifying $\Lambda(1520)$ events. We must also use the background subtraction method described in Chapter 6 to remove any non- $\Lambda(1520)$ events remaining.

As discussed below, it is possible to fully reconstruct an event even if one of the final-state particles is not detected. For this reason, we consider three different event topologies. In the “three-track” topology, we will require the detection of three particles, two positively charged and one negatively charged. In the “missing K^- ” topology, we will only require two positively charged tracks. In the “missing K^+ ” topology, we require one positive track and one negative. Due to the acceptance of the CLAS detector, each of these topologies will have different characteristics. Since the CLAS acceptance of negatively charged particles is much lower than for positively charged ones, the missing K^- topology will have the greatest statistics. The extra information in the three-track topology means it will give us the best resolution and the lowest background. The missing K^+ topology will give us access to events in which the K^+ is very forward-going, where it cannot be detected by CLAS. Events which are selected in the three-track topology are not included in the two-track topologies. This is so that there is no overlap between the three groups of events and each topology can be treated as an independent analysis.

In general, event selection and processing should be exactly the same for data events as for Monte Carlo events (see Chapter 5). Except where noted, the procedure described below applies to both types of events.

4.1 Excluded runs

The g11a run period is divided into short intervals called runs, each run typically lasting several hours and containing around 10 million recorded events. Details on all CLAS runs are available from the CLAS logbook [53]. g11a consists of runs 43490 to 44133. Data from certain of these runs must be excluded from the analysis for various reasons. The runs excluded in this analysis are the same as those excluded by Moriya [54]. In addition, there are several runs for which the two-track data, but not the three-track data, is corrupted, as reported by Dey [12]. These runs must be excluded

Excluded runs	Reason
43490-43525	Commissioning
44108-44133	5.021 GeV beam energy
43675-43676, 43777-43778, 44013	Alternate trigger
43989-43991	DAQ Problems
43981-43982	Drift chamber problems
43878	Empty target run
43558	Abnormal yield
43657, 43900, 44036, 44089, 44101-44102	Very low statistics
43526-43527, 43532-43533, 43540-43541, 43547-43553, 43561	Damaged magnetic tape (two-track topologies only)

Table 4.1: Excluded runs

from our analysis of the missing K^- and K^+ topologies. Runs excluded in this analysis are listed in Table 4.1. Keeping track of the runs excluded is important for calculating integrated photon flux.

4.2 Kinematic fitting

In addition to the measured momenta of the particles we have another piece of relevant information, namely, the laws of physics. We know that momentum and energy must be conserved in the reaction, and using a procedure called kinematic fitting, we can enforce these constraints. The results of the kinematic fitting can be used in two desirable ways. The first is to reject events that are not consistent with our hypothesis for the topology of the event. This is roughly equivalent to placing cuts on missing mass and missing momentum, although less ad-hoc. The second use of kinematic fitting is using the constraints to improve our measurement of the particles' momenta, improving resolution and decreasing uncertainty. This is a unique benefit of kinematic fitting.

Now we describe the procedure of kinematic fitting, focusing on the special cases of photoproduction with all final-state particles detected or with one particle missing. We begin with n measurable quantities. In our case $n = 1 + 3\ell$, with one measurement of the beam photon energy, and a measurement of each of three components of momentum for each of ℓ detected particles. The (unknown) true values of these quantities are denoted \vec{y} and the measured values $\vec{\eta}$. The uncertainties of and correlations between the measurements are described by the covariance matrix C_η . The errors (also unknown) $\vec{\epsilon}$ are:

$$\vec{\epsilon} = \vec{\eta} - \vec{y}. \quad (4.1)$$

We also can have m unmeasured quantities with true values \vec{x} (in our case, $m = 0$ with no missing particles and $m = 3$ with one missing particle). We require that \vec{y} and \vec{x} satisfy r constraint equations of the form:

$$f_k(\vec{x}, \vec{y}) = 0. \quad (4.2)$$

In our case, the constraint equations enforce conservation of 4-momentum, with one equation for each component, hence $r = 4$. It is important to note that the true values \vec{y} are required to satisfy Eq. (4.2), but that the measured values $\vec{\eta}$ will not.

We define X as the quantity we want to minimize if we temporarily ignore the constraints:

$$X(\vec{y}') = (\vec{\eta} - \vec{y}')^T C_\eta^{-1} (\vec{\eta} - \vec{y}'), \quad (4.3)$$

This is a measure of how far the new values \vec{y}' are from the measured values $\vec{\eta}$. To minimize X

subject to constraints, we use the method of Lagrange multipliers, and define L :

$$L(\vec{x}', \vec{y}', \vec{\lambda}) = X(\vec{y}') + \sum_i^r \lambda_i f_i(\vec{x}', \vec{y}'). \quad (4.4)$$

(We must define one Lagrange multiplier λ_i for each constraint equation, but the values of these are irrelevant.) All constrained extrema of X will occur at critical points of L , i.e. points at which

$$\vec{\nabla}L(\vec{x}', \vec{y}', \vec{\lambda}) = 0. \quad (4.5)$$

Thus we can find the minimum value of X for which \vec{x}' and \vec{y}' satisfy all constraints f_k . These values of \vec{x}' and \vec{y}' are our best estimates of \vec{x} and \vec{y} and are denoted \vec{x}^* and \vec{y}^* .

If the constraint functions were linear, Eq. (4.5) would have exactly one solution, which could be found analytically and would (due to Eq. (4.3) and the positivity of the covariance matrix) be guaranteed to be a constrained minimum of X . However the conservation of energy constraint is not linear in the momenta. Instead we approximate the constraint functions as linear and solve this linear problem. Since this linearization is an approximation, the procedure is iterated several times to get a better approximation. This is equivalent to numerically solving (4.5). This procedure is discussed in detail by Williams [41].

One can also calculate the covariance matrices C_{y^*} and C_{x^*} of the new estimates \vec{y}^* and \vec{x}^* , also discussed by Williams.

The goodness of fit is measured by $\chi^2 = X(\vec{y}^*)$, which can be cast into a more useful form: the confidence level

$$CL = \int_{\chi^2}^{\infty} f(z; N) dz, \quad (4.6)$$

where $f(z; N)$ is the standard χ^2 probability density function with $N = r - m$ degrees of freedom. $N = 4$ for a fit with no missing particles, which we call a 4C fit, and $N = 1$ for a 1C fit with one missing particle. The confidence level is the probability that a variable sampled from the χ^2 theoretical distribution is greater than the given χ^2 . For a sample of measurements of events that satisfy the fit hypothesis, the distribution of the confidence level will be flat between 0 and 1, assuming the measurements are unbiased and the errors $\vec{\epsilon}$ are normally distributed as described by the covariance matrix C_η . In reality, errors are not perfectly normally distributed. We can cut out events with low confidence levels to remove events that do not seem to satisfy the fit hypothesis.

In this analysis, the covariance matrices used for charged particle momenta are not those estimated by the CLAS tracking software, but corrected covariance matrices as constructed by Williams [41].

4.3 Energy and momentum corrections

Before kinematic fitting, we apply certain corrections to our measurements to account for known imperfections in the measurement and reconstruction process.

4.3.1 Energy loss corrections

Using the drift chambers, we can reconstruct the momentum of a particle in the drift-chamber region. However, before a particle reaches the drift chambers, it has already lost energy traveling through various materials including the target and the start counter. The eloss package [55] takes a particle's measured momentum and corrects it to account for this energy loss. This correction is applied to all particles.

4.3.2 Momentum corrections and tagger energy corrections

Corrections to the photon energy measured by the tagger are needed due to a physical sag of the hodoscope plane as well as other alignment issues [56]. Corrections to the momenta of detected particles are needed due to wire misalignments and discrepancies between the true magnetic field and the magnetic field map used to calculate the momentum. The appropriate corrections were determined empirically by Williams using a kinematic fit of the reaction $\gamma p \rightarrow \pi^+ \pi^- p$ [41]. The corrections were determined by requiring that all three particles be detected, but then doing a kinematic fit with one particle treated as if it were missing. Any bias in the momentum measurement can then be seen by comparing the missing momentum from the kinematic fit with the measured momentum of the “missing” particles. To determine momentum corrections for positive particles, both kinematic fits with a missing π^+ and fits with a missing p were used. The same corrections were shown to suffice for both types of particles, as expected. Momentum corrections for negative particles were determined using a kinematic fit with a missing π^- . Tagger energy corrections were determined using a kinematic fit with a missing beam photon. The process was iterative: first, tagger corrections were obtained, then those tagger corrections were applied to get the first estimate of the momentum corrections, which are then used to recalculate the tagger corrections, etc.

Momentum corrections are determined in 180 (θ, ϕ) bins in each sector, and are modeled as a polynomial function of the magnitude p in each bin. Momentum corrections depend only on the charge of the particle and its momentum, not on particle ID, so the corrections determined should apply to kaons as well as to pion and protons.

4.4 Particle ID from timing measurements

The main method used to determine the identity of charged tracks (proton, kaon, or pion) involves measuring their time-of-flight. The track-fitting procedure measures the momentum and charge of a track, but not the mass or type of particle. However, given a particle’s momentum p , its velocity β is determined by its mass m . Thus time-of-flight measurements, which allow us to calculate β , allow us to do particle ID. We define the measured time-of-flight:

$$\text{TOF}_{\text{meas}} = t_1 - t_0, \quad (4.7)$$

where t_0 is the event start time (determined by identifying the RF beam bunch using the tagger and propagating the time to the reconstructed event vertex) and t_1 is the time measured when the particle hits the TOF scintillator. We can then calculate

$$\beta = \frac{L}{c \text{TOF}_{\text{meas}}}, \quad (4.8)$$

where L is the path length from the target to the scintillator (determined from the tracking).

We can then define the calculated time-of-flight, the TOF we would expect for a particle with momentum p and mass m :

$$\text{TOF}_{\text{calc}} = \frac{L}{c} \sqrt{1 + \left(\frac{m}{p}\right)^2}, \quad (4.9)$$

We define:

$$\Delta\text{TOF} = \text{TOF}_{\text{meas}} - \text{TOF}_{\text{calc}}. \quad (4.10)$$

Using the standard formulas $E^2 = (pc)^2 + (mc^2)^2$ and $E = \gamma mc^2$, we can also calculate the mass of a particle with β and momentum p :

$$m_{\text{calc}} = \frac{p}{\gamma\beta c}, \quad (4.11)$$

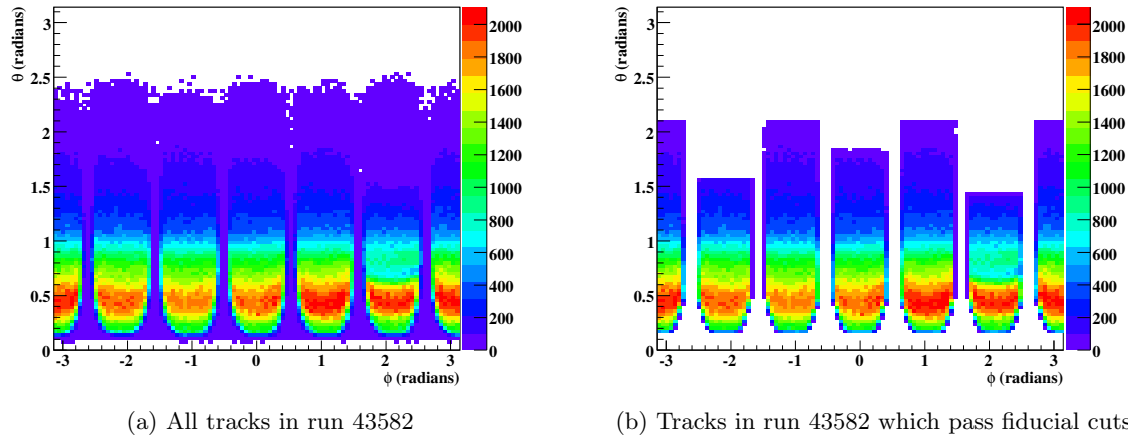


Figure 4.1: Fiducial cuts

where $\gamma = \frac{1}{\sqrt{1-\beta^2}}$ is the standard Lorentz factor. This “calculated mass” can be compared to the known mass for a pion, kaon, or proton.

These two quantities, ΔTOF and m_{calc} , are different ways of looking at the same information. The use of these quantities for particle identification and event selection will be discussed in more detail below.

4.5 Detector performance cuts

4.5.1 Fiducial cuts

Particles that pass through certain areas of the detector are difficult to reconstruct or not well modeled by the Monte Carlo. We must cut out events with reconstructed tracks in these regions. These cuts are called fiducial cuts. The proper fiducial cuts were studied by Matt Bellis. Low momentum protons are difficult to model due to high energy loss while moving through material. Protons with $p < 375$ MeV are not modeled well by the Monte Carlo and so are cut out.

We must also cut out tracks whose trajectories pass near a magnet coil or sector boundary. The boundaries of this cut depend on both ϕ and θ and it has the largest effect at forward angles. In addition, we place a cut on extreme forward-going tracks $\cos\theta > 0.985$ and a sector-dependent cut in the backward direction. The effect of these cuts can be seen in Figure 4.1.

4.5.2 TOF paddles

Some time-of-flight paddles had to be removed from the analysis. These bad TOF paddles were identified by a discrepancy in occupancy distribution between data and Monte Carlo. All tracks detected in one these paddles were not considered in this analysis. The choice of bad TOF paddles is the same as used in Dey’s ϕp analysis [12] and is listed in Table 4.2.

Sector	Removed paddles
1	18, 26, 27, 33
2	none
3	11, 24, 25
4	26
5	20, 23
6	25, 30, 34

Table 4.2: Removed TOF paddles

4.6 pK^+K^- topology

4.6.1 Skimming

The first step in event selection is to create a skim of the g11a dataset, eliminating the vast majority of events which do not at all resemble the desired topology. This is done with a kinematic fit and several loose cuts.

Each event consists of some number of reconstructed positive tracks, some number of negative reconstructed tracks (the total number of tracks is always at least two, due to the trigger), and at least one beam photon, detected in the tagger, that could be associated with the tracks detected.

For this topology, we consider events with at least two positively charged tracks and at least one negatively charged track. Within each event, we loop over all possible combinations of one beam photon, two positive tracks, and one negative track. All of these combinations are considered independently, as if they were separate events. In addition, both hypotheses for the identification of the two positive tracks are considered independently (i.e. we first consider positive track 1 as p and positive track 2 as K^+ , then the opposite assignment). For simplicity, we will refer to these combinations as “events”, even though technically several could come from the same event.

First we apply a very loose cut to eliminate events with missing mass > 0.5 GeV (the true missing mass for pK^+K^- events is 0). This will cut events that have no chance of being the correct topology to save time on the kinematic fit.

At this point the corrections discussed in Section 4.3 are applied. It is important that these corrections are applied before kinematic fitting.

Next a 4C kinematic fit is applied and events with kinematic fit confidence level less than 1% are cut out. The remaining events are written out to a file for further analysis.

4.6.2 Timing Cuts

Figure 4.2 shows the calculated mass distributions for events that have passed the skim. We see signal events centered at the values of the mass of the hypothesized particles. We also see events that have been misclassified: events where the identities of the K^+ and p have been flipped and events where we have misidentified one or more pions as kaons or protons. These misclassified events are cut out as shown in the figure.

We might expect to find a peak at (m_K, m_π) in Figure 4.2b which would indicate final state particles $pK^+\pi^-$, possibly with additional missing particles. This final state is populated by e.g. ground-state Λ production, $\gamma p \rightarrow K^+\Lambda$, $\Lambda \rightarrow p\pi^-$. In fact, no sign of this peak appears. The 4C kinematic fit is excellent at rejecting the $\gamma p \rightarrow K^+\Lambda$ reaction since the Λ mass is well below the pK threshold. It is also able to reject other reactions that would produce a $pK^+\pi^-(X)$ final state, like $\gamma p \rightarrow K^+\Lambda(X)$ or $\gamma p \rightarrow pK^+K^-\pi^+\pi^-$, since these would clearly be indicated by the presence of large missing mass and missing momentum, which would lead the kinematic fit to reject them. Therefore, we do not have to reject events in the region near (m_K, m_π) in Figure 4.2b. (Reminder: the plots are after 1% confidence level applied in the skim, but before further cuts).

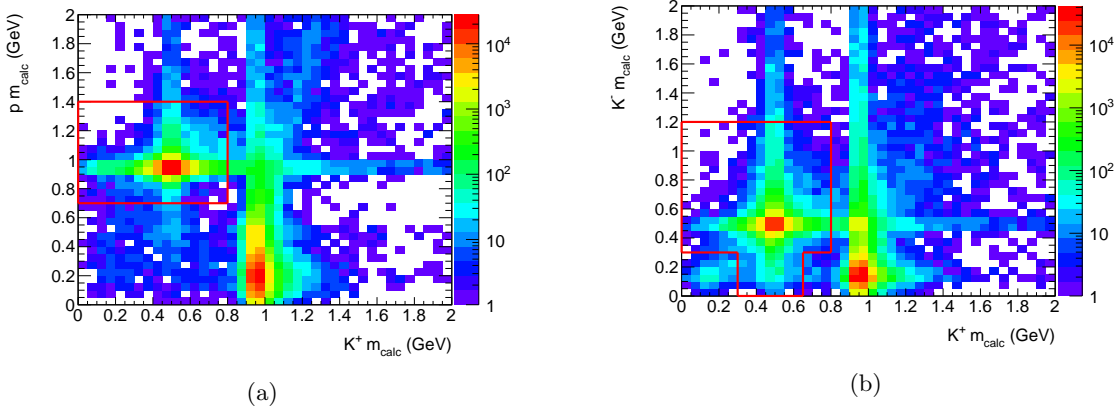


Figure 4.2: Calculated mass plots, 3-track topology, all skimmed events from runs 43800-43899. Areas outside the red outlines are rejected.

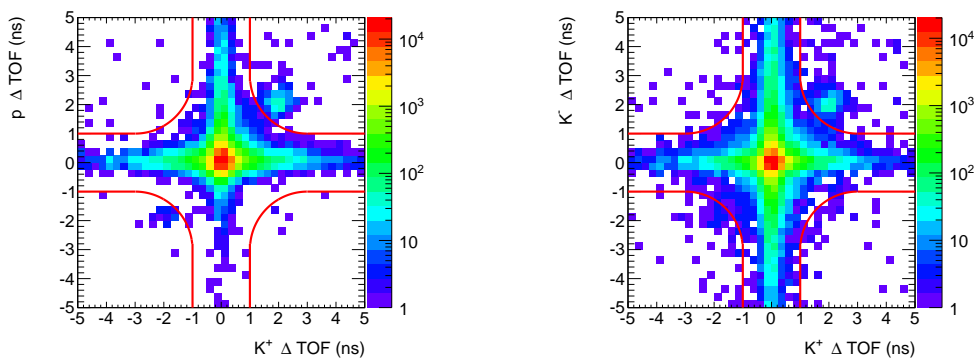
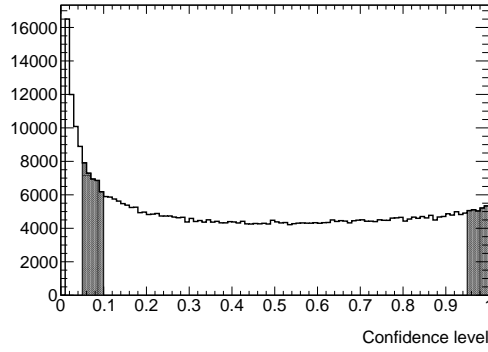
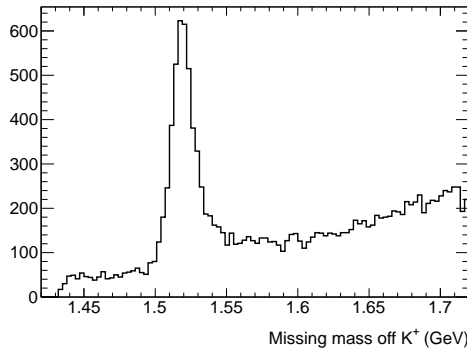


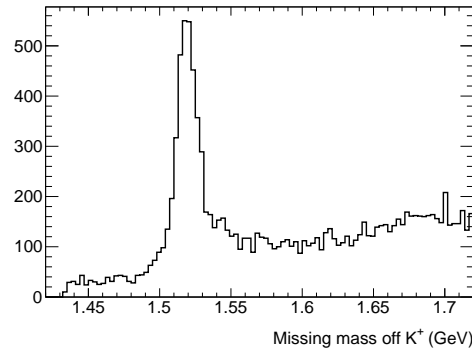
Figure 4.3: Δ TOF, 3-track topology, events from runs 43800-43899 that have passed the calculated mass cut (Figure 4.2). Note the events at $(2, 2)$ and $(-2, -2)$, which come from misidentifying the RF beam bunch. Red curves show cut regions. A similar cut is applied in the $K^+K^- \Delta$ TOF plane.



(a) Confidence level distribution. The shaded regions correspond to the two plots below.



(b) Mass spectrum for events with confidence level between 5-10%



(c) Mass spectrum for events with confidence level between 95-100%

Figure 4.4: Kinematic fit results, 3-track, all skimmed events

After applying this cut, we can look at the ΔTOF of the particles, shown in Figure 4.3. We see clusters of events in which the $|\Delta\text{TOF}|$ of the particles are approximately 2 ns. These are events in which the RF beam bunch has been misidentified and are removed with the cross-shaped cut shown in the figure.

These timing cuts are not as tight as they could be. We hope that any background let through by them will be eliminated by further kinematic fit cuts and the background subtraction procedure described later.

4.6.3 Kinematic fitting

Results of the kinematic fit are shown in Figure 4.4. The confidence level distribution is shown in Figure 4.4a. The non-flat shape of this distribution indicates either the presence of non-signal events or that errors of the measured quantities are not Gaussian distributed. In particular, the large peak at low confidence level in Figure 4.4a would indicate large non-Gaussian tails in the error distribution. To investigate the reason for this non-flat distribution, we can look at the missing mass off K^+ spectrum in the low confidence level and high confidence level regions. Figures 4.4b and 4.4c show that the strength of the $\Lambda(1520)$ signal relative to the background is not much lower in the low confidence level region. So even the events at low confidence level are mostly signal, even though the distribution is not flat. Another way of verifying this is seeing that the same spike at low confidence level appears in our Monte Carlo (Figure 5.1), which has no background. Our 4C

kinematic fit is quite powerful and leaves us with very little background. A 5% confidence level cut seems to be sufficient, and is desirable because this topology has low statistics and we do not want to eliminate too many events.

4.7 $pK^+(K^-)$ topology

As mentioned above, events identified as three-track pK^+K^- events (i.e. events that pass all cuts in Section 4.6) will not be used in the analysis of the $pK^+(K^-)$ topology. Events with three detected tracks can still be present in this sample, as long as they are not in the pK^+K^- sample (for example, if all three particles are detected, but the K^- is not within the fiducial volume). However, the removal of the pK^+K^- events is the last cut to be applied, so all plots in this section include the three-track events.

4.7.1 Skimming

Combinations are looped over in a similar way as described in section 4.6.1, but now no negative tracks are required, only two positive tracks.

Loose cuts are applied before the kinematic fit. To select possible $K^+\Lambda(1520)$ events, we require that the missing mass off the K^+ satisfy $|MM(K^+) - 1.520 \text{ GeV}| < 0.5 \text{ GeV}$. To select events possibly missing a K^- , we require the total missing mass satisfy $|MM - M_{K^-}| < 0.4 \text{ GeV}$. Again these are just loose cuts to save time on running the kinematic fit.

Again, corrections are applied as in section 4.6.1.

Now a 1C kinematic fit to a missing K^- is done. No cut on the kinematic fit confidence level is done at this stage, for reasons explained in Section 6.4.

The following cuts are applied after the kinematic fit. We require $MM(K^+) < 1.8 \text{ GeV}$ to eliminate events well above the $\Lambda(1520)$ mass. We require that $0.2 \text{ GeV} < m_{K^+, \text{calc}} < 0.8 \text{ GeV}$ and $0.4 \text{ GeV} < m_{p, \text{calc}} < 1.2 \text{ GeV}$. These cuts on calculated mass remove a significant number of unwanted events with π 's misidentified as K 's. In Chapter 6, we will need to make use of the MM_{prefit} distribution, so we don't want to distort this distribution by applying a cut on confidence level. However, we can still reduce the number of events by requiring $0.4 \text{ GeV} < MM_{\text{prefit}} < 0.6 \text{ GeV}$ (we must use the missing mass from before the kinematic fit as the missing mass after the kinematic fit is always exactly m_{K^-}).

4.7.2 Timing cuts

After skimming, we make tighter cuts on particle ID. The boundaries of our calculated mass and ΔTOF cuts are shown in Figure 4.5. The calculated mass cuts are much tighter in this case than for the three-track topology because of the large pion background. The same cross-shaped cut is used for the ΔTOF cuts.

4.7.3 Kinematic fitting

For this topology, we will not apply a confidence level cut at this stage. Kinematic fit results are presented in Figure 4.6 for reference. Note that, unlike in the 3-track case, the signal-to-background ratio appears to be much worse in the low confidence level region. We will have to return to the question of where to set the confidence level cut value after we have done background subtraction (Chapter 6).

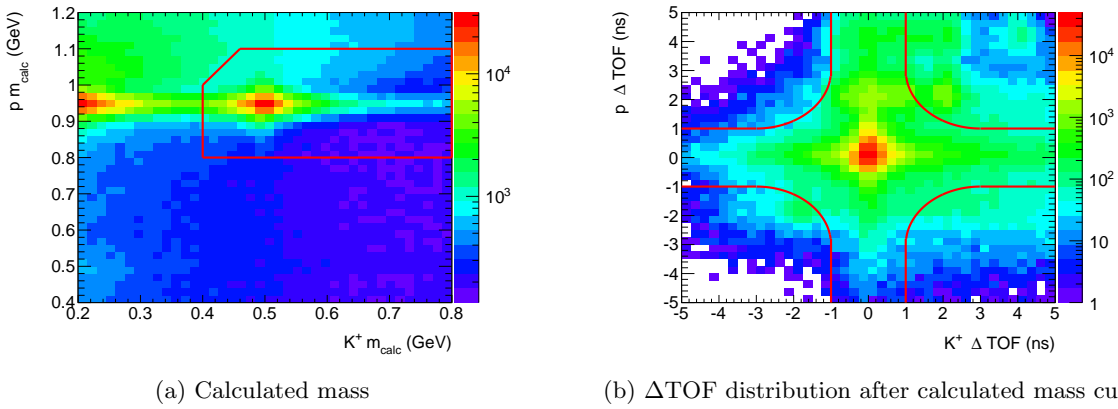


Figure 4.5: Timing cuts for the missing K^- topology. All areas outside the red outlines are rejected. Plots include events from runs 43810-43819.

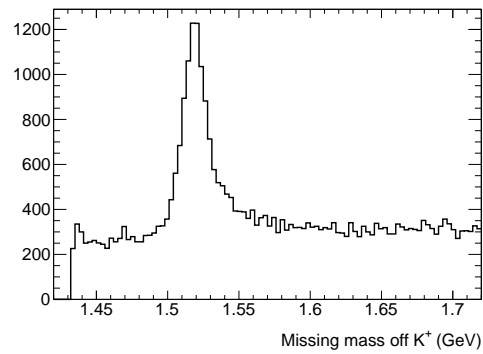
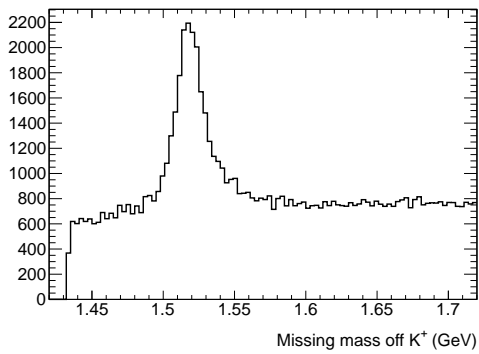
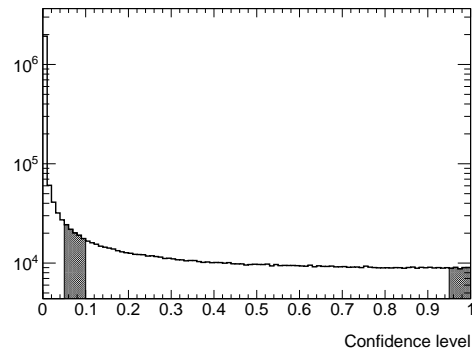


Figure 4.6: Kinematic fit results, missing K^- , skimmed events, runs 43800-43899

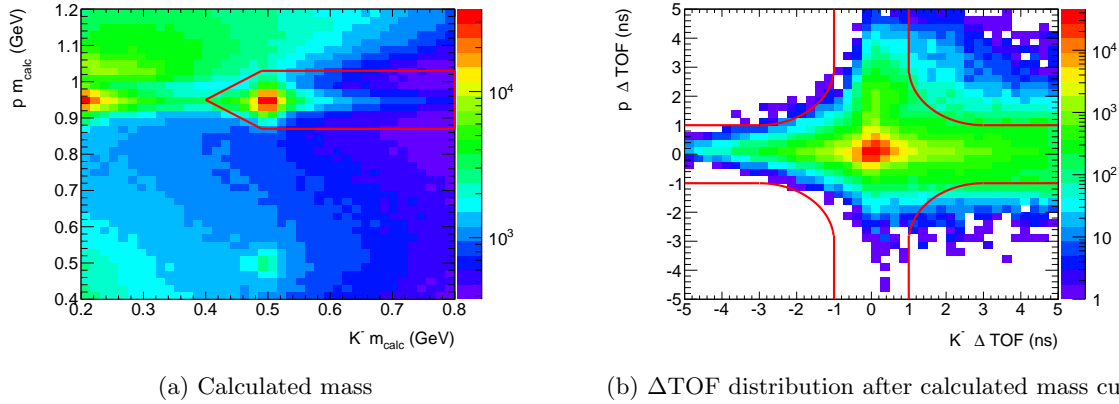


Figure 4.7: Timing cuts for the missing K^+ topology. All areas outside the red outlines are rejected. Plots include events from runs 43810-43899.

4.8 $pK^-(K^+)$ topology

Events in the three-track sample are also removed from this topology.

4.8.1 Skimming

The skimming procedure is similar to Section 4.7.1, except for requiring at least one positive track and at least one negative track.

Before the kinematic fit we require $|IM(pK^-) - 1.520 \text{ GeV}| < 0.5 \text{ GeV}$, where $IM(pK^-)$ is the invariant mass of the pK^- system, and $|MM - M_{K^+}| < 0.4 \text{ GeV}$ and perform corrections.

After performing a 1C kinematic fit to a missing K^+ , we require that the kinematic fit confidence level is $> 1\%$, that $0.2 \text{ GeV} < m_{K^-, \text{calc}} < 0.8 \text{ GeV}$ and $0.4 \text{ GeV} < m_{p, \text{calc}} < 1.2 \text{ GeV}$, and that $IM(pK^-) < 1.8 \text{ GeV}$.

4.8.2 Timing cuts

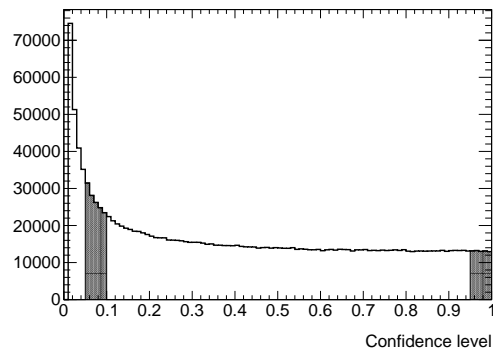
The calculated mass cuts and Δ TOF cuts applied after the skim are shown in Figure 4.7.

4.8.3 Kinematic fitting

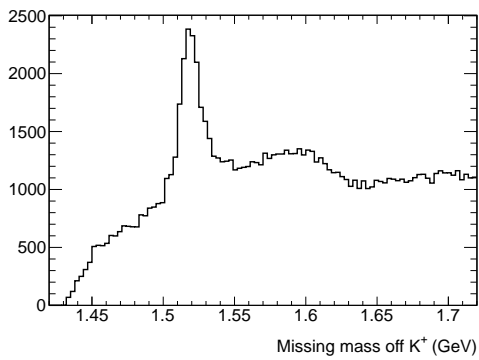
Kinematic fit results are shown in Figure 4.8. Again, we see much lower signal-to-background at lower confidence level. The shape of the spectrum also looks different in the low confidence level region (Figure 4.8b). We apply a 10% confidence level, but possibly a higher cut value could be justified.

4.9 ϕ cut

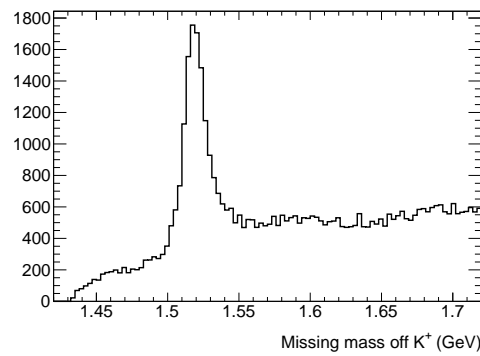
A potential problem in this analysis is that the pK^+K^- final state also has a significant population from the $\gamma p \rightarrow \phi p$ reaction with $\phi \rightarrow K^+K^-$. If the two processes interfere it is not possible to separate $K^+\Lambda(1520) \rightarrow pK^+K^-$ events from $\phi p \rightarrow pK^+K^-$ events. Fortunately the ϕ is a relatively narrow resonance ($\Gamma = 4 \text{ MeV}$), so the kinematic region of overlap between the two states is small. We place a cut on the missing mass of the proton (equivalently, the invariant mass of the K^+K^- system) to remove this overlap region. The baseline version of this cut removes all events



(a) Confidence level distribution. The shaded regions correspond to the two plots below.

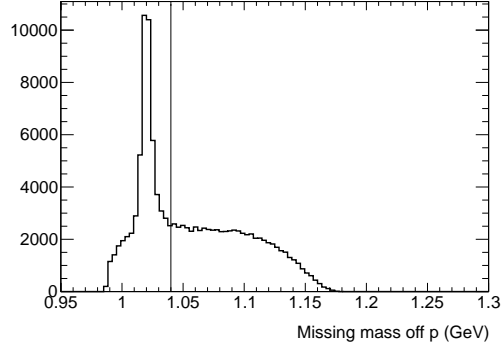


(b) Mass spectrum for events with confidence level between 5-10%

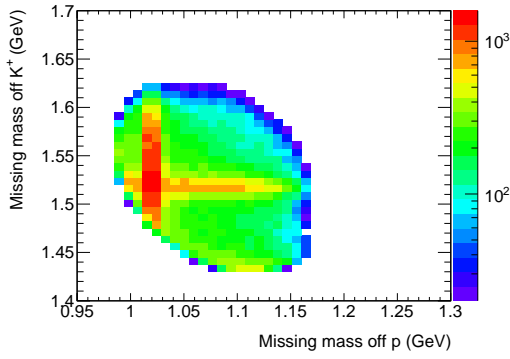


(c) Mass spectrum for events with confidence level between 95-100%

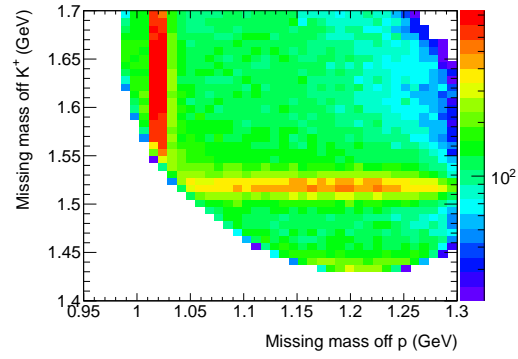
Figure 4.8: Kinematic fit results, missing K^+ topology, all skimmed events.



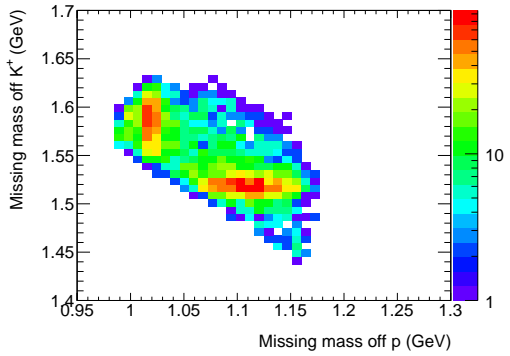
(a) Missing mass off proton spectrum, missing K^- topology, $\sqrt{s} = 2100\text{--}2130$ MeV, after timing cuts and 10% confidence level cut. Cut boundary shown.



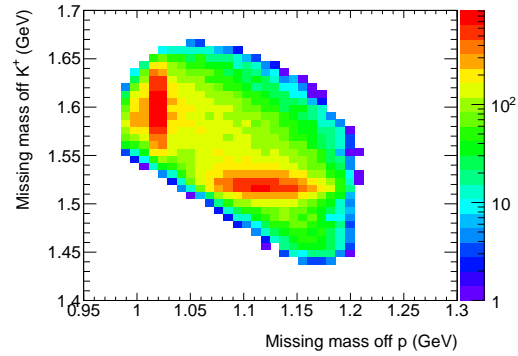
(b) Missing K^- topology, $\sqrt{s} = 2100\text{--}2130$ MeV, after timing cuts and 10% confidence level cut.



(c) Missing K^- topology, $\sqrt{s} = 2250\text{--}2280$ MeV, after timing cuts and 10% confidence level cut.



(d) 3-track topology, $\sqrt{s} = 2100\text{--}2130$ MeV, after timing cuts and 5% confidence level cut.



(e) Missing K^+ topology, $\sqrt{s} = 2100\text{--}2160$ MeV, after timing cuts and 10% confidence level cut.

Figure 4.9: ϕp events are removed using cut shown in (a). Overlap between ϕp and $K^+\Lambda(1520)$ final states occurs in (b), but not in other bins and topologies.

with $MM(p) < 1.040 \text{ GeV}$ ($m_\phi = 1.020 \text{ GeV}$), but the cut value can be varied. Also note that for the missing K^- topology, this cut will not be applied until after we have done the first stage of background subtraction (see Section 6.4).

Figure 4.9 shows the distribution of $MM(p)$, where the ϕ peak is clearly visible. It can be seen from Figure 4.9a that $MM(p) < 1.040 \text{ GeV}$ is a reasonable cut, but that it might be possible to accept events below the ϕ peak ($MM(p) < 1.0 \text{ GeV}$). The reason not to accept these events is because there are few events in this region and the statistics may not be sufficient for the background subtraction procedure to work properly. Also note (Figures 4.9b and 4.9c) that this kinematic overlap between the two processes is only possible at lower \sqrt{s} . Also, in the topologies where the K^- is detected, the detector has no acceptance in the kinematic overlap region of phase space, so the overlap is not visible at all (Figures 4.9d and 4.9e). We still apply the cut in these topologies, but it has little effect.

Chapter 5

Acceptance and Monte Carlo

The distributions we measure are affected by the acceptance of the CLAS detector, the fact that not all particles produced are detected, but rather the chance of detection depends on the particle type, momentum, and angle. Particles in certain regions of phase space will not be detected at all, for example, if they travel through the magnet coils where there are no active detector elements, while even particles in the fiducial region will not be detected with 100% efficiency (for example, a K^- may decay before it reaches the time-of-flight wall). Since we are interested in the distribution of all $K^+\Lambda(1520)$ events, not just the events that we can detect, it is very important to understand the acceptance of the detector before extracting spin density matrix elements. The detector acceptance cannot be modeled by an analytic function, instead we must use the Monte Carlo method. The idea is to simulate the passage of particles through the detector material and the response of detector elements (detector resolution is simulated in addition to detector efficiency). “Raw” events, which consist of just the kinematics of the particles involved, are passed into this simulation, which returns simulated detector signals analogous to raw experimental data. This Monte Carlo data is then passed through the same analysis and event-selection procedure as the real data, which leads to a sample of “accepted” Monte Carlo events. Accepted Monte Carlo is used as described in Sections A.1 and C.13 to correct for acceptance effects when extracting spin density matrix elements and differential cross sections.

5.1 Simulation

5.1.1 Event generation

Simulation begins with event generation. 100 million $\gamma p \rightarrow K^+\Lambda(1520) \rightarrow K^+K^-p$ raw events were generated. Each raw event consists of the 4-momenta of the three final state particles, the photon energy, and the primary vertex position. The thrown photon energy spectrum roughly matches the observed spectrum. The mass of the pK^- system is distributed according to a non-relativistic Breit-Wigner using the PDG values for the mass and width of the $\Lambda(1520)$. The production and decay angles are distributed uniformly in phase space. The z-position of the vertex is uniformly distributed from $z = -30$ – 10 cm, corresponding to the location of the target.

In Section 6.4.1, we discuss a Monte Carlo simulation of other decay modes of the $\Lambda(1520)$. The event generation is the same as above, except for the decay kinematics, which are still uniform in phase space.

5.1.2 GSIM and GPP

GSIM is the standard CLAS simulation software, based on GEANT3 [57]. It contains a model of all the material in the CLAS detector and simulates energy loss, multiple scattering, and particle decays of weakly decaying particles (K^\pm , Λ , Σ) for the particles specified in the raw events as they travel through the detector. It also simulates the signals produced in active detector elements as the simulated particles travel through them. These signals are the output of GSIM.

To make this more realistic, this output is then run through GPP (GSIM Post Processor). This removes hits from dead drift chamber wires and dead TOF counters and smears the times of these signals according to detector resolution.

5.1.3 Momentum smearing

After being processed by GPP, the simulated data is cooked in the same way as the real data. However, we must apply one additional correction before running the kinematic fit.

By looking at the kinematic fit confidence level distribution of the $\gamma p \rightarrow p\pi^+\pi^-$ reaction, Williams found that even after smearing with GPP, the reconstructed momentum resolution is too good compared with data [41]. To correct for this, after the momentum is reconstructed, the momentum is smeared according to a scheme which leads to a flat confidence level distribution in all regions of phase space. McCracken and Dey showed that these corrections also work for analyses with kaons [58, 12]. Figure 5.1 shows confidence level distributions for simulated data for all three topologies studied here, where the kinematic fit is performed after momentum smearing has been applied. The distributions are mostly flat at high confidence levels, indicating that the smearing has served its purpose.

After the momenta have been smeared, the kinematic fit can be run, and the skimming process can be completed. The skims work the same way as described in Chapter 4, except that the momentum and trigger corrections discussed in Section 4.3 are not needed in the skim (energy loss corrections are still used).

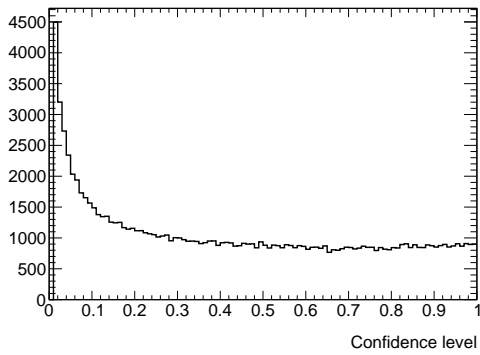
All other cuts are applied as described in Chapter 4.

5.1.4 Trigger simulation

One additional thing we must simulate is the trigger. For example, if we are studying a two-track topology, and both detected tracks are in the same sector, the trigger would not fire. Even if we have two tracks in different sectors, it is not guaranteed that the trigger would fire. The probability that a track with a given momentum in a given sector will fire the trigger in that sector is called the trigger efficiency. This was determined empirically by Krahn [59] by looking at the trigger word (a record of which sectors the trigger conditions were met in) in $\gamma p \rightarrow p\pi^+\pi^-$ data events. Trigger efficiencies were calculated for pions and protons as a function of sector, TOF counter, and azimuthal angle ϕ .

The trigger is simulated by looping over all detected particles and throwing a random number between 0 and 1. If the number is less than the trigger efficiency of the corresponding particle, the particle is considered to have fired the trigger in its sector. If less than two sectors have simulated triggers, then the event is discarded. It is important that all detected tracks, even if they are not part of the desired topology, be included in the trigger simulation. For example, in the $p(K^+)K^-$ topology, it could be the case that both the p and the K^- are in the same sector, but the K^+ is still detected and in a different sector, so the (simulated) trigger should still fire.

Trigger efficiencies were not calculated for kaons. As shown in Figure 5.2, the proton and π^+ trigger maps differ. Since the kaon is intermediate in mass between the pion and the proton, either trigger efficiency map could be used for the K^+ . For this analysis, the π^\pm efficiencies are used for K^\pm . Dey showed that the choice between the p and π^+ trigger efficiencies (for the K^+) does not cause any systematic effects on analysis [12].



(a) 3-track topology

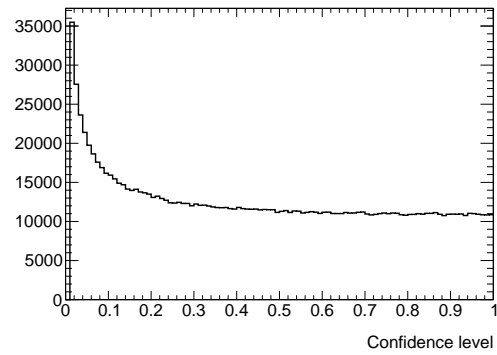
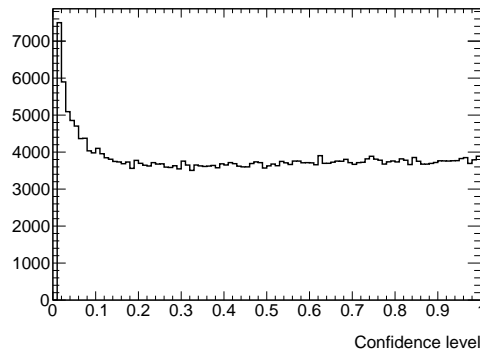
(b) Missing K^- topology(c) Missing K^+ topology

Figure 5.1: Kinematic fit confidence level, 10% of Monte Carlo sample, after momentum corrections, also after timing cuts

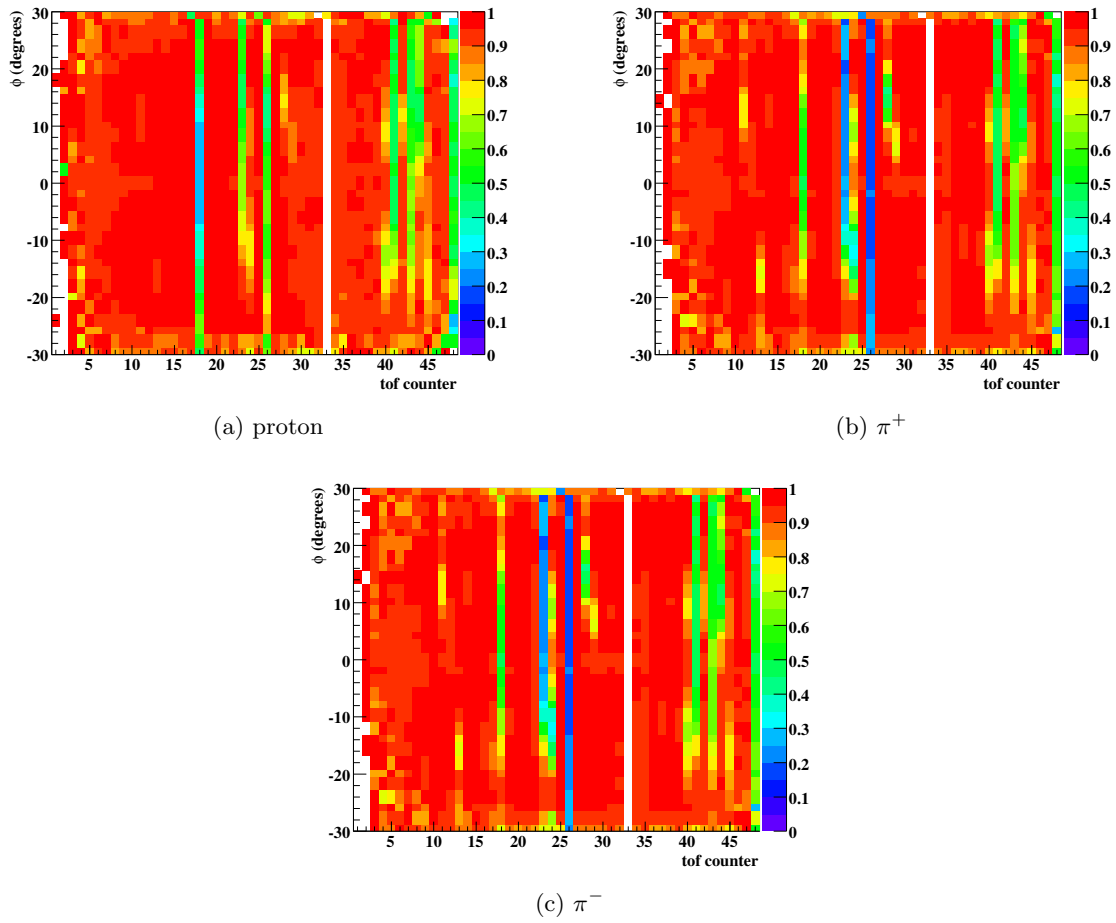


Figure 5.2: Trigger efficiencies for sector 1.

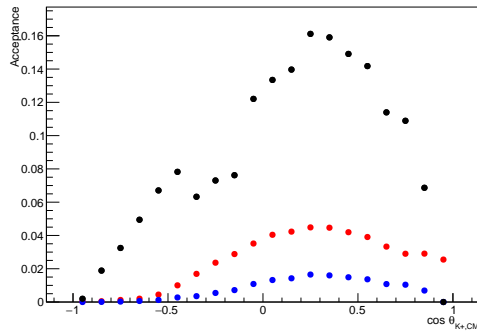


Figure 5.3: Acceptances, $\sqrt{s} = 2340 - 2400$ MeV, for 3-track (blue), missing K^- (black), and missing K^+ (red) topologies. For this plot, we have not removed the 3-track events from the other two topologies.

5.1.5 Summary

Figure 5.3 shows the acceptance as a function of production angle in all three topologies, after all the steps here. We will not use the acceptance in this simple form for further analysis, but it just gives an idea of the overall acceptance.

Chapter 6

Background

Figure 6.1 shows the missing mass off K^+ spectrum after all cuts discussed in Chapter 4. We can clearly see the $\Lambda(1520)$ on top of a non-peaking background. We would like to isolate the contribution of the $\Lambda(1520)$ production process from the other processes. The procedure we use to do this is called the Q-value method, which assigns a probability to each event, estimating the probability that an event with the given kinematics is signal. This procedure makes two assumptions. The first is that the background does not peak. This is so we can use the peak to help distinguish what is signal and background. For the missing K^- topology, this assumption is not satisfied so we must use a more sophisticated method. For the 3-track and missing K^+ , there is no reason why the background would peak at the $\Lambda(1520)$ mass, so this assumption is satisfied. The second assumption is that the signal and background do not interfere. If they interfere, the total spectrum as seen in Figure 6.1 cannot be decomposed into a simple sum of signal spectrum and background spectrum, and the strategy of assigning a signal probability to each event is not meaningful.

6.1 The Q-value method

The Q-value method assigns to each event a probability Q that the given event is signal [60]. One begins with the assumption that the distribution of a particular kinematic variable M can be described by the function $F(M, \vec{\alpha}, \vec{\beta}) = S(M, \vec{\alpha}) + B(M, \vec{\beta})$, which is the sum of a signal component $S(M, \vec{\alpha})$ and a background component $B(M, \vec{\beta})$. $\vec{\alpha}$ and $\vec{\beta}$ are sets of parameters that determine the signal and background functions. For resonances, a good choice for S is probably a Breit-Wigner convolved with a Gaussian, with parameters specifying the Gaussian width and the scale of the peak. Since the form of the background is not known exactly but is assumed to be smoothly varying, B is usually chosen to be a low-degree polynomial function.

We define a metric to determine the similarity between a pair of events. A reasonable choice for the metric would be:

$$d_{ij} = \sum_k \left(\frac{\theta_k^i - \theta_k^j}{r_k} \right)^2, \quad (6.1)$$

where i and j label events, the θ_k are a chosen set of kinematic variables (not including M), and each r_k denotes a characteristic scale of the the corresponding θ_k , which can be taken to be the range of the variable.

One small subtlety should be noted when defining the metric. The “distance” between two angles is not determined by a simple subtraction, but must account for the circular nature of angles, the fact the angles ϕ and $\phi + 2\pi$ are the same. This is easily implemented. Likewise, although we define the range of possible angles as $-\pi$ to π , the maximum distance between two angles is π rather than

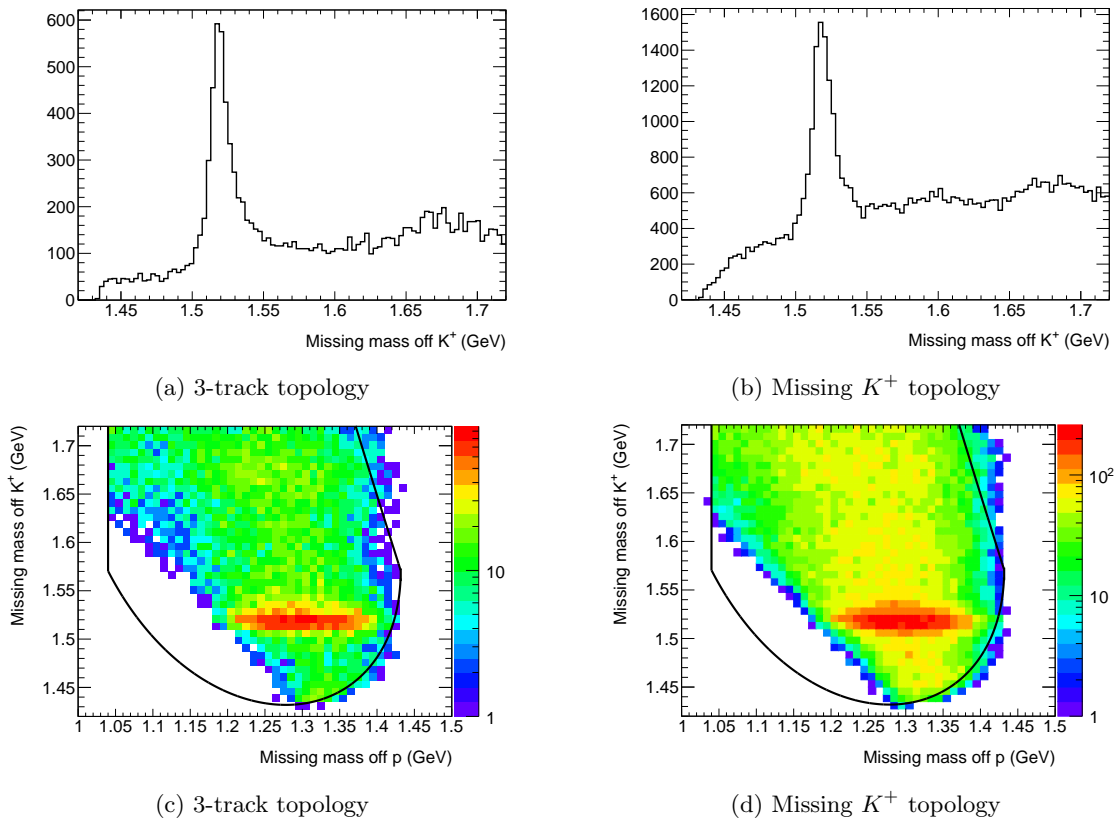


Figure 6.1: Missing mass plots, $\sqrt{s} = 2340\text{--}2400$ MeV. After all cuts. The vertical line in (c) and (d) on the left shows the boundary of the cut that eliminates the ϕ (see section 4.9). The other curves show the boundary of the kinematically allowed region at $\sqrt{s} = 2370$ MeV (the center of the bin). White areas within this region indicate areas where the detector has no acceptance.

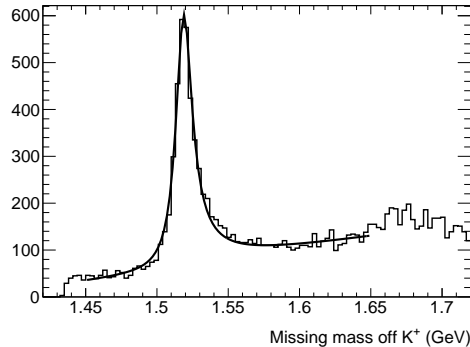


Figure 6.2: Missing mass off K^+ spectrum, $\sqrt{s} = 2340\text{--}2400$ MeV. After all cuts. 3-track topology. This is the same histogram as shown in Figure 6.1a with the fit function (Breit-Wigner plus linear background) plotted on top. The details of the fit function are discussed in the text.

2π , so we would use $r = \pi$ in equation (6.1). In polar coordinates, these considerations apply to the azimuthal angle ϕ , but not the polar angle, because we deal with the cosine $\cos\theta$ rather than the raw angle (this is because an isotropic distribution is uniform in $(\cos\theta, \phi)$).

For each event i , we find the $N - 1$ nearest neighbors with the distance defined by the metric (N is usually chosen to be on the order of 100). We take the M distribution of these N events (including the original event i) and fit the function $F = S + B$ to this distribution, using the maximum likelihood method (see Appendix A), to determine the values $\vec{\alpha}_i$ and $\vec{\beta}_i$ which maximize the likelihood for the given event. Then we define Q for the event i as:

$$Q_i = \frac{S(M_i, \vec{\alpha}_i)}{S(M_i, \vec{\alpha}_i) + B(M_i, \vec{\beta}_i)}. \quad (6.2)$$

As mentioned before, this makes the assumption of a non-peaking background, so that it can be well approximated by a smooth background function, and also the assumption of non-interference of processes.

6.2 3-track topology

Before going into the details of the Q-value fit, we will see how well the total mass spectrum can be described by the sum of a Breit-Wigner plus a background term. In Figure 6.2, we show the mass spectrum for all events in the $\sqrt{s} = 2340\text{--}2400$ MeV bin, together with a fit function. The function fitted is the Breit-Wigner form given by Equation (B.15), plus a linear background. In this fit, the Breit-Wigner is not convolved with a Gaussian. In this fit, we have allowed Γ_0 , which determines the width of the Breit-Wigner according to Equation (B.8), to vary, in addition to varying the scale of the Breit-Wigner and the parameters of the background function. Interestingly, we extract a value of $\Gamma_0 = 14.5$ MeV from the fit, which is smaller than the PDG value of 15.6 ± 1.0 MeV (our simple fit doesn't account for detector resolution; if it did, our extracted value would be even smaller than 14.5 MeV, making the discrepancy more significant). A recent electroproduction measurement by Qiang et al. finds $\Gamma = 18.6 \pm 2$ MeV [28]. This paper uses the same Breit-Wigner form as our fit, although a more complex background parametrization (they note that if a simpler background form is used, their value of Γ drops by ~ 1 MeV). This discrepancy is difficult to explain, since both our results and those of Qiang et al. come from electromagnetic production, so backgrounds should be similar. In all of the fits discussed in the chapter, our data tends to favor low values of Γ_0 .

Fit parameter		Range of values allowed
M_0	Central value of Breit-Wigner	1515–1525 MeV
Γ	Breit-Wigner width	10–20 MeV
σ	Gaussian width	1–12 MeV
C	Breit-Wigner scale	> 0
a	Intercept of background function	unbounded
b	Slope of background function	unbounded
Other parameter		Value
N	Number of nearest neighbors	100
M_{lo}	Only events with $M_{\text{lo}} < M < M_{\text{hi}}$ are used in fit	1450 MeV
M_{hi}		1650 MeV

Table 6.1: Parameters in baseline fit

When doing the full Q-value background fits, it is possible to perform many different variations on the background fit, by varying, e.g., the number of nearest neighbors used, the form of the Breit-Wigner used for the signal, the polynomial degree used for the background, or the “range” of allowed fit parameters. The baseline fit is the simplest fit that produces good results. Other variations on the fit can be compared with the baseline fit to see how much the fit details affect the results.

Before the background fit, we bin the data in \sqrt{s} , with bins of width 60 MeV. In each bin an independent background fit occurs, so that only events from the same bin can be considered nearest neighbors.

6.2.1 Baseline fit

In the baseline fit, the signal was modeled using the Breit-Wigner (convolved with a Gaussian) form given in Equation (B.17), which was found to best match the data. The background is modeled using a linear function.

As discussed above, a feature seen across many of these fits is that the data seems to prefer a value of Γ_0 below the PDG value: if the Breit-Wigner width Γ is fixed at the PDG value 15.6 MeV, the fit function does not match the data, with the observed peak being narrower than the fit peak. For this reason, the parameter Γ is allowed to vary in the fits. Without this, the fits look poor. In addition, better results are seen if the central mass of the Breit-Wigner is allowed to vary from the PDG value of 1519.6 MeV. These deviations from the PDG can be justified by uncertainty in the true value of these parameters as well as experimental uncertainty.

Only events with $MM(K^+)$ from 1450–1650 MeV are used in the fit. This is to avoid having to model the lineshape immediately above threshold, and to cut events far away from the $\Lambda(1520)$ mass peak, especially the region above 1650 MeV where there appears to be a bump (see Figure 6.1).

A list of parameters used in the baseline fit is given in Table 6.1. The kinematic variables used to determine the metric are $\cos\theta_{K^+,CM}$, $\cos\theta_{\text{Hel}}$, and ϕ_{Hel} , with corresponding ranges 2, 2, and π . θ_{Hel} and ϕ_{Hel} are the angles of the K^- in the helicity frame, which is defined in Section 2.2.3. These three variables together with \sqrt{s} (which we have already binned in) and $MM(K^+)$ (the variable whose distribution we will fit) completely specify the kinematics of the event.

The results of the baseline fit are shown in various energy and angle bins in Figures 6.3 and 6.4, which show $MM(K^+)$ signal distributions (events weighted by Q) and background distributions (events weighted by $1 - Q$). An important feature in these plots is the lack of prominent features (bumps or dips) in the background distribution in the region of the $\Lambda(1520)$ peak. If there were a peak in the background distribution underneath the peak in the signal distribution, this would be a clear sign that some true signal was being misclassified as background and the fits were not working properly.

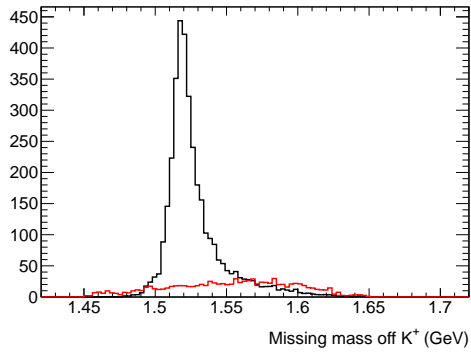
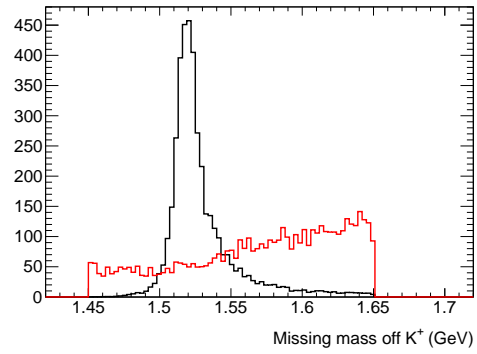
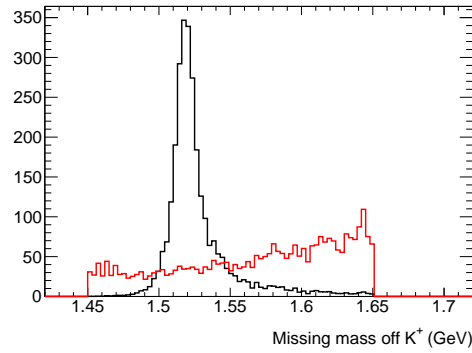
(a) $\sqrt{s} = 2100\text{--}2160$ MeV(b) $\sqrt{s} = 2400\text{--}2460$ MeV(c) $\sqrt{s} = 2700\text{--}2760$ MeV

Figure 6.3: Missing mass off K^+ distribution, 3-track topology, in three different \sqrt{s} bins. In black, events weighted by signal probability Q . In red, events weighted by $1 - Q$. Q calculated using the baseline fit parameters in Table 6.1.

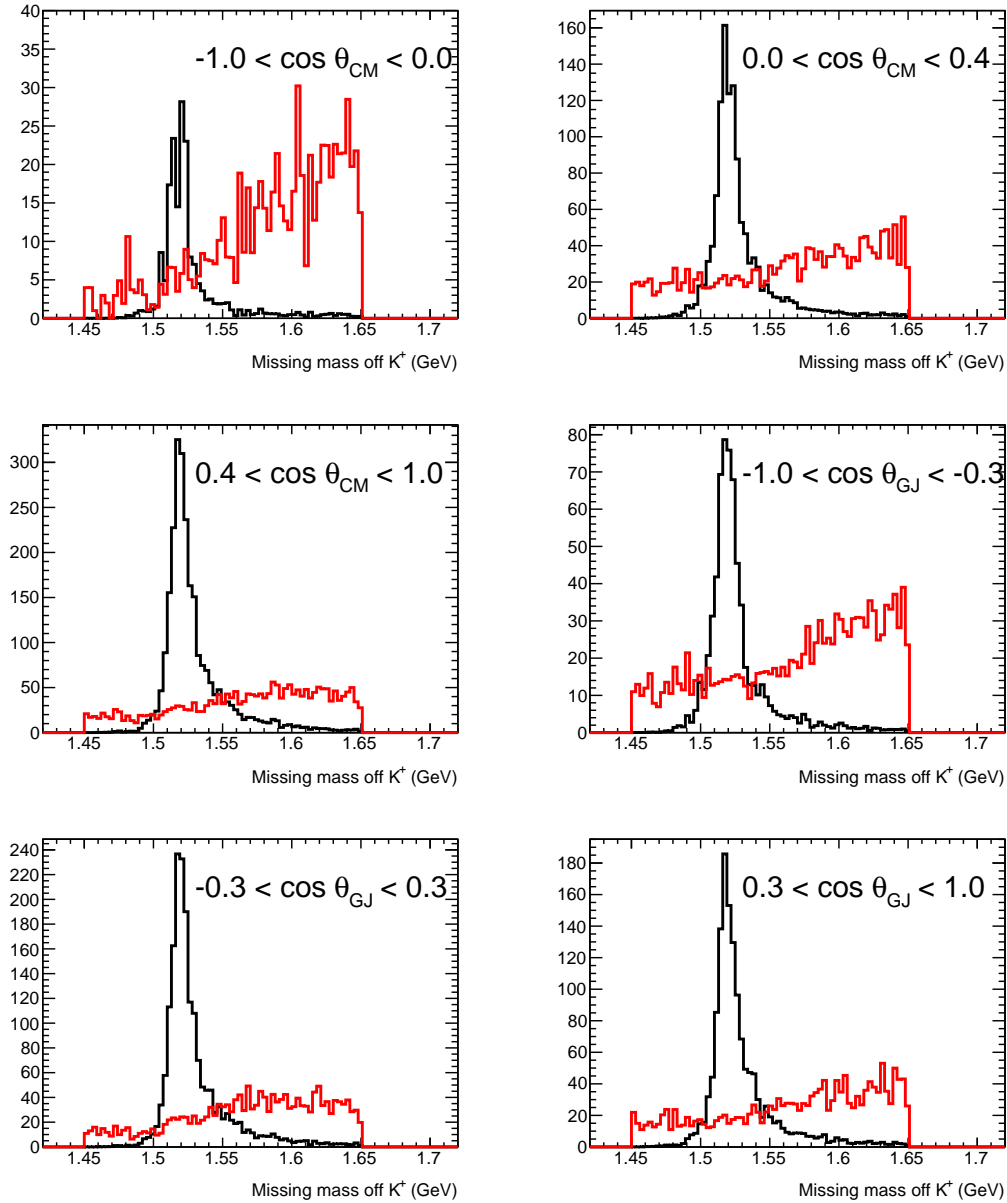


Figure 6.4: Signal (black) and background (red) missing mass off K^+ distribution for various angular slices (in $\cos \theta_{K^+,CM}$ and $\cos \theta_{K^-,GJ}$) in $\sqrt{s} = 2280 - 2340$ MeV. 3-track topology.

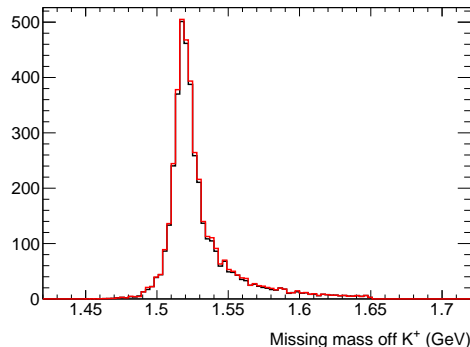


Figure 6.5: Comparison of extracted signal using a linear background function (black) and quadratic background function (blue). $\sqrt{s} = 2280\text{--}2340$ MeV, 3-track topology.

All subsequent analysis is done weighting the events by their signal probability. In addition, after the background fits are done, we cut out all events outside the peak region $1500 \text{ MeV} < IM(pK^-) < 1540 \text{ MeV}$, since we do not necessarily have a good understanding of the lineshape in the tail region.

One additional detail about the fitting procedure is important to note. The parameters Γ and σ have similar roles in the signal function, controlling the width of the Breit-Wigner peak. This means we should not necessarily expect the function we are minimizing (the negative maximum likelihood) to have a single local minimum. Traditional minimization using gradient-descent methods has trouble with this type of function as it will only find a single local maximum, and not find any others that may be the true global minimum. Which local minimum it finds depends entirely on the starting values of the parameters fed to the fit. To avoid these problems, for these fits we used genetic minimization rather than the gradient-descent method. Genetic minimization is a method in which each new iteration of the fit is based on the best results of previous iterations, but with some source of randomness added. The randomness prevents the strong dependence on initial parameter values and can help prevent the fitter from getting “stuck” in a local minimum that is not the global minimum. More details can be found [61]. To implement genetic minimization, we use the `ROOT::Math::GeneticMinimizer` class provided by the CERN ROOT library.

The downsides of genetic algorithms are that they are non-deterministic and not guaranteed to find an exact local minimum. However for this problem, it works quite well. When we only vary one of the width parameters, results are very similar between the gradient descent and genetic algorithm methods, but when both widths are allowed to vary, the genetic algorithm performs better. Because of the randomness, two invocations of the genetic fitting with identical data do not produce identical results, but in this case, the differences are negligible: although individual event weights are different between subsequent fits, the weighted histograms from two different invocations are indistinguishable when plotted.

6.2.2 Variations on the baseline

As mentioned above, we can run fits with parameters which are different from the baseline fit. For example, the difference between a fit with a linear background function and a quadratic background function is shown in Figure 6.5. In Section 7.3.1, we attempt to quantify the uncertainty (on our extracted spin density matrix elements) that this choice of background function (linear vs. quadratic) introduces. Other fit variations, like doubling the number of nearest neighbors and varying the limits on the fit parameters, do not appear to have a large effect on the fit results. However, changing the shape of the signal function does have a large effect, making the fits appear qualitatively much worse.

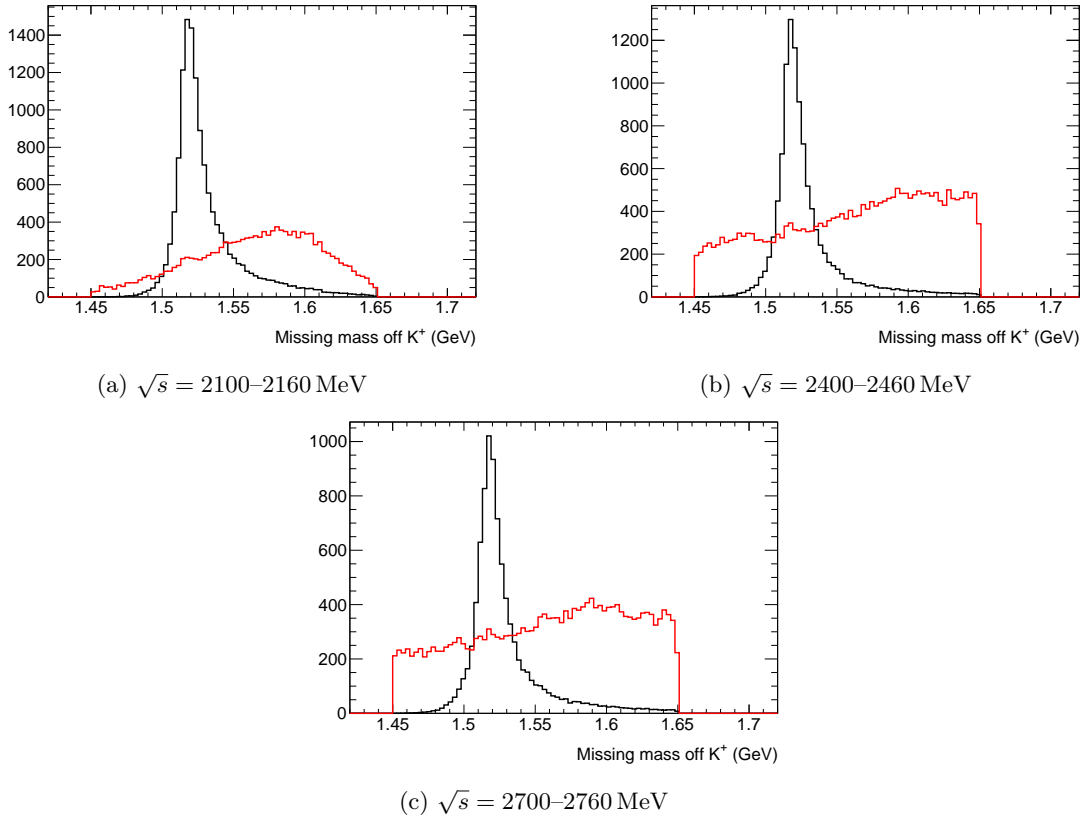


Figure 6.6: Missing mass off K^+ distribution, missing K^+ topology, in three different \sqrt{s} bins. In black, events weighted by signal probability Q . In red, events weighted by $1 - Q$. Q calculated using the baseline fit parameters in Table 6.1.

6.3 Missing K^+ topology

The set-up of this fit is the same as the baseline fit above (Table 6.1). As before, 60 MeV-wide bins are used. Results are shown in Figures 6.6 and 6.7.

We note that in these fits, for certain kinematics, there are bumps in the the background distribution in the $\Lambda(1520)$ region, indicating that the signal is underestimated. In Chapter 7, we will try to estimate how much uncertainty this introduces into the extracted values of the spin density matrix elements.

As with the 3-track topology, all further analysis is done with events in the region 1500 – 1540 MeV, weighted by the signal probability from the baseline fit.

6.4 Missing K^- topology

An additional complication in the missing K^- topology is that background processes (i.e. processes other than $\gamma p \rightarrow K^+ \Lambda(1520) \rightarrow p K^+ K^-$) have the same signature as the signal process. The culprit is $\gamma p \rightarrow K^+ \Lambda(1520)$ events where the $\Lambda(1520)$ decays to something other than $p K^-$. Table 6.2 shows the decays of the $\Lambda(1520)$.

If the missing particles (e.g. the $\pi^- \pi^0$ in the $\Lambda(1520) \rightarrow \Sigma^+ \pi^- \rightarrow p \pi^0 \pi^-$ decay) have an invariant mass around the K^- mass, the event is kinematically indistinguishable from a $p K^+ K^-$ event. Since

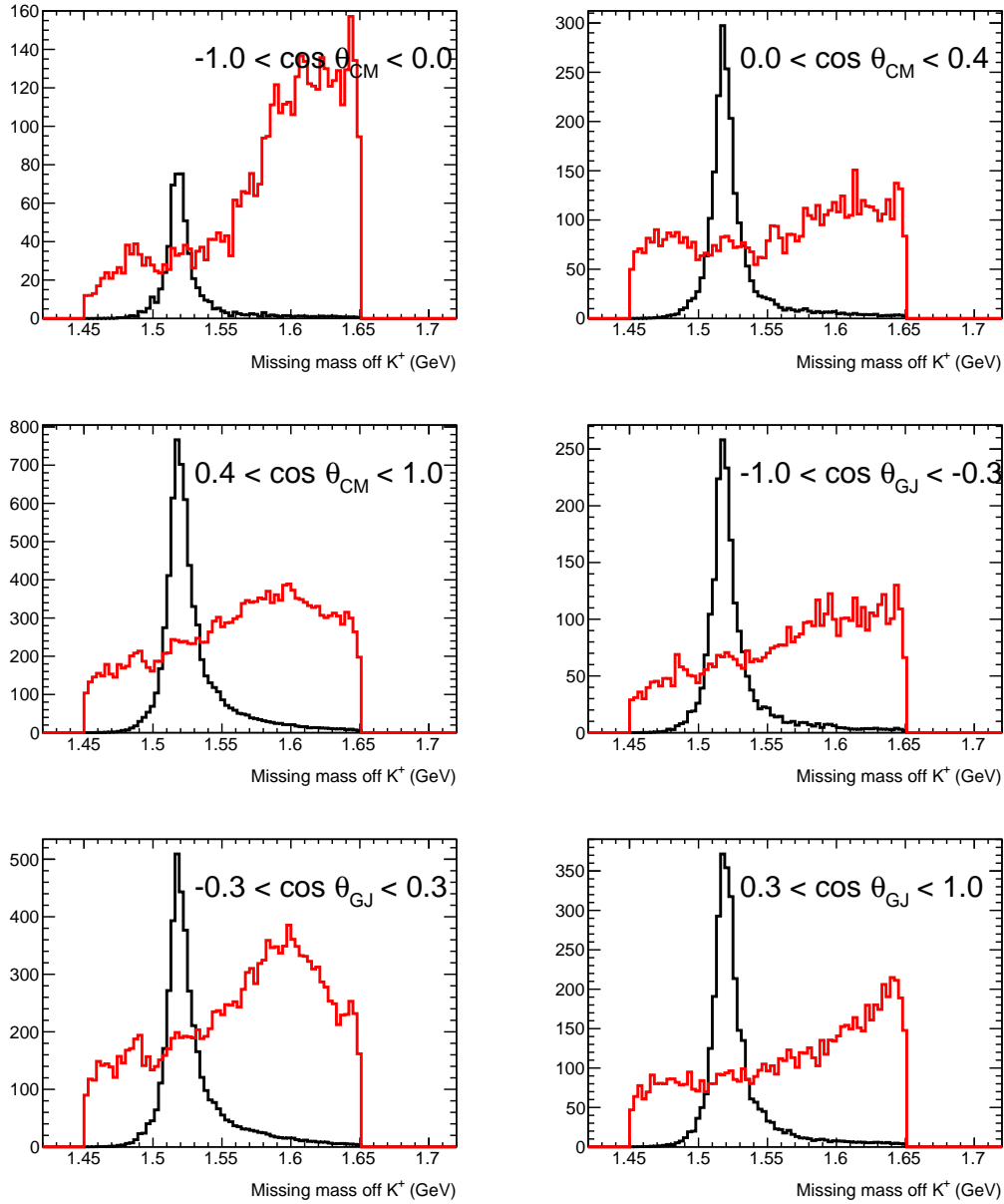
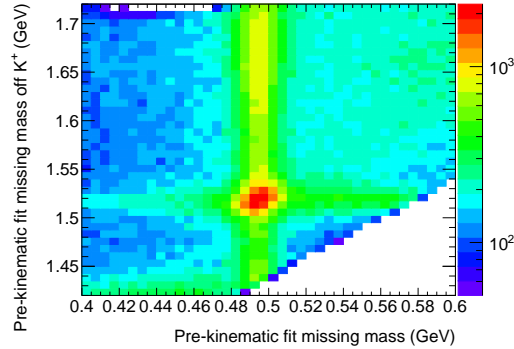


Figure 6.7: Signal (black) and background (red) missing mass off K^+ distribution for various angular slices (in $\cos \theta_{K^+,CM}$ and $\cos \theta_{K^-,GJ}$) in $\sqrt{s} = 2280 - 2340$ MeV bin. Missing K^+ topology.

Decay mode	Final state	Branching fraction	Mimics $pK^+(K^-)$
$\Lambda(1520) \rightarrow pK^-$	pK^+K^-	22.5%	Signal
$\Lambda(1520) \rightarrow n\bar{K}^0$	$nK^+\bar{K}^0$	22.5%	No
$\Lambda(1520) \rightarrow \Sigma^+\pi^-, \Sigma^+ \rightarrow p\pi^0$	$pK^+\pi^-\pi^0$	7%	Yes
$\Lambda(1520) \rightarrow \Sigma^+\pi^-, \Sigma^+ \rightarrow n\pi^+$	$nK^+\pi^-\pi^+$	7%	No
$\Lambda(1520) \rightarrow \Sigma^0\pi^0, \Sigma^0 \rightarrow \Lambda\gamma, \Lambda \rightarrow p\pi^-$	$pK^+\pi^0\pi^-\gamma$	9%	Yes
$\Lambda(1520) \rightarrow \Sigma^0\pi^0, \Sigma^0 \rightarrow \Lambda\gamma, \Lambda \rightarrow n\pi^0$	$nK^+\pi^0\pi^0\gamma$	5%	No
$\Lambda(1520) \rightarrow \Sigma^-\pi^+, \Sigma^- \rightarrow n\pi^-$	$nK^+\pi^-\pi^+$	14%	No
$\Lambda(1520) \rightarrow \Lambda(\pi\pi)^0, \Lambda \rightarrow p\pi^-$	$pK^+\pi^-(\pi\pi)^0$	6%	Yes
$\Lambda(1520) \rightarrow \Lambda(\pi\pi)^0, \Lambda \rightarrow n\pi^0$	$nK^+\pi^0(\pi\pi)^0$	4%	No

Table 6.2: $\Lambda(1520)$ decays. Decays with branching fraction $< 1\%$ are excluded.Figure 6.8: Pre-kinematic fit kinematics, missing K^- topology, $\sqrt{s} = 2340 - 2370$ MeV. The reason for plotting the pre-kinematic fit values of MM and $MM(K^+)$ in this plot is that the kinematic fit forces the MM to m_K and biases the value of $MM(K^+)$ for events when there is not really a missing K^- .

these are also real $K^+\Lambda(1520)$ events they will feature the same peak at $MM(K^+) = 1520$ MeV, we cannot separate them from the signal using the method used above for the other two topologies.

The problem is illustrated in Figure 6.8. The vertical band around $MM = 495$ MeV is dominated by events with a missing K^- . The horizontal band around $MM = 1520$ MeV is dominated by $K^+\Lambda(1520)$ events. We can not separate our signal events from the background just by looking at the $MM(K^+)$ as we could do in the other two topologies. Instead we will use a two-stage background subtraction, as described below.

For this topology, we have much higher statistics, so we will use \sqrt{s} bins of width 30 MeV, rather than 60 MeV.

6.4.1 Stage 1

In the first stage of background subtraction, we would like to identify events with a missing K^- , separating $pK^+(K^-)$ events from $pK^+(X \neq K^-)$. To do this we fit the MM distribution.

We begin with events passing the cuts discussed in Chapter 4, but at this stage do not use the kinematic fit confidence level cut or the cut on $MM(p)$ (which eliminates the ϕ meson). We can't use these cuts since they will distort the distribution that we want to look at. We use the original measurements of momenta of the detected particles, rather than the corrected momenta from the kinematic fit (otherwise the MM distribution would just be a spike at m_{K^-} and there would be

Fit parameter		Range of values allowed
M_0	Mean value of Gaussian	470–520 MeV
σ	Gaussian width	1–12 MeV
C	Gaussian scale	> 0
a	Intercept of background function	unbounded
b	Slope of background function	unbounded
Other parameter		Value
N	Number of nearest neighbors	100
M_{lo}	Only events with $M_{\text{lo}} < M < M_{\text{hi}}$ are used in fit	400 MeV
M_{hi}		600 MeV

Table 6.3: Parameters in stage 1 fit for missing K^- topology

nothing to fit to). We do exclude events included in the 3-track sample.

To determine the Q-values, we fit the MM distribution with a Gaussian roughly centered on the K^- mass for signal function, and a linear function for the background. The full set of parameters is given in Table 6.3. The kinematic variables used to determine the metric are $\cos \theta_{K^+, CM}$, $\cos \theta_{\text{Hel}}$, ϕ_{Hel} , and $MM(K^+)$, with corresponding “ranges” of 2, 2, π , and 100 MeV. The pre-kinematic fit values of the variables are used to calculate the metric. The weights from this fit are denoted Q_1 . Results from this fit are shown in Figure 6.9.

One notable feature is that the mean of the Gaussian is allowed to vary from 470–520 MeV (compared to the K^- mass at 494 MeV), which seems to be a larger range than expected, given the detector resolution. The reason for this can be seen in Figure 6.11, which shows results from a Monte Carlo simulation of $\gamma p \rightarrow K^+ \Lambda(1520) \rightarrow K^+ K^- p$. The measured values of $MM(K^+)$ and MM are correlated, so if we have a group of events above the $\Lambda(1520)$ peak, we would not expect the MM distribution to be centered at exactly the K^- mass, but somewhat above it.

We see a dip in the background MM distribution, largest in the highest energy bin. We can examine this further by looking at angular bins within this bin: Figure 6.10. Since this dip appears in all bins, it will not necessarily have a large effect on the spin density matrix elements, but at this stage, we cannot quantify the effect.

A Monte Carlo investigation

We can simulate all decay modes of the $\Lambda(1520)$ to see their effects on our analysis and to test the usefulness of our “stage 1” background fit. Using the procedure described in Chapter 5, $\gamma p \rightarrow K^+ \Lambda(1520)$ events were simulated with the $\Lambda(1520)$ decaying to pK^- , $\Sigma^+ \pi^-$, $\Sigma^0 \pi^0$, $\Lambda \pi^+ \pi^-$, and $\Lambda \pi^0 \pi^0$ in proportion to the branching fractions given by the PDG. Decays to $n \bar{K}^0$ and $\Sigma^- \pi^+$ were not simulated, as decays without a proton are unlikely to cause a problem. The Monte Carlo program, `gsm`, handled the decays of the ground-state hyperons Λ and Σ taking into account their decay lengths and the finite distance they would travel through the detector. The $K^+ \Lambda(1520)$ events were distributed uniformly in phase space, with the decays also uniform in two- or three-body phase space, as appropriate. We select potential $pK^+(K^-)$ events using the cuts described in Chapter 4.

First we look only at the pK^- decay events to tie up a loose end from above. In Figure 6.11, we can see the correlation between the pre-kinematic fit values of MM and $MM(K^+)$, with events slightly away from the center of the $\Lambda(1520)$ peak having a mean MM offset from the true K^- mass.

Next, we can estimate the size of the background from the non- pK^- decays. At this point, we include the kinematic fit and the confidence level cut, because we are interested in seeing how many non- $pK^+(K^-)$ events mimic $pK^+(K^-)$ even after we have applied all cuts. $MM(K^+)$ distributions are shown in Figure 6.12. Including only events in the $\Lambda(1520)$ peak region (1500–1540 MeV), the

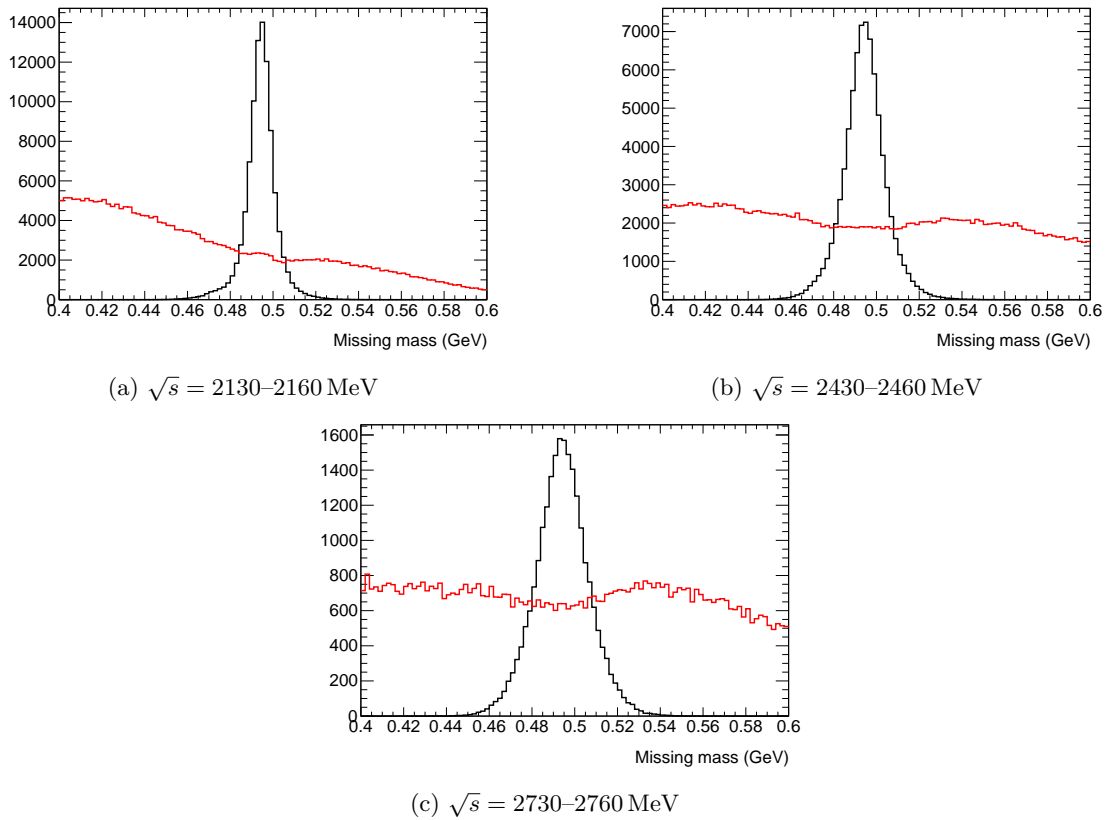


Figure 6.9: Missing mass distribution, missing K^- topology, in three different \sqrt{s} bins. In black, events weighted by signal probability Q_1 . In red, events weighted by $1 - Q_1$.

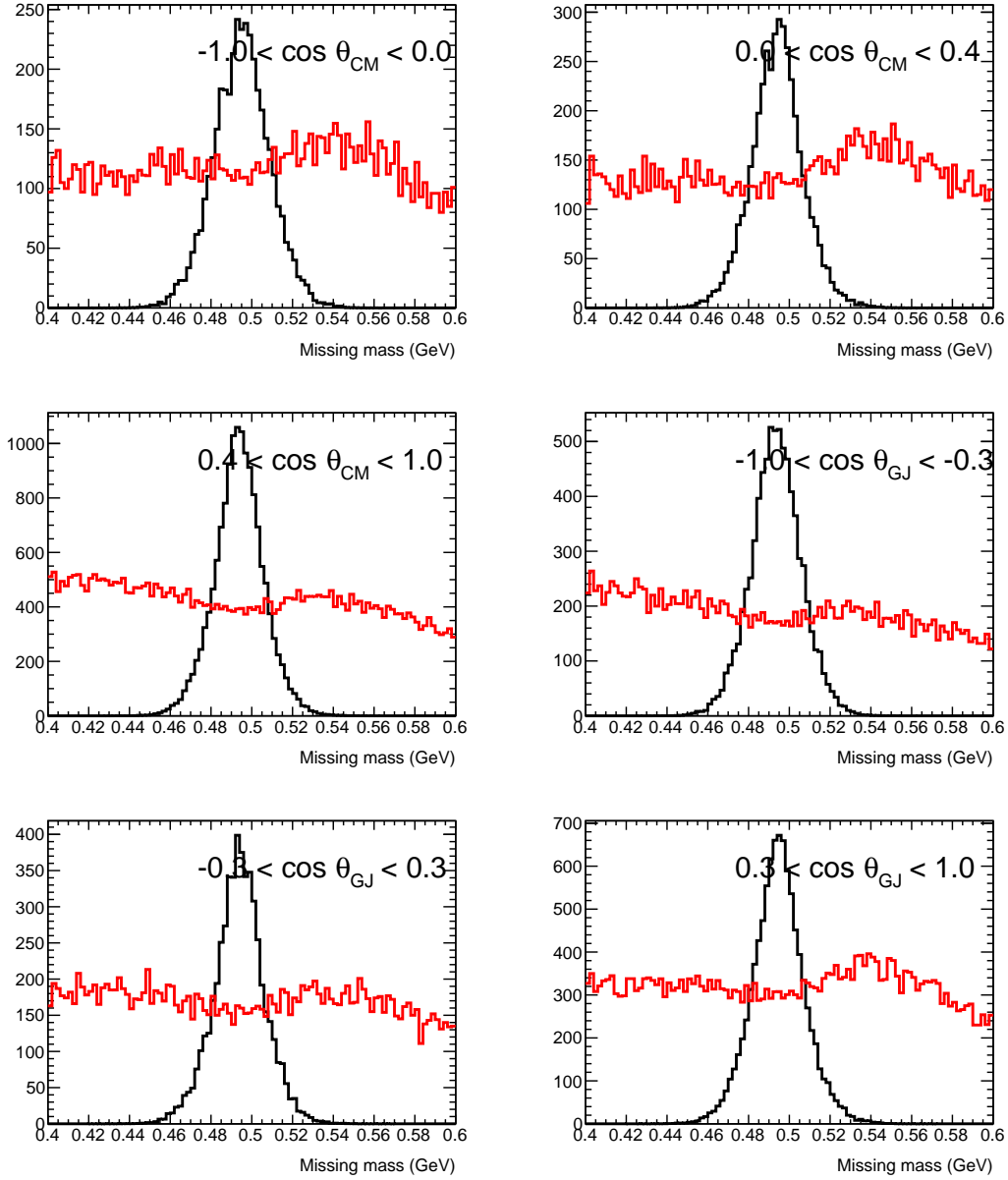


Figure 6.10: Missing mass distribution for various angular slices (in $\cos\theta_{K^+,CM}$ and $\cos\theta_{K^-,GJ}$) in $\sqrt{s} = 2730 - 2760$ MeV bin. Missing K^- topology. In black, events weighted by signal probability Q_1 . In red, events weighted by $1 - Q_1$.

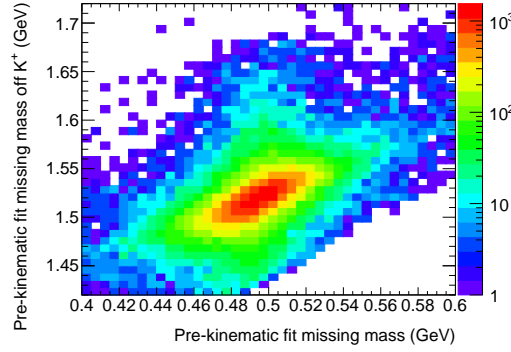


Figure 6.11: Pre-kinematic fit kinematics, Monte Carlo, pK^- decays only, missing K^- topology, $\sqrt{s} = 2730 - 2760$ MeV.

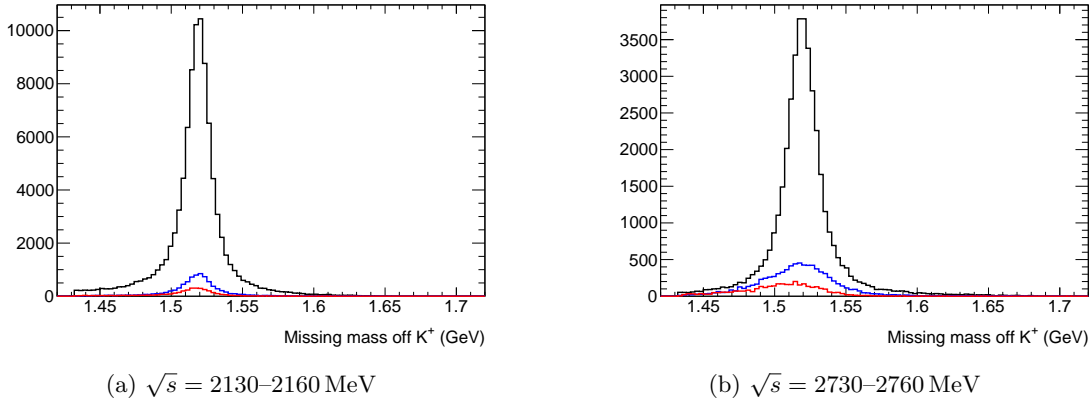


Figure 6.12: Missing off K^+ distribution, Monte Carlo, separated by $\Lambda(1520)$ decay mode. Signal events from the pK^- decays are in black. The $\Sigma^+\pi^-$ and $\Sigma^0\pi^0$ decays are combined and shown in the blue histogram. $\Lambda\pi\pi$ decays are shown in the red histogram.

ratio of background to signal ranges from 12% at lower energies to about 25% at higher energy.

Next, we can run our Stage 1 background fit on the Monte Carlo, to see how well it can separate the signal decay mode from the backgrounds. We combine all the events from different decay modes together and run the fit the same way as on the data (as with the data, the input to fit must not include the confidence level cut and must use the pre-kinematic fit kinematics). Results are shown in Figure 6.13. Comparing the true signal distribution in blue with the extracted signal distribution in black, we see that the fit performs worse at higher energy, consistent with the data shown in Figure 6.9, where the dip in the background distribution is seen most strongly in the same high-energy bin.

Since we are interested in the decay angular distributions, we can compare the extracted signal distribution with the true signal and background distributions as shown in Figure 6.14. The agreement is reasonable between the true signal and the extracted signal, but also appears to get worse at higher energies.

We can extract the spin density matrix elements for this sample of events to estimate how much error the background subtraction procedure introduces. This is done in Section 7.3.4. As explained in that section, it turns out not to be a significant source of error.

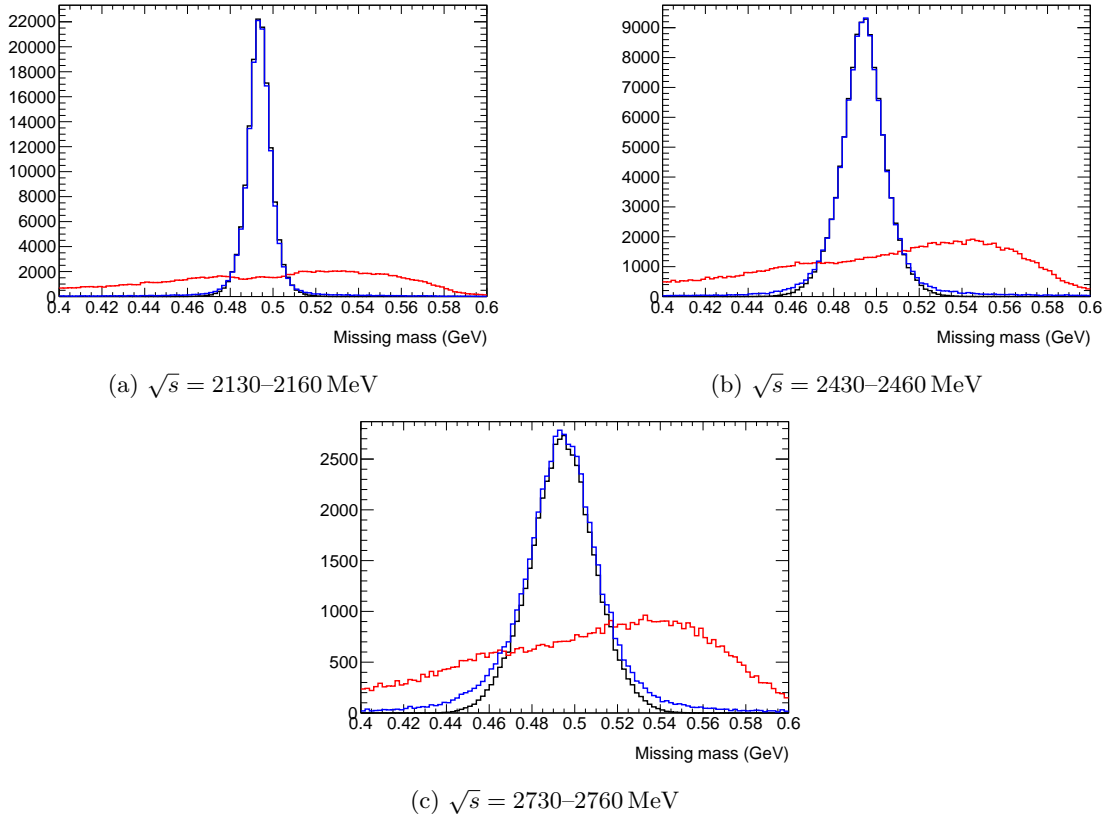


Figure 6.13: Missing mass distribution, Monte Carlo, all $\Lambda(1520)$ decay modes, missing K^- topology, in three different \sqrt{s} bins. In black, events weighted by signal probability Q_1 . In red, events weighted by $1 - Q_1$. In blue are true signal events (i.e. pK^- decays only). Compare this figure to Figure 6.9, which shows the corresponding results for the real data.

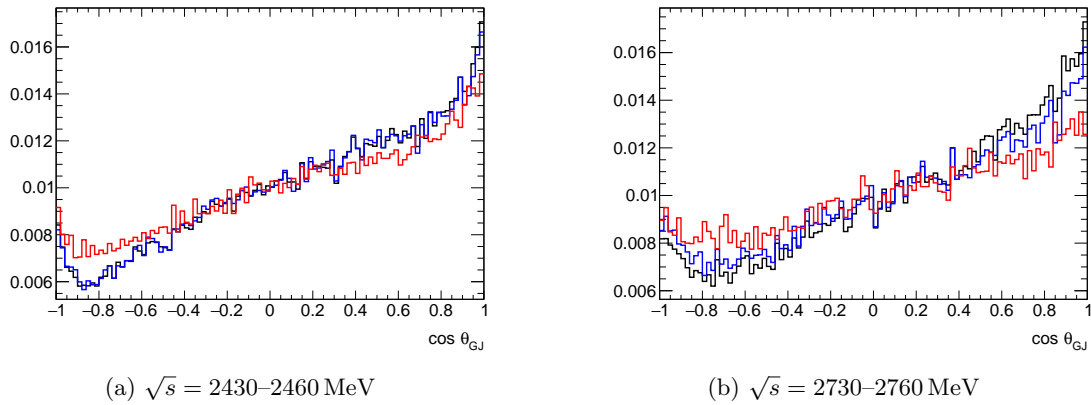


Figure 6.14: Decay angular distributions. True signal (pK^- decays only) (black), extracted signal (blue), and true background (all other decays) (red). All histograms are normalized to have the same integral.

6.4.2 Stage 2

After Stage 1, we then cut on $MM(p)$ to remove the ϕ , and cut out events with $CL < 0.1$, which we could not remove before. At this stage, we assume that we have selected $pK^+(K^-)$ events so we can use the corrected momenta from the kinematic fit without introducing a bias into our kinematics.

Stage 2 of our background subtraction consists of using the results of the Stage 1 fit to do another Q-value fit to identify true $K^+\Lambda(1520)$ events (as opposed to non-resonant pK^+K^- events), using a fit similar to the ones used in Sections 6.2 and 6.3. The Stage 2 fit uses the same parameters as these earlier fits (Table 6.1), but differs from them in one important way: as before, we consider the N nearest neighbor events, regardless of Q_1 , but when forming the measured distribution (which is to be fit to), the neighboring events are weighted by Q_1 (in the context of maximum likelihood fitting, this weighting is implemented using Equation (A.12)). The probabilities output from this fit are called Q_2 . The overall Q-value for the event is given by $Q_t = Q_1Q_2$, which reflects the probability that an event is both from a $pK^+(K^-)$ event and that the pK^- come from a $\Lambda(1520)$ decay, since Q_1 is the probability that an event has a missing K^- and Q_2 is the probability of $\Lambda(1520)$ assuming that the event has a missing K^- (since the Stage 2 fit uses distributions weighted by Q_1). (Q_1 is not double-counted when calculating Q_t . Although the values of Q_1 are used as weights when calculating Q_2 , the value of the calculated Q-value depends only the shape of the fitted distribution, not the scale. Thus the weights Q_1 do not directly scale the magnitude of Q_2 . Therefore the final signal probability must be $Q_t = Q_1Q_2$.) The plots in Figures 6.15 and 6.16 show the results of the fit with the signal (black) curves show events weighted by Q_t and the background (red) curves weighted by $Q_1 - Q_t$, reflecting the distribution of true $pK^+(K^-)$ events that are not from $\Lambda(1520)$ decays. They are plotted this way to be directly comparable to the background fit results from the other two topologies (Figures 6.3 and 6.6).

For further analysis, we only consider events in the region 1500–1540 MeV.

6.5 Differential cross sections

While not the main focus of this work, calculating differential cross sections is a useful check of our background subtraction method. We compute differential cross sections using the method described in Section C.13. After doing so, we can test the internal consistency of our three topologies as well as comparing with two other measurements of $\Lambda(1520)$ cross sections from the same g11a dataset. Moriya et al. measured the $\Lambda(1520)$ cross section using the $\Sigma\pi$ decay mode (all three isospin combinations) [24], and De Vita et al. measured the cross section using the same three topologies as this work: pK^+K^- , $p(K^+)K^-$, and $pK^+(K^-)$, however, using different methods for background subtraction and acceptance correction [62]. The largest source of systematic error in these cross section measurements is the photon normalization, which has an estimated uncertainty about 8%, but since all these measurements are from the same dataset, this error will not appear in comparisons between them and we should expect good agreement between them. Comparisons are shown in Figure 6.17. Agreement is good in most kinematic regions; however, we note a few discrepancies: the $pK^+(K^-)$ topology at lower energies and backwards angles seems to overestimate the cross section, and Moriya’s results in the lowest energy bin seem to underestimate it, although this may be because these results are from a bin with a slightly lower average value of \sqrt{s} .

6.6 Summary

In this chapter, we attempted to separate signal from background by assigning a Q-value to each event. When weighting each event by its Q-value, we recover an approximation of the signal distribution. It is apparent from unwanted dips and bumps in the extracted background distribution, and from discrepancies in the differential cross sections in certain kinematic regions, that the background

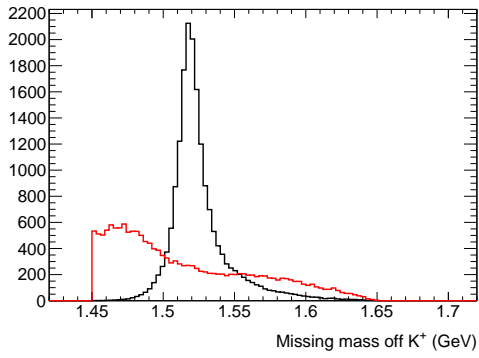
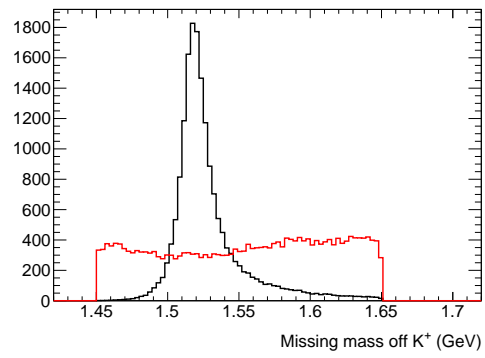
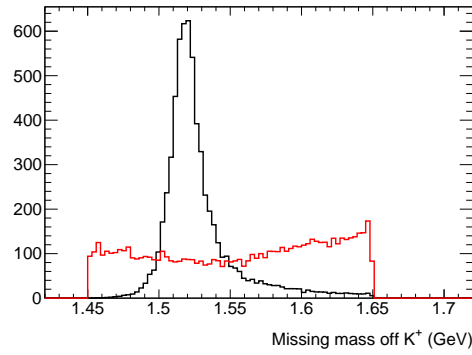
(a) $\sqrt{s} = 2130\text{--}2160$ MeV(b) $\sqrt{s} = 2430\text{--}2460$ MeV(c) $\sqrt{s} = 2730\text{--}2760$ MeV

Figure 6.15: Missing mass off K^+ distribution, missing K^- topology, in three different \sqrt{s} bins. In black, events weighted by signal probability Q_t . In red, events weighted by $Q_1 - Q_t$. Q_1 and Q_t calculated using the baseline fit parameters in Tables 6.1 and 6.3.

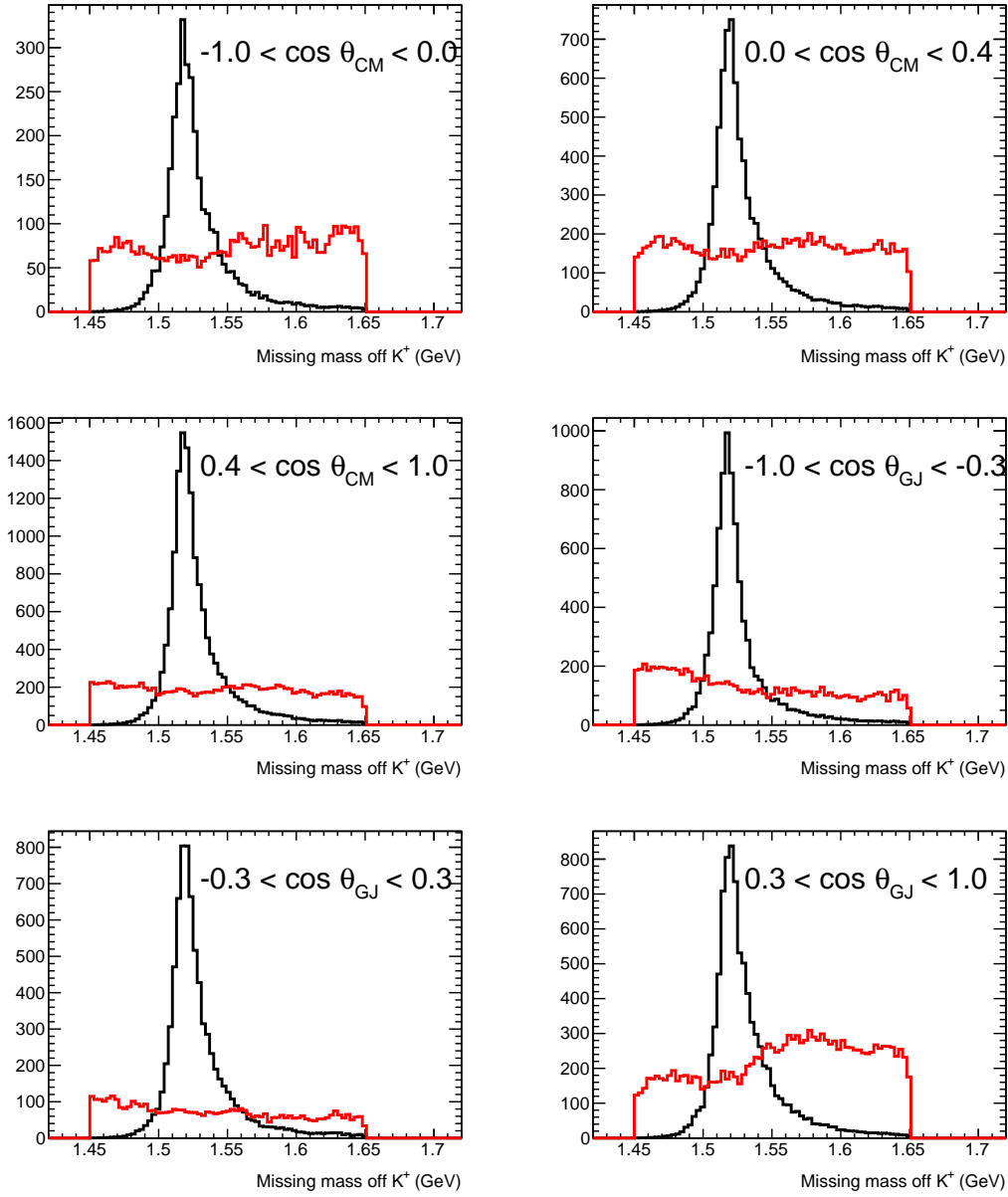


Figure 6.16: Missing mass off K^+ distribution for various angular slices (in $\cos\theta_{K^+,CM}$ and $\cos\theta_{K^-,GJ}$) in $\sqrt{s} = 2280 - 2310$ MeV bin. Missing K^- topology. Signal (black) and background (red)

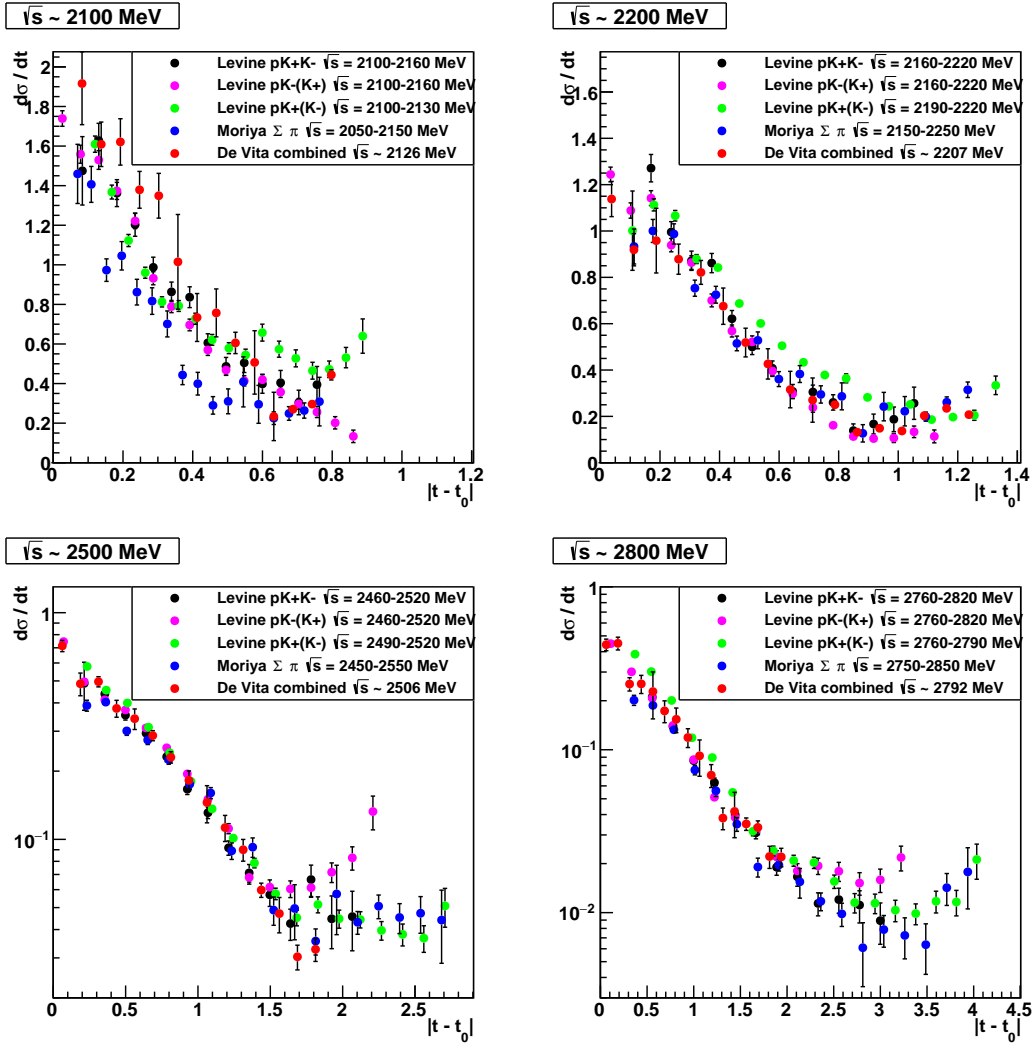


Figure 6.17: Differential cross section vs. t for the current analysis as well as two previous analyses. De Vita data includes all three topologies: pK^+K^- , $p(K^+)K^-$, and $pK^+(K^-)$ [62]. Moriya data uses $\Sigma\pi$ decay modes [24].

subtraction method is not perfect. However, in the next chapter, we will estimate the uncertainty introduced by this imperfect signal-background separation and find that the error introduced is tolerable.

Chapter 7

Results and discussion

7.1 SDME extraction

Before extracting the spin density matrix elements, we bin the data and Monte Carlo in the production angle $\cos\theta_{K^+,CM}$. We use bins of width 0.2 for $-1.0 < \cos\theta < 0.8$, but the forward-most region is divided into two bins from $\cos\theta = 0.8-0.9$ and $\cos\theta = 0.9-1.0$. This is because the pK^+K^- and $pK^+(K^-)$ topologies have no acceptance in the $\cos\theta = 0.9-1.0$ region, so it doesn't make sense to average them with the $p(K^+)K^-$ topology, which does have acceptance there. Also, since the t -channel contributions increase rapidly as $\cos\theta$ increases in this region, it would be interesting to see if there is any change in the SDMEs at these angles.

We now have all the ingredients to extract the SDMEs. We fit the decay angular distribution $(\cos\theta_{GJ}, \phi_{GJ})$ in each $(\sqrt{s}, \cos\theta_{K^+,CM})$ bin to Equation (2.47a) using the maximum-likelihood method, and the fit returns values for the three matrix elements. Events are weighted by the Q -values computed in Chapter 6 (using Q_1Q_2 as the weight for the missing K^- topology). Specifically, we use Equation (A.12), which is the form of the likelihood which both includes weighting of data events and accounts for acceptance using Monte Carlo events. The results of these fits, for all three topologies, are shown in Figures 7.1 (ρ_{11}), 7.2 ($\text{Re}\rho_{31}$), and 7.3 ($\text{Re}\rho_{3-1}$). Empty bins and points with errors greater than 0.15 are removed. The error bars shown in these plots are statistical errors only; the determination of these errors is described in the next section. The agreement between the three topologies is decent, but it is clear that the statistical errors do not explain all discrepancies between them (remember that the three topologies contain no common events). This discrepancy between topologies will be discussed further in Section 7.2.

7.1.1 Statistical errors and the bootstrap method

To calculate the statistical errors for our spin density matrix elements, we use the bootstrap method. We define N as the number of events in a given $(\cos\theta, \sqrt{s})$ bin; thus N is the number of events used to calculate a given SDME value. We then create N_{boot} bootstrap samples, where each bootstrap sample has N events. Each bootstrap sample is created by sampling from the original N events “with replacement”. This means that we pick N events, where for each pick, all N of the original events have a $1/N$ probability of being picked, even events that have been picked before. Thus, each event may appear in a given bootstrap sample zero, one, or more than one times. We can then extract the SDMEs for each of the bootstrap samples. If we denote the SDME extracted from the i th bootstrap sample as ρ_i^B , we can define bootstrap variance

$$\sigma_{\rho^B}^2 = \frac{1}{N_{\text{boot}}} \sum_i^{N_{\text{boot}}} (\rho_i^B)^2 - \left[\frac{1}{N_{\text{boot}}} \sum_i^{N_{\text{boot}}} \rho_i^B \right]^2. \quad (7.1)$$

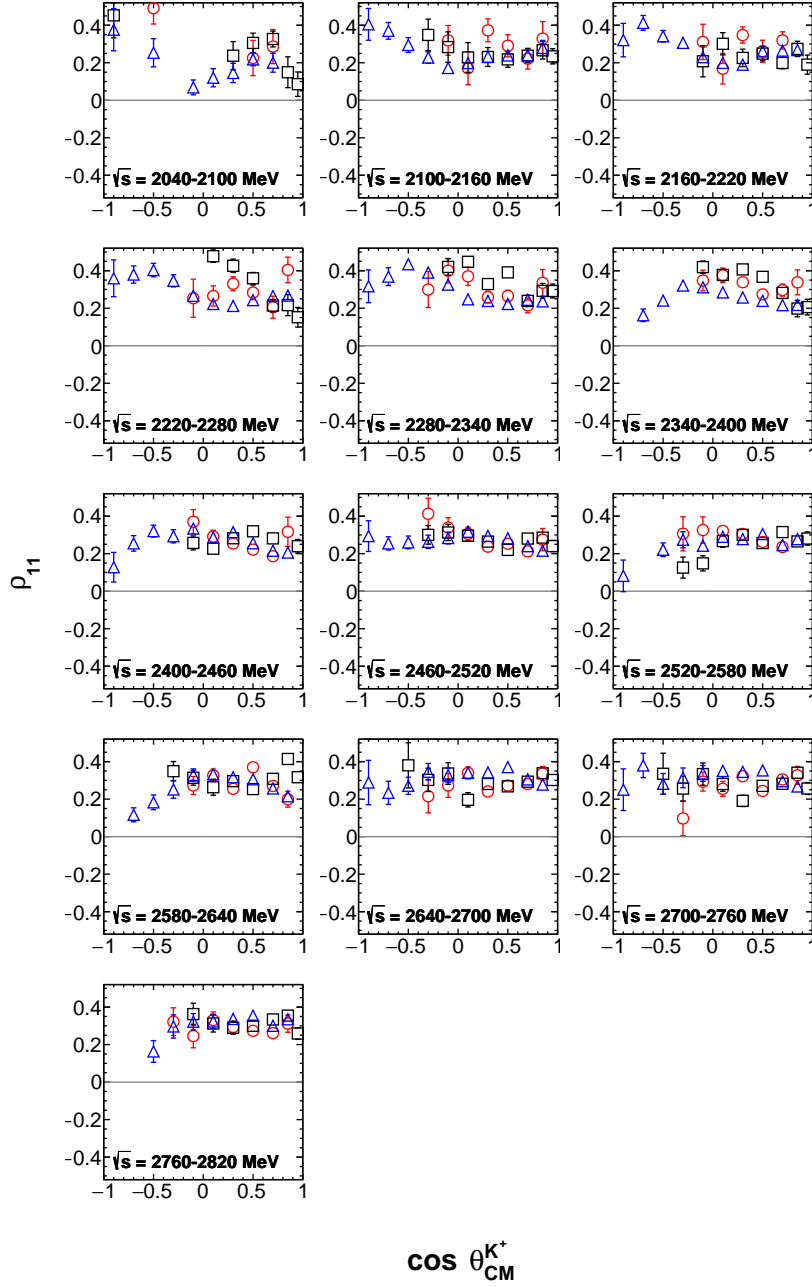


Figure 7.1: ρ_{11} . Comparison of three topologies: 3-track (red circles), missing K^- (blue triangles), and missing K^+ (black squares). Statistical errors only. For the missing K^- topology, only the lower half of the stated energy range is included.

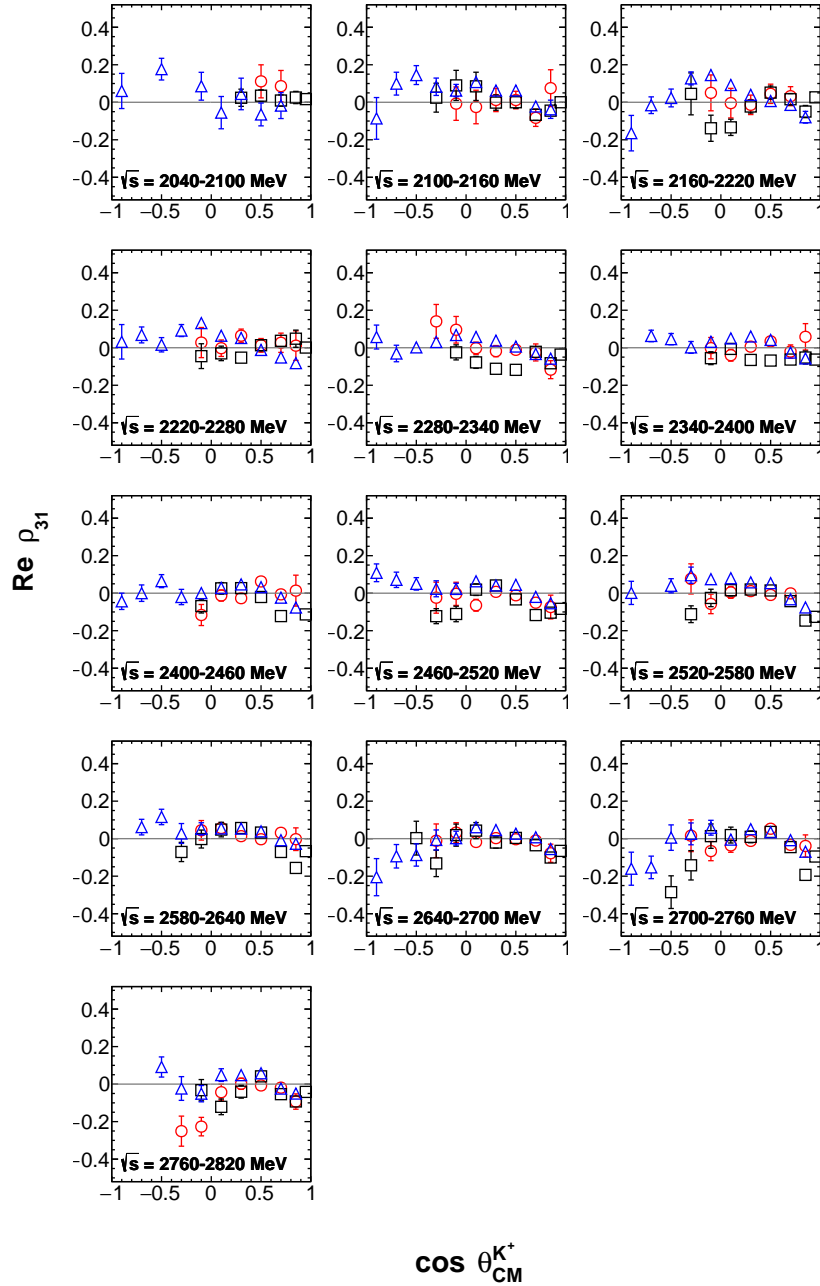


Figure 7.2: $\text{Re } \rho_{31}$. Comparison of three topologies: 3-track (red circles), missing K^- (blue triangles), and missing K^+ (black squares). Statistical errors only. For the missing K^- topology, only the lower half of the stated energy range is included.

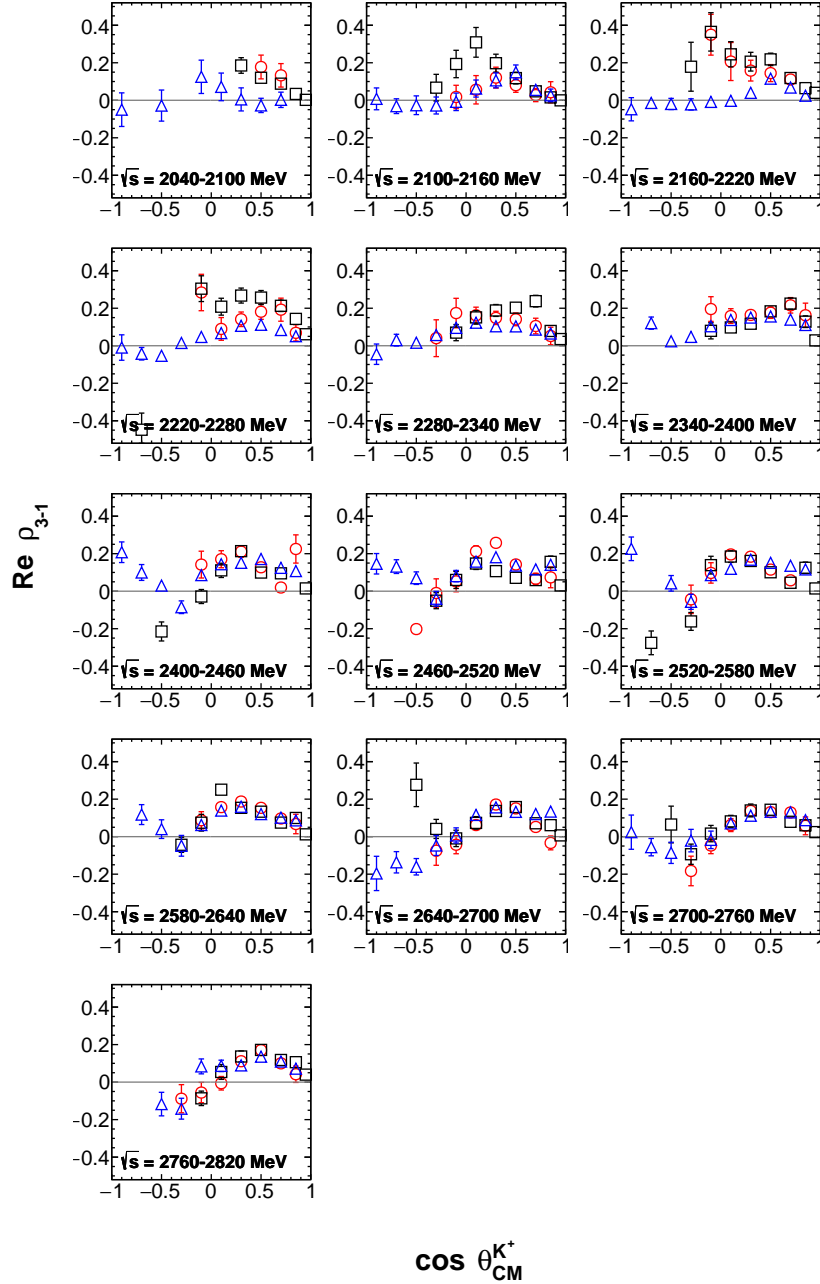


Figure 7.3: $\text{Re } \rho_{3-1}$. Comparison of three topologies: 3-track (red circles), missing K^- (blue triangles), and missing K^+ (black squares). Statistical errors only. For the missing K^- topology, only the lower half of the stated energy range is included.

It can be shown that the statistical uncertainty in the original measurement of ρ is

$$\delta\rho = \sqrt{\frac{N}{N-1}}\sigma_{\rho^B}. \quad (7.2)$$

A good overview of the bootstrap method which includes a justification of this result is given by Young [63]. There is no agreement on what is a sufficiently large value of N_{boot} . For this analysis we use $N_{\text{boot}} = 100$.

For a simple fit, errors on parameter values can be obtained directly from the fit, by calculating how the likelihood (or chi-squared) varies while varying the parameter away from the best-fit value. So the bootstrap method might seem excessive. However, in our case, this simple method will neglect a significant source of statistical error, which comes from the background estimation. Each Q-value will have a statistical error associated with it, which we need to propagate forward to the errors in the SDMEs. This can be done easily with the bootstrap method: do the entire analysis, starting with the Q-value determination, on each of our bootstrap samples. However, this has the downside that the Q-value fits are computationally expensive and it is not really feasible to run them 100 times for every event in every topology. To get around this, we perform an abbreviated bootstrap, in which only the SDME fit (not the background fit) is run on each of 100 bootstrap samples, and extract an “abbreviated” bootstrap error from this. For a smaller number of bins, we perform a full bootstrap, where a Q-value fit is performed for each of the 100 bootstrap samples in the bin. (We choose to do the full bootstrap on the highest-energy bin as well as a low-energy bin, so we can see how the errors vary with energy.) By comparing the full bootstrap error with the abbreviated bootstrap error in corresponding bins, we can estimate how much uncertainty the Q-value fit adds. The comparison between full and abbreviated bootstrap errors is shown in Figure 7.4. We assume that the relationship between the abbreviated bootstrap error and the full bootstrap error is a simple scale factor. Figure 7.4 shows that the scale factor does not depend strongly on the energy bin or the particular matrix element, but it does depend on the topology. It is greatest for the missing K^- topology, where we have two stages of background subtraction, each introducing its own uncertainty. We estimate the scale factors by fitting the graphs shown. The scale factors $\sigma_{\text{full}}/\sigma_{\text{abbrev}}$ are estimated to be 1.025, 1.14, and 1.49 for the three-track, missing K^+ , and missing K^- topologies respectively. To calculate the statistical errors shown in Figures 7.1, 7.2, and 7.3, we calculate the abbreviated bootstrap error for each point and then scale it with the appropriate scale factor.

7.1.2 Fit quality

For maximum-likelihood fits, there is no standard method for determining the goodness of fit. However, we can evaluate the goodness of fit qualitatively, by comparing our angular distributions from the data with angular distributions from the accepted Monte Carlo weighted by the best-fit distribution (i.e. the weight for each Monte Carlo event is given by Equation (2.47a) using the kinematics of that event and the extracted values of ρ in the appropriate $(\sqrt{s}, \cos\theta_{K^+,CM})$ bin). We first look at the $\cos\theta_{GJ}$ distributions. For the 3-track (Figure 7.5) and missing K^+ (Figure 7.6) topologies, the agreement between the fit and data is fair. For the missing K^- topology (Figure 7.7), the agreement looks worse. However, we note that in many of these plots (in particular, all three plots with $\cos\theta_{K^+} = 0.4-0.6$), the fit overestimates the data near $\cos\theta_{GJ} = 1$ and underestimates it near $\cos\theta_{GJ} = -1$. This is evidence of a background or interference term with an odd power of $\cos\theta$. We discuss the effects of such a term in Section 7.3.1.

We can also look at the ϕ_{GJ} distributions, shown in Figure 7.8. In this figure, in addition to the data and the weighted Monte Carlo, we also show the unweighted (phase space) accepted Monte Carlo. We can see that the data (shown in black) differs significantly from the phase-space Monte Carlo (blue), which demonstrates that the underlying physics distribution is not flat in ϕ_{GJ} . Although the fit quality does not look great, we can see that the fit distribution (weighted Monte

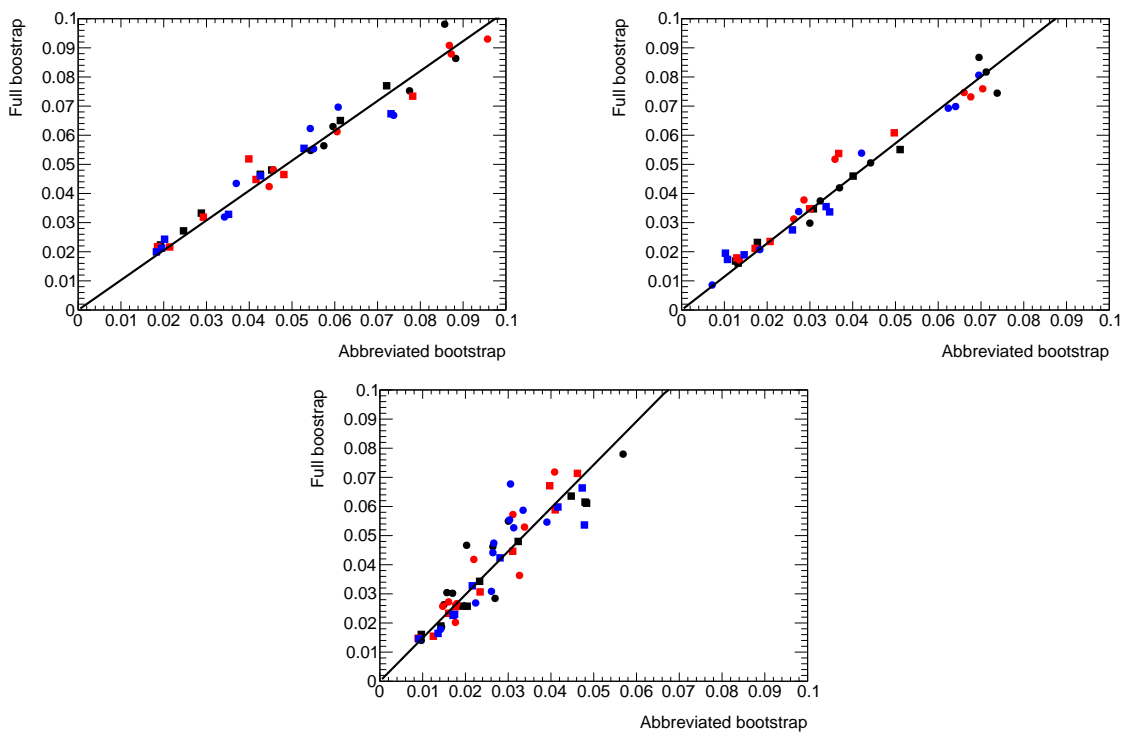


Figure 7.4: Shows full bootstrap errors vs. abbreviated bootstrap errors. All three SDMEs are shown: ρ_{11} (black), $\text{Re } \rho_{31}$ (red), and $\text{Re } \rho_{3-1}$ (blue). Circles are points from the lower energy bin $\sqrt{s} = 2100 - 2160$ ($\sqrt{s} = 2100 - 2130$ for the missing K^- topology) and squares from the higher energy bin $\sqrt{s} = 2760 - 2820$ ($\sqrt{s} = 2790 - 2820$ for missing K^-). The black line shows the best-fit scale factor. The scale factor does not appear to vary based on the energy or the variety of SDME.

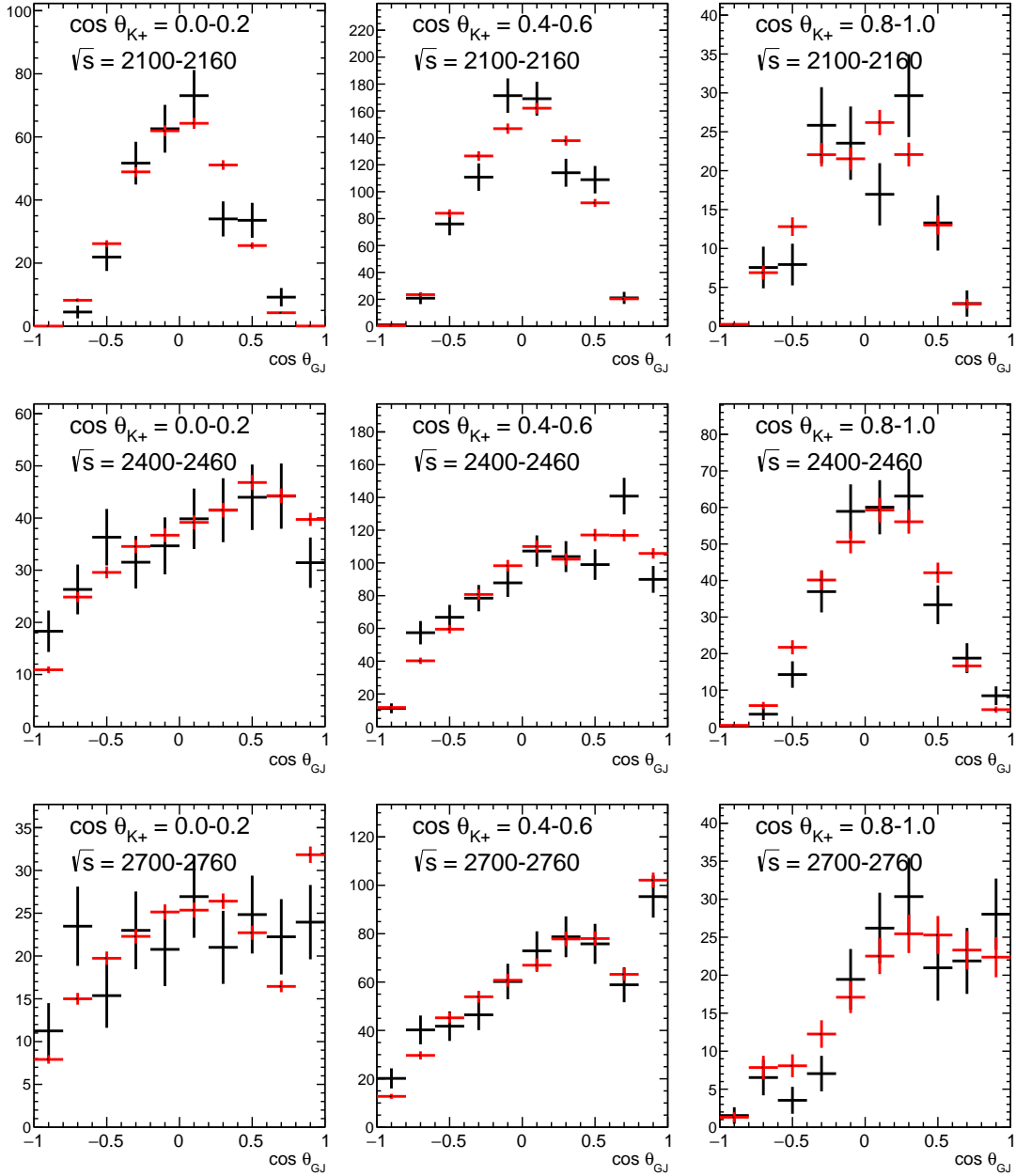


Figure 7.5: $\cos \theta_{GJ}$ distributions. Comparison of data (black) and accepted Monte Carlo weighted by our best-fit distribution (red). 3-track topology. The accepted Monte Carlo distribution is scaled so that it has the same integral as the data distribution.

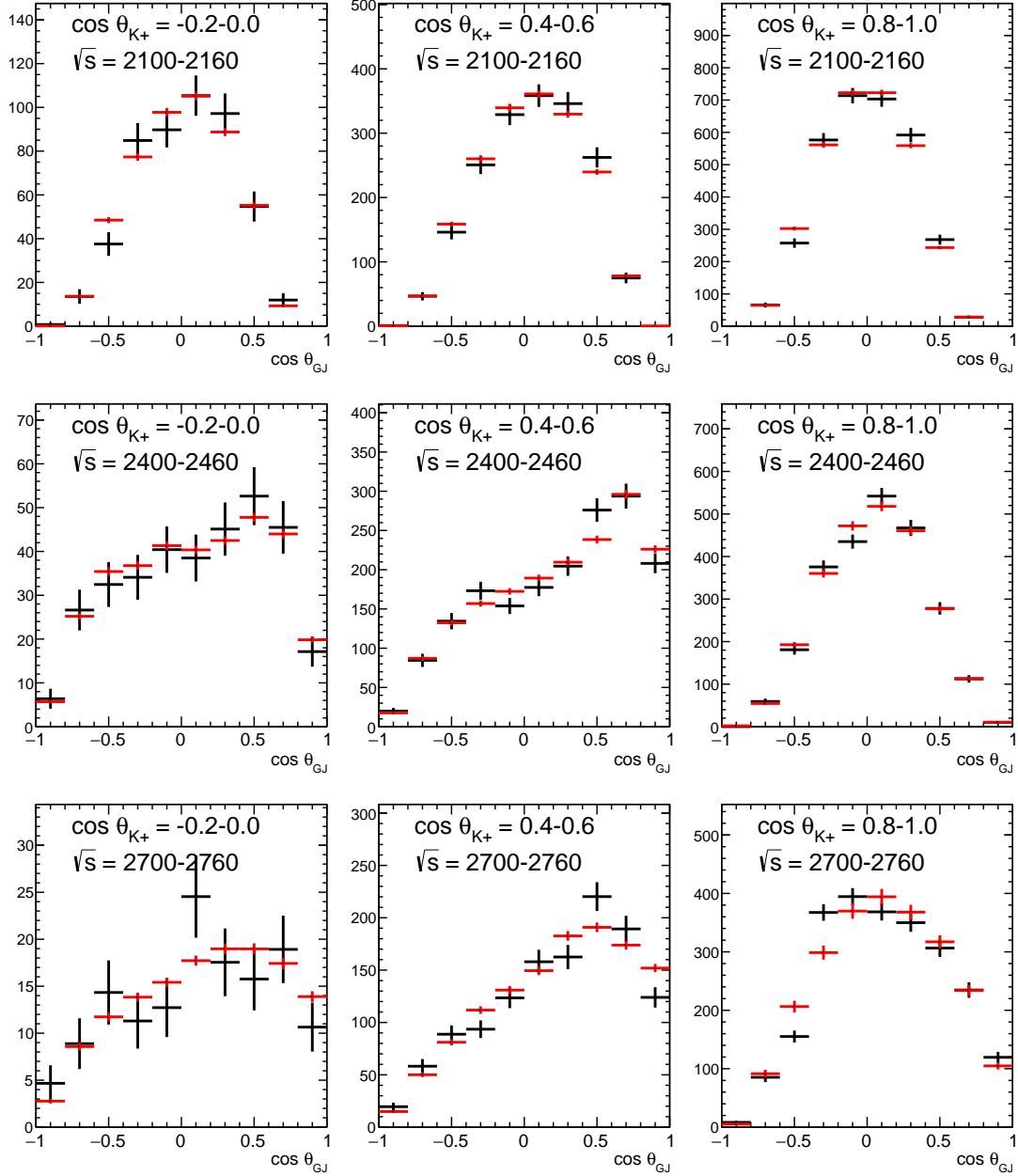


Figure 7.6: $\cos \theta_{GJ}$ distributions. Comparison of data (black) and accepted Monte Carlo weighted by our best-fit distribution (red). Missing K^+ topology. The accepted Monte Carlo distribution is scaled so that it has the same integral as the data distribution.

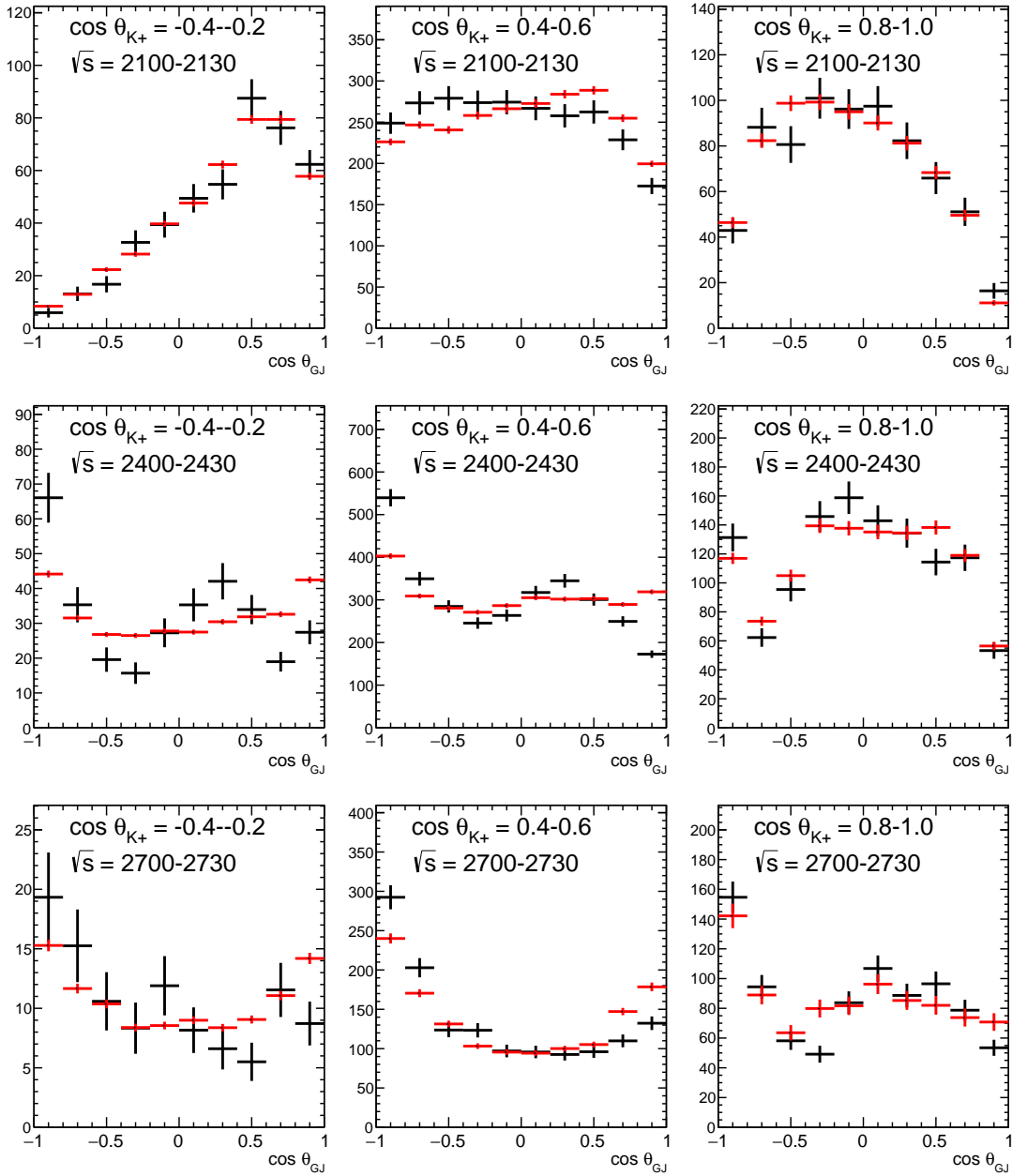


Figure 7.7: $\cos \theta_{GJ}$ distributions. Comparison of data (black) and accepted Monte Carlo weighted by our best-fit distribution (red). Missing K^- topology. The accepted Monte Carlo distribution is scaled so that it has the same integral as the data distribution.

Carlo, shown in red) matches the data where it deviates from the phase-space distribution, showing that our fit is sensitive to this non-flat ϕ_{GJ} distribution.

7.1.3 Acceptance-corrected angular distributions

In the previous section, we plotted measured angular distributions to help evaluate the fit quality. However, these distributions do not directly show the underlying physics distribution, since they are distorted by non-uniform detector acceptance. Our fit does correct for acceptance effects, but this is not shown in the plots in the previous section. In this section, we plot acceptance-corrected angular distributions (although these are not what we directly fit to), since these better reflect the underlying physics process. We show only results from the missing K^- topology, since this is where the acceptance is most uniform over $\cos\theta_{GJ}$ (the other two topologies tend to have very large errors in certain bins). In Figure 7.9, we show $\cos\theta_{GJ}$ distributions in various energy bins, but only events with production angle $0.6 < \cos\theta_{K^+,CM} < 0.8$ (in this topology, this is the production angle bin with the highest statistics). In Figure 7.10, we show distributions from the $\sqrt{s} = 2400\text{--}2430$ MeV bin, in varying bins of production angle.

To do the acceptance correction, we calculate an acceptance in each $(\sqrt{s}, \cos\theta_{K^+,CM}, \cos\theta_{GJ})$ bin. We collect all Monte Carlo events in this bin and weight each event; the weight for event i is given by Equation (2.47a) evaluated using the kinematics of the event (the Gottfried-Jackson angles $\cos\theta_i^{GJ}$ and ϕ_i^{GJ}) and $\hat{\rho}$, the best-fit values of ρ from the fit in the corresponding $(\sqrt{s}, \cos\theta_{K^+,CM})$ bin. We then calculate the acceptance in a given $(\sqrt{s}, \cos\theta_{K^+,CM}, \cos\theta_{GJ})$ bin:

$$\eta = \frac{\sum_{i \in \text{acc}} W^0(\cos\theta_i^{GJ}, \phi_i^{GJ}; \hat{\rho})}{\sum_{i \in \text{raw}} W^0(\cos\theta_i^{GJ}, \phi_i^{GJ}; \hat{\rho})}, \quad (7.3)$$

where the sums include only events in that bin. The reason we must do this weighting is because both the acceptance and the underlying physics distributions are non-uniform in ϕ_{GJ} , which we have not binned the data in. Thus we must use the weights to take into account this ϕ_{GJ} distribution, rather than just dividing the number of accepted MC events by the number of raw MC events. To get the acceptance-corrected yield, we take the extracted yield (the sum of all the Q-values in a $(\sqrt{s}, \cos\theta_{K^+,CM}, \cos\theta_{GJ})$ bin), and divide by the acceptance in the corresponding bin. These acceptance-corrected yields are what is plotted in Figures 7.9 and 7.10.

7.2 Combining topologies

We now would like to average together points from the three topologies, so that we will have a single measurement of each SDME at each kinematic point $(\sqrt{s}, \cos\theta_{K^+,CM})$. We must be careful doing this, because the errors considered so far have only been statistical errors and are an underestimate of the true uncertainty. The standard procedure for averaging together n independent data points ρ_i , which are measurements of the same quantity, is to take the weighted mean

$$\bar{\rho} = \frac{1}{\sum_i^n \sigma_i^{-2}} \sum_i^n \frac{1}{\sigma_i^2} \rho_i, \quad (7.4)$$

where σ_i is the uncertainty on the corresponding data point. The error on the mean is then given by:

$$\sigma_{\bar{\rho}, \text{ideal}}^2 = \frac{1}{\sum_i \sigma_i^{-2}}. \quad (7.5)$$

In our case, this would underestimate the error on the mean.

Before we average together the three topologies, we begin by averaging together pairs of points in adjacent energy bins in the missing K^- topology (which is binned in 30 MeV bins), so that these

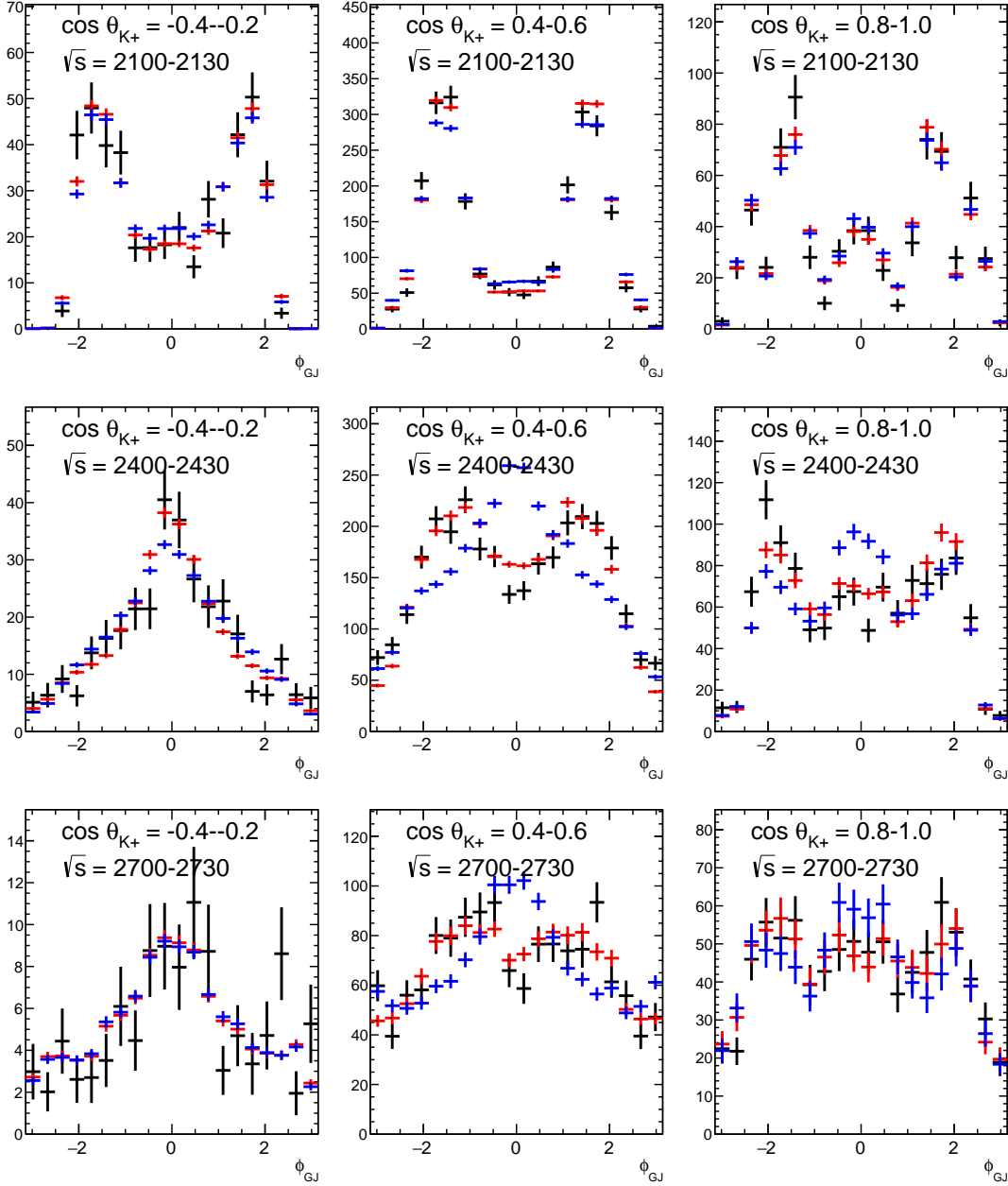
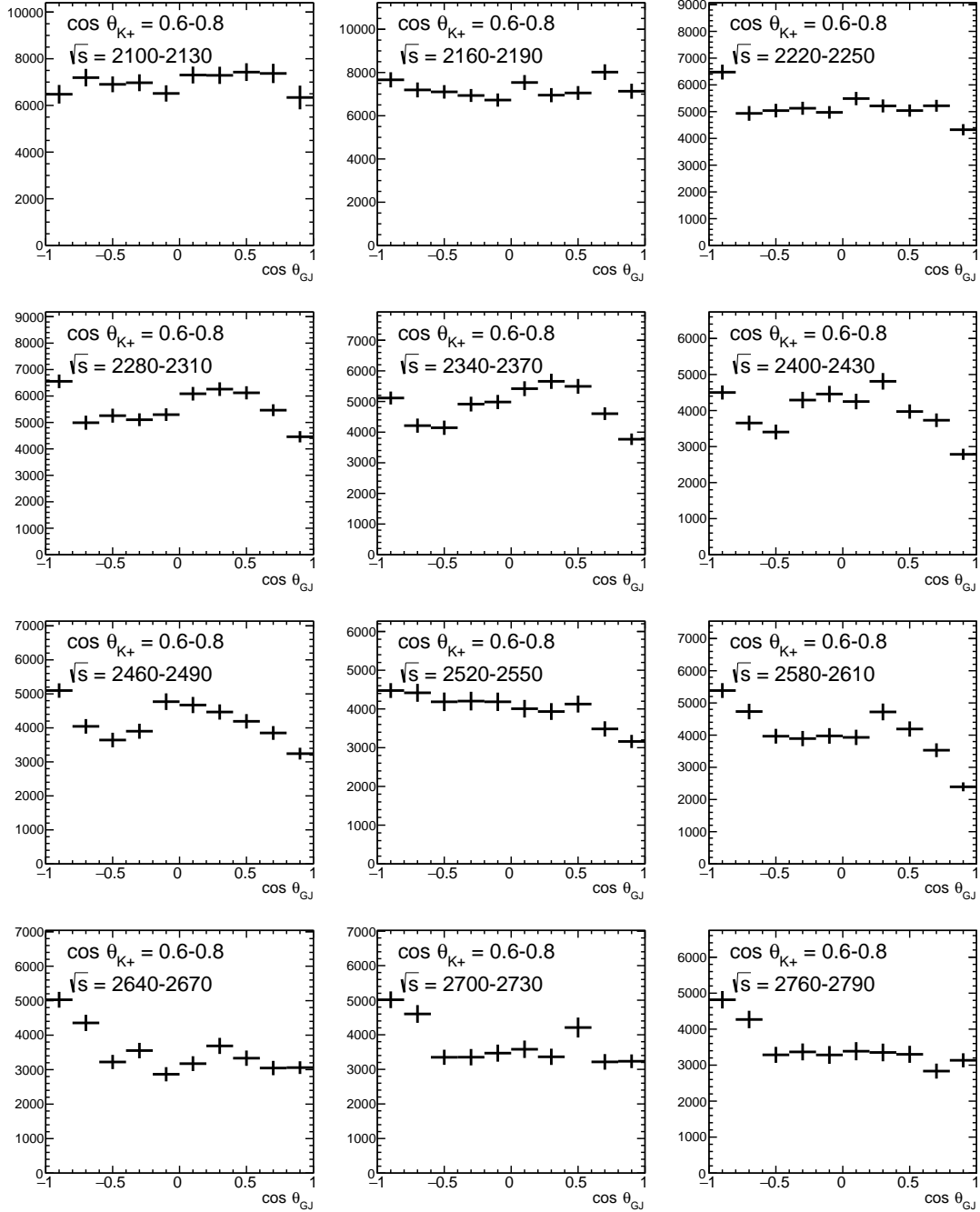


Figure 7.8: ϕ_{GJ} distributions. Comparison of data (black), accepted Monte Carlo weighted by our best-fit distribution (red), and accepted phase-space Monte Carlo (blue). Missing K^- topology. The accepted Monte Carlo distributions are scaled so that they have the same integrals as the data distribution.

Figure 7.9: Acceptance-corrected $\cos \theta_{GJ}$ distributions. Missing K^- topology.

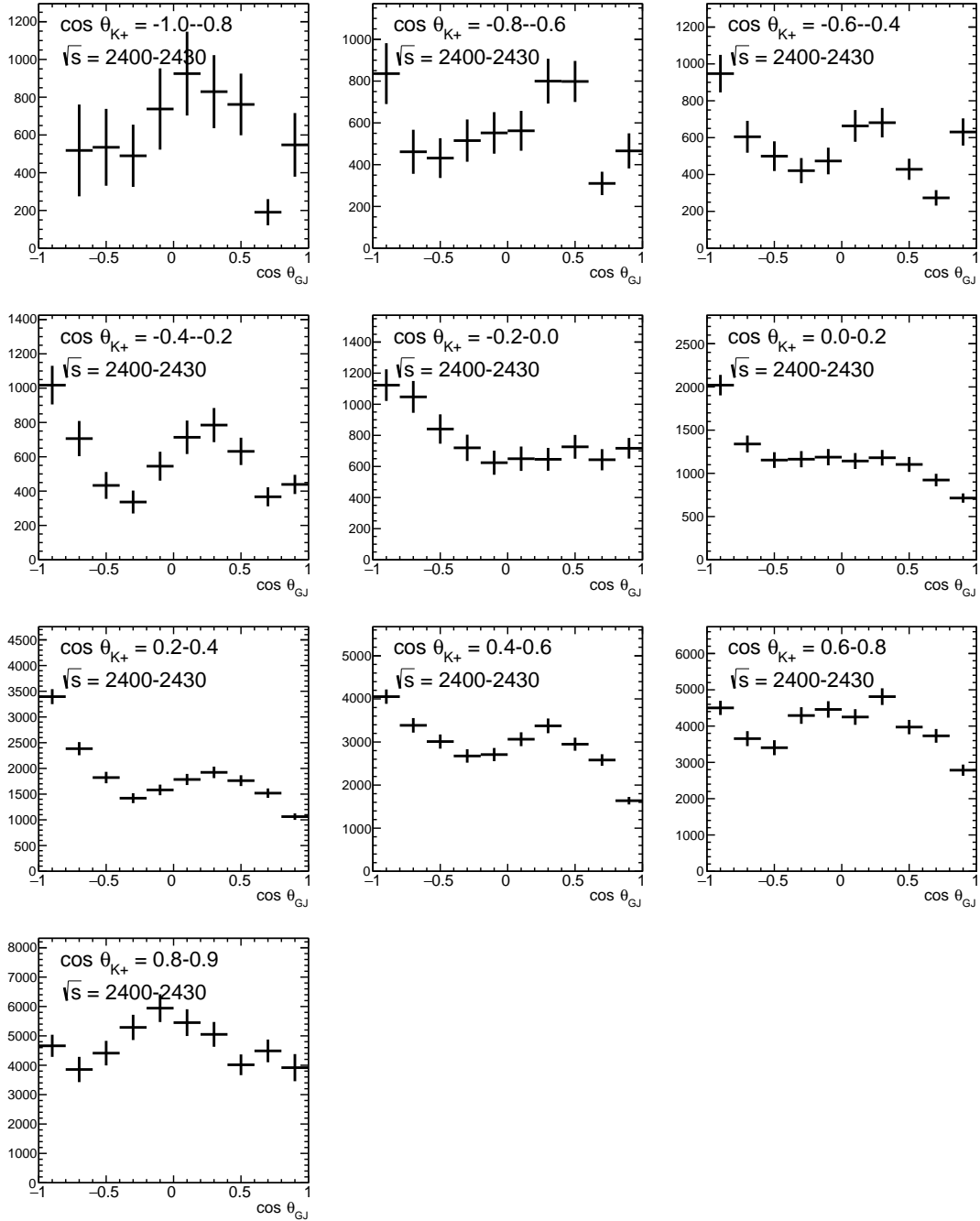


Figure 7.10: Acceptance-corrected $\cos \theta_{GJ}$ distributions. All results from $\sqrt{s} = 2400 - 2430$ MeV bin, with all bins in production angle shown. Missing K^- topology.

points correspond with the other two topologies (which have 60 MeV bins). To average together these two points we just use the standard weighted mean (7.4) and compute the error on the mean using Equation (7.5). This is our new missing K^- point which can now be averaged on an equal basis with points from the other two topologies.

We would like to use the discrepancy between topologies to estimate the systematic error, or more precisely the size of all systematic errors that are not shared between the three topologies. This includes systematic errors due to event selection, some of the error due to backgrounds, and some of the error due to acceptance. To average together the three topologies, we use the standard weighted mean (7.4), and compute a statistical error using Equation (7.5). To estimate the systematic error from non-shared systematics, we begin by calculating the standard deviation for every SDME point for which we have data from all three topologies:

$$\sigma_t = \left[\frac{1}{3} \sum_{i=1}^3 (\rho_i - \bar{\rho})^2 \right]^{\frac{1}{2}}, \quad (7.6)$$

where i labels the three topologies. We ignore points for which we have results from only one or two topologies. For some points, σ_t will be an overestimate or underestimate of the systematic error, so we collect all the σ_t 's (for a particular SDME) in the same \sqrt{s} bin and take the median. We use this as the systematic error for all points in that bin. This allows us to assign a systematic error to points where we only have results from a single topology. The results of this averaging are shown in Figure 7.11. The error bars show the statistical error and the non-shared systematic error added in quadrature.

7.3 Other systematics

Other sources of systematic error may be shared between all three topologies, so not apparent in the spread of values from the three topologies.

7.3.1 Background

It is possible that some non- $K^+\Lambda(1520)$ processes are still present in our sample after background subtraction. Since each topology has different backgrounds, much of the error introduced due to an imperfect background subtraction would already be accounted for in our non-shared systematic error estimate. However, if there were an interfering process, it would not be possible to remove entirely and it would show up across all three topologies.

We consider two types of background. The first is a flat background which could come from non-resonant processes or an S-wave decay of another hyperon. This flat distribution is the same distribution as $\Lambda(1520)$ decay with $\rho_{11} = 0.25$, $\text{Re}(\rho_{31}) = 0$, and $\text{Re}(\rho_{3-1}) = 0$. Since the equation for the decay distribution is linear in the SDMEs, the effects of this background are easy to calculate, assuming that the amount of background present is known. For example, for a sample of events containing 20% background, the extracted matrix element will just be $\rho_{\text{extracted}} = 0.8\rho_{\text{signal}} + 0.2\rho_{\text{flat}}$.

Now we try to get a more realistic estimate for the systematic errors due to the background. We discussed in Chapter 6 that it is apparent that the background subtraction is not perfect because bumps and dips are seen in the background distribution in the vicinity of the signal peak, where the background should be smoothly varying. We would like to estimate the level of background contamination by the size of these features, but it is difficult to do so and furthermore it is not obvious how much of this background contamination is shared between the three topologies. However, from the size of these peaks and dips, it seems that the misidentified background (either signal events classified as background or vice versa) is at most 10%, and probably closer to 5%. We will assume 10% background for the purpose of estimating the systematic errors.

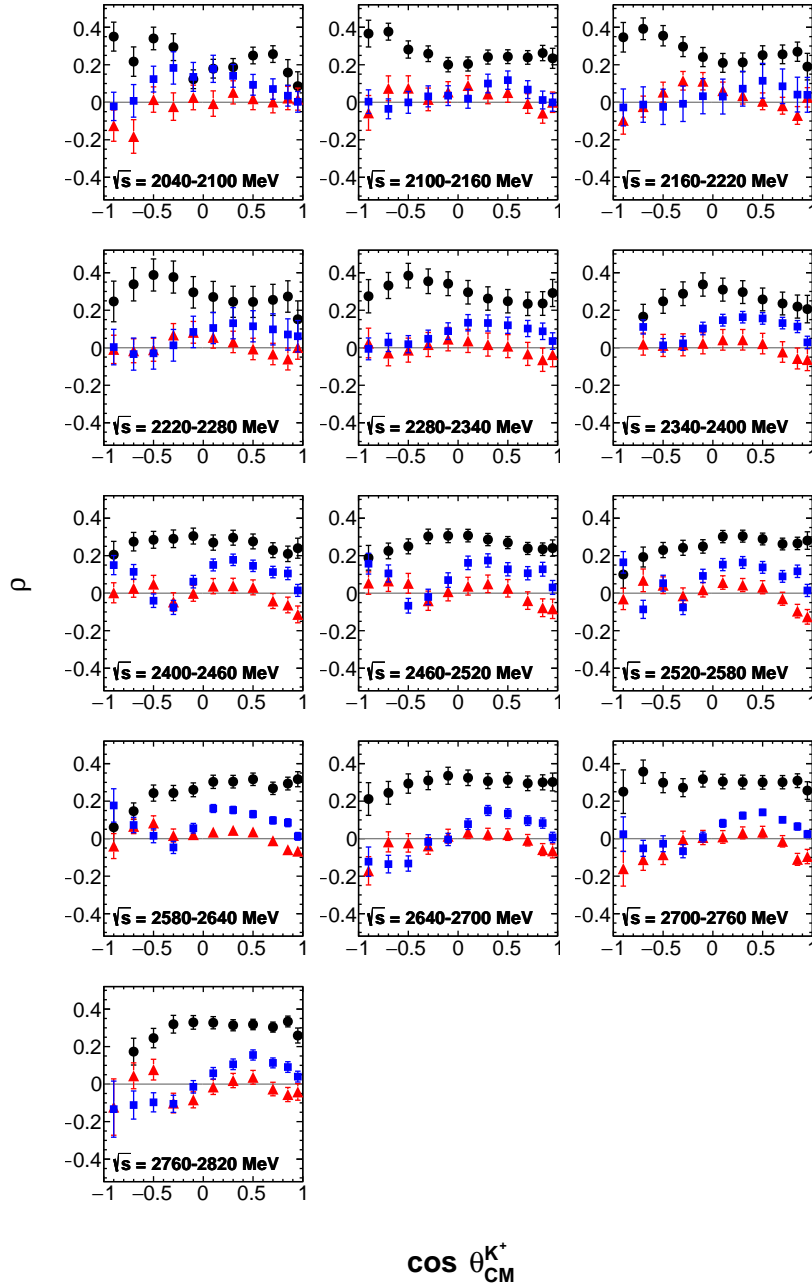


Figure 7.11: All spin density matrix elements: ρ_{11} (black circles), $\text{Re } \rho_{31}$ (red triangles), and $\text{Re } \rho_{3-1}$ (blue squares). All three topologies averaged. Error bars include statistical errors and non-shared systematic errors.

For a flat background, the effect of the background is greatest for the more extreme values of ρ , so we consider the case $\rho_{11} = 0.4$, $\text{Re}(\rho_{31}) = -0.1$, and $\text{Re}(\rho_{3-1}) = 0.2$ since these are roughly the most extreme values we measured. A 10% flat background will shift these values by 0.015, 0.01, and 0.02, respectively, which we take to be the estimate of the systematic errors due to a possible flat background.

The second type of background we consider is something with $\cos\theta$ shape. This might appear due to interference with a $\frac{1}{2}^-$ baryon (the baryon would decay in the S-wave, which would lead to a flat distribution, but interference could lead to a $\cos\theta$ term). Since this is odd in $\cos\theta$, to first order this should not shift the extracted values of ρ_{11} or ρ_{3-1} , which are coefficients of even functions. It could have a large effect on ρ_{31} , which is the coefficient on a term that is odd in $\cos\theta$.

We studied this using Monte Carlo data. We considered our “signal” to have $\rho_{11} = 0.30$, $\text{Re}(\rho_{31}) = 0.0$, $\text{Re}(\rho_{3-1}) = 0.15$, values which are typical for our data. For this case, it is not possible to say precisely that the background contributes at a 10% level. $\cos\theta$ is not a proper distribution (because it is negative for part of its domain), so we can’t simply combine the signal distribution with the background “distribution” at a 90:10 ratio. Instead, what we do is add a $\cos\theta$ term to the signal distribution, where the coefficient in front of the $\cos\theta$ is chosen such that it distorts the original distribution by 30% at the point of maximum deviation. This allows us to match some of the deviation between our data distribution and fitted distributions that we saw in Figure 7.7. We then extract the SDMEs from MC data weighted by this modified distribution. The difference between the extracted values and the signal values is shown in Figure 7.12. As expected, a large systematic shift can be seen for ρ_{31} , with smaller shifts for the other two elements. We estimate the systematic errors due to $\cos\theta$ -type background as 0.01 for ρ_{11} and ρ_{3-1} and 0.06 for ρ_{31} .

Background parametrization

For the baseline versions of all our Q-value fits, we used a linear function to model the background. In Section 6.2.2, we showed the results of a fit with a quadratic background. Here we try to understand if the choice of a different background function systematically shifts our extracted SDMEs. We re-run all our background fits using a quadratic background rather than linear and extract the SDMEs. For the missing K^- topology, we used a quadratic background for both stages of background fitting. The difference between the matrix elements ρ_{11} extracted using the two different background forms is shown in Figure 7.13 for both the missing K^+ and missing K^- topologies. While there does appear to be some systematic difference in the SDMEs between the two background fits, it is not shared between the two topologies, so we will not account for it separately. The same conclusion applies for the other two matrix elements, not shown here.

7.3.2 $\Lambda(1520)$ peak selection

Before fitting for the SDMEs, we always removed events outside the region $MM(K^+) = 1500 - 1540$ MeV. A narrower cut here would increase the signal-to-background ratio and also limit us to an area where we might better understand the $\Lambda(1520)$ peak shape. In this section, we extract the SDMEs using the tighter cut $MM(K^+) = 1510 - 1530$ MeV to see if this causes any systematic shift. About 30% of signal events are lost applying this additional cut. The difference between the matrix elements ρ_{11} extracted using the two different cuts is shown in Figure 7.14 for both the missing K^+ and missing K^- topologies. No shared systematic shift is apparent. We conclude that this is not a significant source of systematic error. The same conclusion applies for the other two matrix elements, not shown here.

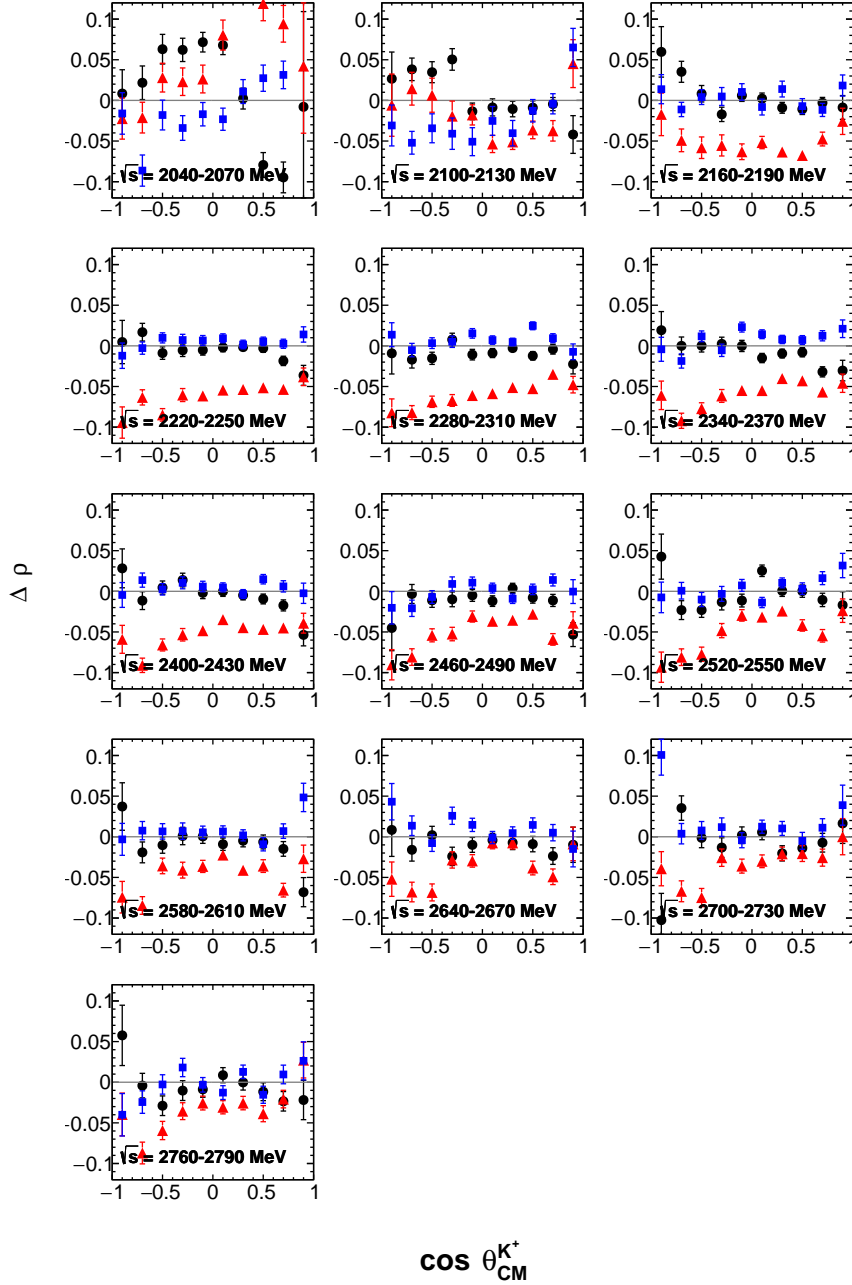


Figure 7.12: Extracted SDMEs from Monte Carlo simulation with signal ($\rho_{11} = 0.30$, $\text{Re}(\rho_{31}) = 0.0$, $\text{Re}(\rho_{3-1}) = 0.15$) combined with $\cos\theta$ background as described in the text. Shown is the difference $\Delta\rho = \rho_{\text{extracted}} - \rho_{\text{signal}}$. All three matrix elements are plotted: ρ_{11} (black circles), $\text{Re}\rho_{31}$ (red triangles), and $\text{Re}\rho_{3-1}$ (blue squares). Missing K^- topology only. Error bars are parameter errors reported by the fit.

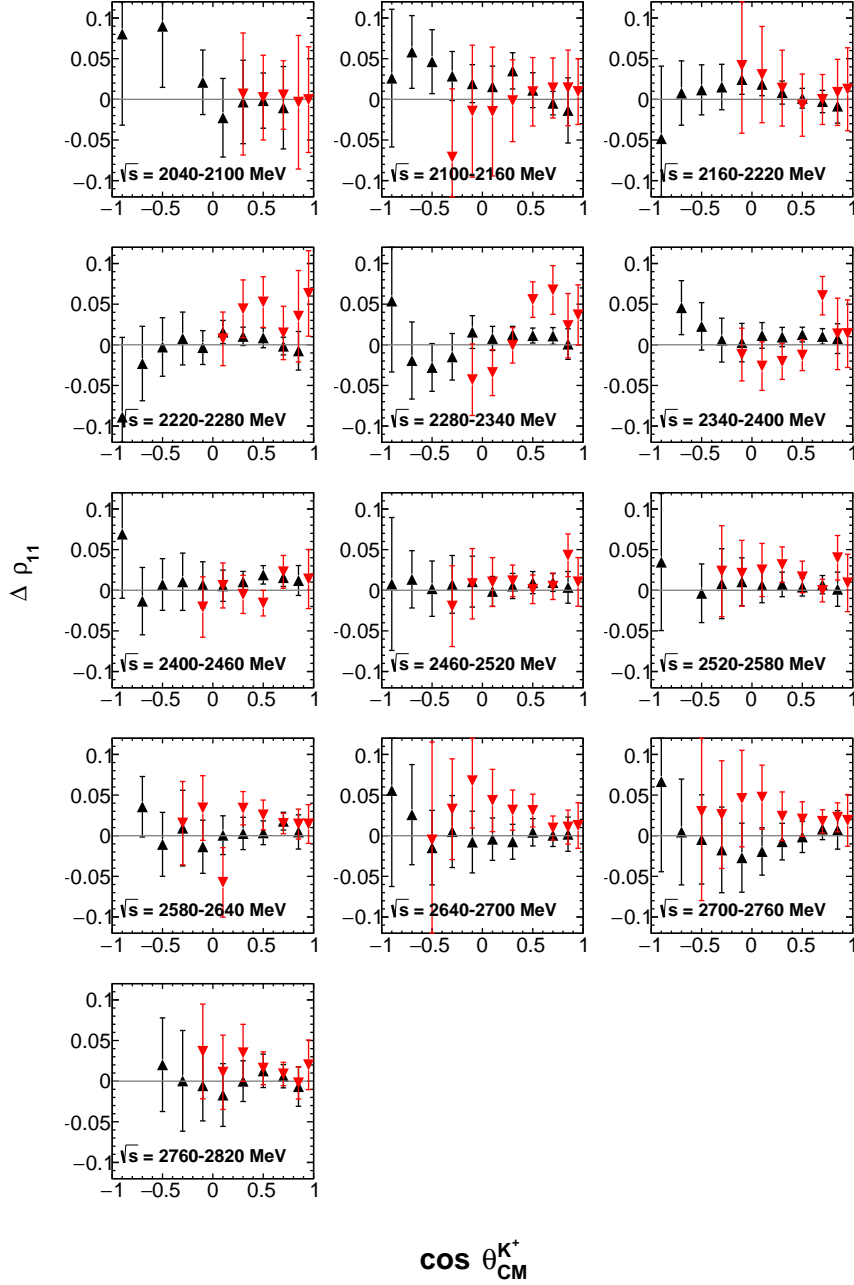


Figure 7.13: Difference $\Delta \rho_{11}$ between the matrix element as extracted using the baseline fit (linear background) and using a quadratic background in the Q-value fit. Two topologies were studied: missing K^+ (red) and missing K^- (black). Error bars shown are statistical errors from original fit. Only the lower half of the stated energy range is used for the missing K^+ topology.

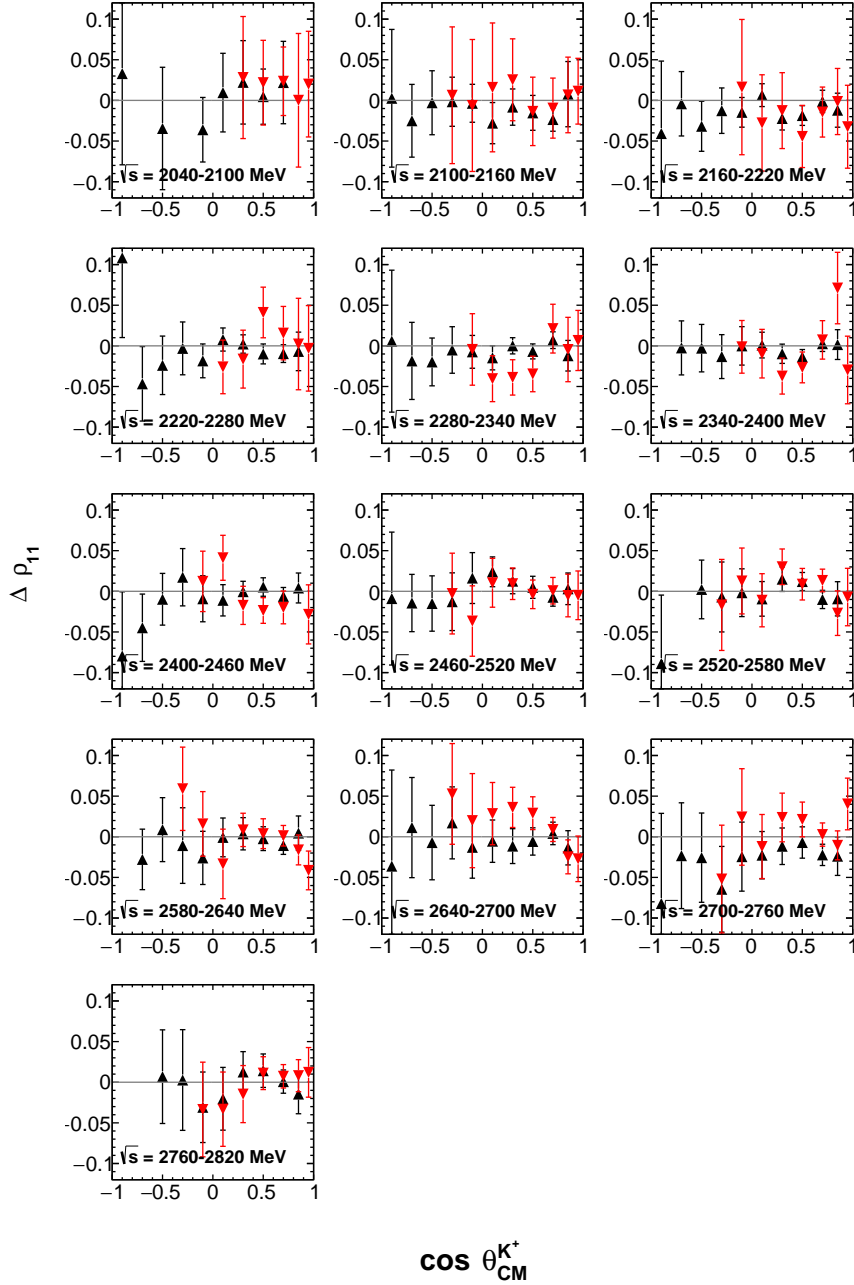


Figure 7.14: Difference $\Delta\rho_{11}$ between the matrix element as extracted using the baseline cut ($MM(K^+) = 1500 - 1540$ MeV) and using the more restrictive cut ($MM(K^+) = 1510 - 1530$ MeV). Two topologies were studied: missing K^+ (red) and missing K^- (black). Error bars shown are statistical errors from original fit. Only the lower half of the stated energy range is used for the missing K^+ topology.

	ρ_{11}	$\text{Re } \rho_{31}$	$\text{Re } \rho_{3-1}$
Non-shared (varies by bin & SDME type)	0.02-0.09		
Flat background	0.015	0.01	0.02
$\cos \theta$ background	0.01	0.06	0.01
ϕ cut (below 2400 MeV)	0.01	0.01	0.02
ϕ cut (above 2400 MeV)	0		

Table 7.1: Systematic errors

7.3.3 ϕ cut

Likewise, we can vary our default $MM(p)$ cut (used to eliminate ϕp events) to see if this causes any shift in the extracted SDMEs. Our baseline cut is to eliminate all events with $MM(p) < 1040$ MeV. We investigate changing this cut value to 1030 MeV and 1050 MeV. Results are shown in Figures 7.15 (ρ_{11}), 7.16 ($\text{Re } \rho_{31}$), and 7.17 ($\text{Re } \rho_{3-1}$).

For bins above 2400 MeV, the phi cut does not remove any $\Lambda(1520)$ events, so there is no systematic error associated with this cut. For bins below 2400 MeV, we see that there is some systematic shift, which is especially apparent for ρ_{3-1} . For these lower energy bins, we estimate the systematic error as 0.01 for ρ_{11} and ρ_{31} and 0.02 for ρ_{3-1} .

7.3.4 Non- pK^- decays of the $\Lambda(1520)$

In this section we conclude the Monte Carlo investigation that began in Section 6.4.1. In that section we created a Monte Carlo sample of events including all decay modes of the $\Lambda(1520)$ which could mimic our signal and then performed a background fit to try to remove this background. We now extract the spin density matrix elements from that Monte Carlo sample (after background subtraction) to see if this leads to any systematic shift in the SDMEs due to an incomplete removal of this background. This background is unique to the missing K^- topology, so this systematic error will not be shared between topologies, and we do not have to consider it separately. We present the results nonetheless to complete the investigation and to show that our procedure is effective in removing the effect of non- pK^- decays.

After combining all the events together and calculating the Q-values, we then cut out events with confidence level less than 10%, $MM(p) < 1040$ MeV, and $MM(K^+)$ outside of the range 1500–1540 MeV, thus applying the same cuts we use with the real data. We then extract the SDMEs normally, except weighting events by Q_1 rather than Q_2Q_1 (because in this Monte Carlo sample, there are no non- $\Lambda(1520)$ events, so the stage 2 fit is not needed). The extraction of SDMEs requires a sample of “accepted Monte Carlo” events; as always, this is composed of the pK^- events only. Our Monte Carlo events were thrown with a phase-space distribution, which corresponds to $\rho_{11} = 0.25$, $\text{Re}(\rho_{31}) = 0$, and $\text{Re}(\rho_{3-1}) = 0$. In Figure 7.18, we plot the difference between the extracted SDMEs and the signal values. The extracted values match very closely the signal values and no systematic shift is seen. Even at higher energies, where the background fit appeared to be poorer, the background has little effect on the extracted SDME. This shows that we are successful at removing the non- pK^- decays.

7.3.5 Combining errors

All shared systematic errors discussed here are added in quadrature to the error previously calculated in Section 7.2 (statistical plus non-shared systematic). The errors from the two sources of background (flat and $\cos \theta$ -type) are considered as separate systematic errors, since they are uncorrelated and could shift the matrix elements in opposite directions. All systematic errors are listed in Table 7.1. Results with full errors are shown in Figure 7.19.

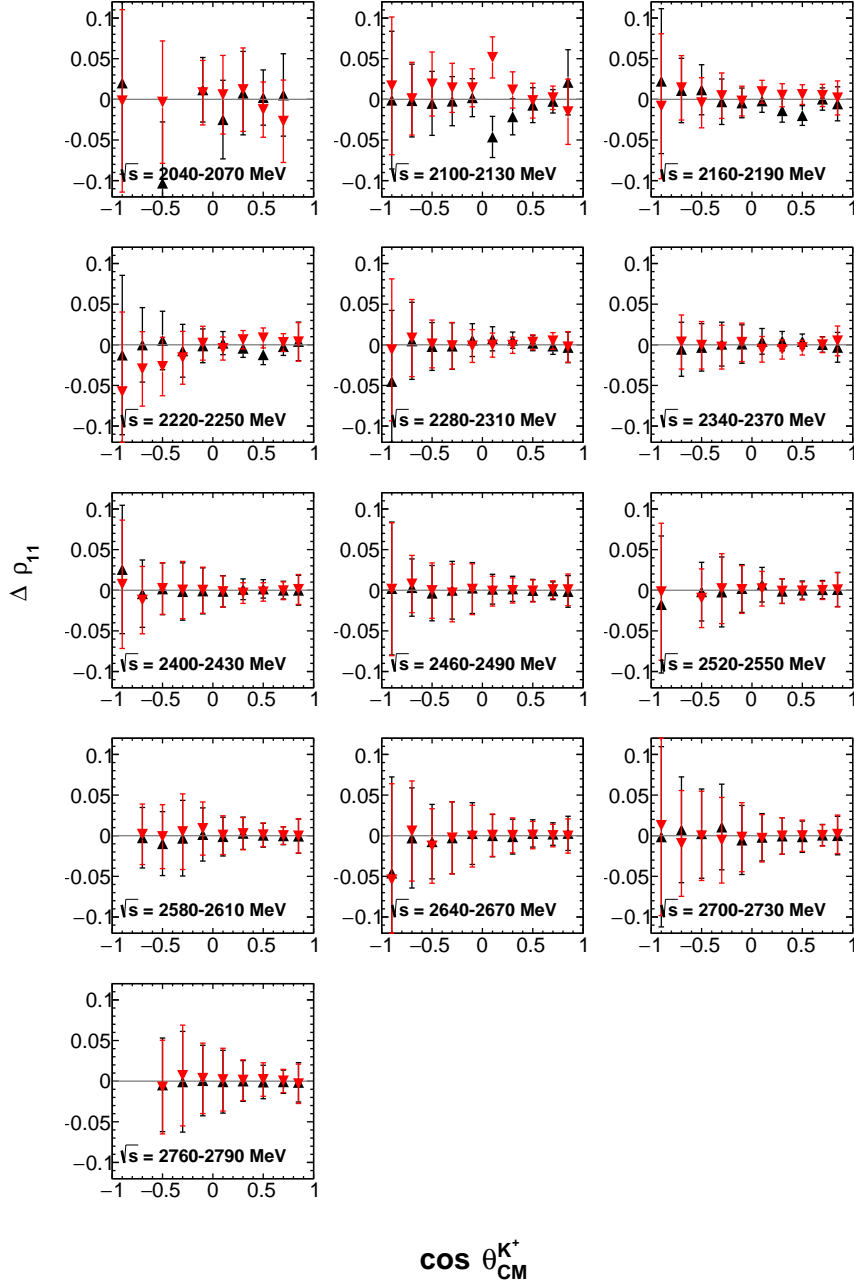


Figure 7.15: Difference $\Delta\rho_{11}$ between the matrix element as extracted using the baseline cut ($MM(p) < 1040$ MeV) and using the alternative cuts: $MM(p) < 1030$ MeV (black points) and $MM(p) < 1050$ MeV (red points). Missing K^- topology. Error bars shown are statistical errors from original fit.

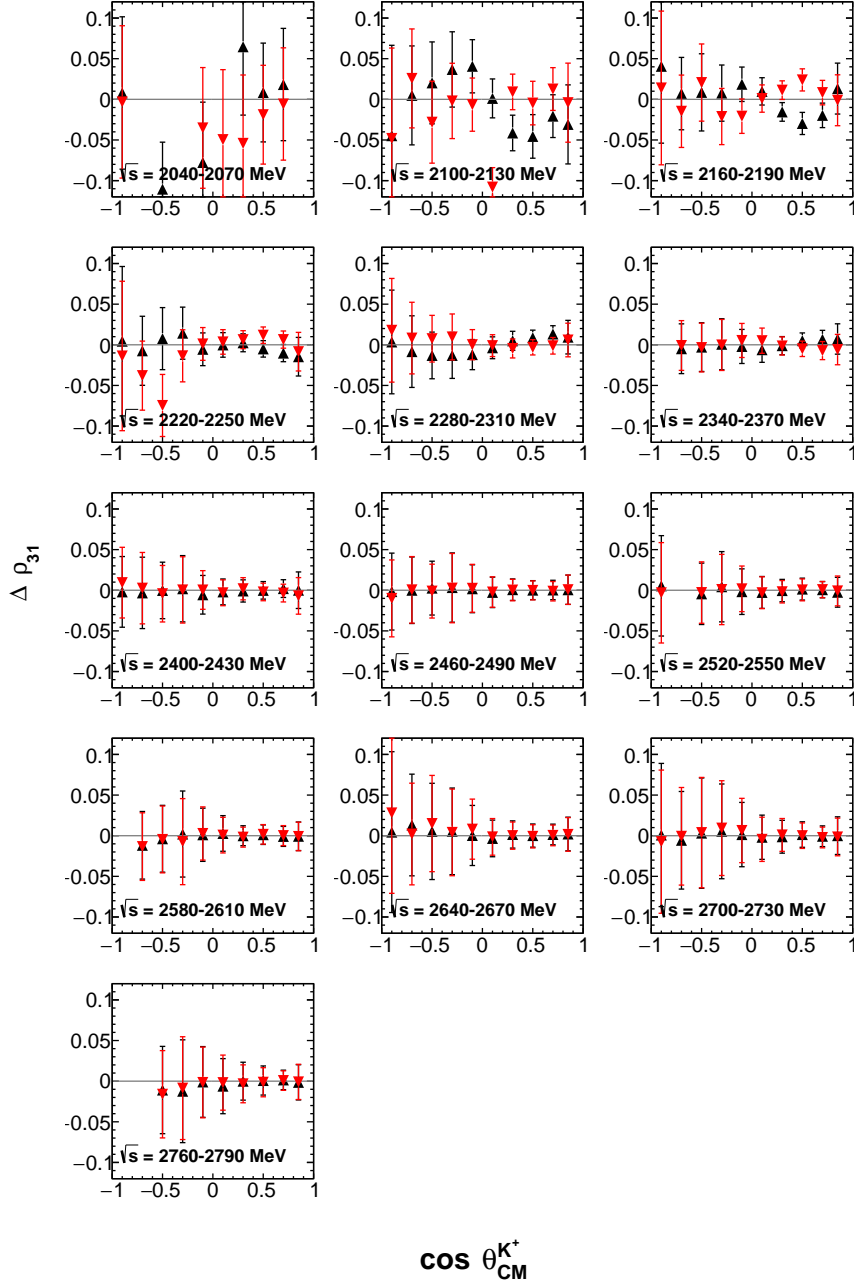


Figure 7.16: Difference $\Delta\rho_{31}$ between the matrix element as extracted using the baseline cut ($MM(p) < 1040$ MeV) and using the alternative cuts: $MM(p) < 1030$ MeV (black points) and $MM(p) < 1050$ MeV (red points). Missing K^- topology. Error bars shown are statistical errors from original fit.

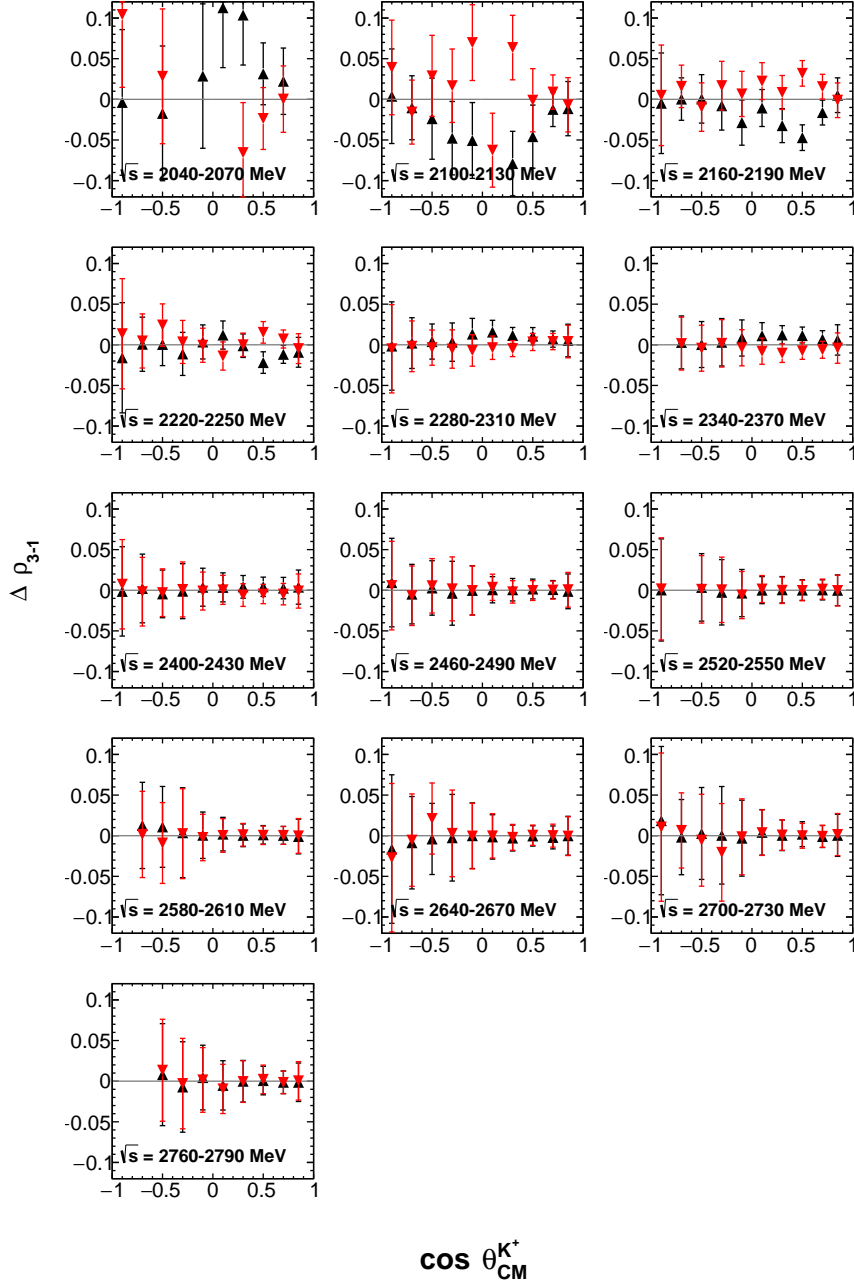


Figure 7.17: Difference $\Delta\rho_{3-1}$ between the matrix element as extracted using the baseline cut ($MM(p) < 1040$ MeV) and using the alternative cuts: $MM(p) < 1030$ MeV (black points) and $MM(p) < 1050$ MeV (red points). Missing K^- topology. Error bars shown are statistical errors from original fit.

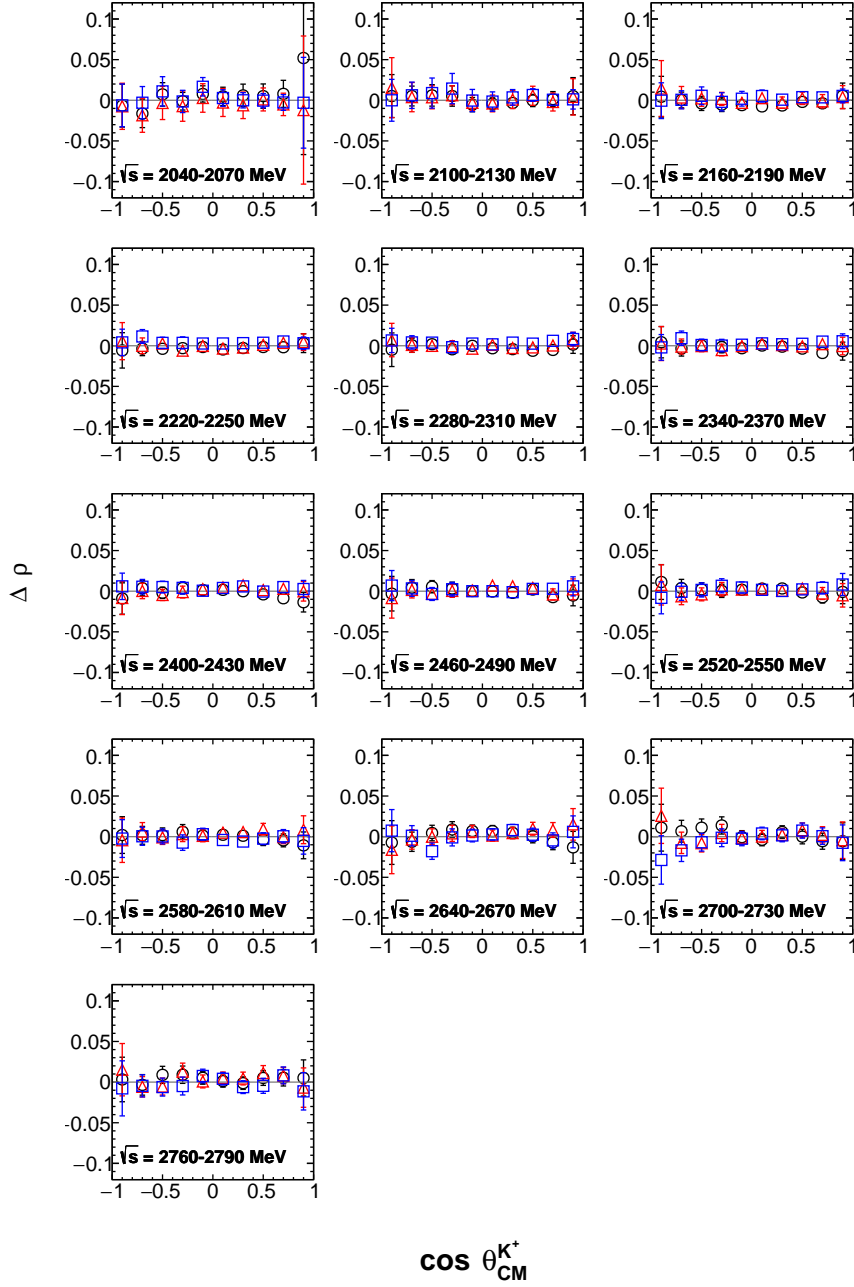


Figure 7.18: SDMEs of Monte Carlo sample after adding non- pK^- events and performing a background fit. Plotted are the differences between extracted spin density matrix elements and true signal values: $\Delta\rho_{11}$ (black circles), $\Delta\rho_{31}$ (red triangles), $\Delta\rho_{3-1}$ (blue squares).

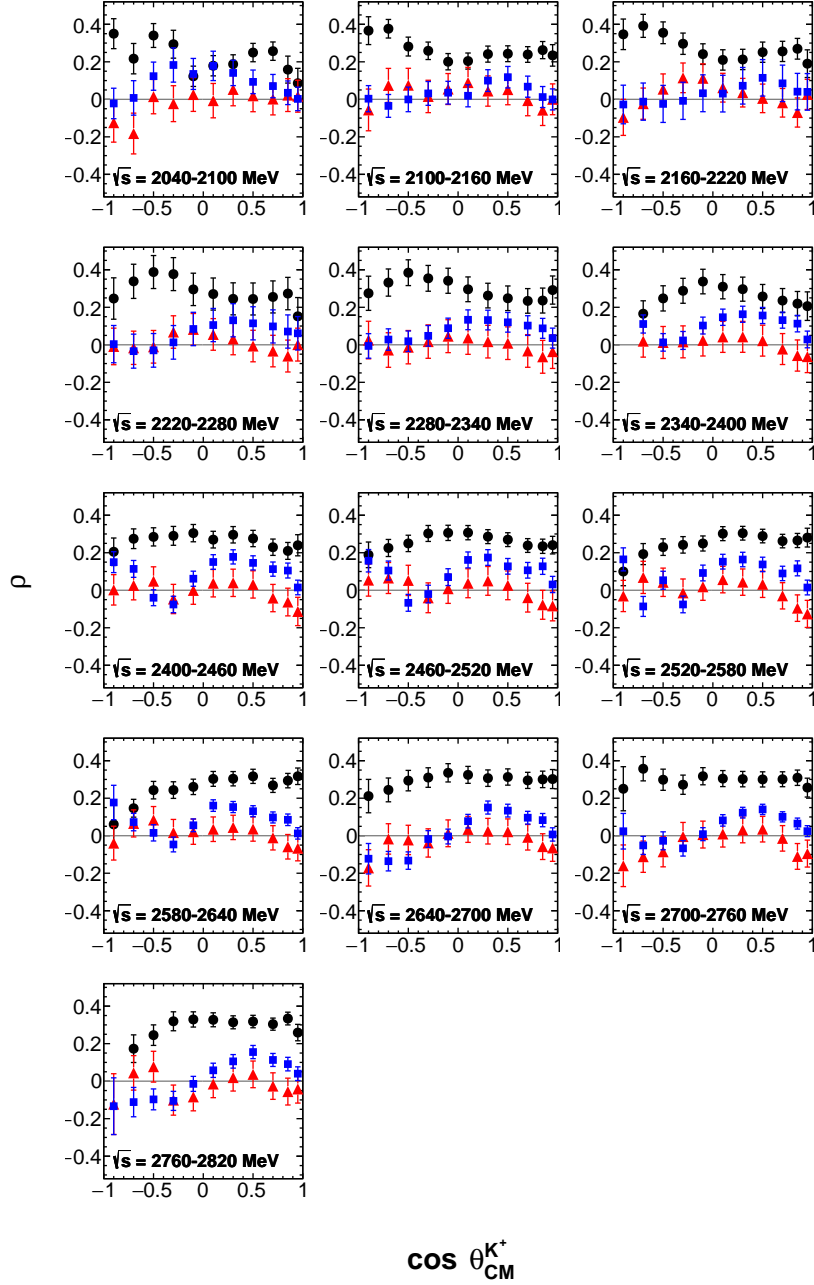


Figure 7.19: All spin density matrix elements: ρ_{11} (black circles), $\text{Re } \rho_{31}$ (red triangles), and $\text{Re } \rho_{3-1}$ (blue squares). All three topologies averaged. Error bars include statistical errors and all systematic errors. The same results, but with separate plots for each matrix element, are shown in Figures D.1, D.2, and D.3.

We also plot these SDMEs vs energy in Figure 7.20. Figure 7.21 shows the same results, but with only statistical errors shown to emphasize that the energy-dependence of the matrix elements is not just due to statistical fluctuations.

7.4 Discussion

Some features of the SDMEs are easily observed in Figures 7.19 and 7.20. ρ_{11} is approximately 0.25 in most kinematic regions. ρ_{31} is consistent with zero almost everywhere. The uncertainties are largest on ρ_{31} due to the presence of a background that is odd in $\cos\theta_{GJ}$. ρ_{3-1} is non-zero and has a pronounced structure in production angle, rising as the angle increases before falling to zero near $\cos\theta_{K^+,CM} = 1.0$. ρ_{11} only varies mildly with angle and energy. To fully interpret this data, it is useful to put it into the context of a model.

7.4.1 Comparison with models

As discussed in the introduction, Nam and Kao have created a model of $\Lambda(1520)$ photoproduction and published their model predictions of the the decay angular distributions. At four points, they have given numerical predictions which we can compare with our data, as shown in Figure 7.22. From these four points, it appears that the agreement between model and data is fair. However, this is an illusion caused by the limited number of points at which we can make a direct comparison. As seen in Figure 1.12a, the model predicts rapid and large variation in the $\cos\theta_{GJ}$ distribution (and thus in ρ_{11}) as the production angle changes, especially at forward angle. This is not seen at all in the data, so the model describes the data poorly.

7.4.2 Comparison with earlier results

LAMP2 (Barber et al.) publish results for all three spin density matrix elements. No binning is done so the results are averaged together over the region $\sqrt{s} = 2500\text{--}3100$ MeV and $-t = 0.2\text{--}0.7$ GeV². We compare these results with our results from our $\sqrt{s} = 2760\text{--}2820$ MeV bin, which is near the center of the energy range. It is not clear what error to use on the LAMP2 ρ_{11} point. The paper reports values $\rho_{33} = 0.38 \pm 0.05$ and $\rho_{11} = 0.12 \pm 0.20$, but since these two values are constrained by the relationship $\rho_{33} + \rho_{11} = 0.5$, the errors on the two points should be the same. We plot the error bar using the value reported for ρ_{11} , but probably this error should be smaller. The comparison is shown in Figure 7.23. There appears to be good agreement between the two results, but the agreement is poor if we use the smaller error on ρ_{11} .

Muramatsu et al. (LEPS Collaboration) publish the results of a fit to the $\cos\theta_{GJ}$ distribution. They report the value of a parameter α which we can translate to ρ_{11} . α is measured in two different regions of production angle. For the backward-angle region, they report two values for α , obtained using two different procedures; we use the average of these two. The comparison of these results with our results is shown in Figure 7.24. The agreement is good in the forward-angle region. At backwards angle the agreement is not so good, although it is better if compared with our results from lower-energy bins which also overlap with the LEPS energy range (not shown here).

The SAPHIR paper [23] does show a fit to the $\cos\theta_{GJ}$ distribution, but does not publish the extracted parameter values. Nevertheless, we can make a qualitative comparison between our data and the SAPHIR data (shown in Figure 1.10). The SAPHIR data is divided into four energy bins starting at threshold and going up to $\sqrt{s} = 2420$ MeV. In the lowest energy bin ($\sqrt{s} = 2010\text{--}2120$ MeV), the contributions from $m = \pm\frac{3}{2}$ and $m = \pm\frac{1}{2}$ are roughly equal. In the $\sqrt{s} = 2120\text{--}2230$ MeV bin, the $m = \pm\frac{3}{2}$ component is stronger. In the $\sqrt{s} = 2230\text{--}2330$ MeV bin, they are roughly equal again. Then in the highest energy bin ($\sqrt{s} = 2330\text{--}2420$ MeV), $m = \pm\frac{1}{2}$ nearly totally dominates. This is not in good agreement with our data. We do not see such strong energy

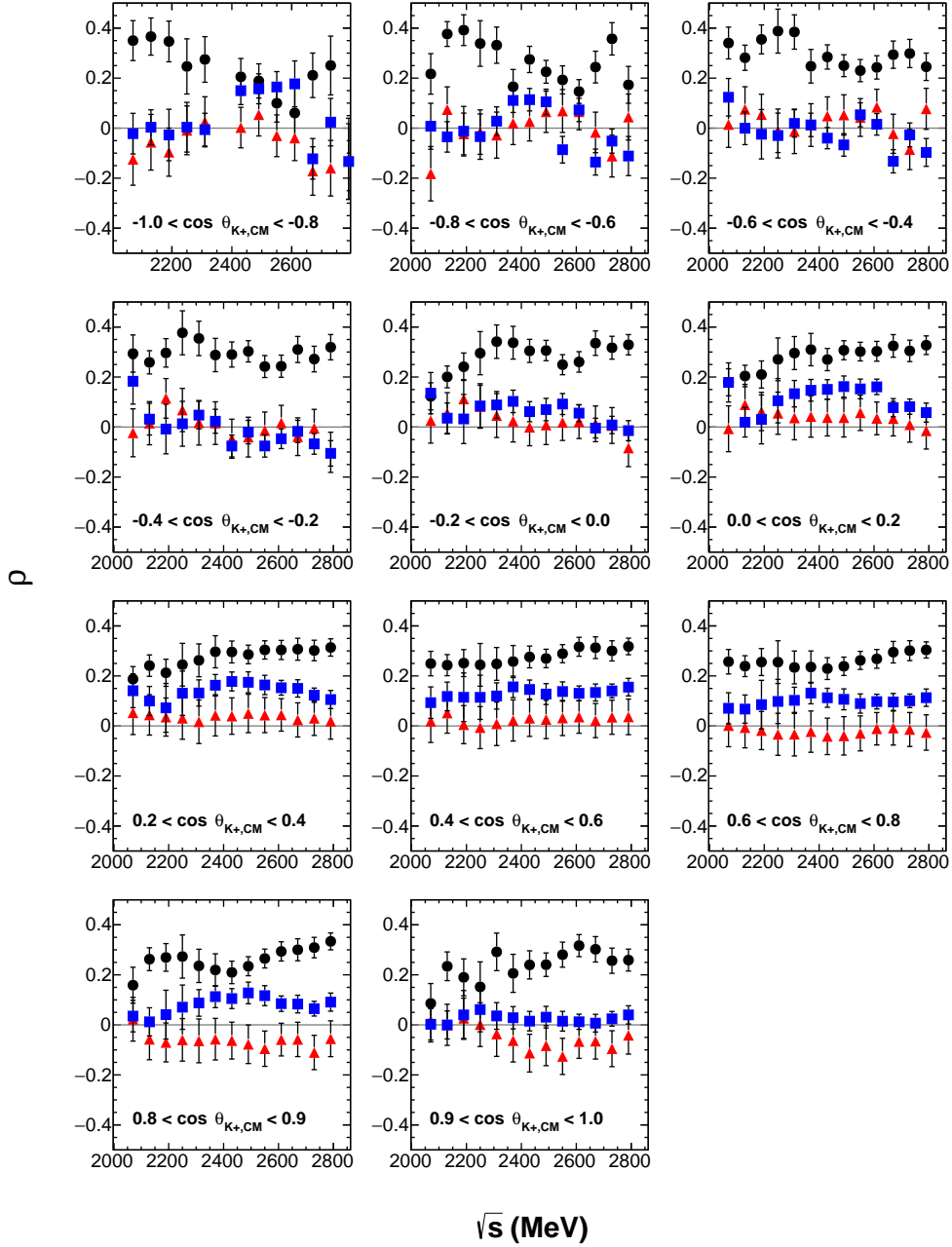


Figure 7.20: All spin density matrix elements: ρ_{11} (black circles), $\text{Re } \rho_{31}$ (red triangles), and $\text{Re } \rho_{3-1}$ (blue squares). All three topologies averaged. Error bars include statistical errors and all systematic errors.

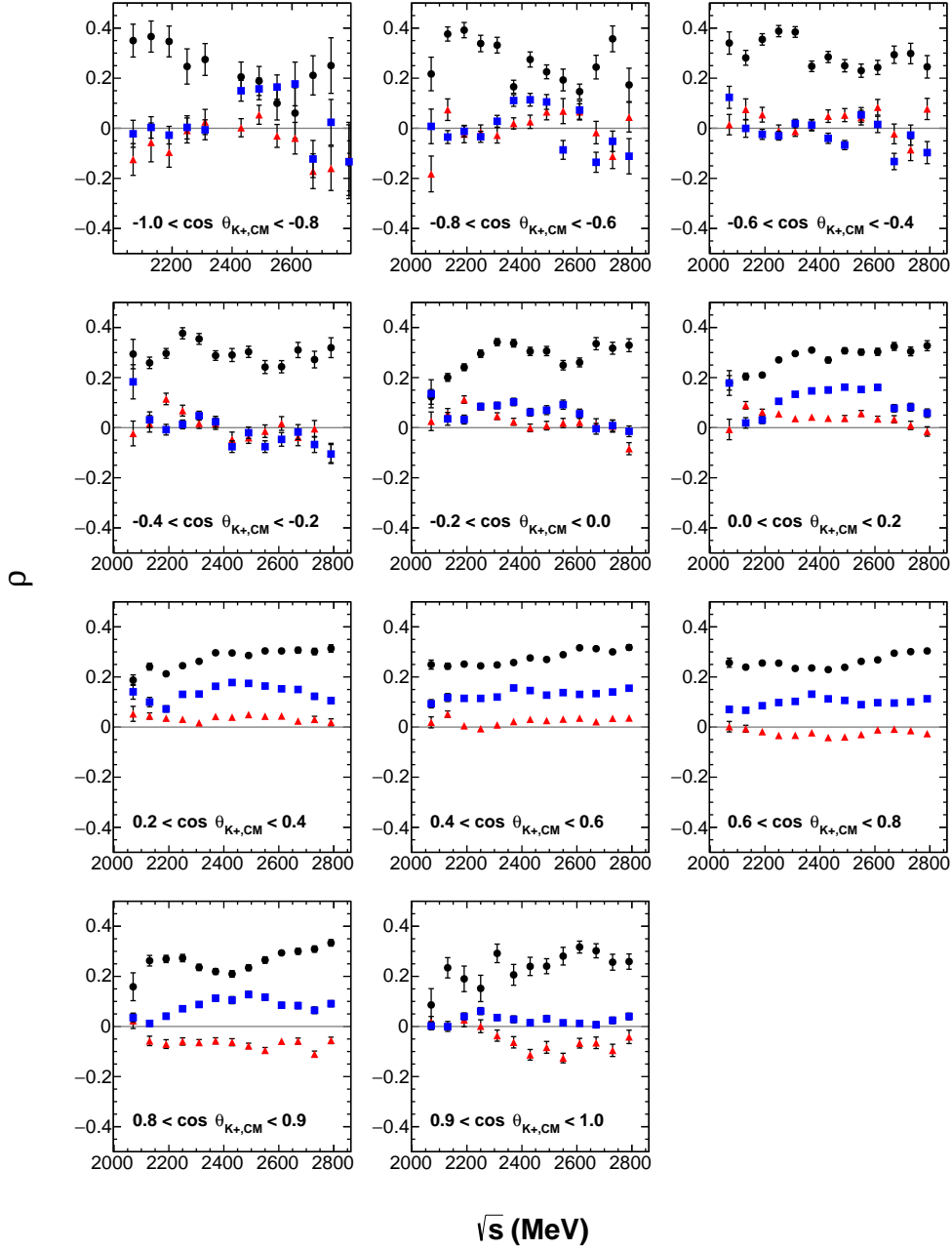


Figure 7.21: All spin density matrix elements: ρ_{11} (black circles), $\text{Re } \rho_{31}$ (red triangles), and $\text{Re } \rho_{3-1}$ (blue squares). All three topologies averaged. Error bars include statistical errors only.

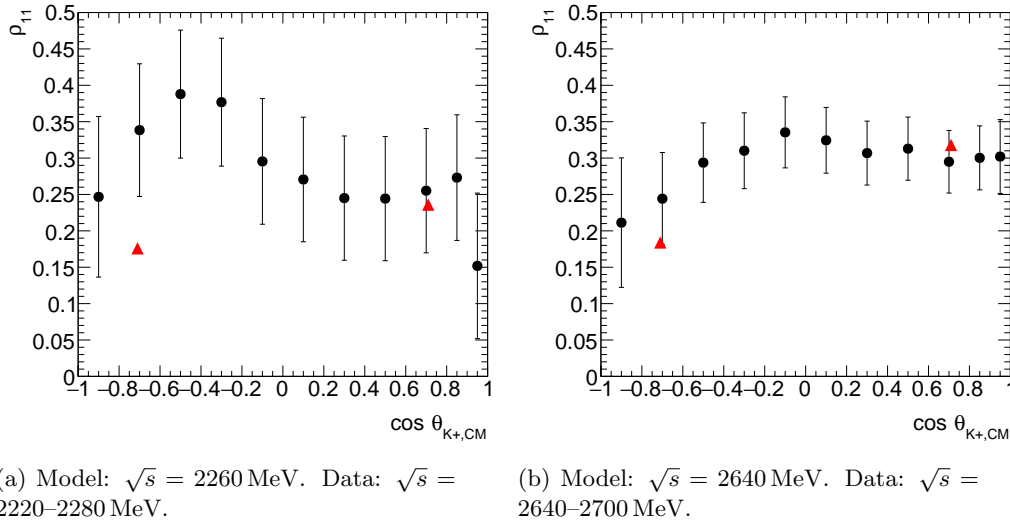


Figure 7.22: Comparison of present work (black circles) with the prediction from the model of Nam and Kao (red triangles) [25].

dependence and we do not see such a $m = \pm\frac{1}{2}$ dominance at high energies. However, it's not even clear if the SAPHIR results use the correct definition of $\cos\theta_{GJ}$ (see Section 1.3.3).

The final result we can compare to is the Barrow et al. (CLAS) study of $\Lambda(1520)$ electroproduction. In this paper, the $\cos\theta_{GJ}$ distribution is measured and fit. The ratio of $m = \pm\frac{3}{2}$ to $m = \pm\frac{1}{2}$ strengths is published, which we can convert to ρ_{11} for comparison with our results. By combining photoproduction results and electroproduction results, we can see how the $\Lambda(1520)$ production changes with Q^2 . In the Barrow paper, angular distributions are presented in four Q^2 bins from 0.9–2.4 GeV², averaged over all other kinematic variables. W , the mass of the $K^+\Lambda(1520)$ system, ranges from 2.01–2.65 GeV. Because of the large range of energies and angles averaged over, it is not possible to make a precise comparison with our results, but in general it appears that the ρ_{11} polarization of the $\Lambda(1520)$ does not vary strongly with Q^2 . In the lowest Q^2 bin (0.9–1.2 GeV²), $\rho_{11} = 0.28 \pm 0.02$, which is generally in good agreement with our results (which are of course at $Q^2 = 0$). In the higher Q^2 bins ρ_{11} increases slightly with reported values 0.33 ± 0.03 , 0.31 ± 0.02 , and 0.32 ± 0.03 .

7.4.3 Summary and conclusion

In the previous results, there appeared to be a disagreement between LAMP2, which supported $m = \pm\frac{3}{2}$ dominance (small ρ_{11}), and the results from CLAS electroproduction and LEPS, which supported roughly equal contributions from $m = \pm\frac{1}{2}$ and $m = \pm\frac{3}{2}$ ($\rho_{11} \approx 0.25$). It was not known if this was a true disagreement because the different experiments studied different energy ranges (and the CLAS result was at $Q^2 \neq 0$). The current results suggest that $\rho_{11} \approx 0.25$ at all energies studied and disagree with the LAMP2 results in the energy region where the two experiments overlap (assuming that the smaller error is correct for the LAMP2 ρ_{11} measurement).

In addition, our data does not support the model of Nam and Kao, who predict a rapid variation of ρ_{11} at forward angles.

Our results present measurements of all three unpolarized spin density matrix elements of the $\Lambda(1520)$ over almost the full range of production angles and from energies near threshold up to $\sqrt{s} = 2820$ MeV. Only one previous measurement of the elements ρ_{31} and ρ_{3-1} exists. In addition, the large amount of data from g11a allows for much finer binning in energy and angle than in all

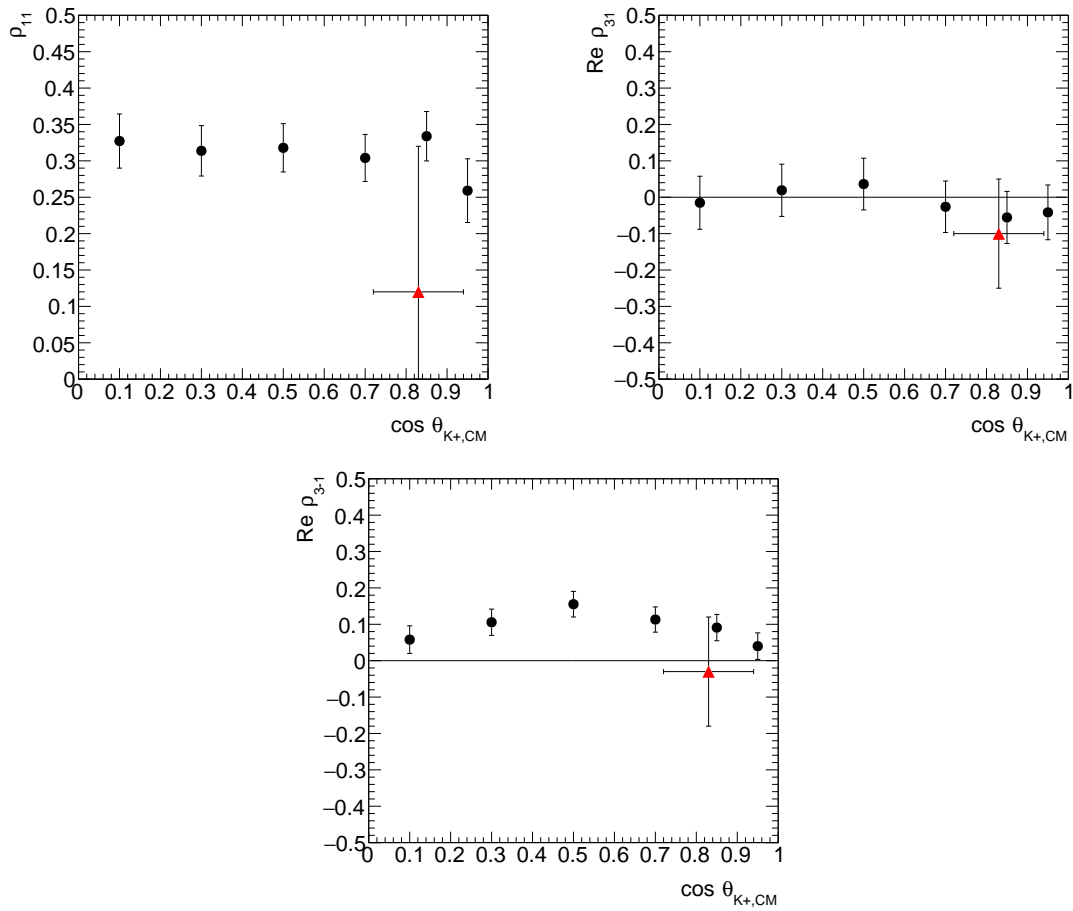


Figure 7.23: Comparison of present work (black circles, $\sqrt{s} = 2760\text{--}2820$ MeV) and LAMP2 [17] (red triangles, $\sqrt{s} = 2500\text{--}3100$ MeV). Horizontal error bar indicates range of $\cos \theta$ values averaged over. The size of the error on the LAMP2 ρ_{11} point is unclear, see the text for details.

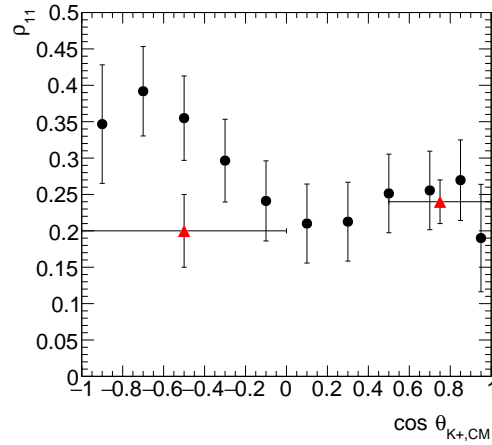


Figure 7.24: Comparison of present work (black circles, $\sqrt{s} = 2160\text{--}2220$ MeV) and LEPS [18] (red triangles). The forward angle LEPS point includes energies from $\sqrt{s} = 2110\text{--}2320$ MeV and the backwards angle point from $\sqrt{s} = 2010\text{--}2320$ MeV. Horizontal error bar indicates range of $\cos \theta$ values averaged over.

previous experiments.

More work is still needed to fully understand $\Lambda(1520)$ photoproduction. On the theoretical side, several models of $\Lambda(1520)$ photoproduction exist, but only one paper has examined the observables discussed here; it would be interesting to see how well other models can reproduce our experimental results. On the experimental side, data from $\Lambda(1520)$ production off the neutron is sparse, as is data using a polarized beam; these measurements would help constrain models. We hope our measurement will spur further theoretical and experimental study of $\Lambda(1520)$ photoproduction.

Bibliography

- [1] J. Beringer et al. (Particle Data Group). *Review of particle physics*. Phys. Rev. D **86**, 010001 (2012).
- [2] K. G. Wilson. *Confinement of quarks*. Phys. Rev. D **10**, 2445 (1974).
- [3] M. Ferro-Luzzi, R. D. Tripp, and M. B. Watson. *Excited hyperon of mass 1520 Mev*. Phys. Rev. Lett. **8**, 28 (1962).
- [4] M. J. Corden et al. *An analysis of the $\Lambda(1520)$ observed in a K^- neutron production experiment*. Nucl. Phys. B **84**, 306 (1975).
- [5] N. Isgur and G. Karl. *P-wave baryons in the quark model*. Phys. Rev. D **18**, 4187 (1978).
- [6] N. P. Samios, M. Goldberg, and B. T. Meadows. *Hadrons and SU(3): A critical review*. Rev. Mod. Phys. **46**, 49 (1974).
- [7] S. Capstick and N. Isgur. *Baryons in a relativized quark model with chromodynamics*. Phys. Rev. D **34**, 2809 (1986).
- [8] L. Roca, S. Sarkar, V. K. Magas, and E. Oset. *Unitary coupled channel analysis of the $\Lambda(1520)$ resonance*. Phys. Rev. C **73**, 045208 (2006).
- [9] S. Capstick and W. Roberts. *Strange decays of nonstrange baryons*. Phys. Rev. D **58**, 074011 (1998).
- [10] S. Ozaki, A. Hosaka, H. Nagahiro, and O. Scholten. *Coupled-channel analysis for ϕ photoproduction with $\Lambda(1520)$* . Phys. Rev. C **80**, 035201 (2009).
- [11] H.-Y. Ryu, A. I. Titov, A. Hosaka, and H.-C. Kim. *ϕ photoproduction with coupled-channel effects*. Prog. Theor. Exp. Phys. **2014**, 023D03 (2014).
- [12] B. Dey. *Differential cross section and polarization extractions for $\gamma p \rightarrow K^+\Sigma^0$ and $\gamma p \rightarrow \phi p$ using CLAS at Jefferson Lab, towards a partial wave analysis in search of missing baryon resonances*. Ph.D. thesis, Carnegie Mellon University (2011).
- [13] H. R. Crouch et al. *Gamma-ray proton interactions between 0.5 and 4.8 BeV*. Phys. Rev. Lett. **13**, 636 (1964).
- [14] W. A. Blanpied et al. *Evidence for the photoproduction of $Y = 0$ states with masses greater than 1900 MeV*. Phys. Rev. Lett. **14**, 741 (1965).
- [15] N. B. Mistry, S. Mori, D. I. Sober, and A. J. Sadoff. *Photoproduction of Y^{*0} resonant states*. Phys. Lett. B **24**, 528 (1967).
- [16] A. M. Boyarski et al. *Photoproduction of K^+ -hyperon from hydrogen and deuterium at 11 GeV*. Phys. Lett. B **34**, 547 (1971).

- [17] D. P. Barber et al. (LAMP2 Group). *Strangeness exchange in the photoproduction of $K^+\Lambda(1520)$ between 2.8 and 4.8 GeV*. Zeitschrift für Physik C **7**, 17 (1980).
- [18] N. Muramatsu et al. (LEPS Collaboration). *Near-threshold photoproduction of $\Lambda(1520)$ from protons and deuterons*. Phys. Rev. Lett. **103**, 012001 (2009).
- [19] Z. Zhao. *Photoproduction of the $\Lambda^*(1520)$ Hyperon off Protons and Neutrons in Deuterium*. Ph.D. thesis, University of South Carolina (2010).
- [20] S. P. Barrow et al. (CLAS Collaboration). *Electroproduction of the $\Lambda(1520)$ hyperon*. Phys. Rev. C **64**, 044601 (2001).
- [21] H. Kohri et al. (LEPS Collaboration). *Near-threshold $\Lambda(1520)$ production by the $\bar{\gamma}p \rightarrow K^+\Lambda(1520)$ reaction at forward K^+ angles*. Phys. Rev. Lett. **104**, 172001 (2010).
- [22] A. I. Titov, B. Kämpfer, S. Daté, and Y. Ohashi. *Coherent Θ^+ and $\Lambda(1520)$ photoproduction off the deuteron*. Phys. Rev. C **72**, 035206 (2005).
- [23] F. W. Wieland et al. *Study of the reaction $\gamma p \rightarrow K^+\Lambda(1520)$ at photon energies up to 2.65 GeV*. Eur. Phys. J. A **47** (2011).
- [24] K. Moriya et al. (CLAS Collaboration). *Differential photoproduction cross sections of the $\Sigma^0(1385)$, $\Lambda(1405)$, and $\Lambda(1520)$* . Phys. Rev. C **88**, 045201 (2013).
- [25] S.-i. Nam and C.-W. Kao. *$\Lambda(1520)$ photoproduction off a proton target with Regge contributions*. Phys. Rev. C **81**, 055206 (2010).
- [26] J. He and X.-R. Chen. *Roles of nucleon resonances in $\Lambda(1520)$ photoproduction off the proton*. Phys. Rev. C **86**, 035204 (2012).
- [27] T. Azemoon et al. *Production of hyperons by virtual photons*. Nucl. Phys. B **95**, 77 (1975).
- [28] Y. Qiang et al. *Properties of the $\Lambda(1520)$ resonance from high-precision electroproduction data*. Phys. Lett. B **694**, 123 (2010).
- [29] S.-I. Nam, A. Hosaka, and H.-C. Kim. *$\Lambda(1520, 3/2^-)$ -photoproduction reaction via $\gamma N \rightarrow K\Lambda^*(1520)$* . Phys. Rev. D **71**, 114012 (2005).
- [30] S.-i. Nam, K.-S. Choi, A. Hosaka, and H.-C. Kim. *Test of the reaction mechanism for $\gamma N \rightarrow K\Lambda(1520)$ using the polarized photon*. Phys. Rev. D **75**, 014027 (2007).
- [31] A. I. Titov, B. Kämpfer, S. Daté, and Y. Ohashi. *Θ^+ formation in inclusive $\gamma D \rightarrow pK^-X$* . Phys. Rev. C **74**, 055206 (2006).
- [32] H. Toki, C. Garca-Recio, and J. Nieves. *Photon induced $\Lambda(1520)$ production and the role of the K^* exchange*. Phys. Rev. D **77**, 034001 (2008).
- [33] J.-J. Xie, E. Wang, and J. Nieves. *Re-analysis of the $\Lambda(1520)$ photoproduction reaction*. Phys. Rev. C **89**, 015203 (2014).
- [34] E. Wang, J.-J. Xie, and J. Nieves. *Regge signatures from CLAS $\Lambda(1520)$ photoproduction data at forward angles*. Phys. Rev. C **90**, 065203 (2014).
- [35] J. He. *Theoretical study of the $\Lambda(1520)$ photoproduction off proton target based on the new CLAS data*. Nucl. Phys. A **927**, 24 (2014).
- [36] A. Sibirtsev, J. Haidenbauer, S. Krewald, U.-G. Meißner, and A. W. Thomas. *$K\bar{K}$ photoproduction from protons*. Eur. Phys. J. A **31**, 221 (2007).

- [37] M. A. Nielsen and I. L. Chuang. *Quantum Computation and Quantum Information*. Cambridge University Press (2000).
- [38] K. Schilling, P. Seyboth, and G. Wolf. *On the analysis of vector-meson production by polarized photons*. Nucl. Phys. B **15**, 397 (1970).
- [39] J. D. Jackson. *Particle and polarization angular distributions for two and three body decays*. In *High Energy Physics: Lectures delivered at Les Houches during the 1965 session of the Summer School of Theoretical Physics*. Gordon and Breach Science Publishers (1965).
- [40] S. U. Chung. *Spin formalisms* (2014). BNL-QGS-02-0900, URL <http://suchung.web.cern.ch/suchung/spinfmt1.pdf>.
- [41] M. Williams. *Measurement of Differential Cross Sections and Spin Density Matrix Elements along with a Partial Wave Analysis for $\gamma p \rightarrow p\omega$ using CLAS at Jefferson Lab*. Ph.D. thesis, Carnegie Mellon University (2007).
- [42] *Jefferson Lab flickr*. URL <https://www.flickr.com/photos/jeffersonlab/>.
- [43] C. W. Leemann, D. R. Douglas, and G. A. Krafft. *The continuous electron beam accelerator facility: CEBAF at the Jefferson Laboratory*. Annual Review of Nuclear and Particle Science **51**, 413 (2001).
- [44] D. I. Sober et al. *The bremsstrahlung tagged photon beam in Hall B at JLab*. Nucl. Inst. & Meth. A **440**, 263 (2000).
- [45] B. A. Mecking et al. *The CEBAF large acceptance spectrometer (CLAS)*. Nucl. Inst. & Meth. A **503** (2003).
- [46] *g11a target cell*. URL <https://userweb.jlab.org/~christo/g11a%20final.pdf>.
- [47] S. Christo. *g11a, eg3a, g8b and g13b target cell*. URL <https://userweb.jlab.org/~christo/g11a%20target.html>.
- [48] Y. G. Sharabian et al. *A new highly segmented start counter for the CLAS detector*. Nucl. Inst. & Meth. A **556**, 246 (2006).
- [49] *CLAS photo album*. URL <https://www.jlab.org/Hall-B/album/>.
- [50] M. D. Mestayer et al. *The CLAS drift chamber system*. Nucl. Inst. & Meth. A **449**, 81 (2000).
- [51] E. S. Smith et al. *The time-of-flight system for CLAS*. Nucl. Inst. & Meth. A **432**, 265 (1999).
- [52] M. Ungaro, R. De Vita, and L. Elouadrhiri. *g11 data processing* (2005). CLAS Note 2005-014, URL <http://hadron.physics.fsu.edu/~skpark/document/CN2005-014.pdf>.
- [53] *Hall B electronic logbook*. URL <http://clasweb.jlab.org/clasonline/prodlogsearch.html>.
- [54] K. Moriya. *Measurement of the Lineshape, Differential Photoproduction Cross Section, Spin and Parity of the $\Lambda(1405)$ Using CLAS at Jefferson Lab*. Ph.D. thesis, Carnegie Mellon University (2010).
- [55] E. Pasyuk. *Energy loss corrections for charged particles in CLAS* (2007). CLAS Note 2007-016, URL <http://hadron.physics.fsu.edu/~skpark/document/CN2007-016.pdf>.

- [56] D. Sober, H. Crannell, and F. J. Klein. *The tagger energy scale: Interpreting the CMU kinematic fit results* (2004). CLAS Note 2004-019, URL https://www.jlab.org/Hall-B/notes/cclas_notes04/2004-019.pdf.
- [57] M. Holtrop. *CLAS GEANT simulation*. URL http://nuclear.unh.edu/~maurik/gsim_info.shtml.
- [58] M. McCracken. *A Study of $K^+\Lambda$ Photoproduction in the CLAS g11a Dataset: Differential Cross Section, Recoil Polarization, and a Partial-Wave Analysis*. Ph.D. thesis, Carnegie Mellon University (2008).
- [59] D. Applegate, M. Bellis, Z. Krahn, C. A. Meyer, and M. Williams. *A detailed study of the sources of systematic errors in the CLAS g11 data* (2006). CLAS Note 2006-017, URL https://userweb.jlab.org/~parkkj/USC/proposal2009/local_disk/g11_analysis/report/g11_trigger/2006-017.g11_trigger_study_cmu.pdf.
- [60] M. Williams, M. Bellis, and C. A. Meyer. *Multivariate side-band subtraction using probabilistic event weights*. Journal of Instrumentation **4**, P10003 (2009).
- [61] R. Berlich, S. Gabriel, and A. García. *Parametric optimization with the Geneva library collection*. URL <http://www.gemfony.eu/fileadmin/documentation/geneva-manual.pdf>.
- [62] R. De Vita. private communication.
- [63] P. Young. *Jackknife and bootstrap resampling methods in statistical analysis to correct for bias*. URL <http://young.physics.ucsc.edu/jackboot.pdf>.
- [64] L. Lyons. *Statistics for nuclear and particle physicists*. Cambridge University Press (1986).
- [65] J. D. Jackson. *Remarks on the phenomenological analysis of resonances*. Il Nuovo Cimento **34**, 1644 (1964).
- [66] B. Dey et al. (CLAS Collaboration). *Data analysis techniques, differential cross sections, and spin density matrix elements for the reaction $\gamma p \rightarrow \phi p$* . Phys. Rev. C **89**, 055208 (2014).
- [67] C. Meyer. *Light and exotic mesons* (1999). 1999 HUGS Summer School, URL <http://argus.phys.uregina.ca/gluex/DocDB/0000/000027/003/lecture.pdf>.
- [68] A. V. Anisovich, E. Klempt, A. V. Sarantsev, and U. Thoma. *Partial-wave decomposition of pion and photoproduction amplitudes*. Eur. Phys. J. A **24**, 111 (2005).
- [69] S. Weinberg. *The Quantum Theory of Fields*. Cambridge University Press (1995).
- [70] M. E. Peskin and D. V. Schroeder. *An Introduction to Quantum Field Theory*. Westview Press (1995).
- [71] W. Rarita and J. Schwinger. *On a theory of particles with half-integral spin*. Phys. Rev. **60**, 61 (1941).
- [72] M. Williams. *Numerical object oriented quantum field theory calculations*. Computer Physics Communications **180**, 1847 (2009).
- [73] J. Ball and E. Pasyuk. *Photon flux determination through sampling of “out-of-time” hits with the Hall B photon tagger* (2005). CLAS Note 2005-002, URL https://www.jlab.org/Hall-B/notes/cclas_notes05/2005-002.pdf.

Appendix A

Maximum likelihood fitting

The maximum likelihood method is used to estimate the value of unknown parameters that describe a distribution. A good introduction is provided by Lyons [64]. We assume that a set of events, with event i specified by variables $\vec{\theta}_i$, is distributed according to a function $F(\vec{\theta}, \vec{\alpha})$, where $\vec{\alpha}$ are a set of unknown parameters. From F we construct a probability density function, P , which describes the probability of measuring a single event:

$$P(\vec{\theta}, \vec{\alpha}) = \frac{1}{M(\vec{\alpha})} F(\vec{\theta}, \vec{\alpha}). \quad (\text{A.1})$$

Since P is a probability density function we must choose the normalization $M(\vec{\alpha})$ so that $\int d\vec{\theta} P(\vec{\theta}, \vec{\alpha}) = 1$. We then construct the likelihood \mathcal{L} of finding an entire sample of events $\{\vec{\theta}_i\}$:

$$\mathcal{L}(\vec{\alpha}) = \prod_i P(\vec{\theta}_i, \vec{\alpha}). \quad (\text{A.2})$$

The values of $\vec{\alpha}$ that maximize \mathcal{L} provide the best estimates of the values of the parameters. As discussed in Lyons, there also exist procedures for estimating the uncertainties and covariances of the parameters, but we will not use them, instead estimating uncertainties using the bootstrap method as described in Section 7.1.1. In practice, instead of maximizing \mathcal{L} , we maximize $\log \mathcal{L}$

$$\ell(\vec{\alpha}) = \log \mathcal{L}(\vec{\alpha}) = \sum_i \log P(\vec{\theta}_i, \vec{\alpha}), \quad (\text{A.3})$$

as it simplifies some calculations and prevents us from having to deal with minuscule numerical values of \mathcal{L} . Sometimes we wish to weight events in our sample differently. For example, when fitting our angular distributions (Chapter 7), we will weight our events with the Q-values determined in Chapter 6. It is easy to change our log-likelihood to account for these weights:

$$\ell(\vec{\alpha}) = \sum_i w_i \log P(\vec{\theta}_i, \vec{\alpha}) \quad (\text{A.4})$$

where w_i is the weight of event i . While this procedure will give us the correct estimate for the estimates of the parameters, it messes up the estimates of the parameter uncertainties [64]. This is a not a problem for us, since we will not determine our uncertainties directly from the fit.

In addition to considering the parameters $\vec{\alpha}$ that determine the shape of the distribution, we can also consider the absolute normalization of the process as an unknown parameter, β . This is useful if, for example, we are trying to determine the rate of a particular process. This is called the extended maximum likelihood method. We modify the likelihood by adding a factor which gives

the probability of measuring N events if the number of events is distributed according to a Poisson distribution with mean β :

$$\mathcal{L}_E(\vec{\alpha}, \beta) = \frac{e^{-\beta} \beta^N}{N!} \mathcal{L}(\vec{\alpha}), \quad (\text{A.5})$$

where N is the number of events measured. As discussed in Lyons, the estimates of $\vec{\alpha}$ will be the same whether using the likelihood or the extended likelihood. The estimate of β will always be N . However, the extended maximum likelihood method will provide an uncertainty on β , while the standard maximum likelihood just assumes that the normalization is fixed. The two methods will also provide different estimates of the uncertainties and covariances of the parameters $\vec{\alpha}$.

We can simplify the calculation of the extended likelihood. Instead of directly introducing the parameter β to estimate the number of events, add an extra parameter γ to F , which will simply scale F (this extra scale will cancel after normalization so it will not affect the pdf (A.1) or the likelihood (A.2)). Define $M(\vec{\alpha}, \gamma) = \int d\vec{\theta} F(\vec{\theta}, \vec{\alpha}, \gamma)$ to be the expected number of events:

$$\mathcal{L}_E(\vec{\alpha}, \gamma) = \frac{e^{-M(\vec{\alpha}, \gamma)} M(\vec{\alpha}, \gamma)^N}{N!} \mathcal{L}(\vec{\alpha}). \quad (\text{A.6})$$

The log (extended) likelihood becomes:

$$\ell_E(\vec{\alpha}, \gamma) = -M(\vec{\alpha}, \gamma) - \log N! + \sum_i \log F(\vec{\theta}_i, \vec{\alpha}, \gamma). \quad (\text{A.7})$$

The $\log N!$ is a constant and we can ignore it while maximizing the function. This form of ℓ_E is computationally faster because it saves us from having to take the logarithm of the normalization M . We can verify that $M(\vec{\alpha}, \hat{\gamma}) = N$ for the best fit parameters $\vec{\alpha}$ and $\hat{\gamma}$.

A.1 Using Monte Carlo method to account for acceptance in maximum likelihood fits

In real experiments, we cannot directly measure the true physics distribution $F(\vec{\theta})$ because our detectors have a non-uniform acceptance $\eta(\vec{\theta})$, which is the probability that an event with kinematics $\vec{\theta}$ is detected and reconstructed. So the distribution we measure is in fact $F(\vec{\theta})\eta(\vec{\theta})$. However, $\eta(\vec{\theta})$ cannot be written in terms of an analytic function and is usually approximated by using a Monte Carlo simulation. There is a simple way to use Monte Carlo method with the maximum likelihood method to fit a theoretical model to data, while taking into account non-uniform acceptance. If our theoretical model predicts a distribution $W(\vec{\theta}, \vec{\alpha})$, this predicts an actual measured distribution $W(\vec{\theta}, \vec{\alpha})\eta(\vec{\theta})$. We can write our pdf, equivalent to (A.1):

$$P(\vec{\theta}, \vec{\alpha}) = \frac{W(\vec{\theta}, \vec{\alpha})\eta(\vec{\theta})}{\int W(\vec{\theta}', \vec{\alpha})\eta(\vec{\theta}')d\vec{\theta}'}. \quad (\text{A.8})$$

Wonderfully, the normalization factor in the denominator is easily calculated using the Monte Carlo method:

$$M(\vec{\alpha}) = \int W(\vec{\theta}', \vec{\alpha})\eta(\vec{\theta}')d\vec{\theta}' = \frac{V}{N_{\text{raw}}} \sum_{i \in \text{acc}} W(\vec{\alpha}, \vec{\theta}_i), \quad (\text{A.9})$$

where the sum is over accepted Monte Carlo events. V is the volume of the space being integrated over and N_{raw} is the number of events simulated, although these constant factors are irrelevant for the maximization. We can now construct the log likelihood:

$$\ell(\vec{\alpha}) = -N \log M(\vec{\alpha}) + \sum_{i \in \text{data}} \log W(\vec{\theta}_i, \vec{\alpha}), \quad (\text{A.10})$$

where N is the number of data events measured. To evaluate ℓ for a specific set of parameters $\vec{\alpha}$, we must sum over accepted Monte Carlo events to calculate the normalization (A.9), and then again over data events (Eq. (A.10)) to get the rest of the likelihood function. We can easily extend to a weighted sample of events:

$$\ell(\vec{\alpha}) = -N_e \log M(\vec{\alpha}) + \sum_{i \in \text{data}} w_i \log W(\vec{\theta}_i, \vec{\alpha}), \quad (\text{A.11})$$

where $N_e = \sum_i w_i$ is the effective number of events. Or for the extended maximum likelihood method, following Eq. (A.7), we find:

$$\ell_E(\vec{\alpha}, \gamma) = -\gamma M(\vec{\alpha}) + \sum_{i \in \text{data}} w_i \log[\gamma W(\vec{\theta}_i, \vec{\alpha})], \quad (\text{A.12})$$

If W is linear in the parameters $\vec{\alpha}$ (like the spin density matrix element formula (2.47)), we can simplify the calculation of the likelihood. For example, consider $W(\theta) = \alpha_1 f(\theta) + \alpha_2 g(\theta)$. The normalization is

$$M(\alpha) \propto \sum_{i \in \text{acc}} W(\vec{\alpha}, \theta_i) = \alpha_1 \sum_{i \in \text{acc}} f(\theta_i) + \alpha_2 \sum_{i \in \text{acc}} g(\theta_i). \quad (\text{A.13})$$

In this case, the sums $\sum_i f(\theta_i)$ and $\sum_i g(\theta_i)$ only need to be calculated once, instead of having to sum over all accepted events for many different values of $\vec{\alpha}$. If W has a more complex dependence on the parameters (like if the parameter is the width of the Gaussian or a Breit-Wigner), then we cannot use this shortcut.

Appendix B

Lineshapes

There are many references on Breit-Wigner lineshapes and similar matters, all of which contradict each other [54, 65, 28, 1, 66, 67]. The Breit-Wigner is a function (or family of functions) that approximates the lineshape of a resonance. The Breit-Wigner lineshape is always an approximation, and is a better approximation for narrow, isolated resonances far above any relevant thresholds. Various forms of the Breit-Wigner are discussed here. However, the form we use to fit our data will be dictated by the data itself and only guided by the considerations discussed here.

The non-relativistic Breit-Wigner form is derived by assuming the amplitude can be written with a simple pole in the complex plane:

$$A \propto \frac{\Gamma_0}{2} \frac{1}{M - M_0 + i\Gamma_0/2}, \quad (\text{B.1})$$

where M is the invariant mass of the resonant system, M_0 is the central mass of the resonance, and Γ_0 is the full width at half-maximum of the resonance. Squaring the amplitude to get the observable lineshape gives us:

$$|A|^2 \propto \frac{\Gamma_0^2}{4} \frac{1}{(M - M_0)^2 + (\frac{\Gamma_0}{2})^2}. \quad (\text{B.2})$$

The normalization is such that the function is equal to 1 at $M = M_0$. This functional form is also called the Lorentzian.

The Voigt function

$$V(x; \sigma, \Gamma) = \int_{-\infty}^{\infty} G(x'; \sigma) L(x - x'; \Gamma) dx' \quad (\text{B.3})$$

is the convolution of the Lorentzian function (normalized so that $\int dx L(x; \Gamma) = 1$)

$$L(x; \Gamma) = \frac{1}{\pi} \frac{\Gamma}{2} \frac{1}{x^2 + \Gamma^2/4} \quad (\text{B.4})$$

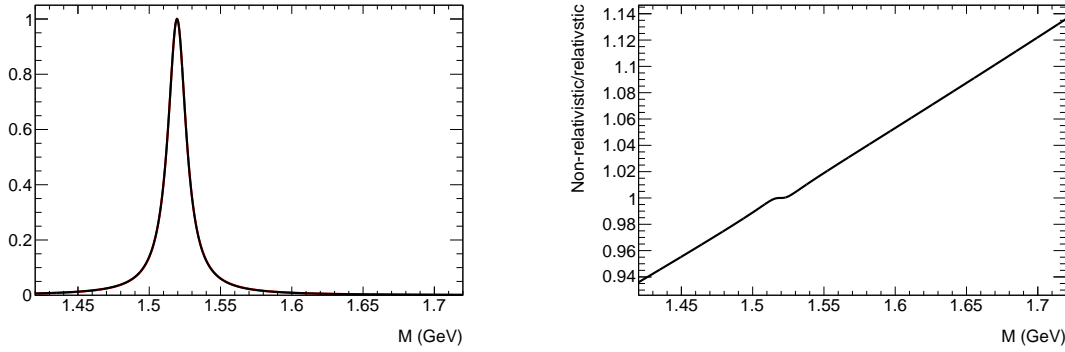
and the normalized Gaussian function

$$G(x; \sigma) = \frac{1}{\sigma\sqrt{2\pi}} e^{-x^2/(2\sigma^2)}. \quad (\text{B.5})$$

The Voigt is useful for including the effects of detector resolution in lineshapes.

The relativistic Breit-Wigner is similar to the form of the propagator for an unstable particle:

$$A \propto \frac{M_0\Gamma_0}{M_0^2 - M^2 - iM_0\Gamma_0}. \quad (\text{B.6})$$



(a) The non-relativistic (red) and relativistic (black) Breit-Wigners are difficult to distinguish as they lie almost on top of each other.

(b) Ratio of non-relativistic BW to relativistic BW

Figure B.1: Comparison of non-relativistic Breit-Wigner (B.2) and relativistic Breit-Wigner (B.7). Both the plot of the lineshapes (a) and their ratio (b) show that the two functions are very similar for the $\Lambda(1520)$ parameters.

Squaring this to get the lineshape:

$$|A|^2 \propto \frac{M_0^2 \Gamma_0^2}{(M^2 - M_0^2)^2 + (M_0 \Gamma_0)^2}. \quad (\text{B.7})$$

Jackson tells us that “the justification for the denominator [in (B.7)] is hardly necessary”, so we will have to take his word for it [65]. Again the numerator is chosen so that the function equals 1 at $M = M_0$. For the $\Lambda(1520)$, with $M_0 = 1519.5$ GeV and $\Gamma_0 = 15.6$ MeV, the non-relativistic and relativistic forms are very similar, as shown in Figure B.1.

To account for the angular momentum involved in the decay of a resonance, we should treat the width Γ as a function of mass M rather than as a constant. We write [54]:

$$\Gamma(M) = \Gamma_0 \left(\frac{q}{q_0} \right)^{2L+1} \left(\frac{M_0}{M} \right) B'_L(q, q_0)^2, \quad (\text{B.8})$$

where B'_L is the Blatt-Weisskopf barrier function, discussed below, L is the angular momentum of the decay, q is the breakup momentum, and q_0 is the value of breakup momentum at $M = M_0$. The breakup momentum is given by:

$$q = \frac{1}{2M} \sqrt{(M^2 - (m_1 + m_2)^2)(M^2 - (m_1 - m_2)^2)}, \quad (\text{B.9})$$

where m_1 and m_2 are the masses of the decay products. For the case of the $\Lambda(1520)$ (a D-wave decay) the $L = 2$ barrier factor is relevant. From the PDG we know [1]:

$$B'_2(q, q_0) = \sqrt{\frac{(z_0 - 3)^2 + 9z_0}{(z - 3)^2 + 9z}}, \quad (\text{B.10})$$

where $z = (qd)^2$, $z_0 = (q_0 d)^2$, and d is a characteristic length scale, usually taken to be $1 \text{ fm} = (197 \text{ MeV})^{-1}$. The PDG also gives another form of the barrier function: $B_L(q)$. The two are related as follows:

$$\left(\frac{q}{q_0} \right)^L B'_L(q, q_0) = \frac{B_L(q)}{B_L(q_0)}. \quad (\text{B.11})$$

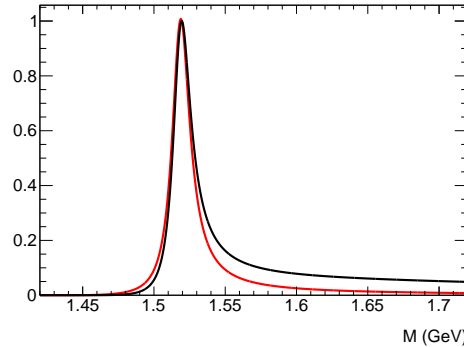


Figure B.2: The red curve shows Equation (B.15). In black is Equation (B.14). The difference between the two is a factor of $\Gamma(M)$.

Using this relation we find an equivalent form of $\Gamma(M)$ (as given by Meyer [67]):

$$\Gamma(M) = \Gamma_0 \frac{M_0}{M} \frac{q}{q_0} \frac{B_L(q)^2}{B_L(q_0)^2}. \quad (\text{B.12})$$

To be complete, we should follow the PDG and take into account all decay channels when calculating the mass-dependent width:

$$\Gamma(M) = \sum_i \Gamma_0^i \left(\frac{q_i}{q_{0,i}} \right)^{2L_i+1} \left(\frac{M_0}{M} \right) B'_{L_i}(q_i, q_{0,i})^2, \quad (\text{B.13})$$

where the sum is over all decay channels, Γ_0^i is the partial decay width for channel i , and L_i , q_i , and $q_{0,i}$ are the relevant values of (angular) momentum for channel i .

Γ_0 should be replaced by $\Gamma(M)$ in both the numerator and denominator in (B.7):

$$\frac{M_0^2 \Gamma(M)^2}{(M^2 - M_0^2)^2 + (M_0 \Gamma(M))^2}. \quad (\text{B.14})$$

Jackson says that (B.14) is only correct for resonance formation in elastic scattering (e.g. $K^- p \rightarrow \Lambda^* \rightarrow K^- p$) and that for production experiments (e.g. $\gamma p \rightarrow K^+ \Lambda^*$) we should only have a single factor of $\Gamma(M)$ in the numerator [65]:

$$\frac{M_0^2 \Gamma_0 \Gamma(M)}{(M^2 - M_0^2)^2 + (M_0 \Gamma(M))^2}. \quad (\text{B.15})$$

Then, according to Jackson, the $\Gamma(M)$ in the numerator is the mass-dependent *partial* width (i.e. just one of the terms in the sum (B.13)) and the one in the denominator is the mass-dependent *total* width (the entire sum (B.13)), but it turns out that, for the $\Lambda(1520)$, it makes little difference whether we use the partial width or the total width in the numerator. Likewise, there's little difference between calculating the total width using the full sum of partial widths (B.13) versus considering just one channel (B.8). Because of this, we simplify our calculations by just using Equation (B.8) to calculate $\Gamma(M)$, as if the $\Lambda(1520)$ decayed only to KN . However, the difference between (B.14) and (B.15) is still significant, as shown in Figure B.2. To decide which one of these we should use, we will have to appeal to our data, but before we can compare with data, we must take into account detector resolution.

To incorporate detector resolution, one should convolve the full mass-dependent relativistic Breit-Wigner with a Gaussian. This can only be done by numerical integration. However, for the $\Lambda(1520)$,

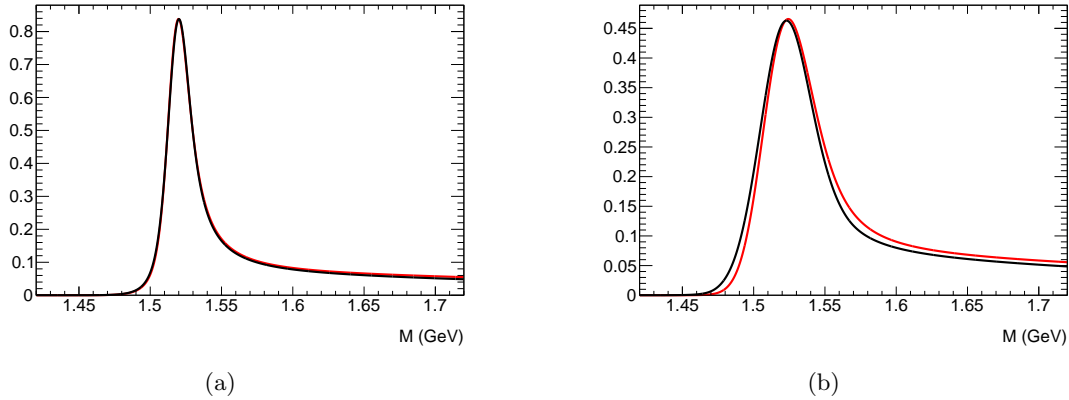


Figure B.3: The black curve is the convolution (computed numerically) of the full relativistic Breit-Wigner (B.14) with a Gaussian. In red is the shortcut function (B.16). The shortcut function is a good approximation for (a) $\sigma = 4$ MeV, but is worse for (b) $\sigma = 15$ MeV. The conclusion is the same comparing Equation (B.15) and Equation (B.17).

we can use another function that approximates the full convolved function reasonably well, at least for small values of the Gaussian width σ . To approximate (B.14), we use:

$$\frac{\Gamma(M)^2}{4} \frac{2\pi}{\Gamma(M)} V(M - M_0; \sigma, \Gamma(M)), \quad (\text{B.16})$$

and to approximate (B.15):

$$\frac{\Gamma_0 \Gamma(M)}{4} \frac{2\pi}{\Gamma(M)} V(M - M_0; \sigma, \Gamma(M)). \quad (\text{B.17})$$

The factors of $\frac{2\pi}{\Gamma(M)}$ are needed to undo the Lorentzian normalization (see (B.4)) from the Voigt (B.3). This approximation is compared to the full convolved function in Figure B.3. The non-relativistic BW approximates the relativistic BW very well (see Figure B.1), thus we expect the Voigt to approximate the convolved relativistic BW very well, but the approximations (B.16) and (B.17) break down somewhat at larger σ because they leave the width $\Gamma(M)$ unconvolved.

Another factor affecting the observed lineshape is the amount of phase space available for the reaction to take place. Taking into account the three-body ($\gamma p \rightarrow \sqrt{s} \rightarrow K^+ K^- p$) phase space, the line shape is modified by a factor of

$$\frac{p_{K^+}^{\text{CM}} p_N^{\Lambda^*}}{p_i^{\text{CM}}} \frac{1}{s}, \quad (\text{B.18})$$

where $p_{K^+}^{\text{CM}}$ is the K^+ momentum in the CM frame, $p_N^{\Lambda^*}$ is the momentum of the decay proton in the $\Lambda(1520)$ rest frame, and p_i^{CM} is the photon momentum in the CM frame. See Moriya for details [54]. This phase space factor has the biggest effect at CM energies just above the $K^+ K^- p$ threshold, where it cuts off the high energy tail of the Breit-Wigner, which is not energetically allowed. See Figure B.4 for an illustration of this effect.

Non-uniform detector acceptance will also distort the measured lineshape from the theoretical forms discussed here.

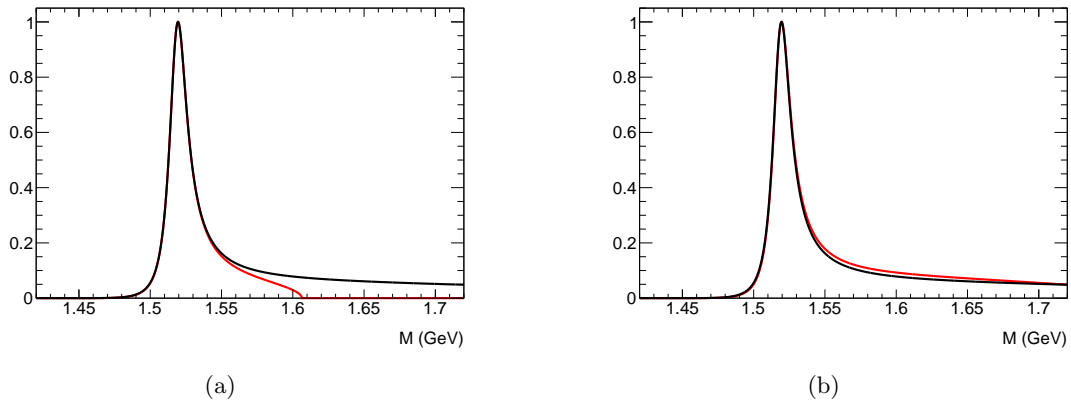


Figure B.4: In black is the standard mass-dependent relativistic BW (B.14). In red is (B.14) multiplied by the phase-space factor (B.18) at (a) $\sqrt{s} = 2100$ MeV and (b) $\sqrt{s} = 2300$ MeV.

Appendix C

Resonant amplitudes, the mother fit, and differential cross section extraction

We wish to construct amplitudes for the process where the $K^+\Lambda(1520)$ system is produced via an s -channel resonance with quantum numbers $J^P: \gamma p \rightarrow J^P \rightarrow K^+\Lambda(1520)$. The reason we do this is to provide a basis for a fit (called the mother fit) which provides a description of our measured distributions and is used to calculate acceptance factors, which are necessary for the extraction of differential cross sections. The mother fit and the calculation of differential cross sections are discussed in the last section of this chapter. Since the differential cross sections are not a main focus of this work, this chapter is provided mostly for reference.

The amplitudes in this chapter are constructed using the relativistic tensor formalism. The idea is to use mathematical objects (vectors, spinors, tensors, etc.) that transform under Lorentz transformations in the same way as the particles they correspond to (spin- $\frac{1}{2}$ fermions, spin-1 particles, etc.). These mathematical objects are irreducible representations of the Lorentz group. We construct amplitudes by combining these objects in such a way that they form a Lorentz-invariant scalar. The amplitudes must also be invariant under any transformations corresponding to any other symmetries of the system like parity transformations. This chapter follows the work of Williams, Anisovich et al., and Chung [41, 68, 40]. For the metric signature, we use the $(1, -1, -1, -1)$ convention.

C.1 Spin- $\frac{1}{2}$ representation

The spin- $\frac{1}{2}$ representation of the Lorentz group is given by the familiar Dirac spinors. (Technically there are also *chiral* spin- $\frac{1}{2}$ representations, but in a parity-invariant theory like QCD we need only consider the Dirac representation [69].) Dirac spinors have four components, however a spin- $\frac{1}{2}$ particle has only two independent degrees of freedom ($m_z = \pm\frac{1}{2}$). The Dirac equation provides two independent constraints on a spinor $u(p, m)$ with a given 4-momentum p and spin-projection m which reduce the number of independent components from four to two:

$$(\gamma^\mu p_\mu - w)u(p, m) = 0, \tag{C.1}$$

where $w = p^2$ is the mass of the particle, and γ^μ is a set of four 4 x 4 matrices that satisfy the condition

$$\gamma^\mu \gamma^\nu + \gamma^\nu \gamma^\mu = 2g^{\mu\nu}. \tag{C.2}$$

We will choose the following representation of the γ matrices:

$$\gamma^0 = \begin{pmatrix} 1 & 0 \\ 0 & -1 \end{pmatrix} \quad (\text{C.3})$$

$$\gamma^i = \begin{pmatrix} 0 & \sigma_i \\ -\sigma_i & 0 \end{pmatrix}, \quad (\text{C.4})$$

where σ_i are the Pauli matrices. We also define

$$\gamma^5 = i\gamma^0\gamma^1\gamma^2\gamma^3 = \begin{pmatrix} 0 & 1 \\ 1 & 0 \end{pmatrix}. \quad (\text{C.5})$$

It can be verified that $\gamma^\mu\gamma^5 + \gamma^5\gamma^\mu = 0$.

We can now construct the explicit form of the spinors. In the particle's rest frame (we only consider massive fermions), the momentum of the particle is given by $p_{\text{rf}} = (w, \vec{0})$ and the Dirac equation becomes

$$\begin{pmatrix} 0 & 0 \\ 0 & -2w \end{pmatrix} u(p_{\text{rf}}, m) = 0. \quad (\text{C.6})$$

The lower two components of the spinor are equal to zero and we can write

$$u(p_{\text{rf}}, m) = \sqrt{2w} \begin{pmatrix} \chi(m) \\ 0 \end{pmatrix}, \quad (\text{C.7})$$

where the factor of $\sqrt{2w}$ is due to normalization and

$$\chi(m = +\frac{1}{2}) = \begin{pmatrix} 1 \\ 0 \end{pmatrix}, \quad \chi(m = -\frac{1}{2}) = \begin{pmatrix} 0 \\ 1 \end{pmatrix} \quad (\text{C.8})$$

are 2-component spinors. The spinors given in (C.7) are eigenvectors of the J_z and J^2 operators and have the expected eigenvalues [70].

To get the spinor for arbitrary momentum, we just apply a boost in the appropriate direction to (C.7). The boost operator is given by Chung and the result of the boost is

$$u(p, m) = \sqrt{E+w} \begin{pmatrix} \chi(m) \\ \frac{\vec{\sigma} \cdot \vec{p}}{E+w} \chi(m) \end{pmatrix}, \quad (\text{C.9})$$

where $E = p^0$ is the energy of the particle.

We define the *adjoint* of a Dirac spinor

$$\bar{u} = u^\dagger \gamma^0. \quad (\text{C.10})$$

It can be shown that the *bilinear* forms $\bar{u}(p', m')u(p, m)$ and $\bar{u}(p', m')\gamma^5 u(p, m)$ are invariant under Lorentz transformations, while $\bar{u}(p', m')\gamma^\mu u(p, m)$ and $\bar{u}(p', m')\gamma^\mu\gamma^5 u(p, m)$ transform like vectors. The transformation under parity of these bilinears is discussed in section C.6.

We can now state the normalization condition

$$\bar{u}(p, m)u(p, m) = 2w, \quad (\text{C.11})$$

which explains the factor of $\sqrt{2w}$ in (C.7).

We also define the spin- $\frac{1}{2}$ projection operator

$$P^{(\frac{1}{2})}(p) = \frac{1}{2w} \sum_m u(p, m)\bar{u}(p, m) = \frac{1}{2w}(\gamma^\mu p_\mu + w). \quad (\text{C.12})$$

When acting on an arbitrary 4-component spinor Π , $P^{(\frac{1}{2})}(p)$ projects out a spinor that satisfies the Dirac equation with momentum p :

$$(\gamma^\mu p_\mu - w)P^{(\frac{1}{2})}(p)\Pi = \frac{1}{2w}(p^2 - w^2)\Pi = 0. \quad (\text{C.13})$$

We also see, that $P^{(\frac{1}{2})}(p)$, when acting on a spinor that does satisfy the Dirac equation (C.1), leaves the spinor unchanged. Thus $[P^{(\frac{1}{2})}]^2 = P^{(\frac{1}{2})}$ and it is a true projection operator. This operator is useful when writing amplitudes for processes with an intermediate-state fermion, where the operator $\sum_m u(p, m)\bar{u}(p, m)$ naturally arises. $P^{(\frac{1}{2})}$ is closely related to (i.e. is the numerator of) the standard fermion propagator.

C.2 Spin-1 representation

We use 4-vectors (i.e. rank-1 tensors) to provide a spin-1 representation of the Lorentz group.

We begin by considering massive vector particles. These have three degrees of freedom, but are described by polarization vectors with four components. The constraint equation

$$p_\mu \epsilon^\mu(p, m) = 0 \quad (\text{C.14})$$

reduces the number of independent components of a polarization vector $\epsilon^\mu(p, m)$ for a vector particle with given 4-momentum p and spin projection m .

In the rest frame of the particle $p_{\text{rf}} = (w, \vec{0})$, (C.14) tells us that the time component of the polarization vector vanishes. The explicit form of the rest-frame polarization vectors is given by

$$\epsilon^\mu(p_{\text{rf}}, \pm 1) = \mp \frac{1}{\sqrt{2}}(0, 1, \pm i, 0), \quad \epsilon^\mu(p_{\text{rf}}, 0) = (0, 0, 0, 1) \quad (\text{C.15})$$

so that they are eigenvectors of J^2 and J_z with the appropriate eigenvalues. The normalization condition is

$$\epsilon_\mu^*(p, m)\epsilon^\mu(p, m') = -\delta_{mm'}. \quad (\text{C.16})$$

To get the polarization vector for arbitrary momentum p , boost the rest-frame polarization vector:

$$\epsilon^\mu(p, m) = \Lambda^\mu{}_\nu(p)\epsilon^\nu(p_{\text{rf}}, m), \quad (\text{C.17})$$

where $\Lambda^\mu{}_\nu(p)$ is the operator that boosts p_{rf} to p .

We define the spin-1 projection operator

$$P_{\mu\nu}^{(1)}(p) = \sum_m \epsilon_\mu(p, m)\epsilon_\nu^*(p, m) = -g_{\mu\nu} + \frac{p_\mu p_\nu}{w^2} \equiv -g_{\mu\nu}^\perp(p). \quad (\text{C.18})$$

It is easy to show that $p^\mu g_{\mu\nu}^\perp(p) = p^\nu g_{\mu\nu}^\perp(p) = 0$. Thus for any arbitrary vector y^μ the vector $y_\mu^\perp = g_{\mu\nu}^\perp(p)y^\nu$ satisfies (C.14). As in the spin- $\frac{1}{2}$ case, this projector is the numerator of the massive vector boson propagator. Note that (C.18) is not a proper projector as $P_{\mu\nu}^{(1)}(p)P^{(1)\nu}{}_\beta(p) = -P_{\mu\beta}^{(1)}(p)$.

In the rest frame the projection operator takes on a particularly simple form:

$$g_{\mu\nu}^\perp(p_{\text{rf}}) = \begin{pmatrix} 0 & 0 & 0 & 0 \\ 0 & -1 & 0 & 0 \\ 0 & 0 & -1 & 0 \\ 0 & 0 & 0 & -1 \end{pmatrix}. \quad (\text{C.19})$$

C.2.1 Massless vector particles

Photons are massless so they must be treated differently. Massless vector bosons only have two spin states, corresponding to the helicities ± 1 , so we must choose an additional constraint on the polarization vector. This is known as gauge-fixing. We choose the Coulomb gauge:

$$\vec{k} \cdot \vec{\epsilon}(k, m) = 0. \quad (\text{C.20})$$

This constraint, along with (C.14) reduce the number of independent components in the photon polarization vector to two.

We consider only the case where the photon momentum is parallel to the z -axis. In this case, the spin states $m = \pm 1$ correspond with the helicity states $\lambda = \pm 1$. We write the polarization vectors as follows:

$$\epsilon^\mu(p = (k, 0, 0, k), \pm 1) = \mp \frac{1}{\sqrt{2}}(0, 1, \pm i, 0). \quad (\text{C.21})$$

Gauge invariance must be enforced in all reactions involving photons. All amplitudes describing process with an external photon line must contain a polarization vector corresponding to that photon. Thus they can be written

$$A = A^\mu \epsilon_\mu(k, m). \quad (\text{C.22})$$

Gauge invariance requires that

$$A^\mu k_\mu = 0, \quad (\text{C.23})$$

where k is the momentum of the photon. Dey explains why the amplitudes we construct below will not violate gauge invariance [12].

When discussing experiments with a polarized photon beam, the connection between the polarization of the beam and the helicity state of the photons is given in the density matrix formalism, discussed in Section 2.1.1.

C.3 Integer spin $J > 1$ polarization tensors

Spin-2 polarization tensors can be constructed using two spin-1 polarization vectors:

$$\epsilon_{\mu\nu}(p, m) = \sum_{m_1, m_2} (1m_1 1m_2 | 2m) \epsilon_\mu(p, m_1) \epsilon_\nu(p, m_2), \quad (\text{C.24})$$

where $(1m_1 1m_2 | 2m)$ is a Clebsch-Gordan coefficient.

We can use the same idea to iteratively build spin- J polarization tensors for arbitrary J :

$$\epsilon_{\mu_1 \dots \mu_J}(p, m) = \sum_{m_2 = -(J-1)}^{J-1} \sum_{m_1 = -1}^1 ((J-1)m_2 1m_1 | Jm) \epsilon_{\mu_1 \dots \mu_{J-1}}(p, m_2) \epsilon_{\mu_J}(p, m_1). \quad (\text{C.25})$$

A general rank- J tensor has 4^J independent elements, while a spin- J particle has only $2J+1$ degrees of freedom. The following conditions provide the needed constraints to eliminate these extra degrees of freedom:

$$p^{\mu_i} \epsilon_{\mu_1 \dots \mu_i \dots \mu_J}(p, m) = 0 \quad (\text{C.26})$$

$$\epsilon_{\mu_1 \dots \mu_i \dots \mu_j \dots \mu_J}(p, m) = \epsilon_{\mu_1 \dots \mu_j \dots \mu_i \dots \mu_J}(p, m) \quad (\text{C.27})$$

$$g^{\mu_i \mu_j} \epsilon_{\mu_1 \dots \mu_i \dots \mu_j \dots \mu_J}(p, m) = 0. \quad (\text{C.28})$$

It can be shown that the tensors defined in (C.25) automatically satisfy these conditions. The spin- J projection operator can be defined as

$$P_{\mu_1 \dots \mu_J \nu_1 \dots \nu_J}^{(J)}(p) = \sum_m \epsilon_{\mu_1 \dots \mu_J}(p, m) \epsilon_{\nu_1 \dots \nu_J}^*(p, m). \quad (\text{C.29})$$

Another form of projection operator projects out spin- J states of a rank- r tensor where $J \neq r$. We first must construct tensors that transform like spin- J states but are of rank r :

$$\epsilon_{\mu_1 \dots \mu_r}^J(p, m) = \sum_{m_1=-(r-1)}^{r-1} \sum_{m_2=-1}^1 ((r-1)m_1 1 m_2 | J m) \epsilon_{\mu_1 \dots \mu_{r-1}}(p, m_1) \epsilon_{\mu_r}(p, m_2). \quad (\text{C.30})$$

The projection operators are then

$$P_{\mu_1 \dots \mu_r \nu_1 \dots \nu_r}^{(J)}(p) = \sum_m \epsilon_{\mu_1 \dots \mu_r}^J(p, m) \epsilon_{\nu_1 \dots \nu_r}^{J*}(p, m). \quad (\text{C.31})$$

C.4 $J > \frac{1}{2}$ fermions

For particles with odd half-integer spin $J > \frac{1}{2}$, we construct objects by combining a Dirac spinor with a spin- n tensor (where $n = J - \frac{1}{2}$):

$$u_{\mu_1 \dots \mu_n}(p, m) = \sum_{m_1=-n}^n \sum_{m_2=-\frac{1}{2}}^{\frac{1}{2}} (n m_1 \frac{1}{2} m_2 | J m) \epsilon_{\mu_1 \dots \mu_n}(p, m_1) u(p, m_2). \quad (\text{C.32})$$

The Rarita-Schwinger conditions are needed to reduce the number of independent components to $2J + 1$ [71]:

$$(\gamma^\mu p_\mu - w) u_{\mu_1 \dots \mu_n}(p, m) = 0 \quad (\text{C.33})$$

$$u_{\mu_1 \dots \mu_i \dots \mu_j \dots \mu_n}(p, m) = u_{\mu_1 \dots \mu_j \dots \mu_i \dots \mu_n}(p, m) \quad (\text{C.34})$$

$$\gamma^{\mu_i} u_{\mu_1 \dots \mu_i \dots \mu_n}(p, m) = 0 \quad (\text{C.35})$$

$$p^{\mu_i} u_{\mu_1 \dots \mu_i \dots \mu_n}(p, m) = 0 \quad (\text{C.36})$$

$$g^{\mu_i \mu_j} u_{\mu_1 \dots \mu_i \dots \mu_j \dots \mu_n}(p, m) = 0. \quad (\text{C.37})$$

It can be shown that (C.32) satisfies all of these conditions.

The spin- J projector is

$$P_{\mu_1 \dots \mu_n \nu_1 \dots \nu_n}^{(J)}(p) = \frac{1}{2w} \sum_m u_{\mu_1 \dots \mu_n}(p, m) \bar{u}_{\nu_1 \dots \nu_n}(p, m). \quad (\text{C.38})$$

The explicit form of the spin-3/2 projection operator:

$$P_{\mu\nu}^{(\frac{3}{2})}(p) = P^{(\frac{1}{2})}(p) \left(g_{\mu\nu}^\perp(p) - \frac{1}{3} g_{\mu\alpha}^\perp(p) \gamma^\alpha g_{\nu\beta}^\perp(p) \gamma^\beta \right), \quad (\text{C.39})$$

where $P^{(\frac{1}{2})}(p)$ is given by (C.12). Analogously to (C.30) and (C.31) we can build spin- J projectors in rank- r space for half-integer J and $r \neq J - \frac{1}{2}$.

$$u_{\mu_1 \dots \mu_r}^J(p, m) = \sum_{m_1=-r}^r \sum_{m_2=\pm\frac{1}{2}} (r m_1 \frac{1}{2} m_2 | J m) \epsilon_{\mu_1 \dots \mu_r}(p, m_1) u(p, m_2). \quad (\text{C.40})$$

The projection operators are then

$$P_{\mu_1 \dots \mu_r \nu_1 \dots \nu_r}^{(J)}(p) = \frac{1}{2w} \sum_m u_{\mu_1 \dots \mu_r}^J(p, m) \bar{u}_{\nu_1 \dots \nu_r}^J(p, m). \quad (\text{C.41})$$

We will need the explicit form of the spin-1/2 projection operator in rank-1 space:

$$P_{\mu\nu}^{(\frac{1}{2})}(p) = P^{(\frac{1}{2})}(p) \frac{1}{3} g_{\mu\alpha}^\perp(p) \gamma^\alpha g_{\nu\beta}^\perp(p) \gamma^\beta. \quad (\text{C.42})$$

C.5 Orbital angular momentum tensors

We wish to write amplitudes in which two particles, a and b , are in a state with definite orbital angular momentum ℓ . We define the total momentum $P = p_a + p_b$ and the relative momentum $p_{ab} = \frac{1}{2}(p_a - p_b)$. To construct the orbital angular momentum tensor, we construct a rank- ℓ tensor out of the relative momentum and then project out the angular momentum ℓ part using (C.29):

$$L_{\mu_1 \dots \mu_\ell}^{(\ell)}(p_a, p_b) = (-1)^\ell \frac{(2\ell - 1)!!}{\ell!} P_{\mu_1 \dots \mu_\ell \nu_1 \dots \nu_\ell}^{(\ell)}(P) p_{ab}^{\nu_1} \dots p_{ab}^{\nu_\ell}. \quad (\text{C.43})$$

The normalization used here follows Anisovich et al. [68]. These tensors satisfy the following relations:

$$P^{\mu_i} L_{\mu_1 \dots \mu_i \dots \mu_\ell}^{(\ell)}(p_a, p_b) = 0 \quad (\text{C.44})$$

$$L_{\mu_1 \dots \mu_i \dots \mu_j \dots \mu_\ell}^{(\ell)}(p_a, p_b) = L_{\mu_1 \dots \mu_j \dots \mu_i \dots \mu_\ell}^{(\ell)}(p_a, p_b) \quad (\text{C.45})$$

$$g^{\mu_i \mu_j} L_{\mu_1 \dots \mu_i \dots \mu_j \dots \mu_\ell}^{(\ell)}(p_a, p_b) = 0. \quad (\text{C.46})$$

C.6 Parity

In addition to Lorentz transformations (boosts and rotations), we must also consider parity transformations. Since we only consider strong processes, all the amplitudes we write down must be invariant under parity. So we must understand how our tensors and spinors transform under parity.

Under parity, a 4-vector transforms like so:

$$p^\mu \rightarrow \mathbf{P}^\mu{}_\nu p^\nu, \quad (\text{C.47})$$

where

$$\mathbf{P}^\mu{}_\nu = \begin{pmatrix} +1 & 0 & 0 & 0 \\ 0 & -1 & 0 & 0 \\ 0 & 0 & -1 & 0 \\ 0 & 0 & 0 & -1 \end{pmatrix} \quad (\text{C.48})$$

flips the sign of the spatial components of the 4-vector while preserving the time component.

A pseudovector transforms like:

$$a^\mu \rightarrow -\mathbf{P}^\mu{}_\nu a^\nu. \quad (\text{C.49})$$

So the polarization vector of a spin-1 particle will transform like

$$\epsilon^\mu \rightarrow -\eta \mathbf{P}^\mu{}_\nu \epsilon^\nu, \quad (\text{C.50})$$

where η is the intrinsic parity of the particle.

The transformation of higher spin- ℓ polarization tensors can be found through the construction in terms of a combination of ℓ spin-1 tensors (C.25). For example, to build a positive-parity rank-2 tensor, we just combine two (negative-parity) vectors according to (C.24). The transformation under parity is then easily found using (C.50) and (C.24). Likewise, the transformation of the orbital angular momentum tensors $L^{(\ell)}$ can be found from their construction in terms of a product of ℓ momentum vectors using (C.43) and (C.47).

Chung gives the transformation of spinors under parity:

$$u(p, m) \rightarrow \eta \gamma^0 u(p, m) \quad (\text{C.51})$$

$$\bar{u}(p, m) \rightarrow \eta \bar{u}(p, m) \gamma^0, \quad (\text{C.52})$$

where η is the intrinsic parity of the spin- $\frac{1}{2}$ particle.

Using the identities $\gamma^0\gamma^0 = 1$, $\gamma^0\gamma^5\gamma^0 = -\gamma^5$, and $\gamma^0\gamma^\mu\gamma^0 = \gamma^{\mu\dagger} = \mathbf{P}^\mu_\nu\gamma^\nu$ and the shorthand forms $\bar{u}_f = \bar{u}(p_f, m_f)$ and $u_i = u(p_i, m_i)$, we find the bilinear forms transform in the following way under parity:

$$\bar{u}_f u_i \rightarrow \eta_i \eta_f \bar{u}_f u_i \quad (\text{C.53})$$

$$\bar{u}_f \gamma^5 u_i \rightarrow -\eta_i \eta_f \bar{u}_f \gamma^5 u_i \quad (\text{C.54})$$

$$\bar{u}_f \gamma^\mu u_i \rightarrow \eta_i \eta_f \mathbf{P}^\mu_\nu \bar{u}_f \gamma^\nu u_i \quad (\text{C.55})$$

$$\bar{u}_f \gamma^\mu \gamma^5 u_i \rightarrow -\eta_i \eta_f \mathbf{P}^\mu_\nu \bar{u}_f \gamma^\nu \gamma^5 u_i. \quad (\text{C.56})$$

$\bar{u}_f u_i$ and $\bar{u}_f \gamma^5 u_i$ are either scalars or pseudoscalars depending on the parities of the particles involved. As discussed in section C.1, both $\bar{u}_f \gamma^\mu u_i$ and $\bar{u}_f \gamma^\mu \gamma^5 u_i$ transform like vectors under Lorentz transformations, so these quantities are either pseudovectors or vectors, again depending on the intrinsic parities.

For the higher spin fermions, we look at (C.32). For example, to build a $\frac{3}{2}^-$ fermion, we would combine a spinor that transforms like a $\frac{1}{2}^+$ with a normal vector according to (C.32). For spin- $\frac{3}{2}^+$ combine a $\frac{1}{2}^-$ spinor with a vector. For a spin- $\frac{5}{2}^+$ particle combine a $\frac{1}{2}^+$ spinor with a (positive-parity) rank-2 polarization tensor. Etc.

C.7 $J^P \rightarrow NV$

We write the amplitudes for a baryon with J^P coupling to a nucleon ($\frac{1}{2}^+$ baryon) and a vector (1^-) particle. There are a few additional subtleties if the vector particle is a real photon.

The momenta of the $\frac{1}{2}^+$ baryon and the vector particle are denoted by p_N and p_V respectively. $P = p_N + p_V$ is the momentum of the J^P baryon and $p_{pV} = \frac{1}{2}(p_N - p_V)$ is the relative momentum of the NV system. The z -components of spin are given by m_N , m_V , and M .

The construction of these amplitudes follows Williams and Anisovich et al. [41, 68].

C.7.1 Angular Momentum Coupling

The spins of the pV system couple to form a system with total spin $s = \frac{1}{2}$ or $s = \frac{3}{2}$. The spin can then couple with an orbital angular momentum ℓ in the following way:

$\ell = 0$	$s = \frac{1}{2}$	$\frac{1}{2}^-$
	$s = \frac{3}{2}$	$\frac{3}{2}^-$
$\ell = 1$	$s = \frac{1}{2}$	$\frac{1}{2}^+, \frac{3}{2}^+$
	$s = \frac{3}{2}$	$\frac{1}{2}^+, \frac{3}{2}^+, \frac{5}{2}^+$
$\ell = 2$	$s = \frac{1}{2}$	$\frac{3}{2}^-, \frac{5}{2}^-$
	$s = \frac{3}{2}$	$\frac{1}{2}^-, \frac{3}{2}^-, \frac{5}{2}^-, \frac{7}{2}^-$
$\ell = 3$	$s = \frac{1}{2}$	$\frac{5}{2}^+, \frac{7}{2}^+$
	$s = \frac{3}{2}$	$\frac{3}{2}^+, \frac{5}{2}^+, \frac{7}{2}^+, \frac{9}{2}^+$

By rearranging this table, we associate each J^P with two or three (ℓ, s) pairs:

$\frac{1}{2}^-$	$(0, \frac{1}{2}) (2, \frac{3}{2})$
$\frac{1}{2}^+$	$(1, \frac{1}{2}) (1, \frac{3}{2})$
$\frac{3}{2}^-$	$(0, \frac{3}{2}) (2, \frac{1}{2}) (2, \frac{3}{2})$
$\frac{3}{2}^+$	$(1, \frac{1}{2}) (1, \frac{3}{2}) (3, \frac{3}{2})$
$\frac{5}{2}^-$	$(2, \frac{1}{2}) (2, \frac{3}{2}) (4, \frac{3}{2})$
$\frac{5}{2}^+$	$(1, \frac{3}{2}) (3, \frac{1}{2}) (3, \frac{3}{2})$

C.7.2 $P = (-)^{J+\frac{1}{2}}$ amplitudes $(\frac{1}{2}^-, \frac{3}{2}^+, \frac{5}{2}^-, \dots)$

First we will look at the $\frac{1}{2}^-$ case before considering higher spins. $\frac{1}{2}^-$ couples to two (ℓ, s) combinations: $(0, \frac{1}{2})$ and $(2, \frac{3}{2})$. We must construct amplitudes using the complex conjugate of a polarization vector to represent the final state vector meson, a spinor for the initial state $\frac{1}{2}^-$, and an adjoint spinor for the final state nucleon.

The $\ell = 0$ orbital angular momentum tensor is just the unit operator, so the only way to write the S-wave amplitude is to contract the polarization vector with a gamma matrix. Due to the intrinsic parities involved, it is the $\bar{u}_f \gamma^\mu \gamma^5 u_i$ combination that will be a vector and must be coupled to the vector ϵ_μ to get a scalar amplitude:

$$A_{\frac{1}{2}^- \rightarrow pV}^{\ell=0; s=\frac{1}{2}} = \bar{u}(p_N, m_N) \epsilon_\mu^*(p_V, m_V) \gamma^\mu \gamma^5 u(P, M). \quad (\text{C.57})$$

For the D-wave amplitude, we must add a $L^{(2)}$ tensor. There is only one to write down a scalar amplitude:

$$A_{\frac{1}{2}^- \rightarrow pV}^{\ell=2; s=\frac{3}{2}} = \bar{u}(p_N, m_N) \epsilon_\mu^*(p_V, m_V) L^{(2)\mu\nu}(p_{pV}) \gamma_\nu \gamma^5 u(P, M). \quad (\text{C.58})$$

We need not consider the amplitude $\bar{u}_f \epsilon_\mu^* L^{(2)\nu} \gamma^\mu u_i$. It will vanish due to the traceless condition (C.46).

For higher spins $(\frac{3}{2}^+, \frac{5}{2}^-, \dots)$ there are three possible (ℓ, s) combinations: $(J - \frac{1}{2}, \frac{1}{2})$, $(J - \frac{1}{2}, \frac{3}{2})$, $(J + \frac{3}{2}, \frac{3}{2})$.

We begin by writing the amplitude for $(J + \frac{3}{2}, \frac{3}{2})$:

$$A_{JP \rightarrow pV}^{\ell=J+\frac{3}{2}; s=\frac{3}{2}} = \bar{u}(p_N, m_N) \epsilon^{*\mu_1}(p_V, m_V) L_{\mu_1 \mu_2 \dots \mu_\ell}^{(\ell)}(p_{pV}) \gamma^{\mu_2} \gamma^5 u^{\mu_3 \dots \mu_\ell}(P, M). \quad (\text{C.59})$$

This is the generalization of (C.58). The permutation of the various indices μ_i do not matter due to the symmetry conditions (C.45) and (C.34).

For the $\ell = J - \frac{1}{2}$ transition, we can write down two independent amplitudes:

$$A_{JP \rightarrow pV}^{\ell=J-\frac{1}{2}; 1} = \bar{u}(p_N, m_N) \epsilon^{*\nu}(p_V, m_V) L_{\mu_1 \dots \mu_\ell}^{(\ell)}(p_{pV}) \gamma_\nu \gamma^5 u^{\mu_1 \dots \mu_\ell}(P, M), \quad (\text{C.60})$$

which is the generalization of (C.57), and

$$A_{JP \rightarrow pV}^{\ell=J-\frac{1}{2}; 2} = \bar{u}(p_N, m_N) \epsilon_\nu^*(p_V, m_V) L_{\mu_1 \dots \mu_\ell}^{(\ell)}(p_{pV}) \gamma^{\mu_1} \gamma^5 u^{\nu \mu_2 \dots \mu_\ell}(P, M), \quad (\text{C.61})$$

which has no equivalent for $\frac{1}{2}^-$. Note that we do not consider the amplitude $\bar{u} \epsilon^{*\mu_1} L_{\mu_1 \dots \mu_\ell}^{(\ell)} \gamma_\nu \gamma^5 u^{\nu \mu_2 \dots \mu_\ell}$ since this would vanish due to (C.35).

Anisovich calls (C.60) the $s = \frac{1}{2}$ amplitude and (C.61) the $s = \frac{3}{2}$ amplitude, probably by analogy with the $\frac{1}{2}^-$ case. However, Williams writes the $s = \frac{1}{2}$ and $s = \frac{3}{2}$ amplitudes differently.

C.7.3 $P = (-)^{J-\frac{1}{2}}$ amplitudes $(\frac{1}{2}^+, \frac{3}{2}^-, \frac{5}{2}^+, \dots)$

For $\frac{1}{2}^+$ we have (ℓ, s) combinations $(1, \frac{1}{2})$ and $(1, \frac{3}{2})$. We can write down two scalar amplitudes:

$$A_{\frac{1}{2}^+ \rightarrow pV}^{\ell=1; 1} = \bar{u}(p_N, m_N) \epsilon^{*\mu}(p_V, m_V) L_\mu^{(1)}(p_{pV}) u(P, M), \quad (\text{C.62})$$

$$A_{\frac{1}{2}^+ \rightarrow pV}^{\ell=1; 2} = \bar{u}(p_N, m_N) \epsilon^{*\mu}(p_V, m_V) L^{(1)\nu}(p_{pV}) \gamma_\nu \gamma^5 u(P, M). \quad (\text{C.63})$$

Anisovich calls (C.63) the $s = \frac{1}{2}$ amplitude and (C.62) the $s = \frac{3}{2}$ amplitude. (C.63) is called the $s = \frac{1}{2}$ amplitude by analogy to the $\frac{1}{2}^-$ amplitudes, where the $s = \frac{1}{2}$ amplitude is formed by contracting the polarization vector with a γ matrix.

Williams writes the amplitudes differently:

$$A_{\frac{1}{2}^+ \rightarrow pV}^{\ell=1; s=\frac{1}{2}, \frac{3}{2}} = \bar{u}(p_N, m_N) \epsilon^{*\mu}(p_V, m_V) P_{\mu\nu}^{(s)}(P) L^{(1)\nu}(p_{pV}) u(P, M). \quad (\text{C.64})$$

Where the $P^{(s)}$ projects out either the $s = \frac{1}{2}$ or $s = \frac{3}{2}$ part of the system.

For higher spins ($\frac{3}{2}^-, \frac{5}{2}^+, \dots$) three (ℓ, s) combinations are possible: $(J - \frac{3}{2}, \frac{3}{2})$, $(J + \frac{1}{2}, \frac{1}{2})$, $(J + \frac{1}{2}, \frac{3}{2})$. The amplitudes for $\ell = J + \frac{1}{2}$ are similar to the $\frac{1}{2}^+$ amplitudes (C.62) and (C.63):

$$A_{J^P \rightarrow pV}^{\ell=J+\frac{1}{2}; 1} = \bar{u}(p_N, m_N) \epsilon^{*\mu_1}(p_V, m_V) L_{\mu_1 \dots \mu_\ell}^{(\ell)}(p_{pV}) u^{\mu_2 \dots \mu_\ell}(P, M), \quad (\text{C.65})$$

$$A_{J^P \rightarrow pV}^{\ell=J+\frac{1}{2}; 2} = \bar{u}(p_N, m_N) \epsilon_\nu^*(p_V, m_V) L_{\mu_1 \dots \mu_\ell}^{(\ell)}(p_{pV}) \gamma^\nu \gamma^{\mu_1} u^{\mu_2 \dots \mu_\ell}(P, M). \quad (\text{C.66})$$

Williams writes the equivalent amplitudes as follows (following (C.64)):

$$A_{J^P \rightarrow pV}^{\ell=J+\frac{1}{2}; s=\frac{1}{2}, \frac{3}{2}} = \bar{u}(p_N, m_N) \epsilon^{*\alpha}(p_V, m_V) P_{\alpha\nu}^{(s)}(P) L^{(\ell)\nu\mu_1\mu_2 \dots \mu_{\ell-1}}(p_{pV}) u_{\mu_1\mu_2 \dots \mu_{\ell-1}}(P, M). \quad (\text{C.67})$$

The $(J - \frac{3}{2}, \frac{3}{2})$ amplitude:

$$A_{J^P \rightarrow pV}^{\ell=J-\frac{3}{2}; s=\frac{3}{2}} = \bar{u}(p_N, m_N) \epsilon_\nu^*(p_V, m_V) L_{\mu_1\mu_2 \dots \mu_\ell}^{(\ell)}(p_{pV}) u^{\nu\mu_1\mu_2 \dots \mu_\ell}(P, M). \quad (\text{C.68})$$

Williams and Anisovich write this amplitude in the same way. Note that here we don't need a spin projection operator because we cannot construct a resonance with $J = l + \frac{3}{2}$ with $s = \frac{1}{2}$ (what this means is that adding a $s = \frac{1}{2}$ projector would make the amplitude vanish, while adding a $s = \frac{3}{2}$ projector would leave it unchanged).

C.8 $\gamma p \rightarrow J^P$

Since the photon is also a vector particle ($J^P = 1^-$), we might guess that the $\gamma p \rightarrow J^P$ amplitudes would be the same as the $J^P \rightarrow NV$ amplitudes above, after taking the complex conjugate to account for the flip of initial and final state particles. This is correct, though there is an additional subtlety introduced by the masslessness of the photon. With a massless photon, the amplitudes (C.59) and (C.60) give identical angular distributions and only differ by an energy-dependent scale factor [41]. Since we bin data in \sqrt{s} -bins this factor is not important. We would like to write down amplitudes in a more natural basis.

This is done in the multipole basis. We begin by coupling the photon (1^-) with arbitrary orbital angular momentum ℓ to form a system with spin-parity j^P . We then couple this system with the $\frac{1}{2}^+$ proton to get a system with J^P quantum numbers. We call multipoles with $p = (-1)^j$ electric multipoles and those with $p = (-1)^{j+1}$ magnetic. We label the electric multipoles $1^-, 2^+$ as $E1, E2$, etc. and magnetic multipoles as $1^+, 2^-$ as $M1, M2$, etc.

	j^P	J^P
$\ell = 0$	$1^- = E1$	$\frac{1}{2}^-, \frac{3}{2}^-$
$\ell = 1$	$0^+ = X$	$\frac{1}{2}^+$
	$1^+ = M1$	$\frac{1}{2}^+, \frac{3}{2}^+$
	$2^+ = E2$	$\frac{3}{2}^+, \frac{5}{2}^+$
$\ell = 2$	$1^- = E1$	$\frac{1}{2}^-, \frac{3}{2}^-$
	$2^- = M2$	$\frac{3}{2}^-, \frac{5}{2}^-$
	$3^- = E3$	$\frac{5}{2}^-, \frac{7}{2}^-$
$\ell = 3$	$2^+ = E2$	$\frac{3}{2}^+, \frac{5}{2}^+$
	$3^+ = M3$	$\frac{5}{2}^+, \frac{7}{2}^+$
	$4^+ = E4$	$\frac{7}{2}^+, \frac{9}{2}^+$

Although listed above, the 0^+ multipole does not actually exist. To see why, consider how we construct a multipole using the tensor formalism. We combine an orbital angular momentum tensor with a photon polarization vector and then project out the spin- j part:

$$P_{\alpha_1 \dots \alpha_\ell \beta \mu_1 \dots \mu_\ell \nu}^{(j)} L^{(\ell) \mu_1 \dots \mu_\ell} \epsilon^\nu. \quad (\text{C.69})$$

For the 0^+ multipole this becomes $P_{\alpha\beta\mu\nu}^{(0)} L^{(1)\mu} \epsilon^\nu$. We can evaluate this explicitly in the center of mass frame, with the photon momentum $(k, 0, 0, k)$ parallel to the z -axis. Construct the total momentum $P = (k + E_p, 0, 0, 0)$ and relative momentum $p = (\frac{1}{2}(k - E_p), 0, 0, k)$. Using (C.43), we find the angular momentum tensor is simply $L^{(1)} = (0, 0, 0, k)$. We can construct $P_{\alpha\beta\mu\nu}^{(0)}$ using (C.30) and (C.31):

$$\epsilon_{\mu\nu}^0(P) = \sqrt{\frac{1}{3}} \epsilon_\mu(P, m=1) \epsilon_\nu(P, m=-1) + \sqrt{\frac{1}{3}} \epsilon_\mu(P, m=-1) \epsilon_\nu(P, m=1) - \sqrt{\frac{1}{3}} \epsilon_\mu(P, m=0) \epsilon_\nu(P, m=0), \quad (\text{C.70})$$

$$P_{\alpha\beta\mu\nu}^{(0)}(P) = \epsilon_{\alpha\beta}^0(P) \epsilon_{\mu\nu}^{0*}(P). \quad (\text{C.71})$$

Using the explicit forms of the polarization vectors (C.15) and (C.21), we see that $\epsilon_{\mu\nu}^0(P) L^{(1)\mu} \epsilon^\nu(k, \pm 1) = 0$, because the first two terms in (C.70) vanish when contracted with $L^{(1)}$ and the last vanishes when contracted with $\epsilon(\pm 1)$, which are the only physical states of the photon. Thus $P_{\alpha\beta\mu\nu}^{(0)} L^{(1)\mu} \epsilon^\nu = 0$ and we cannot construct a 0^+ multipole. This is equivalent to showing that in the CM frame (with the photon momentum along the z -axis), the angular momentum only has a $m_\ell = 0$ component. Since the photon must have $m_\gamma = \pm 1$ the spin-projection of the multipole $m_j = m_\ell + m_\gamma$ must also be ± 1 so we cannot have a $j = 0$ multipole.

Rearranging the chart and removing the 0^+ multipole we see that the J^P couple with the multipoles as follows:

$\frac{1}{2}^+$	$M1$
$\frac{1}{2}^-$	$E1$
$\frac{3}{2}^+$	$M1, E2$
$\frac{3}{2}^-$	$E1, M2$
$\frac{5}{2}^+$	$E2, M3$
$\frac{5}{2}^-$	$M2, E3$

C.8.1 $P = (-)^{J+\frac{1}{2}}$ amplitudes $(\frac{1}{2}^-, \frac{3}{2}^+, \frac{5}{2}^-, \dots)$

Start with $\frac{1}{2}^-$, which only couples to the $E1$ multipole. Constructing the $E1$ multipole with $\ell = 0$ using (C.69), we get $P_{\mu\nu}^{(1)}(P)\epsilon^\nu(k, m)$ which is just $-\epsilon_\mu(k, m)$. So we can the amplitude as follows:

$$A_{\gamma p \rightarrow \frac{1}{2}^-}^{j^p=1^-} = \bar{u}(P, M)\gamma^\mu\gamma^5 u(p_i, m_i)\epsilon_\mu(k, m_\gamma). \quad (\text{C.72})$$

We see that higher spins couple with the $M(J - \frac{1}{2})$ and $E(J + \frac{1}{2})$ multipoles, which can be constructed with $\ell = J - \frac{1}{2}$. The amplitude for both $j = J - \frac{1}{2}$ and $j = J + \frac{1}{2}$ is

$$A_{\gamma p \rightarrow J^p}^{j^p} = \bar{u}^{\mu_1 \dots \mu_\ell}(P, M)\gamma^\nu\gamma^5 u(p_i, m_i)P_{\mu_1 \dots \mu_\ell \nu \alpha_1 \dots \alpha_\ell}^{(j)}(P)L^{(\ell)\alpha_1 \dots \alpha_\ell}(p_{p\gamma})\epsilon^\beta(k, m_\gamma). \quad (\text{C.73})$$

C.8.2 $P = (-)^{J-\frac{1}{2}}$ amplitudes $(\frac{1}{2}^+, \frac{3}{2}^-, \frac{5}{2}^+, \dots)$

In this case, the J^P baryon couples to $E(J - \frac{1}{2})$ and $M(J + \frac{1}{2})$ multipoles (although there's no $j = J - \frac{1}{2}$ multipole for $J^P = \frac{1}{2}^+$), which can both be constructed with $\ell = J + \frac{1}{2}$:

$$A_{\gamma p \rightarrow J^p}^{j^p} = \bar{u}^{\mu_1 \dots \mu_{\ell-1}}(P, M)\gamma^{\mu_\ell}\gamma^\nu u(p_i, m_i)P_{\mu_1 \dots \mu_{\ell-1} \nu \alpha_1 \dots \alpha_{\ell-1}}^{(j)}(P)L^{(\ell)\alpha_1 \dots \alpha_{\ell-1}}(p_{p\gamma})\epsilon^\beta(k, m_\gamma). \quad (\text{C.74})$$

C.9 $\frac{3}{2}^- \rightarrow \frac{1}{2}^+ 0^-$

In this section we investigate the decay of a $\frac{3}{2}^-$ baryon to a $\frac{1}{2}^+$ baryon and pseudoscalar meson. This covers both the NK and $\Sigma\pi$ decay modes of the $\Lambda(1520)$. We have already written down this decay amplitude in the helicity formalism (2.40). Here we use the tensor formalism to integrate with our other amplitudes in this chapter.

The decay can only proceed in the D-wave. The amplitude is straightforward to write down:

$$A_{\frac{3}{2}^- \rightarrow \frac{1}{2}^+ 0^-} = \bar{u}(p_{\frac{1}{2}^+}, m_{\frac{1}{2}^+})\gamma^\mu\gamma^5 L_{\mu\nu}^{(2)}(p)u^\nu(p_{\frac{3}{2}^-}, m_{\frac{3}{2}^-}), \quad (\text{C.75})$$

where $p = \frac{1}{2}(p_{\frac{1}{2}^-} - p_{0^-})$. According to the parity transformations given in section C.6, it looks like this amplitude is a pseudoscalar. But in fact, the pseudoscalar meson in the decay, which does not appear explicitly in the amplitude as written (since it transforms trivially under Lorentz transformations), contributes an extra factor of (-) parity, which makes the whole amplitude invariant under parity as it should be. One way to think about it is that the baryon ‘‘piece’’ of the amplitude is coupling to a pseudoscalar, so for the overall amplitude to be a scalar the baryon ‘‘piece’’ must be a pseudoscalar. Since the only quantity explicitly written in (C.75) is the baryon part, it looks like a pseudoscalar.

C.10 $J^P \rightarrow \frac{3}{2}^- 0^-$

Here we consider the decay of a J^P baryon into a $\frac{3}{2}^- 0^-$ system (such as the $\Lambda(1520)K$ system). It should be noted the amplitudes given here for the $J^P \rightarrow \frac{3}{2}^- 0^-$ decay are identical to those for $J^P \rightarrow \frac{3}{2}^+ 0^-$ (e.g. decay to $\Delta\pi$). The amplitude construction in this section follows the work of Anisovich et al. [68].

Different orbital angular momentum waves couple with the $\frac{3}{2}^- 0^-$ system in the following way:

$\ell = 0$	$\frac{3}{2}^+$
$\ell = 1$	$\frac{1}{2}^-, \frac{3}{2}^-, \frac{5}{2}^-$
$\ell = 2$	$\frac{1}{2}^+, \frac{3}{2}^+, \frac{5}{2}^+, \frac{7}{2}^-$
$\ell = 3$	$\frac{3}{2}^-, \frac{5}{2}^-, \frac{7}{2}^-, \frac{9}{2}^-$

C.10.1 $P = (-)^{J+\frac{1}{2}}$ amplitudes $(\frac{1}{2}^-, \frac{3}{2}^+, \frac{5}{2}^-, \dots)$

We see from the above table that the $P = (-)^{J+\frac{1}{2}}$ states couple with the $\ell = J - \frac{3}{2}$ and the $\ell = J + \frac{1}{2}$ waves.

The $\ell = J + \frac{1}{2}$ amplitude is

$$A_{J^P \rightarrow \frac{3}{2}^- 0^-}^{\ell=J+\frac{1}{2}} = \bar{u}^{\mu_1}(p_{\frac{3}{2}^-}, m_{\frac{3}{2}^-}) L_{\mu_1 \dots \mu_\ell}^{(\ell)}(p) u^{\mu_2 \dots \mu_\ell}(p_{J^P}, m_{J^P}), \quad (\text{C.76})$$

where p is the relative momentum of the $\frac{3}{2}^- 0^-$ system. As discussed in section C.9, the pseudoscalar meson secretly contributes an extra parity flip, so the amplitude is a scalar, even though it looks a pseudoscalar.

The $\ell = J - \frac{3}{2}$ amplitude is

$$A_{J^P \rightarrow \frac{3}{2}^- 0^-}^{\ell=J-\frac{3}{2}} = \bar{u}_\nu(p_{\frac{3}{2}^-}, m_{\frac{3}{2}^-}) L_{\mu_1 \dots \mu_\ell}^{(\ell)}(p) u^{\nu \mu_1 \dots \mu_\ell}(p_{J^P}, m_{J^P}). \quad (\text{C.77})$$

This decay is not possible with the $\frac{1}{2}^-$ state.

C.10.2 $P = (-)^{J-\frac{1}{2}}$ amplitudes $(\frac{1}{2}^+, \frac{3}{2}^-, \frac{5}{2}^+, \dots)$

This decay is possible with $\ell = J - \frac{1}{2}$ and $\ell = J + \frac{3}{2}$.

The $\ell = J + \frac{3}{2}$ amplitude:

$$A_{J^P \rightarrow \frac{3}{2}^- 0^-}^{\ell=J+\frac{3}{2}} = \bar{u}^{\mu_1}(p_{\frac{3}{2}^-}, m_{\frac{3}{2}^-}) L_{\mu_1 \dots \mu_\ell}^{(\ell)}(p) \gamma^{\mu_2} \gamma^5 u^{\mu_3 \dots \mu_\ell}(p_{J^P}, m_{J^P}). \quad (\text{C.78})$$

The $\ell = J - \frac{1}{2}$ amplitude:

$$A_{J^P \rightarrow \frac{3}{2}^- 0^-}^{\ell=J-\frac{1}{2}} = \bar{u}_\nu(p_{\frac{3}{2}^-}, m_{\frac{3}{2}^-}) L_{\mu_1 \dots \mu_\ell}^{(\ell)}(p) \gamma^{\mu_1} \gamma^5 u^{\nu \mu_2 \dots \mu_\ell}(p_{J^P}, m_{J^P}). \quad (\text{C.79})$$

This decay is not possible with the $\frac{1}{2}^+$ state.

C.11 Full amplitude

We must combine the results of the previous three sections to get the full amplitude for the process $\gamma p \rightarrow J^P \rightarrow K^+ \Lambda(1520) \rightarrow K^+ K^- p$. We combine the amplitudes for the three constituent processes, summing over the internal degrees of freedom M , the z -component of spin of the J^P state, and $m_{\frac{3}{2}}$, the z -component of spin of the $\Lambda(1520)$. The amplitude then depends on the remaining internal degrees of freedom (the multipole quantum numbers j^P , the resonance quantum numbers J^P , and the orbital angular momentum of the resonance decay ℓ), as well as the external degrees of freedom (m_γ , m_i , and m_f , the z -components of spin of the photon, the initial proton, and the final proton, respectively):

$$A_{\gamma p \rightarrow J^P \rightarrow K^+ \Lambda(1520) \rightarrow K^+ K^- p}^{J^P, j^P, \ell; m_i, m_f, m_\gamma} = \sum_M \sum_{m_{\frac{3}{2}}} A_{\frac{3}{2}^- \rightarrow \frac{1}{2}^+ 0^-}^{m_{\frac{3}{2}}, m_f} A_{J^P \rightarrow \frac{3}{2}^- 0^-}^{\ell, m_{\frac{3}{2}}, M} A_{\gamma p \rightarrow J^P}^{j^P, M, m_i, m_\gamma} \quad (\text{C.80})$$

If we were to write out the amplitude explicitly, the sum over M and $m_{\frac{3}{2}}$ would allow us to replace the Dirac spinors associated with these with projection operators using Equation (C.29).

C.12 How the amplitudes are really calculated

The qft++ software package [72] can compute amplitudes written in the tensor formalism like those above. However, as the number of indices in a tensor increases, the amount of memory required grows exponentially, so qft++ becomes impossibly slow for calculating amplitudes with high spin. This means that practically we must compute amplitudes without using the tensor formalism. We would like to construct a formula that matches the full amplitude (C.80), but without using tensors. We do this by using the helicity states as discussed by Chung [40], but rotating back to what Chung calls the canonical basis, so that the amplitudes will be labeled by z -components of spin m (as in (C.80)) rather than by helicities λ . We consider the process $\gamma p \rightarrow J^P \rightarrow J_1^{P_1} J_2^{P_2}$. The production ($\gamma p \rightarrow J^P$) proceeds via a specified multipole j^p with allowed couplings to J^P states as described above. The decay ($J^P \rightarrow 1, 2$) takes place through a specified (L, S) combination, where the allowed couplings again are as described above. We define $\ell_{\text{MP}} = J - \frac{1}{2}$ if $P = (-)^{J+\frac{1}{2}}$ and $\ell_{\text{MP}} = J + \frac{1}{2}$ otherwise. This is the orbital angular momentum needed to construct the multipole.

The amplitudes is split into two parts. The production part of the amplitude is written

$$\sqrt{E_i + w_p^2(E_\gamma)^{\ell_{\text{MP}}}} \sqrt{2\ell_{\text{MP}} + 1} (1m_\gamma \ell_{\text{MP}} 0 | j m_\gamma) (j m_\gamma \frac{1}{2} m_i | J M), \quad (\text{C.81})$$

where E_i and E_γ are the energies of the initial proton and photon, w_p is the proton mass, and m_γ , m_i , and M are the z -components of spin for the photon, proton, and J^P resonance. The first part of the amplitude includes a normalization factor from the proton and energy dependence from the angular momentum. The second part expresses the angular momentum coupling using Clebsch-Gordan coefficients. We notice immediately that this amplitude is not invariant. It depends on the frame you use. We must use the CM frame with the photon momentum parallel to the z -axis.

The decay part is written

$$\begin{aligned} & \sum_{\lambda_1 = -J_1}^{J_1} \sum_{\lambda_2 = -J_2}^{J_2} (p_1)^L \sqrt{2L + 1} N(J_1, \lambda_1) N(J_2, \lambda_2) (J_1 \lambda_1 J_2 - \lambda_2 | S \lambda_J) (L 0 S \lambda_J | J \lambda_J) \\ & \times D_{M \lambda_J}^{*J}(\phi_1, \theta_1, 0) D_{m_1 \lambda_1}^{J_1}(\phi_1, \theta_1, 0) D_{m_2 \lambda_2}^{J_2}(\phi_2, \theta_2, 0) \end{aligned} \quad (\text{C.82})$$

where $\lambda_J = \lambda_1 - \lambda_2$ and the N are normalization factors for the two final state particles. The first D matrix performs a rotation to “connect” the production amplitude with the decay amplitude. The second two D matrices relate the helicity states of the final state particles with the canonical states.

Multiplying the two pieces together, we get the full amplitude for a given $LS j^p$ combination. Since we have rotated back to the canonical basis, we can continue to use (C.75) to calculate the $\Lambda(1520) \rightarrow pK^-$ decay amplitude.

C.13 Mother fit and differential cross section extraction

In the mother fit, we use the amplitudes above to construct a very general model of $\Lambda(1520)$ photo-production with a large number of free parameters and fit this model to our data. The model does not tell us about the physics of the reaction, but simply gives us a distribution that matches the data, which allows us to calculate the acceptance. The acceptance is needed to extract differential cross section. It is based on the method of Williams [41].

The mother fits uses the full amplitude given in equation in Equation (C.80). The fit determines the weights to be given to each wave, that is to each set of internal quantum numbers (J^P, j^p, ℓ) allowed. Following Williams, the total amplitude used by the fit is

$$A_{m_i, m_f, m_\gamma}^{\text{total}} = \sum_{J^P} \sum_{j^p} \sum_{\ell} f_{j^p}(\theta_{J^P}) e^{i\phi_{J^P}} r_{J^P, \ell} A_{\gamma p \rightarrow J^P \rightarrow K^+ \Lambda(1520) \rightarrow K^+ K^- p}^{J^P, j^p, \ell; m_i, m_f, m_\gamma}, \quad (\text{C.83})$$

where θ_{JP} , ϕ_{JP} , and $r_{JP,\ell}$ are fit parameters. The ϕ_{JP} parameters allow relative phases between the different waves and the $r_{JP,\ell}$ set the strengths of the different waves and decay modes. f_{j^P} is given by:

$$f_{j^P}(\theta_{JP}) = \begin{cases} \cos \theta_{JP}, & \text{for electric multipoles} \\ \sin \theta_{JP}, & \text{for magnetic multipoles} \end{cases}, \quad (\text{C.84})$$

so that each θ_{JP} describes the ratio of electric to magnetic multipole production for the corresponding J^P wave (there is no θ_{JP} for $J^P = \frac{1}{2}^\pm$, since both these waves have only one possible multipole). This set of parameters does not exhaust every possible combination of fit amplitudes, but still should give the fit sufficient freedom to match the data.

For an unpolarized experiment we can derive the Lorentz-invariant intensity given the total amplitude (C.83) by squaring the amplitude and summing over spins:

$$|\mathcal{M}|^2 = \sum_{m_i, m_f, m_\gamma} |A_{m_i, m_f, m_\gamma}^{\text{total}}|^2. \quad (\text{C.85})$$

Once we multiply this by a phase space factor, it will be proportional to the number of events predicted by the model given by A^{total} . Accounting for detector acceptance, the number of events detected will be proportional to

$$|\mathcal{M}(\vec{\theta}, \vec{\alpha})|^2 \eta(\vec{\theta}) \phi(\vec{\theta}), \quad (\text{C.86})$$

where $\vec{\theta}$ are the kinematic variables, $\vec{\alpha}$ are the fit parameters, $\eta(\vec{\theta})$ is the acceptance, and $\phi(\vec{\theta})$ is the differential phase-space element. However, we do not need worry about the phase space here, because we bin in \sqrt{s} and our raw Monte Carlo events are distributed uniformly in phase space in all other variables. We have already discussed how to handle acceptance in maximum likelihood fitting using the Monte Carlo method (Section A.1). So to fit our model to the data, we just use Equations (A.12) and (A.9), where our theoretical distribution (denoted as W in Appendix A) is just $|\mathcal{M}(\vec{\theta}, \vec{\alpha})|^2$. Of course, data events in the fit are weighted by the appropriate Q-values.

We do a fit independently in each \sqrt{s} bin. After fitting, we can compute differential cross sections. The differential cross section is not directly extracted from the amplitudes from the fit, but the amplitudes are used to calculate the acceptance. To calculate the differential cross section, we need information on the target, the flux of incident photons, the number of detected events, and the acceptance:

$$\frac{d\sigma}{d\cos\theta} = \left(\frac{m}{\mathcal{F}(\sqrt{s})\rho\ell} \right) \frac{\mathcal{Y}(\sqrt{s}, \cos\theta)}{\eta(\sqrt{s}, \cos\theta)\Delta\cos\theta BF}, \quad (\text{C.87})$$

where ρ , ℓ , and m are the density, length, and atomic mass of the target, $\mathcal{F}(\sqrt{s})$ is the number of photons incident on the target in a given \sqrt{s} bin, $\mathcal{Y}(\sqrt{s}, \cos\theta)$ is the number of detected events in the $(\sqrt{s}, \cos\theta)$ bin, $\eta(\sqrt{s}, \cos\theta)$ is the efficiency in the same bin, $\Delta\cos\theta$ is the width of the $\cos\theta$ bin, and BF is the branching fraction of the detected decay. The ‘‘ $\cos\theta$ ’’ in (C.87) could actually be any kinematic variable, but we will use the production angle in the center-of-mass frame $\cos\theta_{CM}^{K^+}$ and bins of width $\Delta\cos\theta = 0.1$. The average target density is $\rho = 0.7177 \text{ g/cm}^3$ [41], the target length is $\ell = 40 \text{ cm}$, and the target hydrogen mass $m = 1.008 \text{ amu} = 1.673 \times 10^{-27} \text{ kg}$. The PDG lists the branching fraction for $\Lambda(1520) \rightarrow N\bar{K}$ as $45 \pm 1\%$, and by isospin symmetry we expect equal number of decays to $n\bar{K}^0$ as to pK^- , so we use $BF(\Lambda(1520) \rightarrow pK^-) = 0.225$. We will discuss how $\mathcal{F}(\sqrt{s})$ is calculated in Section C.13.1 below. Because of the presence of background, we do not actually count the number of detected events. Instead we calculate the yield using our probabilistic event weights, determined using the procedures in Chapter 6:

$$\mathcal{Y}(\sqrt{s}, \cos\theta) = \sum_i Q_i, \quad (\text{C.88})$$

where the sum is over all detected events in the $(\sqrt{s}, \cos \theta)$ bin. The acceptance is calculated using the results of the mother fit in the given \sqrt{s} bin:

$$\eta(\sqrt{s}, \cos \theta) = \frac{\sum_{i \in \text{acc}} |\mathcal{M}_i|^2}{\sum_{i \in \text{raw}} |\mathcal{M}_i|^2}, \quad (\text{C.89})$$

where the sums only include events in the given $(\sqrt{s}, \cos \theta)$ bin and $|\mathcal{M}_i|^2$ is calculated using the kinematics from event i and the best fit parameters from the mother fit.

The total systematic error for the $\gamma p \rightarrow \phi p$ differential cross sections as measured in the g11a dataset using the $\phi \rightarrow K^+ K^-$ decay mode and the $pK^+(K^-)$ topology is about 11% and the largest contribution is from the normalization uncertainty [66]. Since the two processes have the same final state, this is probably a good estimate of the systematic uncertainty of the $\gamma p \rightarrow K^+ \Lambda(1520)$ cross section as measured with the $\Lambda(1520) \rightarrow pK^-$ decay in the same dataset. Although the systematic error might be somewhat greater for the $\Lambda(1520)$ due to the difficult background subtraction.

Actually, when we present our differential cross section measurements in Section 6.5, we show $\frac{d\sigma}{dt}$ rather than $\frac{d\sigma}{d \cos \theta}$ to facilitate comparisons with other measurements. The two quantities simply differ by a factor of $\frac{dt}{d \cos \theta}$. We can show that

$$t = m_K^2 - 2k\sqrt{m_K^2 + p^2} + 2pk \cos \theta, \quad (\text{C.90})$$

where p is the K^+ momentum in the CM frame, k is the photon energy in the CM frame and m_K is the charged K mass, so that

$$\frac{dt}{d \cos \theta} = 2pk. \quad (\text{C.91})$$

In addition to the differential cross section, we can also project out the spin density matrix elements directly from the fit amplitude, once we have determined the fit parameters that best describe the data. This is discussed in Section 2.2.6. We use the parameters from the mother fit, but a slightly different amplitude: instead of the full amplitude (C.83), we leave off the $\Lambda(1520) \rightarrow pK^-$ decay amplitude and the sum over $\Lambda(1520)$ spin states, so that the amplitude is labeled by $m_{\Lambda(1520)}$ instead of m_f . Then we can get the SDMEs from Equation (2.30). Since we set up these amplitudes with the z -axis defined as the direction of the photon momentum, the SDMEs extracted by this method will not be in the Gottfried-Jackson or helicity frames which were discussed earlier, but in the so-called Adair frame. However, they can easily be rotated to the desired frame. This approach to extracting the SDMEs has the advantage that the extracted spin density matrix elements can never have an unphysical value, but it has the disadvantage that, within the same \sqrt{s} bin, SDMEs at different $\cos \theta$ values are not independent measurements but are highly correlated. We do not use this approach.

C.13.1 Photon flux and normalization

To find the number of photons incident on the target, we determine the rate of electrons reaching the tagger and adjust this rate to account for photons produced at the radiator that do not reach the target. To get the flux in a given energy range, we look at the rate of hits in the corresponding tagger T-counter, but to get an unbiased estimate, we must not consider the T-counter that fired the trigger, only “out-of-time” counters. We must also know what percentage of beam photons reach the target. To do this, a total absorption counter is placed at the target during special low-current normalization runs. This will tell us the ratio of photons at the target to T-counter hits. This ratio is about 0.8, but is energy dependent. The flux is calculated in this manner by the gflux program [73].

In addition, corrections must be made for the amount of time the detector is available to take data. These live-time corrections are discussed by Williams [41].

Appendix D

Table of results and additional plots

D.1 Table of spin density matrix elements

\sqrt{s} (MeV)	$\cos \theta_{CM}^{K^+}$	ρ_{11}	$\sigma_{11}^{\text{stat}}$	σ_{11}^{sys}	$\text{Re } \rho_{31}$	$\sigma_{31}^{\text{stat}}$	σ_{31}^{sys}	$\text{Re } \rho_{3-1}$	$\sigma_{3-1}^{\text{stat}}$	$\sigma_{3-1}^{\text{sys}}$
2070	-0.9	0.350	0.066	0.046	-0.125	0.063	0.082	-0.022	0.054	0.061
2070	-0.7	0.217	0.067	0.046	-0.182	0.071	0.082	0.008	0.069	0.061
2070	-0.5	0.340	0.044	0.046	0.015	0.041	0.082	0.124	0.044	0.061
2070	-0.3	0.294	0.059	0.046	-0.023	0.049	0.082	0.183	0.068	0.061
2070	-0.1	0.123	0.029	0.046	0.026	0.037	0.082	0.135	0.056	0.061
2070	0.1	0.179	0.029	0.046	-0.007	0.041	0.082	0.178	0.049	0.061
2070	0.3	0.187	0.021	0.046	0.053	0.030	0.082	0.141	0.030	0.061
2070	0.5	0.249	0.018	0.046	0.019	0.022	0.082	0.093	0.016	0.061
2070	0.7	0.257	0.018	0.046	0.002	0.021	0.082	0.071	0.013	0.061
2070	0.85	0.159	0.056	0.046	0.023	0.031	0.082	0.035	0.017	0.061
2070	0.95	0.086	0.065	0.046	0.017	0.023	0.082	0.002	0.016	0.061
2130	-0.9	0.366	0.062	0.041	-0.056	0.078	0.080	0.003	0.043	0.055
2130	-0.7	0.376	0.028	0.041	0.074	0.043	0.080	-0.035	0.026	0.055
2130	-0.5	0.281	0.030	0.041	0.075	0.042	0.080	-0.000	0.036	0.055
2130	-0.3	0.259	0.023	0.041	0.015	0.033	0.080	0.032	0.032	0.055
2130	-0.1	0.201	0.016	0.041	0.055	0.022	0.080	0.035	0.026	0.055
2130	0.1	0.204	0.014	0.041	0.089	0.015	0.080	0.019	0.021	0.055
2130	0.3	0.241	0.014	0.041	0.044	0.012	0.080	0.100	0.019	0.055
2130	0.5	0.243	0.012	0.041	0.052	0.013	0.080	0.118	0.016	0.055
2130	0.7	0.239	0.010	0.041	-0.007	0.014	0.080	0.068	0.011	0.055
2130	0.85	0.263	0.021	0.041	-0.058	0.019	0.080	0.012	0.011	0.055
2130	0.95	0.234	0.040	0.041	0.000	0.020	0.080	-0.000	0.010	0.055
2190	-0.9	0.347	0.062	0.053	-0.096	0.059	0.076	-0.027	0.035	0.097
2190	-0.7	0.392	0.030	0.053	-0.023	0.035	0.076	-0.012	0.022	0.097
2190	-0.5	0.355	0.023	0.053	0.054	0.029	0.076	-0.024	0.020	0.097
2190	-0.3	0.296	0.020	0.053	0.115	0.023	0.076	-0.008	0.021	0.097
2190	-0.1	0.241	0.014	0.053	0.112	0.015	0.076	0.032	0.018	0.097
2190	0.1	0.210	0.010	0.053	0.062	0.012	0.076	0.030	0.014	0.097
2190	0.3	0.213	0.010	0.053	0.036	0.008	0.076	0.072	0.013	0.097
2190	0.5	0.251	0.008	0.053	0.005	0.008	0.076	0.115	0.010	0.097

2190	0.7	0.256	0.008	0.053	-0.018	0.009	0.076	0.085	0.009	0.097
2190	0.85	0.270	0.015	0.053	-0.070	0.017	0.076	0.041	0.012	0.097
2190	0.95	0.190	0.051	0.053	0.026	0.027	0.076	0.040	0.013	0.097
2250	-0.9	0.247	0.070	0.085	-0.009	0.050	0.084	0.004	0.046	0.088
2250	-0.7	0.338	0.033	0.085	-0.016	0.029	0.084	-0.034	0.022	0.088
2250	-0.5	0.388	0.022	0.085	-0.011	0.024	0.084	-0.030	0.018	0.088
2250	-0.3	0.377	0.022	0.085	0.068	0.022	0.084	0.013	0.017	0.088
2250	-0.1	0.295	0.015	0.085	0.082	0.012	0.084	0.084	0.013	0.088
2250	0.1	0.271	0.009	0.085	0.055	0.010	0.084	0.105	0.010	0.088
2250	0.3	0.245	0.007	0.085	0.031	0.007	0.084	0.131	0.009	0.088
2250	0.5	0.244	0.007	0.085	-0.007	0.007	0.084	0.115	0.008	0.088
2250	0.7	0.255	0.008	0.085	-0.033	0.007	0.084	0.098	0.008	0.088
2250	0.85	0.273	0.015	0.085	-0.060	0.014	0.084	0.071	0.010	0.088
2250	0.95	0.152	0.053	0.085	0.001	0.026	0.084	0.061	0.014	0.088
2310	-0.9	0.275	0.064	0.065	0.025	0.050	0.087	-0.006	0.040	0.052
2310	-0.7	0.332	0.031	0.065	-0.028	0.031	0.087	0.028	0.024	0.052
2310	-0.5	0.384	0.021	0.065	-0.013	0.019	0.087	0.019	0.017	0.052
2310	-0.3	0.354	0.022	0.065	0.017	0.020	0.087	0.048	0.018	0.052
2310	-0.1	0.341	0.014	0.065	0.046	0.014	0.087	0.088	0.013	0.052
2310	0.1	0.296	0.010	0.065	0.036	0.009	0.087	0.133	0.009	0.052
2310	0.3	0.262	0.007	0.065	0.017	0.007	0.087	0.132	0.007	0.052
2310	0.5	0.248	0.006	0.065	0.009	0.006	0.087	0.120	0.007	0.052
2310	0.7	0.234	0.007	0.065	-0.033	0.007	0.087	0.102	0.007	0.052
2310	0.85	0.236	0.013	0.065	-0.064	0.012	0.087	0.088	0.011	0.052
2310	0.95	0.292	0.037	0.065	-0.036	0.022	0.087	0.036	0.012	0.052
2370	-0.9									
2370	-0.7	0.166	0.026	0.064	0.019	0.022	0.082	0.111	0.023	0.042
2370	-0.5	0.247	0.021	0.064	0.012	0.023	0.082	0.013	0.020	0.042
2370	-0.3	0.288	0.019	0.064	0.016	0.022	0.082	0.023	0.022	0.042
2370	-0.1	0.337	0.015	0.064	0.024	0.014	0.082	0.103	0.015	0.042
2370	0.1	0.310	0.011	0.064	0.042	0.009	0.082	0.147	0.009	0.042
2370	0.3	0.297	0.008	0.064	0.042	0.007	0.082	0.163	0.007	0.042
2370	0.5	0.258	0.006	0.064	0.022	0.006	0.082	0.156	0.008	0.042
2370	0.7	0.236	0.007	0.064	-0.023	0.007	0.082	0.131	0.007	0.042
2370	0.85	0.219	0.012	0.064	-0.057	0.012	0.082	0.113	0.012	0.042
2370	0.95	0.206	0.042	0.064	-0.063	0.023	0.082	0.028	0.014	0.042
2430	-0.9	0.205	0.059	0.043	0.002	0.036	0.072	0.150	0.042	0.037
2430	-0.7	0.275	0.030	0.043	0.026	0.027	0.072	0.114	0.025	0.037
2430	-0.5	0.285	0.022	0.043	0.048	0.025	0.072	-0.040	0.020	0.037
2430	-0.3	0.290	0.026	0.043	-0.047	0.029	0.072	-0.076	0.023	0.037
2430	-0.1	0.305	0.017	0.043	-0.001	0.015	0.072	0.062	0.015	0.037
2430	0.1	0.270	0.011	0.043	0.038	0.010	0.072	0.151	0.012	0.037
2430	0.3	0.296	0.008	0.043	0.040	0.008	0.072	0.178	0.008	0.037
2430	0.5	0.276	0.007	0.043	0.031	0.006	0.072	0.146	0.007	0.037
2430	0.7	0.229	0.007	0.043	-0.042	0.007	0.072	0.113	0.008	0.037
2430	0.85	0.210	0.013	0.043	-0.063	0.014	0.072	0.105	0.014	0.037
2430	0.95	0.240	0.036	0.043	-0.113	0.021	0.072	0.015	0.012	0.037
2490	-0.9	0.189	0.058	0.036	0.054	0.038	0.076	0.157	0.043	0.041
2490	-0.7	0.225	0.028	0.036	0.065	0.032	0.076	0.105	0.029	0.041
2490	-0.5	0.250	0.025	0.036	0.053	0.026	0.076	-0.067	0.018	0.041
2490	-0.3	0.303	0.022	0.036	-0.040	0.022	0.076	-0.020	0.023	0.041

2490	-0.1	0.306	0.018	0.036	0.008	0.017	0.076	0.070	0.018	0.041
2490	0.1	0.307	0.012	0.036	0.037	0.011	0.076	0.162	0.010	0.041
2490	0.3	0.286	0.009	0.036	0.050	0.008	0.076	0.175	0.008	0.041
2490	0.5	0.270	0.007	0.036	0.026	0.007	0.076	0.128	0.008	0.041
2490	0.7	0.239	0.007	0.036	-0.040	0.007	0.076	0.106	0.007	0.041
2490	0.85	0.234	0.012	0.036	-0.078	0.011	0.076	0.128	0.013	0.041
2490	0.95	0.241	0.030	0.036	-0.083	0.023	0.076	0.031	0.013	0.041
2550	-0.9	0.100	0.067	0.035	-0.030	0.046	0.070	0.165	0.048	0.038
2550	-0.7	0.193	0.043	0.035	0.069	0.050	0.070	-0.086	0.037	0.038
2550	-0.5	0.230	0.027	0.035	0.043	0.029	0.070	0.053	0.029	0.038
2550	-0.3	0.242	0.026	0.035	-0.014	0.025	0.070	-0.076	0.023	0.038
2550	-0.1	0.249	0.019	0.035	0.018	0.019	0.070	0.092	0.018	0.038
2550	0.1	0.302	0.012	0.035	0.057	0.012	0.070	0.152	0.011	0.038
2550	0.3	0.304	0.009	0.035	0.043	0.009	0.070	0.164	0.008	0.038
2550	0.5	0.289	0.007	0.035	0.032	0.008	0.070	0.138	0.008	0.038
2550	0.7	0.262	0.007	0.035	-0.030	0.007	0.070	0.090	0.007	0.038
2550	0.85	0.265	0.013	0.035	-0.095	0.011	0.070	0.117	0.013	0.038
2550	0.95	0.281	0.035	0.035	-0.126	0.019	0.070	0.015	0.011	0.038
2610	-0.9	0.061	0.101	0.037	-0.040	0.063	0.064	0.177	0.087	0.029
2610	-0.7	0.146	0.030	0.037	0.066	0.032	0.064	0.073	0.037	0.029
2610	-0.5	0.243	0.028	0.037	0.084	0.031	0.064	0.015	0.033	0.029
2610	-0.3	0.243	0.024	0.037	0.017	0.027	0.064	-0.047	0.027	0.029
2610	-0.1	0.260	0.018	0.037	0.021	0.019	0.064	0.056	0.018	0.029
2610	0.1	0.303	0.014	0.037	0.035	0.011	0.064	0.161	0.012	0.029
2610	0.3	0.304	0.010	0.037	0.044	0.008	0.064	0.153	0.008	0.029
2610	0.5	0.317	0.008	0.037	0.036	0.007	0.064	0.131	0.007	0.029
2610	0.7	0.268	0.006	0.037	-0.011	0.007	0.064	0.097	0.007	0.029
2610	0.85	0.294	0.011	0.037	-0.059	0.011	0.064	0.085	0.011	0.029
2610	0.95	0.317	0.024	0.037	-0.067	0.019	0.064	0.012	0.010	0.029
2670	-0.9	0.211	0.078	0.042	-0.171	0.069	0.068	-0.123	0.074	0.033
2670	-0.7	0.244	0.047	0.042	-0.017	0.045	0.068	-0.136	0.040	0.033
2670	-0.5	0.294	0.034	0.042	-0.023	0.039	0.068	-0.133	0.033	0.033
2670	-0.3	0.310	0.030	0.042	-0.039	0.033	0.068	-0.018	0.030	0.033
2670	-0.1	0.335	0.024	0.042	0.013	0.023	0.068	-0.004	0.022	0.033
2670	0.1	0.324	0.016	0.042	0.034	0.014	0.068	0.077	0.015	0.033
2670	0.3	0.307	0.012	0.042	0.024	0.010	0.068	0.150	0.010	0.033
2670	0.5	0.313	0.010	0.042	0.021	0.009	0.068	0.134	0.008	0.033
2670	0.7	0.295	0.008	0.042	-0.008	0.008	0.068	0.096	0.008	0.033
2670	0.85	0.300	0.012	0.042	-0.058	0.012	0.068	0.083	0.012	0.033
2670	0.95	0.302	0.028	0.042	-0.065	0.023	0.068	0.007	0.013	0.033
2730	-0.9	0.250	0.111	0.039	-0.160	0.088	0.068	0.024	0.091	0.026
2730	-0.7	0.357	0.052	0.039	-0.112	0.049	0.068	-0.052	0.041	0.026
2730	-0.5	0.298	0.041	0.039	-0.086	0.043	0.068	-0.027	0.040	0.026
2730	-0.3	0.272	0.033	0.039	-0.004	0.033	0.068	-0.067	0.032	0.026
2730	-0.1	0.317	0.024	0.039	0.006	0.024	0.068	0.008	0.023	0.026
2730	0.1	0.305	0.018	0.039	0.009	0.017	0.068	0.082	0.016	0.026
2730	0.3	0.302	0.013	0.039	0.031	0.012	0.068	0.123	0.012	0.026
2730	0.5	0.300	0.011	0.039	0.035	0.010	0.068	0.140	0.009	0.026
2730	0.7	0.301	0.008	0.039	-0.014	0.008	0.068	0.101	0.007	0.026
2730	0.85	0.309	0.012	0.039	-0.110	0.012	0.068	0.065	0.013	0.026
2730	0.95	0.256	0.032	0.039	-0.095	0.024	0.068	0.024	0.013	0.026

2790	-0.9				-0.122	0.146	0.070	-0.134	0.147	0.034
2790	-0.7	0.173	0.067	0.031	0.044	0.059	0.070	-0.112	0.070	0.034
2790	-0.5	0.245	0.045	0.031	0.077	0.042	0.070	-0.097	0.044	0.034
2790	-0.3	0.319	0.040	0.031	-0.101	0.039	0.070	-0.105	0.038	0.034
2790	-0.1	0.329	0.026	0.031	-0.084	0.024	0.070	-0.014	0.021	0.034
2790	0.1	0.327	0.020	0.031	-0.015	0.019	0.070	0.058	0.017	0.034
2790	0.3	0.314	0.015	0.031	0.019	0.014	0.070	0.106	0.012	0.034
2790	0.5	0.318	0.011	0.031	0.036	0.010	0.070	0.155	0.009	0.034
2790	0.7	0.304	0.008	0.031	-0.026	0.007	0.070	0.113	0.007	0.034
2790	0.85	0.334	0.013	0.031	-0.056	0.013	0.070	0.091	0.012	0.034
2790	0.95	0.259	0.031	0.031	-0.042	0.027	0.070	0.040	0.013	0.034

D.2 Additional plots

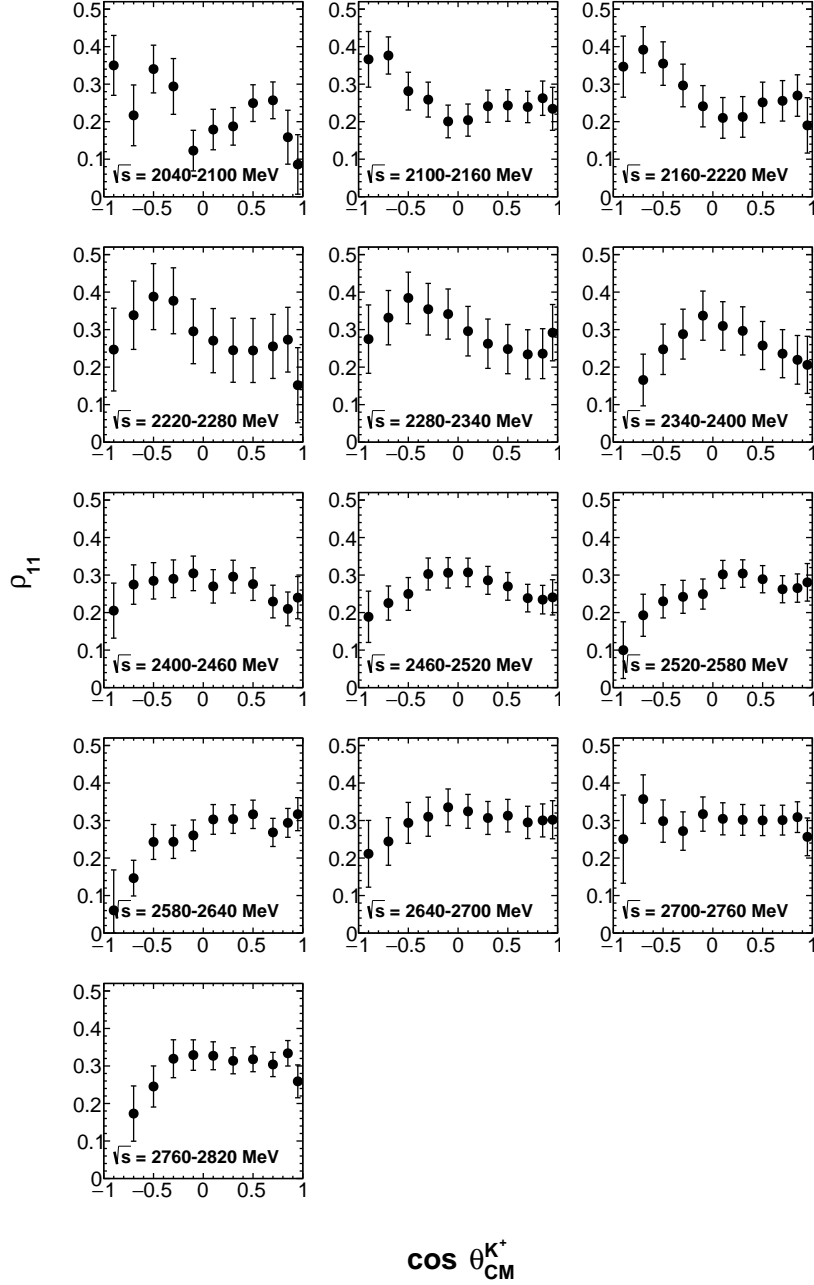


Figure D.1: ρ_{11} . All three topologies averaged. Error bars include statistical errors and all systematic errors. Points are the same as those in Figure 7.19.

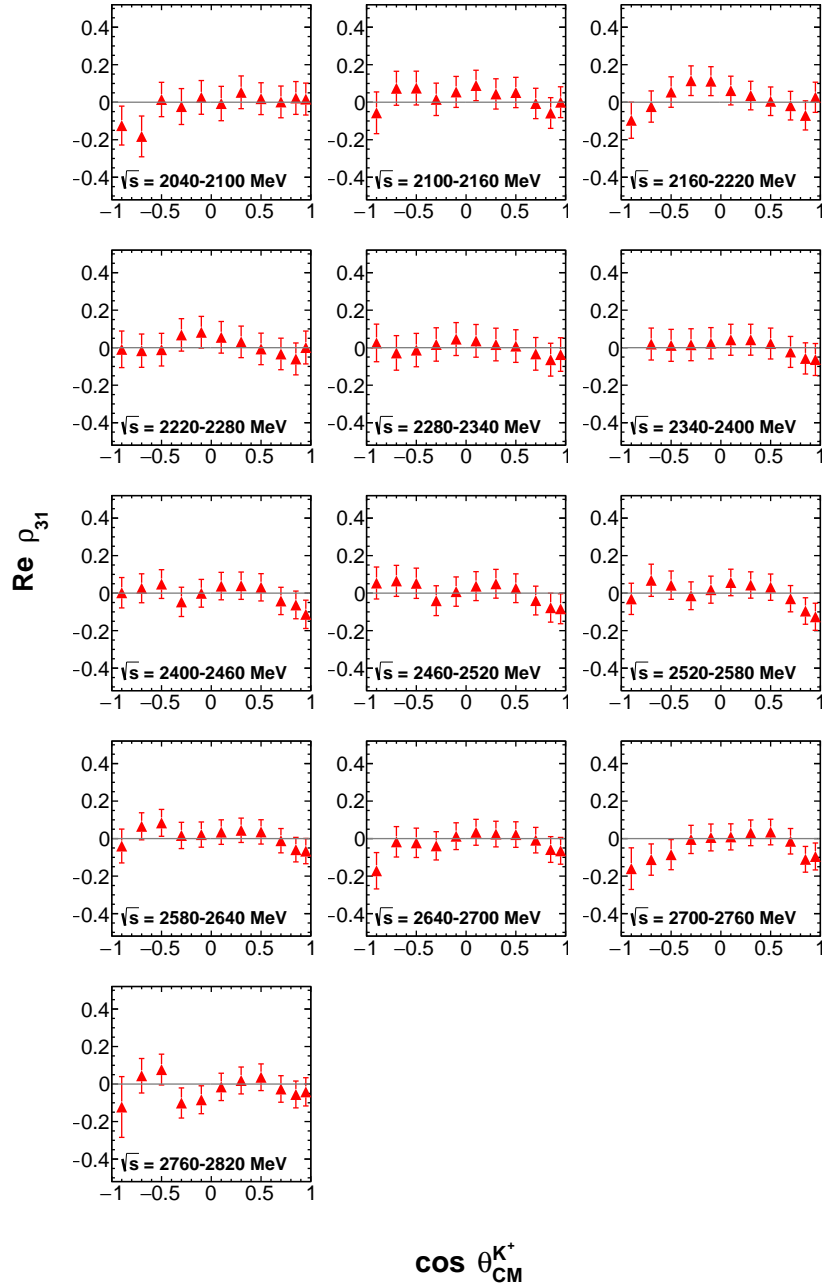


Figure D.2: $\text{Re } \rho_{31}$. All three topologies averaged. Error bars include statistical errors and all systematic errors. Points are the same as those in Figure 7.19.

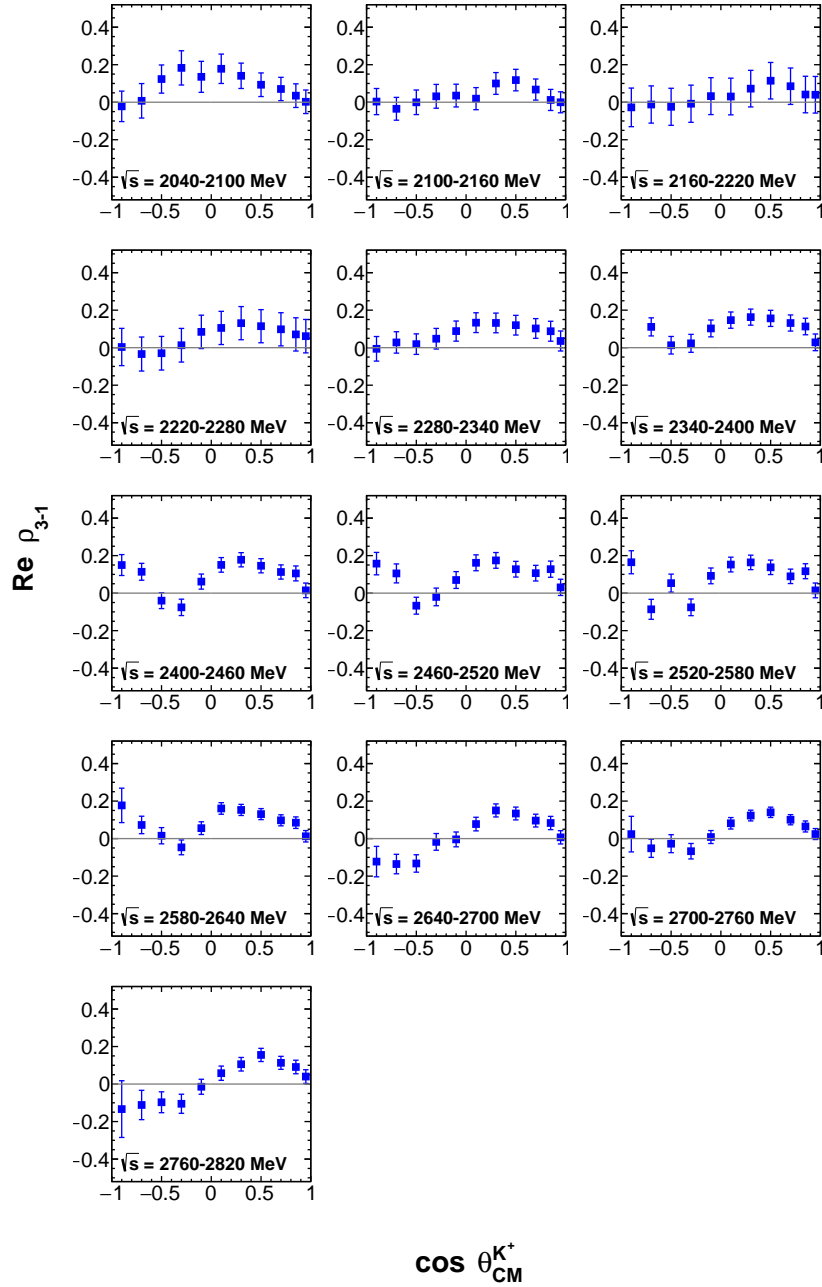


Figure D.3: $\text{Re } \rho_{3-1}$. All three topologies averaged. Error bars include statistical errors and all systematic errors. Points are the same as those in Figure 7.19.